Scuola Internazionale Superiore di Studi Avanzati - Trieste

B-MODE POLARIZATION EXPERIMENTS FOR THE COSMIC MICROWAVE BACKGROUND

Map-making and Foreground Modeling

GIUSEPPE PUGLISI

DISSERTATION SUBMITTED FOR THE DEGREE OF
"DOCTOR PHILOSOPHIÆ"

SUPERVISORS:
Carlo Baccigalupi
Giulio Fabbian

Academic Year 2016-2017
SISSA - Via Bonomea 265 - 34136 TRIESTE - ITALY

Giuseppe Puglisi : *B-mode Polarization Experiments for the Cosmic Microwave Background,* Map-making and Foreground Modeling, ©

SUPERVISORS:
Carlo Baccigalupi
Giulio Fabbian

EXTERNAL REFEREES:
Ingunn Kathrine Wehus
Paolo Natoli

Trieste , October 11, 2017

To Cate,
who shares the adventure of this life with me.

ABSTRACT

The Cosmic Microwave Background (CMB) is a relic radiation generated at the decoupling of matter and radiation as the temperature of the Universe dropped below 3000 K. As a probe of the early phases of the universe, it is made of tiny fluctuations (1 part over 100,000) where the seeds of structure formation are encoded. The study of temperature anisotropies in the CMB carried out by a plethora of satellite and ground-based experiments (COBE[1], BOOMERanG[2], MAXIMA[3], WMAP[4], Planck etc.) has been outstandingly successful measuring average properties of the Universe like geometry, matter-energy content and is one of the cornerstones of what has come to be called the standard cosmological model (known as Λ Cold Dark Matter, ΛCDM). It is worth noticing that the existence of Dark Energy, the latest cosmological component to be discovered, responsible for a late time phase of cosmic acceleration, has been discovered thanks to the CMB anisotropies in combination with high redshift Supernovae data.

Linear polarization of CMB anisotropies was expected from theory, so that in the last decades efforts for detection intensified and in 2002 the DASI[5] experiment succeeded for the first time. CMB polarization pattern can be decomposed into two scalar quantities called E- and B-modes. To date, most of the research studies aimed at observing the latter since they are related to the gravitational lensing of large scale structures at the arcminute angular scales, whereas at the degree scales, B-modes are induced by a stochastic background of gravitational waves produced during the inflationary era of the Universe. Unfortunately, the B-modes amplitude is expected to be orders of magnitude smaller, making their detection at large angular scales very challenging. To further worsen the situation and complicate this scenario, it has been found that the polarized emission from the Galaxy emitting at the very same frequencies represents one of the biggest obstacles in observing CMB polarization anisotropies. The list of Galactic foregrounds is long and includes anything between us and the CMB: thermal dust, synchrotron radiation, free-free (or bremsstrahlung) and several molecular line emissions all emanating from our Galaxy. All these emissions are partially polarized: synchrotron and dust are polarized at $\lesssim 20\%$ level, molecular lines are expected to be polarized at $\lesssim 1\%$, free-free emission is essentially considered unpolarized.

This is the reason of the recent effort to observe the CMB polarization in a very large range of frequencies to accurately know the distribution

1 COsmic Background Explorer
2 Balloon Observations Of Millimetric Extragalactic Radiation ANd Geophysics
3 Millimeter wave Anisotropy eXperiment IMaging Array
4 Wilkinson Microwave Anisotropy Probe
5 Degree Angular Scale Interferometer

in the sky and the frequency dependence of each Galactic polarized foreground. Moreover, such an investigation allows us to design data analysis algorithms known as component separation for extracting B-modes out of a multi-frequency experimental setup.

On the other hand, in order to constrain the inflation parameters from the faint B-mode signal, the CMB experiments have been constantly increasing the accuracy of the measurements by means of larger and larger samples of number of detectors in the focal plane. Reconstructing CMB maps is computationally expensive since it requires a lot of resources to compress trillions of time samples to pixels in a map: hence, for current and forthcoming CMB experiments, the map-making procedure is required to be computationally efficient and fast.

The work presented in this Thesis addresses both the challenges presented above in observing CMB B-modes and it has been further motivated by the needs of a specific CMB experiment, Polarbear, to which we belong. We have participated in the analysis of the first seasons of observations and specifically we developed and tested a map-making pipeline to process the data of the future seasons of observations. In the context of Galactic foregrounds, we built a model, `MCMole3D`, aimed at simulating Carbon Monoxide rotational lines emission in molecular clouds taking into account their 3D spatial distribution with different geometrical properties to assess the contamination to B-modes of an undetected molecular cloud which could be eventually observed within a patch of a ground based experiment.

Both investigations led to results which have been published and represent major contribution to the data analysis and simulation infrastructure of the experiment. Moreover, they are being further developed and expanded, for application in the ongoing and future Polarbear experiment, and other B-mode observations as well.

LIST OF PUBLICATIONS

1. Puglisi, G., Poletti, D., Fabbian, G., Baccigalupi, C., Stompor, R., and Heltai, L., (2017). Making polarization Cosmic Microwave Background maps with preconditioning, in preparation

2. The POLARBEAR Collaboration, (2017). A Measurement of the Cosmic Microwave Background BB-Mode Polarization Power Spectrum at Sub-Degree Scales from 2 years of POLARBEAR Data, arXiv:1705.02907

3. Puglisi, G., Fabbian, G., Baccigalupi, C., (2017). A 3D model for carbon monoxide molecular line emission as a potential cosmic microwave background polarization contaminant, Mon.Not.Roy.Astron.Soc. 469 (2017) no.3, 2982-2996 STX1029 doi: 10.1093/mnras/stx1029

4. Takakura, S., Aguilar, M., Akiba, Y., Arnold, K., Baccigalupi, C., et al., (2017). Performance of a continuously rotating half-wave plate on the POLARBEAR telescope, JCAP 1705 (2017) no.05, 008 doi: 10.1088/1475-7516/2017/05/008

5. Poletti, D., Fabbian, G., Jeune, M. Le, Peloton, J., Arnold, K., Baccigalupi, C., et al., (2016). Making maps of Cosmic Microwave Background polarization for B-mode studies: the POLARBEAR example. Astron.Astrophys. 600 (2017) A60. doi: 10.1051/0004-6361/201629467

6. Suzuki, A., Ade, P., Akiba, Y., Aleman, C., Arnold, K., Baccigalupi, C., et al., (2016). The Polarbear-2 and the Simons Array Experiments. Journal of Low Temperature Physics. doi: 10.1007/s10909-015-1425-4

7. Inoue, Y., Ade, P., Akiba, Y., Aleman, C., Arnold, K., Baccigalupi, C., et al., (2016). POLARBEAR-2: an instrument for CMB polarization measurements. Proc.SPIE Int.Soc.Opt.Eng. 9914. DOI: 10.1117/12.2231961

8. Stebor, N., Ade, P., Akiba, Y., Aleman, C., Arnold, K., Baccigalupi, C., et al., (2016). The Simons Array CMB polarization experiment. In W. S. Holland and J. Zmuidzinas (Eds.), Proc.SPIE Int.Soc.Opt.Eng. (Vol. 9914, p. 99141H). http://doi.org/10.1117/12.2233103

9. The EBEX Collaboration (2016). Temperature calibration of the E and B experiment, arXiv:1601.07923

10. The POLARBEAR Collaboration (2015). POLARBEAR constraints on cosmic birefringence and primordial magnetic fields. Physical Review D, 92(12), 123509. doi:10.1103/PhysRevD.92.123509.

11. Errard, J. and the Polarbear Collaboration (2015). Modelling atmospheric emission for CMB ground-based observations. The Astrophysical Journal, 809(1), 63. doi:10.1088/0004-637X/809/1/63

ACKNOWLEDGEMENTS

Viver
E não ter a vergonha de ser feliz
Cantar e cantar e cantar
A beleza de ser um eterno aprendiz
Ah meu Deus!
Eu sei, eu sei que a vida devia ser
Bem melhor e será mas isso nao impede
Que eu repita é bonita, é bonita e é bonita. [6]

— Gonzaguinha, *O que é? O que é?*

I sincerely thank first of all my advisor Carlo Baccigalupi: most of the work presented here started from a discussion with him in front of a cup of *Illy* coffee. He taught me that scientific research is a big adventure to be approached with enthusiasm and passion especially when the situations got hard. At the end of the PhD, I have realized that every aspect of life can be lived like this, as an opportunity for me.
Thanks to Giulio Fabbian, more than an advisor, he supported me as an *older brother* in everything happened during these years. Thanks for having patiently devoted me a lot of his time to deal with my confused ideas and questions about our research projects.
I thank Davide Poletti for having carefully read some of the chapters of this Thesis and for his sincere and useful comments about it.
I am very grateful to the Polarbear team at APC in Paris, led by Radek Stompor for the very useful chats we have had about the unbiased map-making methodologies, thanks for having given the opportunity to spent several months at APC.
I am very thankful to Adrian T. Lee and all the members of the Polarbear Collaboration: working on the data analysis of the experiment has been a great experience.
I am grateful to the whole Astrophysics Sector, especially to my PhD colleagues for making the fifth floor of SISSA building a lively and stimulating environment.

6 Life is not being afraid to be happy, sing the beauty of being eternally a learner. Oh Lord! I know life should be way better and surely it will, but this doesn't prevent me in repeating that life is beautiful.

CONTENTS

LIST OF FIGURES

LIST OF TABLES

ACRONYMS

CMB Cosmic Microwave Background

CES Constant Elevation Scan

TOD Time Ordered Data

PCG Preconditioned Conjugate Gradient

SPD Symmetric Positive Definite

r.h.s. right hand side of a given equation

RHS Right Hand Side vector of map-making linear system

BBN Big Bang Nucleosynthesis

MC Monte-Carlo

HGL High Galactic Latitude

SO Simons Observatory

SA Simons Array

S4 Stage 4 of CMB experiments

SVD Singular Value Decomposition

HFI High Frequency Instrument of Planck satellite

Part I

MODERN COSMOLOGY AND CMB OBSERVATIONS

In the first part of this work, we would like to introduce and give to the reader a general overview of the astrophysical context needed to present our research studies.

1 THE STANDARD COSMOLOGICAL MODEL

> The most incomprehensible thing of the Universe is that it is comprehensible.
>
> Albert Einstein

1.1 INTRODUCTION

It is really fascinating to state how long the path of mankind knowledge has been and see the realm of processes that nowadays we are able to explain and describe by means of very simple theories. Scientific answers can be given to the truly deep questions of where we have come from and where we are going. We think *cosmology* rose up when human kind started coping with those questions.

However, the cosmological studies changed abruptly in the last century (since the 1920's) because quite at the same time the theory of General Relativity, and observations opened an unforeseen scenario. However, in studying cosmology, both aspects have been combined together to increase our insight into what is happening. This was the case when Edwin Hubble in 1929 observed the velocity by means of Doppler shift z, of the emission lines of several extra-Galactic nebulae and measured their distances, d, by means of Cepheid stars in those. He found a very stunning proportionality relation:

$$z = \frac{H_0}{c} d, \tag{1.1}$$

meaning that the Universe is undergoing an expansion at a rate given by H_0 measured by Hubble to be $\sim 500 \mathrm{km\,s^{-1}\,Mpc^{-1}}$ (Hubble, 1929).

Moreover, (1.1) leads at large enough distances to super-luminal velocities $v = cz > c$[1]. This is not in contrast with the special relativity constraints,

1 In the following we assume natural units, i. e. $c, G, \hbar = 1$.

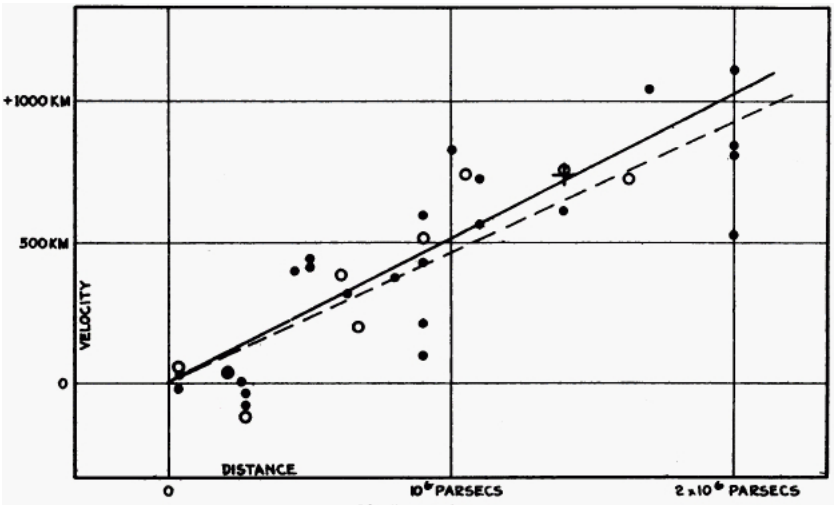

Figure 1.1: The first $v - R$ diagram drawn by Hubble (Hubble, 1929). The Hubble constant H_0 as been measured as the slope of the linear best fit line.

since it is the sapecetime itself which is expanding faster than the speed of light and it further suggests that a relativistic theory is required to describe the dynamics of the Universe and to relate density of mass and energy to the curvature of the spacetime. The curvature is specified by a *metric* tensor, which describe the line element in a curved spacetime. In the next section we address the problem of finding a metric of the Universe corresponding to the cosmological principle presented above.

1.2 THE FRIEDMANN-LEMAITRE-ROBERTSON-WALKER UNIVERSE

The (1.1) is referred as the *Hubble law* and it is in perfect agreement with the assumptions of the *cosmological principle* stating that *on the largest scales the Universe is both homogeneous and isotropic*.

Homogeneity means that it is invariant under translation and hence its general properties such as the density and the composition are the same everywhere. Isotropy means that it is rotationally invariant, i.e. its properties do not change by looking in different directions. Notice that the requirements to be the Universe isotropic *and* homogeneous is equivalent to the requirement that it appears isotropic from all locations. One of the consequences of the spatial homogeneity is that it must have the same curvature everywhere. From the *Manifold theory* (refer (Wald, 1984) for further readings), we know that only three possible geometries can have constant *Gaussian* curvature, K. $K = 0$ corresponds to a *flat* curvature, i.e. a plane in a three-dimensional analogy, whereas $K > 0$ and $K < 0$ correspond respectively to the surface of a three-dimensional sphere and of a hyperboloid. However, the Hubble law certifies that the Universe is evolving in time, i.e.

the Universe is *spatially* isotropic at a given time. By accounting all of these facts, we can write the spacetime metric as:

$$ds^2 = -dt^2 + R^2(t)d\Sigma^2 = -dt^2 + a^2(t)\left[\frac{dr^2}{1-Kr^2} + r^2(d\theta^2 + \sin^2\theta d\phi^2)\right] \quad (1.2)$$

where r, θ, ϕ are the *comoving coordinates*, i.e. the coordinates in a reference frame expanding with the Universe according to the *scale factor*, $a(t)$ that is a dimensionless quantity encoding the dynamics of the Universe; conventionally it is normalised to be $a_0 = a(t_0) = 1$ at the present time t_0. One may notice that if $\dot{a} > 0$, i.e. a grows with time, every observer sees other points in the Universe receding away radially, just as Vesto Slipher firstly observed in 1920. The (1.2) is usually known as the Friedmann-Lemaitre-Robertson-Walker (FLRW) metric (Wald, 1984) since they independently proposed and investigated these kinds of solutions to the Einstein field equations.

Since in cosmology we deal with distances, we firstly define the distance light could have travelled since the Big Bang $t = 0$ and it is usually referred as the *comoving horizon*,

$$\eta = \int_0^t \frac{dt'}{a(t')}, \quad (1.3)$$

since in a time dt light travels a comoving distance $dx = dt/a$. No information could have propagated further than η since $t = 0$. Thus regions separated by distance greater than η are not causally connected, for this reason the eq.(1.3) is also known as the *particle horizon*.

Another remarkable comoving distance is that between us and a distance object emitting radiation at scale factor $a(t) < 1$:

$$d(a) = \int_{t(a)}^t \frac{dt'}{a(t')} = \int_a^1 \frac{da'}{a'^2 H(a')}. \quad (1.4)$$

The velocity of such a galaxy at distance $d(a)$ is:

$$v = \dot{d} = \frac{\dot{a}}{a} d, \quad (1.5)$$

i.e. we recover the Hubble law (1.1) by identifying $H_0 = (\dot{a}/a)_{t_0}$.

It is very common to find H_0 parametrized as

$$H_0 = 100\, h\, \mathrm{km\, s^{-1}\, Mpc^{-1}} \text{ with } h \in [0, 1]$$

Note that $\dot{a}/a$ quantifies how rapidly the scale factor changes, and it is then useful to define the Hubble rate as

$$H(t) = \frac{\dot{a}(t)}{a(t)}.$$

positive for an expanding Universe, negative for a collapsing one.

From the Hubble rate, we can define the *comoving Hubble radius* , $1/aH$, representing the distance over which particles can travel in the course of the time in which $a(t)$ doubles. These concepts will be very useful in understanding the following sections.

1.3 THE DYNAMICS OF THE UNIVERSE

In order to study the dynamics of the isotropic and homogeneous expanding Universe one needs to solve the Einstein field Equations (Einstein, 1917):

$$G_{\mu\nu} = 8\pi T_{\mu\nu}, \tag{1.6}$$

i.e. a second-order derivative equation[2] that connects the FLRW metric and its derivatives, expressed by the Einstein tensor $G_{\mu\nu}$, to the energy matter content of the Universe in terms of its stress energy tensor $T_{\mu\nu}$. Most of the mass-energy in the present Universe is believed to be found in ordinary matter, i.e. galaxies and gas and can be modelized as "grains of dust". Due to the small random velocities of the galaxies, the pressure can be neglected. However, radiation is another form of energy of our Universe and it can also be described by a *perfect fluid* stress-energy tensor, with non-zero pressure related to the radiation energy density via $p = \rho/3$. The most generic form for $T_{\mu\nu}$ being consistent with the assumption of isotropy and homogeneity of the Universe is the perfect fluid stress-energy tensor at rest in the comoving coordinate frame,

$$T_{\mu\nu} = \rho u_\mu u_\nu + p g_{\mu\nu},$$

being u^μ the four-velocity and $g_{\mu\nu}$ the metric tensor. The two quantities ρ and p are related by means of the local conservation of the stress energy tensor, $\nabla_\mu T^\mu_\nu = 0$,

$$\dot{\rho} + 3\frac{\dot{a}}{a}(\rho + p) = 0 \tag{1.7}$$

By explicitly writing equation (1.6) in terms of the metric and stress energy tensor quantities, one obtains the two Friedmann equations:

$$H^2 = \left(\frac{\dot{a}(t)}{a(t)}\right)^2 = \frac{8\pi}{3}\rho - \frac{K}{a^2} \tag{1.8}$$

$$\frac{\ddot{a}(t)}{a(t)} = -\frac{4\pi}{3}(\rho + 3p) \tag{1.9}$$

It is remarkable to observe that at a given epoch it is possible to define a *critical density* which nullifies the curvature of the Universe, making the comoving part of the metric Euclidean:

$$\rho_c = \frac{3H^2}{8\pi}. \tag{1.10}$$

2 We adopt natural units, i.e. $G, c = 1$.

At present $\rho_{c,0} = 1.879 \times 10^{-29}\, h^2\, g\, cm^{-3}$. A super-critical Universe will be spatially closed, whereas a sub-critical one will be spatially open. It is natural to define the *cosmological density parameter* as the ratio of i-th density component of the Universe to the critical density:

$$\Omega_i \equiv \rho_i/\rho_{c,0}$$

and similarly we define the *curvature density* as

$$\Omega_K \equiv -\frac{K}{a_0^2 H_0^2}$$

such that the (1.8), estimated at the present day, becomes :

$$1 - \sum_i \Omega_i = \Omega_K. \tag{1.11}$$

The solution to the (1.8) and (1.9) for $a(t)$ gives a description of the history and future of the Universe. However, by specifying the equation of state of the form

$$p(\rho) = w\rho,$$

one can easily integrate the (1.7) to obtain

$$\rho \propto a^{-3(1+w)} \tag{1.12}$$

from which we can identify two important cases reported below.

- A **matter-dominated** Universe is dominated by non-relativistic, collisionless particles with $p \approx 0$, which has the solution:

  $$\rho \propto a^{-3} \text{ and } a \propto t^{2/3}.$$

  Three species of matter are identified to compose the total matter content: baryons, leptons, neutrinos and the so called *Cold Dark Matter*. Among these the most dominant one is the third one, whilst the ordinary (baryonic) matter is only the $\sim 5\%$ of the total matter of the Universe. This is one of the most intriguing and unclear topics of modern cosmology: the composition of most of the matter is unknown (maybe particulate) and it hardly interacts with the baryonic one. Several candidates of dark matter particles are proposed including particle *beyond the standard model*(as the *Higgs Boson* (Aad et al., 2013; Chatrchyan et al., 2013) or the *super-symmetric* model particles (West, 1990)), they are commonly referred as *Weakly Interacting Massive Particles, WIMPs*. When the Universe was at very high temperature, the number density of WIMPs (or any other particle species) was roughly equal to the radiation number density. However, when the temperature finally dropped below the WIMP mass creation of WIMPs became very rare though annihilation still proceeded. When the WIMP density dropped at values low enough that the probability of two WIMP particles to

annihilate became very small, the WIMP number density stopped decreasing[3] and it is the most abundant (80% of the total matter density) matter component in the Universe today.

- a **radiation-dominated** Universe is dominated by ultrarelativistic particles (e. g.photons) whose equation of state is $p = 1/3\rho$, implying:

$$\rho \propto a^{-4} \text{ and } a \propto t^{1/2}.$$

The first thing to observe is that both the species listed above are such that the term in the right hand side of (1.9) is positive, i.e. $\rho + 3p > 0$, implying that these species decelerate the expansion of the Universe, i. e. $\ddot{a} < 0$. On the other hand, this means that the expansion has happened at a faster and faster rate as one goes backward in time. This allows us to set the limit of the time when the expansion started. In fact if the Universe had expanded at the present rate, then at the time $\tilde{t} = 1/H_0$ we would have had $a = 0$. However, as the expansion rate was faster at earlier times, the starting time when a was zero is closer to the present.

Thus, one of the most amazing cosmological prediction of general relativity is that under the assumption of isotropy and homogeneity one can predict that at a time $\tilde{t} \leqslant H_0^{-1}$ the Universe was in a *singular* state, the distance between all points of space was zero and the density, the temperature of the matter and the curvature of the spacetime were infinite. Nowadays we refer to this singular state of the Universe as the *big bang*.

Secondly, one may ask the reason why in a radiation dominated Universe the density decreases faster than the matter dominated regime. In fact on one hand, the number density of the photon decreases as the number density of non-relativistic particles. On the other hand, we have to account for the loss of energy that each photon experiences during the expansion.

As the distance between two points increases as the Universe expands, similarly it does the wavelength of the photons travelling through an expanding Universe. This is commonly referred as cosmological redshift: the photon frequency experiences a shift toward "red" frequencies accordingly to how much the Universe has expanded since the moment of the photon emission. Therefore, the redshift defined as $z = (\nu_{em} - \nu_{obs})/\nu_{obs}$ can be related to the scale factor as :

$$\frac{\nu_{em}}{\nu_{obs}} \equiv 1 + z \equiv \frac{1}{a_{em}}.$$

1.4 THE COSMOLOGICAL CONSTANT

When Einstein realized that a constant curvature spacetime and a homogeneous distribution of matter on a large scale could imply a non-stationary

3 Of course it is also assumed that WIMPs are stable and they do not decay in cosmological time, otherwise we would not have observed any dark matter.

Universe, he proposed a modification to the (1.6), (Einstein, 1917). The reason is related on one hand to his philosophical conception of the Universe as something static and immutable, and on the other hand to the lack of astrophysical data by that time:

> The most important fact that we draw from experience as to the distribution of matter is that the relative velocities of the stars are very small as compared with the velocity of light. So I think for the present we may base our reasoning upon the following approximative assumption. There is a system of reference relatively to which matter may be looked upon as being permanently at rest.[...] the system of equations allows a readily suggested extension which is compatible with relativity postulate. For on the left hand side of field equation we may add the fundamental tensor $g_{\mu\nu}$ multiplied by a universal constant, Λ, at present unknown, without destroying the general covariance.
>
> $$G_{\mu\nu} + \Lambda g_{\mu\nu} = 8\pi T_{\mu\nu}$$
>
> [...] That term is necessary only for the purpose of making possible a quasi-static distribution of matter, as required by the fact of the small velocities of the stars.[4]

With this modification (1.8) and (1.9) become[5]:

$$\left(\frac{\dot{a}(t)}{a(t)}\right)^2 = \frac{8\pi}{3}\rho - \frac{K}{a^2} + \frac{\Lambda}{3}, \tag{1.13}$$

$$\frac{\ddot{a}(t)}{a(t)} = -\frac{4\pi}{3}(\rho + 3p) + \frac{\Lambda}{3}. \tag{1.14}$$

Thus, if one neglects the contribution from matter and radiation, $\rho = p = 0$ then $\ddot{a} > 0$, i.e. the cosmological constant has the net effect of accelerating the Universe, and can be seen as a counter-gravity term. However, as the expansion of Universe became an experimental evidence, the Λ term, known as the *cosmological constant*, has been discarded since inserted *ad hoc* by Einstein.

Though it has resurfaced several times over the years to explain a number of different observations, in the last decades, the cosmological constant has been restored: evidence is mounting that a Λ-like term may be required to describe the dynamics of our Universe (models with non-zero Λ are known as *Lemaitre* models). Starting in 1997, several attempts have extended the measurements of H_0 by means of light of supernovae (SNae) Ia hosted in distant galaxies and emitted when the cosmological expansion rate was different than the present one (Perlmutter et al., 1999; Riess et al., 1998). Most surprisingly, the data suggested that the Universe has been accelerating the expansion for the last six billion years.

4 See for further readings Einstein (1917).
5 The (1.7) remains unchanged.

The standard model of cosmology considers $\Lambda g_{\mu\nu}$ as a term in the right hand side of (1.6),i. e. the matter energy content has to be slightly modified and therefore postulates that the Universe is globally filled by a fluid, called *Dark Energy* which behaves as a cosmological constant and thus modifies the dynamics of the Universe in such a way as to convert the predicted deceleration of the expansion due to the presence of matter into an acceleration.

The stress-energy tensor thus reads as:

$$\tilde{T}_{\mu\nu} = \rho u_\mu u_\nu + (p + p_\Lambda) g_{\mu\nu}, \tag{1.15}$$

with $p_\Lambda = -\Lambda < 0$, i. e.the dark energy fluid has a *negative* pressure. The density of such a fluid, ρ_Λ, is related to p_Λ via the equation of state with $w = -1$:

$$\rho_\Lambda = \frac{\Lambda}{8\pi}.$$

By looking at (1.7), it is straightforward to state that the dark energy density does not evolve in time but it remains constant during the evolution of the Universe. A particular solution to the Friedmann equations (1.8) and (1.9) is the one encoding the presence of a dominating positive cosmological constant, as known as *de Sitter* solutions which implies:

$$\rho_\Lambda \propto a_0 \text{ and } a \propto \exp(Ht). \tag{1.16}$$

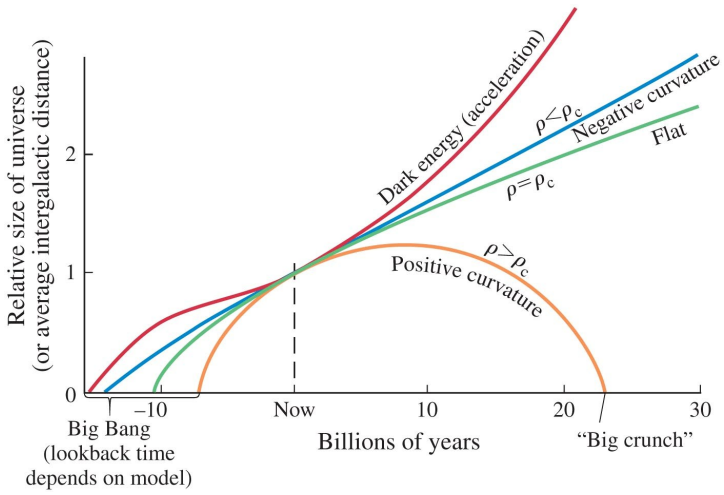

Figure 1.2: Evolution of the scale factor of the Universe with cosmic time, depending on the energy-matter content.

Even in this case, it is possible to define $\Omega_\Lambda = \rho_\Lambda/\rho_c$ and from figure 1.2 one can easily get how the dynamics of a changes as a function of the matter-energy content of the Universe. The Friedman equation (1.8) and the comoving distance can be espressed in terms of the redshift as :

$$H(z) = H_0 \left[\Omega_m (1+z)^3 + \Omega_\Lambda (1+z)^{3(1+w)+\Omega_K (1+z)^2}\right]^{1/2},$$

$$d_C(z) = \int_0^z \frac{dz'}{H(z')}.$$

Moreover, two further important distances are to be defined in this context:

- the *angular distance* d_A, as the distance of an object at redshift z whose angular size is $\delta\theta$:

$$d_A = \frac{1}{\sqrt{|\Omega_K|}(1+z)} f_K\left(\sqrt{|\Omega_K|} d_C(z)\right); \tag{1.17}$$

- when the intrinsic luminosity L of an object is known, one can get its *luminosity distance* d_L, by means of the measured flux S since $d_L = \sqrt{L/4\pi S}$. This distance turned out to be very useful for measurements involving the so called *standard candles*, i. e. supernovae Ia and Cepheids:

$$d_L = \frac{1+z}{\sqrt{|\Omega_K|}} f_K\left(\sqrt{|\Omega_K|} d_C(z)\right), \tag{1.18}$$

where $f_K(x) = \sinh(x), x, \sin(x)$ if respectively $\Omega_K > 0$, $\Omega_K = 0$, $\Omega_K < 0$.

Once a Hubble diagram has been accurately drawn one can look for the *best fit* relation that better resembles the data as a function of the cosmological parameters $H_0, \Omega_\Lambda, \Omega_m, \ldots$, as it is shown in fig.1.3. These are the results recently published of the PAN-STARSS1 survey (Rest et al., 2014), from which one can easily infer that a non-zero Λ is highly *preferred* by high-redshift data.

Riess et al. (2016) recently published one of the latest and most accurate value of H_0, $73.24 \pm 1.74 \mathrm{km\,s^{-1}\,Mpc^{-1}}$.

1.5 THERMAL HISTORY OF THE UNIVERSE

At the early stage after the Big Bang, the Universe was in a hyper-dense and hot state where all the particles were ultra-relativistic and tightly coupled each other by means of strongly interactions, so that we usually refer it to a Universe dominated by radiation. As it will be shown in Section 1.6, the Universe is filled with a black-body radiation at $T = 2.7$ K. Therefore, it is possible to estimate the radiation density, ρ_r via the *Stefan-Boltzman law*,

$$\rho_r \approx 4.5 \times 10^{-34} \mathrm{g\,cm^{-3}}$$
$$\Omega_r = \frac{\rho_r}{\rho_c} \approx 4.2 \times 10^{-5} h^{-2}$$

By looking at fig.1.4 one can notice that there is a time when the radiation and matter densities are equal. This happened at:

$$a_{eq} = \frac{\Omega_r}{\Omega_m} = 4.2 \times 10^{-5} h^{-2} \Omega_m^{-1}.$$

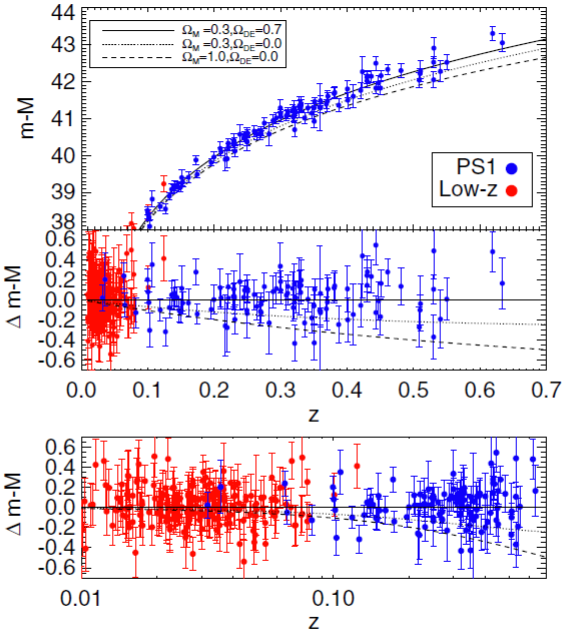

Hubble Diagram Pan-Starrs Rest et al. 2014, ApJ, 795, 44

Figure 1.3: Hubble diagram for the combined Pan-Starrs 1 and low-redshift samples. Three model Universes are given: the ΛCDM Universe, a Universe with $\Omega_m = 1$,and a Universe with $\Omega_m = 0.3$. The distance modulus $\mu(H_0, \Omega_m, \Omega_\Lambda, w, z)$ is found from the luminosity distance d_L, defined in(1.18), such that $\mu = m - M = 5 \log d_L + 25$.[6] Lines shows that predictions for different energy contents in the Universe. The residuals $\Delta m - M$ is defined as the difference of the observed distance modulus and the theoretical one. The bottom panel shows residuals vs the logarithmic redshift in order to visualize the low-z SNe Ia residuals.

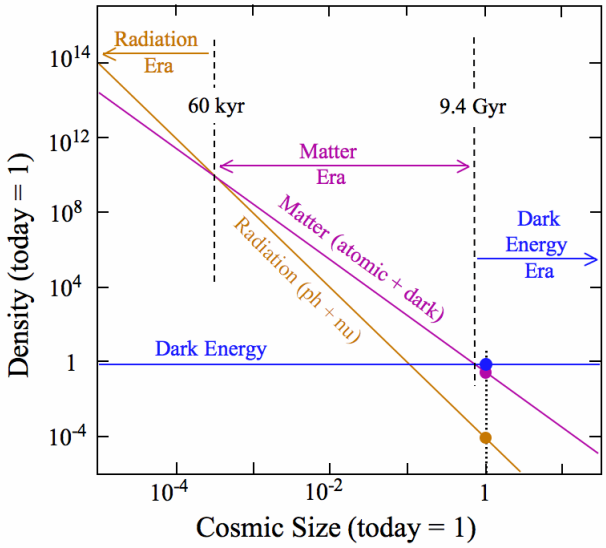

Figure 1.4: Energy density vs. scale factor for different species of a flat Universe. Shown are non-relativistic matter, radiation (photons and neutrinos), and a cosmological constant. All are in units of the critical density today.

In both radiation and matter dominated scenarios, the scale factor is found to be zero at the big bang time, i. e. $a(t = 0) = 0$. However, we know that $t = 0$ is a singularity in the FLRW metric and the energy density diverges to infinite. It is straightforward to note that being the energy density of relativistic particles proportional to the temperature to the fourth power (via the Stefan-Boltzman law), the relation among temperature and the scale factor will be simply $T \propto a^{-1}$: i. e. as the Universe expands, the temperature of radiation cools down. Though the physics around the singular state is not yet understood (see Section 1.8 for an insight), we decide to start describing the thermal history of the Universe at the point where the temperature has been low enough that all the known particles within the standard model have already formed and are in thermodynamic equilibrium.

The key to understand the thermal history of the Universe is the comparison between the rate of interactions Γ and the rate of expansion H. When $\Gamma \gg H$, then the time scale of particle interactions is much smaller than the characteristic expansion time scale:

$$t_c \equiv \frac{1}{\Gamma} \ll t_H \equiv \frac{1}{H}$$

Local thermal equilibrium is then reached before the effect of the expansion becomes relevant. One can notice that at very early times the thermal equilibrium among the various particles is guaranteed: indeed from (1.8), the expansion time scales as $t_H \propto \rho^{-1/2}$ and thus becomes very short at high density, whereas the two body interaction rate is proportional to ρ^2, so that the collision time scale as ρ^{-2}.

As the Universe cools, the rate of interactions may decrease faster than the expansion rate. At $t_c \sim t_H$, the particles decouple from the thermal bath. Different particle species may have different interaction rates and so may decouple at different times. For example, electrons and positrons are in equilibrium with the CMB at $T \gtrsim 1$MeV through the reaction:

$$e^+ + e^- \rightleftharpoons \gamma + \gamma.$$

Similarly, neutrinos are kept in equilibrium through

$$\nu + e \rightleftharpoons \nu + e \qquad\qquad e^+ + e^- \rightleftharpoons \nu + \bar{\nu}$$

and nucleons through

$$p + e^- \rightleftharpoons n + \nu.$$

Fast reactions keep particles in equilibrium and thus different species shared a common temperature $T \gg m$, e. g. at $T \sim 10$ MeV, all the above reactions are in thermal equilibrium with radiation and one can expect other particles to be in equilibrium at even higher temperatures, $T \sim 200$ MeV, (e. g. μ^+, μ^-, π^+, π^- and π^0).

In this context, it is therefore convenient to introduce the concept of *distribution function* of a species, which counts the number of particles in a

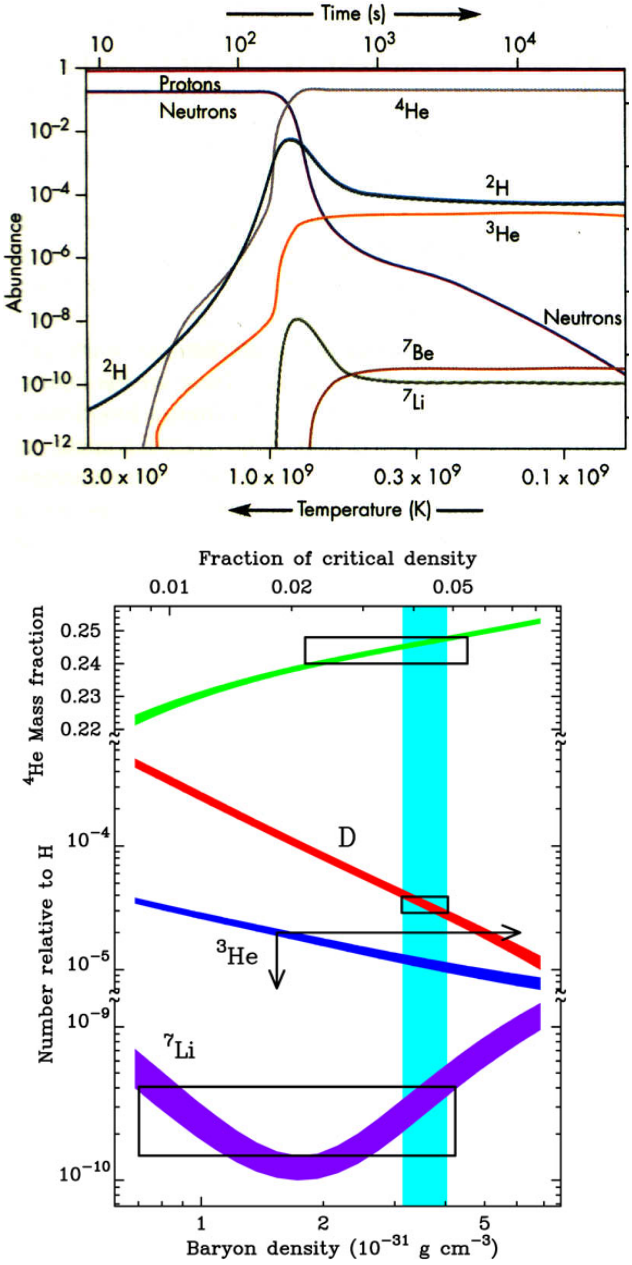

Figure 1.5: Top panel: evolution of the abundances of the lightest elements during the BBN. Bottom panel: Constraints on the baryon density from BBN. Predictions are shown for four light elements, the solid vertical band is fixed by measurements of primordial deuterium. The boxes are observations.

given region of the phase space (whose parameters are the spatial coordinates x and the momentum p). The energy of a species is defined as the sum of energy over all phase-space elements: $E_{tot} = \sum f(x,p)E(p)$, with $E(p) = \sqrt{m^2 + p^2}$

$$f_{\pm} d^3p = \frac{g}{(2\pi)^3} \frac{d^3p}{e^{(E-\mu)/kT} \pm 1}$$

being either the *Bose-Einstein* (f_-) or the *Fermi-Dirac* distribution (f_+) depending if respectively bosons or fermions are considered, μ the chemical potential and g the *spin-degeneracy* weight (e. g. 2 for electrons and photons, 1 for neutrinos).[7]

As the Universe expands, the temperature at a certain point drops below the mass of the particle, $T \ll m$. A certain species becomes non-relativistic, and *decouple* from the primordial plasma and their distribution function receives an exponential suppression, i. e. at the decoupling time the reaction rate drops, ($\Gamma/H \leqslant 1$) and the particle density *freezes-out* to the value it had just before the decoupling.

Thus, we have all the tools at hands for describing and summarizing the thermal history of the Universe:

SYMMETRY BREAKING. At $T \gg 100\,\mathrm{GeV}$ several processes are supposed to break original symmetries present in unification theories resulting into the asymmetries we observe today. One of those is the matter and anti-matter particle annihilation through processes such as $e^+ + e^- \to \gamma + \gamma$. If initially the Universe was filled with equal amounts of matter and anti-matter then we expect these annihilations to lead to a Universe dominated by radiation. However, we do observe an over-abundance of matter (mostly baryons) over anti-matter in the Universe today.

ELECTROWEAK PHASE TRANSITION. At ~ 100 GeV, the mediators of the unified electroweak force, γ, $W^{\pm}$, Z_0 become different, and through the Higgs mechanism, the photon only keeps being massless, becoming the mediator of the electromagnetic interaction, while the others become massive and mediate the weak nuclear force.

QUANTUM CHROMO-DYNAMICS PHASE TRANSITION. While quarks are *asymptotically free* (i.e. weakly interacting) at high energies, below about 150 MeV, the strong interactions between them and the gluons become important and the lowest stable energy states are the bound states of two and three quarks respectively mesons and baryons.

7 Notice that these distributions do not depend on the position or on the direction of the momentum $\hat{p}$, but simply on its magnitude. This is a zero-order feature. When one comes to consider inhomogeneities and anisotropies the distribution functions have small perturbations around these zero order values, and they will depend on both position and direction of propagation.

NEUTRON FREEZE-OUT AND NEUTRINO DECOUPLING. At this point, the primordial plasma is mostly made of e^+, e^-, γ, ν, protons and neutrons. All are in thermal equilibrium since the weak interaction rate is much larger than the expansion rate H. Moreover, the energy is not low enough to bind the lightest nuclei (deuterium, tritium, and helium binding energies are of the order of MeV). The ratio of neutrons to protons is particularly important here, since essentially all neutrons will form ^{4}He. This ratio can be calculated by taking into account the weak interaction that is responsible for the balance between neutrons and protons:

$$n \rightleftharpoons p + e^- + \bar{\nu}, \tag{1.19}$$

$$\nu + n \rightleftharpoons p + e^-, \tag{1.20}$$

$$e^+ + n \rightleftharpoons p + \bar{\nu}. \tag{1.21}$$

The neutron-to-proton ratio is expected to be very close to 1 at this energy regime. As the temperature decreases $T \sim 1$ MeV, the neutron-to-proton ratio also decreases and protons outnumber the heavier neutrons. This decrease in the ratio could continue indefinitely, but when $T < 0.8$ MeV, the mean time for reaction (1.20) becomes longer than the age of the Universe at that epoch, i.e. $t_c > t = 2s$. This means that the neutrons and protons, which were converted from one to the other via this reaction, are no longer in thermodynamic equilibrium. Therefore, neutrons can no longer be created, the neutron-to-proton ratio "freezes" at a value of $1/7$. However, because of the spontaneous decay of neutrons, this ratio does not remains strictly constant, but decreases slowly with time. Defining the abundance of a nucleus A as the mass fraction:$X_A = n_A A/n_N$, where n_N is the baryon number density $n_N = n_p + n_n + \sum A n_A$, the nuclear species at this stage are still in equilibrium and with very small abundances ($X_2 = 10^{-12}$, $X_4 = 10^{-23}$).

At about the same time, neutrinos which only interact with the primordial plasma through weak interactions, cease to be in thermal equilibrium with the rest of the matter and they decouple forming the *Cosmic Neutrino Background*.

ELECTRON-POSITRON ANNIHILATION. At $T = 0.5$ MeV, electrons and positrons annihilate shortly after neutrino decoupling. The energy of the annihilation pairs gets transferred to the photons and thus slightly increasing their temperature which deviates from the expected value following the expansion as $T_\gamma \propto a^{-1}$.

BIG-BANG NUCLEOSYNTHESIS (BBN). At $T = 0.3 - 0.1$ MeV and $t = 3$min all the produced neutrons are bounded within He. The mass fraction of He is thus easily given by:

$$X_4 \approx \frac{4n_4}{n_b} = \frac{4(n_n/2)}{n_n + n_p} = \frac{2(n_n/n_p)}{1 + n_n/n_p} \approx 0.25\,.$$

Heavier elements, in principle, could also form abundantly at later epoch, because their binding energy is larger than ^{4}He. However, the lack of stable isotopes with $A = 5$ and $A = 8$ and the presence of a significant Coulomb barrier prevents the formation of significant atoms beyond ^{4}He. Some traces of deuterium, ^{3}He, ^{7}Li and beryllium are produced as shown in fig.1.5.

MATTER DOMINATION. At $T \sim 0.75$ eV and $t \sim 60$ kyr, the expansion passed from a radiation dominated ($a \sim t^{1/2}$) to a matter dominated Universe $a \sim t^{2/3}$.

RECOMBINATION AND PHOTON DECOUPLING. At $T \sim 0.3$ eV and $t \sim 400$ kyr, neutral hydrogen combines through the reaction $e^- + p \rightarrow H + \gamma$ when the temperature has become low enough that the reverse reaction is energetically disfavoured. This sharp drop in the free electron density makes inefficient the Thomson interaction between electrons and photons, $e^- + \gamma \rightarrow e^- + \gamma$ and thus matter and radiation decouple, making the Universe transparent to radiation wavelengths longer than the Lyman α (Lyα $= 122$ nm). Since then photons have been freely streaming through the Universe and can be observed today as the *Cosmic Microwave Background* (CMB).

REIONIZATION. First stars form and reionize the Universe at the time of $100 - 400$ Myr becoming transparent only to radiation wavelengths shorter than the Lyα.

DARK-ENERGY DOMINATION. At ~ 9 Gyr, the dynamics further changes the expansion from a deceleration due to the predominance of matter to acceleration under the influence of dark-energy.

Clearly, by measuring the abundances of the primordial ^{4}He or D it is possible to estimate the value of the baryon density Ω_b. The abundance of ^{4}He is usually inferred by observing atmospheres of metal-poor stars, and by extrapolating the measured Helium at zero metallicity. Measurements of this species are considered now quite robust, and thus the Helium provides a very robust upper limit on baryon-to-photon ratio. Lithium has been traditionally difficult to measure because of its low abundance. However, due to two different channels for its production, Lithium abundance has provided relatively strict bounds on Ω_b. Today, the combination of estimates ^{4}H and especially of D + ^{3}He is thought to give more stringent limits. The predicted abundances are very consistent with the observations carried out on many different astronomical data sets (Tytler, O'Meara, Suzuki, & Lubin, 2000) representing one of the first observational successes of the hot Big Bang model. Tytler et al. (2000) firstly constrained Ω_b starting from the element abundances and found:

$$\Omega_b h^2 = 0.019 \pm 0.0024\,.$$

1.6 THE COSMIC MICROWAVE BACKGROUND RADIATION

Before the time of recombination, when the Universe was hot enough to have its temperature higher than 3000K, the atoms were all ionized. A plasma of free electrons and nuclei provided a continuum opacity for any radiation present. This means that radiation would not travel very far before getting scattered; the Universe was opaque, matter and radiation were kept in equilibrium, so that one should expect a black-body emission from this radiation. However, the density and the temperature decreased, as the Universe expanded. When radiation was not able any more to keep balanced the reaction $p + e \leftrightharpoons H + \gamma$, various estimates place this at $t = 380,000$ yr. Electrons and protons or Helium atoms *combined* together into atoms. Since neutral atoms do not absorb radiation very efficiently (except within a narrow range of frequencies related to the spectral lines), the Universe becomes transparent to radiation. The recombination era thus coincides with the epoch at which radiation decoupled from matter.

At the temperature $T < 10^5$ K, $\sim 10eV$, photons stop interacting via Thomson scattering with electrons. After that, they continue to be scattered by free electrons, but without any appreciable gain or loss of energy. In fact, each recombination to the hydrogen ground state generated a high-energy photon being capable of ionizing a nearby neutral hydrogen atom. This is the reason why we do not have a net effect: each recombination is rapidly followed by a new ionization.

Moreover, if a recombination occurs directly to the ground state, a photon with $h\nu > \chi = 13.6\,eV$ would be produced. Such photons are clearly bad news for the recombination: they travel until they ionize an other neutral atom. Multiple absorption of these photons will cause reionization once they become abundant, so it would appear that recombination can never occur. How could it be possible, then?

There are two possible solutions to this problem:

- Because of the Universe expansion, the re-emitted photons are redshifted and thus they are no more able to re-ionize new atoms. However, this mechanism is not efficient since the Γ for the electromagnetic interactions is too high, thus the photon mean free path was too short to get redshifted by the cosmological expansion at the time or recombination.

- Some atoms reach the state through a *two-photon emission*, $2s \rightarrow 1s + 2\gamma$ (Peacock, 1999). Indeed the $2s \rightarrow 1s$ transition is strictly forbidden at first order and on can only conserve energy and angular momentum in the transition by emitting a pair of photons[8] (with a single photon we cannot have energy and momentum conservation). Thus, since recombination has to pass through this bottleneck (being a second order process, this is slow ~ 0.1 s), this could be a mechanism to get rid of energy from the ionized atom in form of non-ionizing photons.

8 The inverse process is a three-body reaction, which is rare and thus unimportant.

In order to understand the two-photon emission, we consider a simple model for the hydrogen atom composed by two levels only: the ionized state, and the 2s state. We have then the following relations for the number density of electrons n_e and of 2s hydrogen atoms, n_2:

$$\frac{dn_e}{dt} = -Rn_e n_p + n_2 \Lambda_u,$$
$$\frac{dn_2}{dt} = Rn_e n_p - n_2(\Lambda_u + \Lambda_{2\gamma}),$$

where $R = R(T)$ is the recombination coefficient, $\Lambda_u = \Lambda_u(T)$ is the rate for the $2s + \gamma \to e + p$ ionization reaction, and $\Lambda_{2\gamma} = \Lambda_{2\gamma}(T)$ is the rate for the $2s \to 1s + 2\gamma$ reaction. By assuming n_2 constant:

$$n_2 = \frac{Rn_e n_p}{\Lambda_u + \Lambda_{2\gamma}},$$

we get:

$$\frac{dn_e}{dt} = -Rn_e^2 \left(1 - \frac{\Lambda_u}{\Lambda_u + \Lambda_{2\gamma}}\right) = -Rn_e^2 \left(\frac{\Lambda_{2\gamma}}{\Lambda_u + \Lambda_{2\gamma}}\right). \tag{1.22}$$

In this equation the quantities Λ_u, $\Lambda_{2\gamma}$, and R are function of the temperature T and do not directly depend on the cosmological parameters. In order to show the dependence of the solution from the cosmological parameters, note that $n_e = nx \propto \Omega_b h^2$. By rewriting $d/dt = (dz/da)(da/dt)d/dz$, and by using the relevant expressions in a matter dominated Universe for the various differentials, we can write the expected dependence of the solution $x(z)$ on the cosmological parameters:

$$x(z) \propto \frac{(\Omega_m h^2)^{1/2}}{\Omega_b h^2}, \tag{1.23}$$

The real solution can be found by numerically integrating (1.22). Because of the simple factorization of the cosmological parameters expressed in (1.23), effectively one can solve (1.22) for a particular cosmological model, and rescale the solution from (1.23). The final result is well approximated by:

$$x(z) \approx 2.4 \times 10^{-3} \left(\frac{z}{1000}\right)^{12.75} \frac{(\Omega_m h^2)^{1/2}}{\Omega_B h^2}, \tag{1.24}$$

where the redshift z is taken to be about ~ 1000.

The optical depth for Thomson scattering is given by the integral in comoving coordinates:

$$\tau = \int d\eta \, n_e \sigma_T x, \tag{1.25}$$

where σ_T is the Thomson cross section. Since $n_e \propto n_B \sim \Omega_B h^2$, $d\eta = cdt/a$ and by making use of Friedmann's equation in the matter dominated case,

$$\frac{\dot{a}}{a} = H_0\sqrt{\Omega_m a^{-3}},$$

we find (Peacock, 1999):

$$\tau(z) = 0.37\left(\frac{z}{1000}\right)^{14.25}.$$

Surprisingly, this does not depend on the cosmological parameters, but only on the redshift. Because τ scales rapidly with z, the distribution function for the redshift at which photons were last scattered, $e^{-\tau}d\tau/dz$, is sharply peaked, and is well fitted by a Gaussian with mean at $\mu_z = 1065$ and standard deviation $\sigma_z = 80$.

Moreover, once these photons streamed freely they get *cooled down* by the cosmological redshift as the Universe expands.

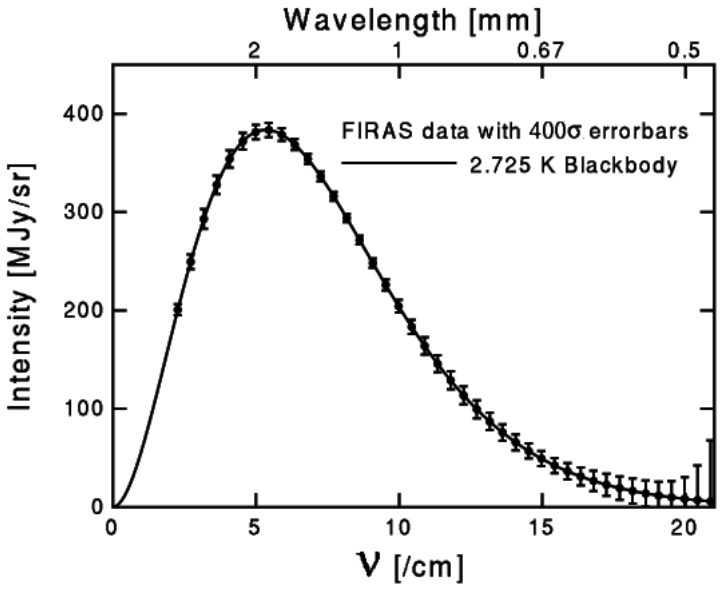

Figure 1.6: Comparison of the intensity of radiation observed with the FIRAS radiometer carried by COBE with a blackbody spectrum with temperature 2.725K. The 1σ experimental uncertainty in intensity is indicated by the tiny vertical bars; the uncertainty in wavelength is negligible (Fixsen et al., 1996).

This radiation is nowadays known as the CMB and it was detected by (Penzias & Wilson, 1965). Originally they only reported an excess of the antenna temperature at a wavelength 7.5 cm to be 3.5 ± 1.0 K. After several attempts from ground telescopes which were mainly contaminated by the atmosphere, the COsmic Background Explorer (COBE) satellite was launched in 1989 to measure the spectrum of CMB. As one can see from fig.1.6, it was found that the CMB spectrum is compatible to a black-body spectrum in

the wavelength regime from 0.5 cm to 0.05 cm and the black-body temperature was measured by the COBE Far Infrared Absolute Spectrophotometer (FIRAS) instrument at 95 % confidence level (Fixsen et al., 1996):

$$T = 2.725 \pm 0.004\,\mathrm{K}.$$

It is interesting to notice that a black-body spectrum at a given time does not change its functional shape since the number of photons is conserved during the expansion:

$$n_{\nu'} = \frac{n_\nu}{(1+z)^3} = \frac{2\nu^2}{c^2(1+z)^3}\frac{d\nu}{e^{\frac{h\nu}{k_B T}}-1} = \frac{2\nu'^2}{c^2}\frac{d\nu'}{e^{\frac{h\nu'}{k_B T'}}-1},$$

where we restored physical units,k_B is the Boltzmann constant and $T' = T/(1+z)$. The equivalent temperature however gets reduced between recombination time and present. The FIRAS measurements confirmed for the first time that the Universe at the time of recombination was constituted of a tight coupled photon baryon plasma in thermodynamic equilibrium.

Thus, if we were able to look at the sky with some glasses sensitive to microwave we would expect to observe in each direction photons that have been emitted from a *last scattering surface* at $z \approx 1065$. This radiation can provide an answer to the Olbers' paradox about the darkness of the night: with those special glasses the sky in the night would not be dark at all!

1.7 INITIAL CONDITIONS FOR THE BIG BANG PARADIGM

The hypotheses of isotropy and homogeneity lead to the big bang picture appearing if we assume that its thermal history has always been dominated by some species with $w \geqslant 0$.

Unfortunately, these assumptions represent rather unusual *initial conditions* which have to be assumed in order to justify the state of the Universe observed today. In fact, the physical approach is usually to predict the evolution of a system given a certain initial state. No theory is generally given for the initial conditions. On the contrary, it would be nice to have a theory predicting that Universe has begun in a natural state, i. e.in some not-well defined, not finely tuned state.

Due to the isotropy and homogeneity postulates assumptions, we do expect the CMB to be remarkably uniform across the sky. This was the case until 1992, when COsmic Background Explorer (COBE) satellite discovered temperature variations at the level of 10^{-5} (Smoot et al., 1992). The map of these temperature *anisotropies* represents a snapshot image of the tiny density fluctuations in the primeval Universe. The same are thought to grow by gravitational attraction into the structures we see today (stars, galaxies, and clusters of galaxies) accordingly to the gravitational instability model of structure formation. One of the initial conditions assumed in the FLRW cosmological model is: there must be a mechanism able to reproduce the *inhomogeneities* at the level we see today.

In addition to this, there are two main puzzles which have to be related with initial conditions.

THE PROBLEM OF HORIZON. We consider the physical meaning of the horizon defined in (1.3) η as in Dodelson (2003):

> it is the maximum comoving distance travelled by light since the beginning of the Universe. [...] objects separated by comoving distances larger than η today were not ever in causal contact: there is simply no way information could have propagated over distances larger than η.

At the time of recombination $\eta \sim 150\,\mathrm{Mpc}$, corresponding to $\sim 2°$ in the sky today. Thus CMB photons, had not enough time to causally connect all the angular scales. This is in contrast with observations: the CMB is highly isotropic at all scales. *How did photons coming from regions separated by many horizons thermalize, i. e. share the very same temperature with differences almost at* 10^{-5}*?*

THE PROBLEM OF FLATNESS. One of the most surprising facts is that the so called curvature density, Ω_K, observed by means of CMB measurements (see next chapter), is smaller than $\sim 10^{-2}$. Recalling that:

$$\Omega_K(a) = -\frac{K}{a^2H^2(a)} = -\frac{\Omega_{K,0}}{\Omega_{m,0}a^{-1} + \Omega_{\Lambda,0}a^2 + \Omega_{r,0}a^{-2} + \Omega_{K,0}} \tag{1.26}$$

Since, Ω_K increases with time, it was even closer to zero at earlier epochs. For instance, by estimating (1.26) at the BBN epoch $|\Omega_K| \lesssim 10^{-18}$; and at the time where the Universe had a temperature comparable to the Planck energy, $|\Omega_K| \lesssim 10^{-63}$. *Why the Universe preferred a flat geometry, i. e.* $K = 0$*, as its initial state ?*

In the following, the Hubble radius $1/aH$ is a crucial quantity. Indeed both the curvature density and the comoving horizon can be written in its terms, being the former proportional to it and the latter expressed in terms of the Hubble radius, as:

$$\eta = \int \frac{dt}{a} = \int \frac{da}{a^2H} = \int \frac{d\log(a)}{aH}.$$

Notice that there is a small difference between the Hubble radius and the comoving horizon: particles, whose distance is larger than η, *never* could have communicated with the others, whilst if they are separated by distance larger than $1/aH$ they are not in causal contact but it could be that they were, in previous epochs. This is somewhat unexpected in the standard cosmological model: indeed most of the contribution to the particle horizon during radiation and matter dominated epochs comes from late times, since $a \approx 0$ at very early epochs. However, if we allow the Hubble radius to be initially much larger than what it currently is, then most of the contribution to the horizon came from the early Universe, of course previously to the

radiation dominated era. This could be a possible solution to the horizon problem: since $\eta_0 \ll (aH)^{-1}$, particles today cannot communicate but they could have been in causal contact early on.

Furthermore, one can notice that Ω_K should start from a general value and then decrease with time in order to fix the flatness fine-tuning puzzle and justify its observed value today.

This can be achieved if some non-standard species is assumed to dominate the early phases of the dynamics of the Universe such that $1/aH$ dramatically decreased during this epoch. This means that vice versa aH must increase and thus:

$$\frac{d(aH)}{dt} = \frac{d\dot{a}}{dt} = \ddot{a} > 0,$$

i. e. the Universe expansion should be accelerated. As stated in (1.9), this should imply a Universe dominated by a species whose equation of state satisfies $w < -1/3$. *Inflation* represents a beautiful solution accounting for all these conditions and is briefly described in the next section.

1.8 THE INFLATION PARADIGM

In the following two Sections we give a brief overview of the Inflation, considering both cosmological expansion and the generation of perturbations. My purpose is to give highlights of the most important aspects of this central issue in modern cosmology, defining key quantities which will be used in the following. We refer to Guth (1981); Starobinsky (1982) for more details.

Inflation postulates that the Universe underwent an early epoch of rapid accelerated quasi-exponential expansion, driven by a scalar field, with a negative-pressure equation of state $w \approx -1$, called the *inflaton* whose quantum fluctuations generated density and metric perturbations in the Universe.

The simplest example of inflaton is a scalar field on the top of a rather flat potential. These kinds of models are known as *slow-roll inflation.* The action of this scalar field can be written as :

$$S = \int d^4x\sqrt{-g}\left[\frac{M_{Pl}^2}{2}R + \frac{1}{2}g^{\mu\nu}\partial_\mu\varphi\partial_\nu\varphi - V(\varphi)\right], \tag{1.27}$$

where the first term is the Einstein-Hilbert term of General Relativity, the second and third therms represent the action of a scalar field S_φ and $M_{pl} = (8\pi G)^{-1/2}$. The idea of inflation is that the early Universe was filled with a homogeneous distributed scalar field slowly rolling down its potential. The stress tensor of φ is defined as:

$$T_{\mu\nu}^{(\varphi)} = -\frac{2}{\sqrt{-g}}\frac{\delta S_\varphi}{\delta g^{\mu\nu}} = \partial_\mu\varphi\partial_\nu\varphi - g_{\mu\nu}\left(\partial^\sigma\varphi\partial_\sigma\varphi + V(\varphi)\right), \tag{1.28}$$

where for an homogeneous field configuration one can easily recognize the associated scalar field density, pressure and the equation of state:

$$\rho_\varphi = \frac{1}{2}\dot{\varphi} + V(\varphi),$$
$$p_\varphi = \frac{1}{2}\dot{\varphi} - V(\varphi),$$
$$w_\varphi = \frac{p_\varphi}{\rho\varphi} = \frac{\frac{1}{2}\dot{\varphi} - V(\varphi)}{\frac{1}{2}\dot{\varphi} + V(\varphi)}.$$

One can note that $\ddot{a} > 0$, if $\dot{\varphi}^2 \ll V(\varphi)$, which means $p < 0$ and $w_\varphi \approx -1 < -1/3$. Therefore the expansion during inflation was exponential as in (1.16).

$$a(t) = a(t_e)e^{H(t-t_e)}, \text{ with } t < t_e,$$

being t_e the time at the end of inflation and H during inflation descends from the Friedman equation:

$$H^2 = \frac{1}{3M_{Pl}^2}\left(\frac{1}{2}\dot{\varphi}^2 + V(\varphi)\right).$$

Notice that since $\dot{\varphi}^2 \ll V$, and $V \approx const$, $H \sim const$, the Hubble rate did not variate during inflation. Moreover, by explicitly writing:

$$\ddot{a} > 0 \Rightarrow a(\dot{H} + H^2) > 0 \Leftrightarrow -\frac{\dot{H}}{H^2} < 1.$$

we can relate the expansion rate and its derivative to the kinetic and potential terms of the inflaton, by means of the first slow-roll parameter $\hat{\epsilon}$:

$$\hat{\epsilon} = -\frac{\dot{H}}{H^2} \sim \frac{\dot{\varphi}^2}{V} \ll 1, \tag{1.29}$$

The equation of motion for the scalar field reads:

$$\frac{\delta S}{\delta \varphi} = 0 \Rightarrow \ddot{\varphi} + 3H\dot{\varphi} + V_{,\varphi} = 0, \tag{1.30}$$

where $V_{,\varphi} \equiv dV/d\varphi$. One can easily recognize the equation of motion of a particle rolling down its potential subjected to a friction term (see fig. 1.7). As in a particle trajectory, the solution $\dot{\varphi} = V_{,\varphi}/(3H)$ is an attractor if the friction is large enough. We define the second slow-roll parameter quantifying how $\hat{\epsilon}$ changes during a Hubble time:

$$\hat{\eta} = \frac{\dot{\hat{\epsilon}}}{H\hat{\epsilon}}. \tag{1.31}$$

If η is small it implies that inflation persists and that the second time derivative in (1.30) is negligible. The parameters defined in (1.29) and (1.31) depend only on H and its first two derivatives. However, because of their

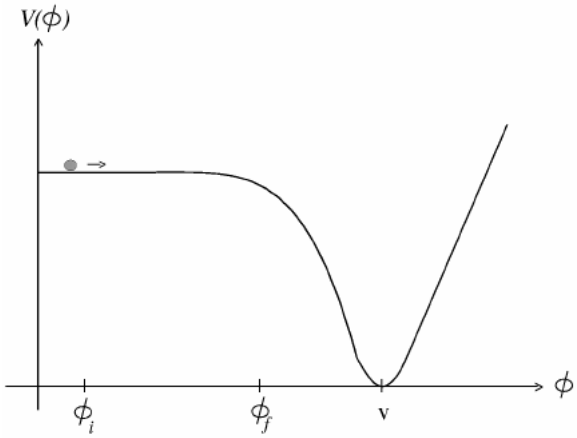

Figure 1.7: Example of inflationary potential with a "flat" region. After the slow-roll of the inflaton field φ, the reheating phase starts and the field is supposed to oscillate around the minimum of the potential and to decay in other particles.

relation to the analytical properties of the field potential, it is remarkable to quantify them with some observables (we will see in the next section how).

The inflation ended when $w \neq -1$, i. e. $\hat{\epsilon} \sim \hat{\eta} \sim 1$; as the field rolled down its potential two things happened: the Hubble rate decreases and provides less friction and the potential becomes too steep to guaranteed the kinetic term to be negligible. At this point a period dominated by a form of energy with $w = 1/3$ is expected to begin as shown in fig.1.8.

It is very common to quantify the duration of inflation in terms of number of *e-foldings* in order to solve both the flatness and the horizon problems. Usually N depends on the physical model driving inflation, the energy scale when inflation ended and on the epochs posterior to the inflation. However, N is typically several tens:

$$N = \log\left(\frac{a_e}{a_b}\right) \approx 40 \div 60.$$

At the end of inflation the inflaton is expected to begin to oscillate around the bottom of its potential. This epoch is called *reheating phase*: being the Universe *supercooled* by the exponential expansion[9], it got reheated by the inflaton decaying into the standard model particles, so that energy density of the inflaton field decreased as (Dolgov & Linde, 1982)

$$\rho_\varphi(t) = \rho_\varphi(t_I)\left(\frac{a(t_I)}{a(t)}\right)^3 e^{-\Gamma(t-t_I)},$$

where Γ is the rate of decay of φ into other particles and t_I is taken at the beginning of the inflaton decay.

9 Several inflationary models predict an abrupt drop of 5 orders of magnitude in temperature (Mukhanov & Chibisov, 1981).

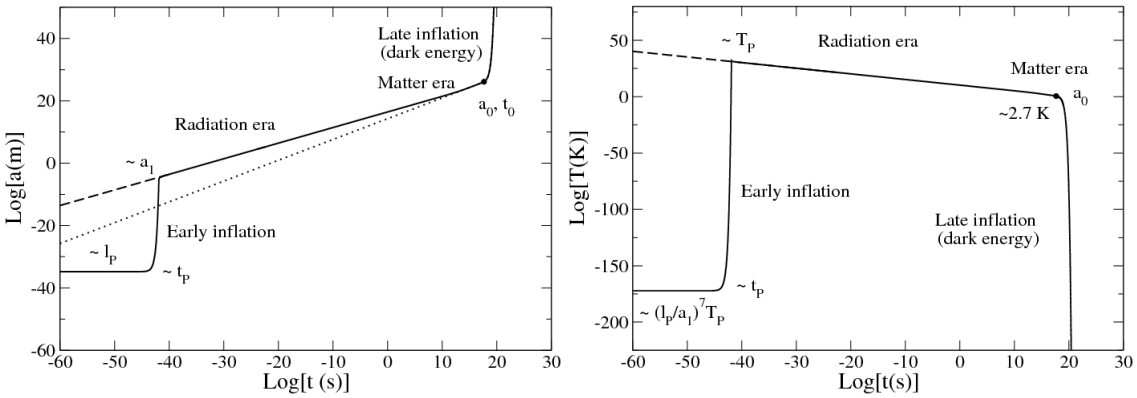

Figure 1.8: Temporal evolution of the scale factor (left) and temperature (right) in logarithmic scales. The early Universe undergoes a phase of inflation that takes it to the radiation era. This is followed by the matter era and the dark energy era responsible for the accelerated expansion of the Universe. The Universe exhibits two types of inflation: An early inflation corresponding to the Planck density ρ_P due to quantum mechanics and a late inflation corresponding to the dark energy density ρ_Λ due to the cosmological constant. The evolution of the early and late Universe is remarkably symmetric. We have represented with a dashed line the standard model leading to the big bang primordial singularity. The dotted line corresponds to the model where the radiation is neglected.

The energy density ρ_m of the particles into which φ decayed satisfies a conservation equation as the (1.7), but corrected to take account of the flow of energy from the inflaton:

$$\dot{\rho}_m + 3H\rho_m(1+w) = \Gamma\rho_\varphi.$$

The matter energy density starts equal to zero at $t = t_I$, then rises at first, and finally falls as attenuated by the expansion of the Universe. It is of some interest to find the maximum value of $\rho_m(t)$ since this is very telling about the maximum temperature ever reached after inflation, it controls the kinds of relics -cold dark matter, baryons,etc. - left over from the early Universe. Two extremal cases can be useful to calculate the maximum density : $\Gamma \gg H(t_I)$ and $\Gamma \ll H(t_I)$. In the former case, all the energy of the inflaton at the end of inflation $\rho_\varphi(t_I)$ was converted into ordinary (relativistic) matter and radiation ρ_m and then decreased with the usual a^{-4} factor. In the latter case, there has been a period where the energy density was still dominated by the inflaton, during this period the density decreased as a^{-3} and thus ρ_m at the beginning of the radiation dominated era would have been much less than ρ_φ at the end of inflation.

1.9 THE GENERATION OF PERTURBATIONS

We have seen that one of the most powerful observational facts of inflation is the capability of correlating scales that would have been otherwise causally

disconnected. During inflation, the Universe spacetime metric at the zero-order is the FLRW one and the expansion was driven by the uniform scalar field of inflaton.

However, as expected from Quantum Field Theory, scalar fields do fluctuate, thus the nearly exponential expansion amplifies the inflaton quantum fluctuations, yielding the small anisotropies that today we observe in the CMB. Thus the average of the fluctuations is zero whereas the variance (i. e. the square of the fluctuations) is not (Starobinsky, 1982).

The variance of a statistically homogeneous and isotropic quantity X is related to the *correlation function*, ξ as it follows:

$$\xi(\mathbf{x}, \mathbf{x}') = \langle X(\mathbf{x})X(\mathbf{x}')\rangle = \xi(|\mathbf{x} - \mathbf{x}'|),$$

where $\langle\cdot\rangle$ denotes the expected value. The Fourier transform of X is:

$$\tilde{X}_{\mathbf{k}} = \int d^3x X(\mathbf{x}) e^{-i\mathbf{k}\cdot\mathbf{x}},$$

from which we can define the power spectrum of X as:

$$\langle \tilde{X}_{\mathbf{k}}, \tilde{X}_{\mathbf{k}'}\rangle = (2\pi)^3 \delta(\mathbf{k} + \mathbf{k}') P_X(k). \tag{1.32}$$

The power spectrum measures the amplitude of the fluctuations at a given scale k. However, another definition of power spectrum is given by the quantity $\Delta^2_X(k)$ related to $P_X(k)$ by the relation:

$$\Delta^2_X(k) = \frac{k^3}{2\pi^2} P_X(k).$$

We will see in the following that these quantum fluctuations in the inflaton and in the metric are capable to generate the scalar and tensor primordial power spectra. Therefore, we perturb the two tensors appearing in the Einstein equations (1.6) to get the differential equations describing the dynamics of the perturbations. Generally, a *perturbed* FLRW metric can be put in the following form

$$ds^2 = -(1 + 2\Psi)dt^2 + 2a(t)B_i dx^i dt + a^2(t)\Big[(1 - 2\Phi)\delta_{ij} + E_{ij}\Big] dx^i dx^j, \tag{1.33}$$

where Ψ, Φ are scalars, B_i is a 3-vector, and E_{ij} is a symmetric traceless 3-tensor. The (1.33) is usually known as *Newtonian* gauge (Bardeen, 1980) if one imposes non-diagonal scalar perturbations of the metric to vanish. The stress-energy perturbations are commonly written as:

$$\delta\rho(\mathbf{x}, t) = \rho(\mathbf{x}, t) - \bar{\rho}(t),$$
$$\delta p(\mathbf{x}, t) = p(\mathbf{x}, t) - \bar{p}(t).$$

In addition to them an anisotropic stress tensor $\Sigma_{\mu\nu}$ is expected too at first order.

Now it is possible to show that at linear level and in a rotation invariant background, scalar, vector and tensor modes do not couple but they

evolve independently. However, one can notice that the split "background-perturbation" leads to *gauge dependent* quantities both for scalars and vectors, i. e. it depends on the particular choice of coordinate system. On the contrary, tensor perturbations are gauge invariant at linear level. We are mostly interested in scalar and tensor perturbations in the following chapters, while we neglect vector perturbations since they are damped during expansion. The gauge dependences can be circumvented even for scalar and vector perturbations by expressing the results in terms of gauge independent quantities, as the *comoving curvature perturbation*, $\mathcal{R}$, (Bardeen, 1980):

$$\mathcal{R} = -\frac{H}{\dot{\varphi}}\delta\varphi.$$

We define k the wavenumber of perturbations roughly equal to the inverse of the comoving wavelength of a certain perturbation mode. Perturbations are divided according to $k\eta$ values, that represent the ratio of the comoving horizon and the perturbation comoving wavelength.

As shown in a fig.1.9, if $k\eta \ll 1$, then the mode in question has a wavelength larger than the horizon so that no causal physics could possibly have affected it: this corresponds to *super-horizon* perturbations. So, before inflation started, the comoving Hubble radius was so large that all scales were well within the horizon in causal contact and could thermalize. When these cosmological modes were comparable to the horizon $k\eta \gtrsim 1$, causal physics restarted to operate on them, becoming *sub-horizon* perturbations.

Thus, the equation describing the evolution of both scalar and tensor[10] modes for a given Fourier mode $\mathbf{k}$ is:

$$(a\delta\varphi_k)'' + \left(k^2 - \frac{z''}{z}\right)(a\delta\varphi_k) = 0, \tag{1.34}$$

$$(ah_k^{+,\times})'' + \left(k^2 - \frac{a''}{a}\right)(ah_k^{+,\times}) = 0, \tag{1.35}$$

here the prime quantities denote derivatives with respect to the conformal time $d\tau = dt/a$ and $z \equiv a\dot{\varphi}/H$.

Since the primordial perturbations are small, orders of 10^{-5} in the CMB the linearized eqs. (1.34) and (1.35) provide an accurate description for the generation and subsequent evolution of the cosmological perturbations during inflation. We can distinguish two functional behaviour to the solution of (1.35). When $k\eta < 1$, i. e. after the mode crosses the horizon and enters in the super-horizon regime, the perturbations in Fourier domain remain constant. Today we are able to see the perturbations that re-enter the horizon and became sub-horizon again, such fluctuations evolves with an oscillating behaviour. In the approximation of slow-roll inflation and a quasi-De Sitter evolution for the background,

$$v_k = \frac{e^{-ik\eta}}{\sqrt{2k}}\left[1 - \frac{i}{k\eta}\right].$$

10 As tensors presents 2 states of helicity, tensor perturbations are divided among two polarization states, $h^+, h^\times$.

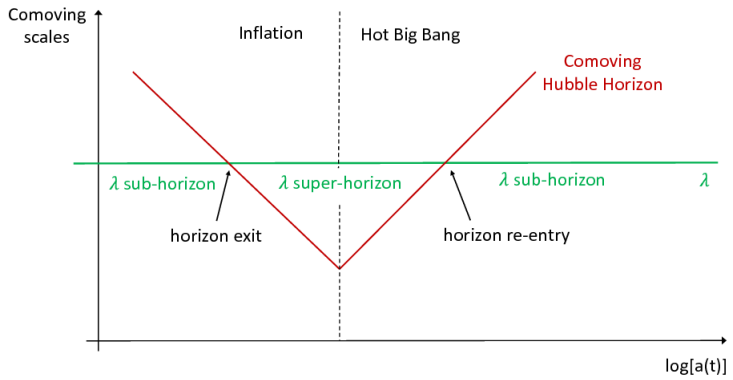

Figure 1.9: Evolution of the Hubble radius and of a physical wavelength during the inflationary phase and the subsequent radiation and matter dominated epochs. Without inflation, the wavelengths of all the modes are super-horizon initially, whereas in the case where inflation takes place, they were sub-horizon at early times and they thermalized.

The variance for sub-horizon modes (i. e. $|k\eta| \gg 1$)is then:

$$\frac{1}{a^2}\langle v_k v_{k'}\rangle = (2\pi)^3\delta(\mathbf{k}+\mathbf{k}')\frac{H^2}{2k^3}.$$

Since the power spectrum amplitude for scalar and tensor perturbations remains constant, the value of H would be close to the one at horizon crossing, H_*.

$$\Delta_S^2(k) \equiv \Delta_{\mathcal{R}}^2(k) = \frac{1}{8\pi^2}\frac{H_*^2}{M_{Pl}^2}\frac{1}{\hat{\epsilon}_*},$$

$$\Delta_T^2(k) \equiv 2\Delta_h^2(k) = \frac{2}{\pi^2}\frac{H_*^2}{M_{Pl}^2}.$$

Usually the amplitude is referred at some pivot scale $k_0 \sim 0.05\,h/\mathrm{Mpc}$. The ratio of both the amplitudes Δ_T^2 and Δ_S^2 is usually referred as *tensor-to-scalar* ratio, and it is related to the slow-roll parameter :

$$r \equiv \frac{\Delta_T^2}{\Delta_S^2} = 16\hat{\epsilon}_*.$$

Measuring primordial power spectra allows us to probe the Universe at very high energy, indeed H_*/M_{Pl}^2 gives a rough estimate of the energy of the Universe when inflation started. As we will see in the next section a measure of tensor perturbation power spectrum is capital in order to constrain the energy scale of inflation by means of the following relation:

$$V^{\frac{1}{4}} \simeq \left(\frac{r}{0.01}\right)^{\frac{1}{4}} 10^{16}\,\mathrm{GeV}. \tag{1.36}$$

Moreover, we do expect the power spectra to be scale invariant, i. e.with very small spectral index (or tilt):

$$n_X = \frac{d\ln\Delta_X^2}{d\ln k}.$$

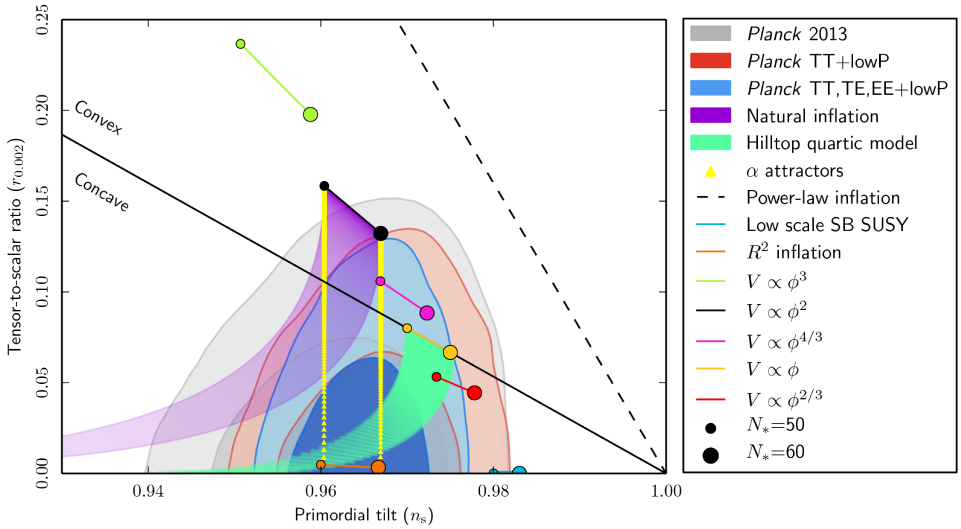

Figure 1.10: Marginalized joint 68% and 95% confidence level regions for n_s and r at $k = 0.002\text{Mpc}^{-1}$ from (Planck Collaboration, Ade, Aghanim, Arnaud, Arroja, et al., 2016b) compared to the theoretical predictions of selected inflationary models.

Since the power spectrum is taken to be scale invariant (i. e. $n_\chi = 0$), the running of the spectral index $dn/d\ln k$ is typically neglected. It is possible to relate an observable quantity such as the spectral index to the inflationary parameters as it follows:

$$n_S = 1 + 2\hat{\eta} - 4\hat{\epsilon},$$
$$n_T = -\frac{r}{8}.$$

So far, we considered a *single-field* inflation, i. e. there was only one field responsible in driving the inflationary expansion. However, in last decades a so wide plethora of inflationary models have been proposed. Martin, Ringeval, and Vennin (2014) collected them all in a comprehensive review: the common property shared by all the models is the presence of one or more fields φ_i, with associated potentials V_i. Depending on the shape and on the magnitude of V we have several field models and different values for the inflation parameters and hence spectral indices.

Recent CMB measurements combining temperature and polarization data from the Planck satellite (Planck Collaboration, Ade, Aghanim, Arnaud, Arroja, et al., 2016b) provided accurate estimates of $n_S = 0.968 \pm 0.006$, $dn_s/d\ln k = -0.003 \pm 0.007$, showing with very high significance the deviations from the scale invariance at $n_S = 1$. Moreover, it provided interesting constraints to the inflationary models disfavouring several inflationary models as shown in fig.1.10 predicting a larger tensor-to-scalar ratio, such as $V \propto \varphi^3$ inflation.

Scalar perturbations couple to the density of matter and radiation and ultimately are responsible for most of the inhomogeneities and anisotropies

in the Universe. The tensor fluctuations perturb the metric tensor and are in the form of a stochastic background of gravitational waves. They do not couple to the scalar density perturbations and so they are not responsible for the large scale structure of the Universe, but they induce signatures observable in the polarization of the CMB, though in the temperature CMB anisotropies tensor fluctuations are negligible with respect to the scalar ones, as we will see in the next chapter.

1.10 THE ΛCDM MODEL

We conclude this Chapter by summarizing the present constraints on the most important cosmological parameters. The latter are constrained by a variety of observables, including the distribution of large scale structures and CMB. We do not have time to review all those in the present work, and we give just the final results. The CMB part of those, and the future expectations related to it, represent the subject of the other chapters of this Thesis.

The commonly accepted cosmological model includes both a non vanishing cosmological constant Λ and Cold Dark Matter as the dominant matter component leading the large scale structure formation and is generally referred to as the ΛCDM model. This model is based upon a spatially-flat, expanding Universe whose dynamics are governed by eq. (1.13) and (1.14). The primordial seeds of structure formation are Gaussian adiabatic fluctuations produced at the time of inflation with an almost scale-invariant spectrum.

This model is described by only six key parameters as listed in tab.(1.1). Despite its simplicity, the base ΛCDM model has proved to successfully describe a wide range of cosmological data from the CMB, including the SNae Ia to the large-scale clustering of galaxies. Furthermore, as we discussed in this chapter the studies related to the early Universe have led to a rich phenomenology of inflationary models. ΛCDM would be accurately constrained in the incoming decades because of the huge quantity of data sheding light on several dark sectors of the Universe.

PARAMETER	VALUE
$\Omega_b h^2$	0.02222 ± 0.00023
$\Omega_c h^2$ †	0.1199 ± 0.0022
H_0	67.26 ± 0.98
n_S	0.965 ± 0.006
$\ln(10^{10} A_S)$ ‡	1.881 ± 0.014
τ_{reion}	0.078 ± 0.019

Table 1.1: Latest values from Planck Collaboration, Ade, Aghanim, Arnaud, Ashdown, et al. (2016) of the base 6 parameters of ΛCDM cosmological model. † Cold dark matter density today. ‡ Log power of primordial scalar perturbations ($k_0 = 0.05\,\mathrm{Mpc}^{-1}$).

2

CMB ANISOTROPIES

> The first corporeal form, which some call corporeity, I hold to be light. For light of its own nature diffuses itself in all directions, so that from a point of light a sphere of light of any size may be instantly generated, provided an opaque body does not get in the way.
>
> Robert Grosseteste, *De luce*, 1225

As we have seen in the previous chapter, the CMB is the ultimate carrier of electromagnetic information concerning the physics of the early Universe. In this chapter we give a description of the theory and phenomenology of CMB anisotropies, along with its relation with measure of relevant cosmological processes.

2.1 CMB TEMPERATURE ANISOTROPIES

At the last scattering surface, $z \simeq 1100$, the gravitational instability theory says that fractional density perturbations δ of the order of 10^{-3} must have existed for galaxies and clusters of galaxies to have formed and be observed at present time. A long standing challenge in cosmology has been to detect the corresponding fluctuations in brightness temperature, the so called anisotropies of the CMB (fig. 2.1), and it took roughly 25 years before the first detections were obtained by the COBE satellite in 1992 (Smoot et al., 1992). The subsequently intense activity to map the sky at increasing levels of sensitivity and angular resolution led to a series of ground and balloon-based measurements as well as two space missions: the NASA Wilkinson Microwave Anisotropy Probe (WMAP, Hinshaw et al. (2013)) and more re-

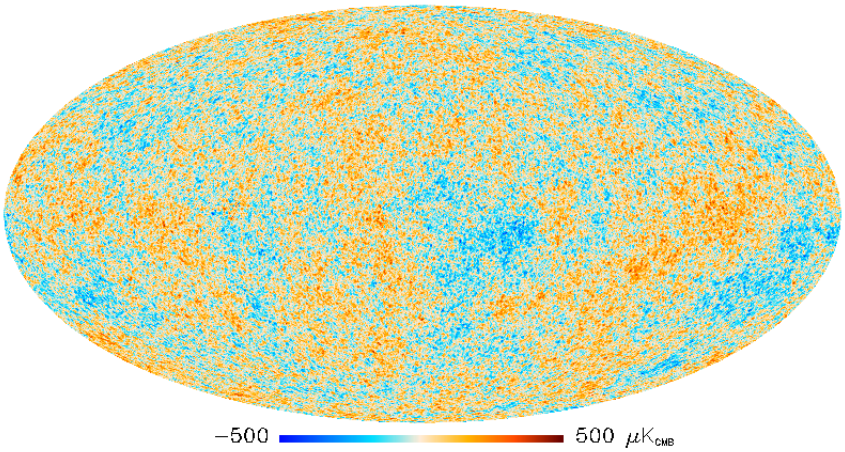

Figure 2.1: Map of temperature CMB anisotropies observed by Planck (Planck Collaboration, Ade, Aghanim, Alves, et al., 2014a).

cently the ESA Planck satellite (Planck Collaboration, Ade, Aghanim, Arnaud, Ashdown, et al., 2016). These observations have led to a stunning confirmation of the "Standard Model of Cosmology". Moreover, the CMB anisotropy measurements place quite precise constraints on a number of cosmological parameters, and have initiated us into the so called era of *precision cosmology*.

We distinguish *primary* anisotropies, which arise from effects at the time of recombination, from the *secondary* ones which are generated by scattering along the line of sight. Mainly there are three primary effects, which are important on, respectively, large, intermediate and small angular scales.

In what follows, we denote with $' = d/d\eta$, derivatives with respect the conformal time,i. e. the time spent by light to travel a comoving horizon distance, and thus it is exactly η since in our units $c = 1$; for proper time derivatives we adopt dots as in the previous chapter.

2.1.1 *The physical processes generating the CMB anisotropies*

In Sect.1.6 we defined the Thomson scattering rate $\Gamma = \sigma_T a n_e x_e$, which evolves as $a^{-2} x_e$. Before recombination, it was very efficient since $\Gamma \gg H$ and the Universe was opaque. However, Γ suddenly dropped after recombination and the Universe became transparent until reionization of the inter-Galactic medium at low redshift causing rescattering.

The parameter that gives the probability that a CMB photon experienced its last scattering at recombination is the so called *visibility function*, $g(\eta) = -\tau' e^{-\tau}$, with τ being the optical depth (see eq.(1.25) for the dependence on η). The visibility function is negligible before recombination, and it narrowly peaks at the time of recombination, whose duration is given by the width of g . Then it drops again because of the optical depth plateau $\tau' = 0$

between recombination and reionization. It presents a lower and wider peak since a small part of photons have re-scattered around the reionization.

In order to derive the evolution of photons in terms of time and local distribution, we need to solve the Boltzmann equation at first order:

$$\frac{d}{d\eta} f = C[f, f_e], \tag{2.1}$$

where $C[f, f_e]$ stands for the photon-electron coupling due to Thomson scattering. Here, we recall that since electrons and baryons were tightly coupled via Coulomb scattering it is indifferent to choose among photon-baryon and photon-electron coupling. Moreover, since photons are in thermal equilibrium with electrons, they are entirely described at a given point by the local equilibrium temperature $T(\eta, \mathbf{x})$, so that:

$$f(\eta, \mathbf{x}, \mathbf{p}) = \frac{1}{e^{\frac{p}{T(\eta,\mathbf{x})}} - 1}.$$

As in Sect.1.9 we can expand the Bose-Einstein distribution function f as a background part and a first order perturbation:

$$\bar{f}(\eta, \mathbf{x}, \mathbf{p}) = \frac{1}{e^{\frac{p}{T(\eta)}} - 1} \tag{2.2}$$

$$\delta f = \frac{d\bar{f}}{d \log p} \frac{\delta T(\eta, \mathbf{x})}{T(\eta)} \tag{2.3}$$

The geodesic equation express the evolution of photon momentum after decoupling, in the Newtonian gauge (see (1.33)) it reads:

$$\frac{d(ap)}{d\eta} = -ap\Phi' - ap\hat{n} \cdot \nabla\Psi. \tag{2.4}$$

In a perfectly homogeneous Universe the photons would experience only the cosmological redshift, i. e. $p \propto a^{-1}$ and thus $pa = const$. The presence of metric perturbations Φ and Ψ induces variation in the product ap. The first term $ap\Phi'$ accounts for *dilation*, i. e. the fact that locally the expansion is more advanced or delayed than the average since the *perturbed* scale factor is $(1 + \Phi)a$ in (1.33). The second term is the gravitational blueshift (redshift) of photons falling into (leaving) a potential well. If we rewrite (2.4) as :

$$\frac{d \ln(ap)}{d\eta} = -\Phi' - \hat{n} \cdot \nabla\Psi,$$

p disappears from the right hand side (r.h.s.): i. e. photons with different momenta travelling through a perturbed Universe along geodesics, experience the same relative momentum variation. This implies that the Bose-Einstein functional shape does not change in a perturbed Universe. However, it acquires an extra-term related to the direction of propagation $\hat{n} \equiv \mathbf{p}/p$ of photons travelling along different geodesics since they experience different redshifting. Defining $\Theta \equiv \delta T/\bar{T}$, the Boltzmann equation can now be used

to find Θ as a function of $(\eta, \mathbf{x}, \hat{n})$, i. e. spacetime location and photon propagation direction.

As in Sect.1.9, we work in Fourier domain and we can derive an expression for $\tilde{\Theta}(\eta, \mathbf{k}, \hat{n})$. Notice that because of the statistical isotropy of the FLRW Universe Θ should not depend explicitly on $\mathbf{k}$ nor on $\hat{n}$, but only on the product $(\mathbf{k} \cdot \hat{n})/k = \mu$. By means of Legendre transformation, we have:

$$\Theta(\eta, \mathbf{k}, \mu) = \sum_{\ell=0}^{+\infty} (-i)^{\ell} (2\ell + 1) \Theta_{\ell}(\eta, \mathbf{k}) P_{\ell}(\mu). \tag{2.5}$$

Here, Θ_{ℓ}s are temperature anisotropy multipoles, Θ_0 is called *monopole*[1] locally related to the photon density fluctuations δ_{γ}, Θ_1 the *dipole* related to peculiar velocity with respect to the background, Θ_2 the quadrupole etc. The Boltzmann equation in this fashion can be written as an infinite hierarchy of equations of motion as a function of the coupled multipoles. In real space (2.1) it becomes:

$$\Theta' + \hat{n} \cdot \nabla(\Theta + \Psi) + \Phi' = -\Gamma \left[\Theta - \Theta_0 - \hat{n} \cdot \mathbf{v}_e\right], \tag{2.6}$$

and in Fourier space,

$$\tilde{\Theta}' + ik\mu(\tilde{\Theta} + \tilde{\Psi}) + \tilde{\Phi}' = -\Gamma \left[\tilde{\Theta} - \tilde{\Theta}_0 - \mu \tilde{v}_e\right], \tag{2.7}$$

where v_e is the peculiar velocity of electron that for the tight coupling is equal to the baryon one, $\mathbf{v}_e = \mathbf{v}_b$, as well as density perturbations $\delta_e \equiv \delta_b$. One of the most remarkable facts from (2.6) is that at early times when photons, electrons and baryons form a tightly coupled fluid, $\Gamma \gg 1$, therefore it forces Θ to evolve in such a way that the parenthesis in the r.h.s. must vanish: meaning that $\Theta = \Theta_0 + \Theta_1$, with the dipole $\Theta_1 \equiv \hat{n} \cdot \mathbf{v}_b$. All the other multipoles vanish and the photon perturbations can be described in terms of only two independent variables Θ_0 and Θ_1 as in a perfect fluid. However, both for (2.6) and (2.7) we need to derive an expression for the baryons quantities[2]: δ_b and v_b. The procedure is very similar to the one sketched above for the photons, but we consider collision from Coulomb and Thomson scattering. In Fourier space they read as:

$$\begin{aligned} &\tilde{\delta}_b' + ik\tilde{v}_b + 3\Phi' = 0, \\ &\tilde{v}_b' + \frac{a'}{a}\tilde{v}_b + ik\Psi = -\Gamma \frac{4\bar{\rho}_{\gamma}}{3\bar{\rho}_b} \left[3i\tilde{\Theta}_1 + \tilde{v}_b\right]. \end{aligned} \tag{2.8}$$

The first equation describe the evolution of ordinary matter perturbation in a perturbed metric. Whereas the second one describe the coupling of matter with radiation. Even for (2.8), the tight-coupled regime $\Gamma \gg 1$ implies that $3\Theta_1 \simeq v_b$. We refer to the factor $R \equiv 4\bar{\rho}_{\gamma}/3\bar{\rho}_b \propto a$ which implies a relation for photon and baryon density perturbations: $\delta_{\gamma} = \frac{4}{3}\delta_b$.

1 Θ_0 can be seen as the average of $\Theta(\eta, \mathbf{k}, \hat{n})$ over all directions.

2 As Dodelson (2003) remarked, the nomenclature is misleading: due to tight coupling with *baryons* we means both protons and electrons (which are leptons).

By multiplying (2.7) by $P_0(\mu)$ and $P_1(\mu)$ and integrating over μ, we get two first-order coupled equations equations for Θ_0 and Θ_1. By means of (2.8), we can turn these into one second-order equation:

$$\Theta_0'' + \frac{a'}{a}\frac{R}{1+R}\Theta_0' + k^2 c_s^2 \Theta_0 = -\frac{k^2}{3}\Psi - \frac{a'}{a}\frac{R}{1+R}\Phi' - \Phi''. \tag{2.9}$$

As long as electrons, baryons and photons are tightly coupled we can assume the Universe as filled by an effective fluid in which density waves propagate at the sound speed

$$c_s = \sqrt{\frac{1}{3(1+R)}},$$

the sound speed depends on the baryon density in the Universe, and in the absence of baryons it has the standard value for a relativistic fluid, $c_s = 1/\sqrt{3}$. We can define the *sound horizon*, s as the maximum distance sound could travel:

$$s = a\int_{\eta_{ini}}^{\eta} c_s \, d\eta' \simeq a c_s \eta,$$

with $\eta \gg \eta_{ini}$. The presence of baryons, makes the fluid heavier and lowers the sound speed. The second term on the left-hand side is a damping term, increasing with the contribution of baryons to the total energy of the fluid, while the third term accounts for pressure forces in the effective fluid. The first term on the r.h.s. accounts for the gravitational force and the last two terms for dilation effects. Eq. (2.9) can be alternatively written as[3]

$$\left\{\frac{d^2}{d\eta^2} + \frac{R'}{1+R}\frac{d}{d\eta} + k^2 c_s^2\right\}[\Theta_0 + \Phi] = \frac{k^2}{3}\left[\frac{1}{1+R}\Phi - \Psi\right].$$

2.1.2 *Acoustic oscillations*

Equation (2.9) reduces to that of a simple harmonic oscillator if $R = const$ in absence of gravitational source terms, since the friction vanishes and the sound speed is constant. This basically means that pressure gradients act as a restoring force to any initial temperature perturbation in the system which thereafter oscillates and propagates through the plasma with speed c_s. Physically these temperature oscillations represent the heating and cooling of a fluid that is compressed and rarefied by a standing acoustic wave. The solution would be of the form:

$$\Theta(\eta) = \Theta_{ini}\cos(k s_* + \varphi),$$

with the $*$ we refer to quantities evaluated at recombination and the two constants (Θ_{ini}, φ) set by the integration. In particular, for *adiabatic* initial

3 Since $R \propto a$, $R' = a'/aR$.

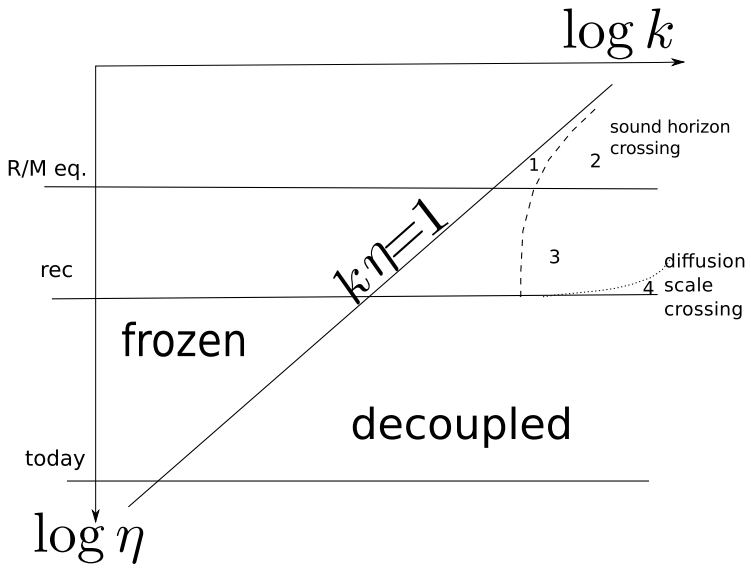

Figure 2.2: Different regions in (k, η) space, corresponding to qualitatively different behaviours for photon (and baryon) perturbations.

conditions [4] and in Newtonian gauge, photon density/temperature fluctuations should be constant in the super-horizon limit, $k\eta \ll 1$: this fixes the phase to $\varphi = 0$. As we have introduced in sect.1.9 inflation set the *ab initio* model of all clumpiness in the Universe and thus it sets the initial phase to be zero for all the Fourier modes. It follows that, remarkably, as a prediction there will be peaks and troughs in the amplitude of oscillations as a function of the wave number.

Moreover, since inflation predicts approximatively scale invariant amplitude of initial perturbations, it will leads to roughly a scale invariant oscillation power spectrum. The limit between constant and oscillatory regime is not set by the value of $k\eta$ but by that of $kc_s\eta$. In fact, the condition $kc_s\eta \ll 1$ is equivalent to $\lambda \gg s_*$, where λ is the physical wavelength $\lambda = 2\pi a/k$. Modes start oscillating when their wavelength becomes smaller than the sound horizon, and later on, the number of oscillations n is given by the ratio s_*/λ. In the following, we distinguish *even* and *odd* peaks for the modes corresponding to peaks which follow $k_n = n\pi/s_*$ depending on the value of n.

Moreover, the modes that are caught at recombination at maxima or minima of their oscillation, will correspond to peaks in the power spectrum level, i. e. the square of the variance of $\Theta(k, \eta_*)$.

However, this description holds when $R = const$ and gravitational terms can be considered negligible. Vice versa, we have seen that $R \propto a$ grows

4 This is the easiest way to generate perturbations in a uniform Universe: by adiabatically compressing and expanding volume elements. This would change the matter density and the photon number density by the same factor. Therefore, adiabatic perturbations would affect energy densities of matter and radiation in different ways, i. e. $\delta_r = 4\delta_m/3$. The opposite approach is to perturb the entropy density instead of the energy one, this leads to *isocurvature* perturbation, see Peacock (1999) for further readings.

with time and at the time of decoupling $R(\eta_{dec}) \simeq 1$. One may ask at which regime gravitational source terms start to play a key role.

To answer these questions it could be useful to describe qualitatively the evolution of Θ_0 in different regions of the (k, η) space, shown in fig.2.2. In this figure the super-horizon and sub-horizon regions are defined by the solid diagonal line $k\eta = 1$, which is equivalent to $k = aH$ during radiation dominated era. This allows us to refer to those regions as *sub-Hubble* and *super-Hubble* regions respectively where a physical wavelength is smaller or larger than the Hubble scale $1/H$. From top to bottom the horizontal lines correspond to the time of matter-radiation equality, the recombination time and the time today. The dashed line, corresponds to the line $kc_s\eta = 1$ separating the wavelengths bigger (smaller) than the sound horizon s_* before decoupling (after decoupling it is meaningless to use this notion). At early times $c_s = 1/\sqrt{3}$, and this implies $k\eta = \sqrt{3}$; just before decoupling R increases, c_s decreases, and the comoving sound horizon becomes roughly constant.

As expected, in super-Hubble region Θ_0 is frozen to its initial value. The dotted line separates wavelengths larger (or smaller) than the diffusion wavelength $\lambda_d \simeq a r_d$, where r_d is the comoving distance over which photons, in Brownian motion in the hot plasma, travel between time η_i to η_e,

$$r_d \simeq \left[\int_{\eta_i}^{\eta_e} d\eta \Gamma^{-1}\right]^{1/2}.$$

The region 1 in fig.2.2 corresponds to modes that are crossing the sound horizon before decoupling. In this region gravitational terms give important contribution by shifting the zero-point of oscillations and boosting their amplitude. This happens for a limited amount of time, since the metric fluctuations quickly decay inside the sound horizon during radiation domination. The zero-point of oscillations in radiation domination can be found by neglecting baryons $R' = 0$ in (2.9) :

$$\Theta_0^{eq} = -\frac{1}{3c_s^2}\Psi = -(1+R)\Psi.$$

Since the gravitational term is non-zero on super-Hubble scales the equilibrium point is shifted away from zero on those scales, whereas it reaches asymptotically zero on the sub-sound-horizon scales. The zero-point shift in oscillations is somehow expected since temperature and metric perturbation are intimately related. In the Newtonian gauge Φ represents the spatial metric fluctuations, whereas Ψ the time-time $\delta t/t$ ones. Temporal shifts can be related to the fractional change of CMB temperature, since $a \propto t^{2/[3(1+w)]}$

$$\Theta = -\frac{\delta a}{a} = -\frac{2}{3}(1+w)^{-1}\frac{\delta t}{t},$$

producing temperature perturbation of $-\Psi/2$ and $-2\Psi/3$ respectively in radiation and matter dominated eras.

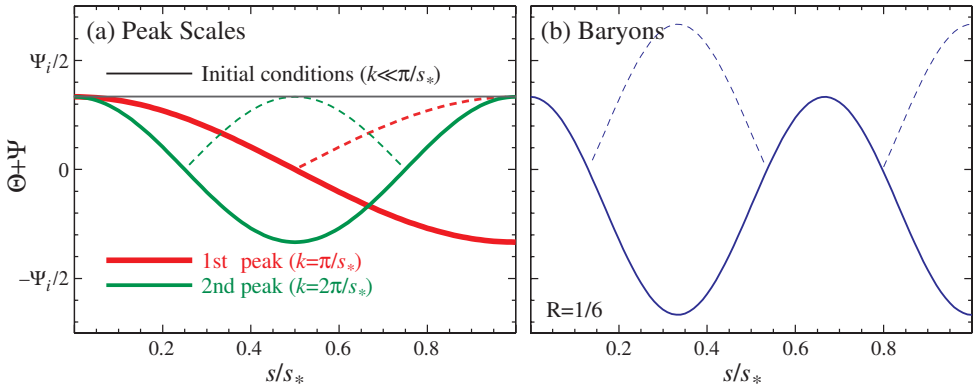

Figure 2.3: Plots from Hu and Dodelson (2002). (a) Peak scales in radiation dominated era: the wave mode that completes half an oscillation by recombination sets the physical scale of the first peak. Both minima and maxima correspond to peaks in power (dashed lines show absolute values) and so higher peaks are integral multiples of this scale with equal height. Plotted here is the behaviour described in (2.10) (constant potentials, no baryon loading). (b) Baryon loading. Baryon loading boosts the amplitudes of every other oscillation with $R = 1/6$ for the third peak.

The zero-point of oscillations in radiation domination can be found by neglecting baryons $R' = 0$ in (2.9), with $c_s = 1/\sqrt{3}$:

$$\Theta_0'' + \frac{k^2}{3}\Theta_0 = -\frac{1}{3c_s^2}\Psi - \Phi''.$$

Hence, by replacing Θ_0 with $\Theta + \Psi$ the solution is still oscillatory:

$$[\Theta + \Psi](\eta) = [\Theta + \Psi](\eta)\cos(ks_*), \tag{2.10}$$

even without an initial temperature fluctuation to displace the oscillator, acoustic oscillations would arise by the infall and compression of the fluid into gravitational potential wells. The quantity $\Theta + \Psi$ can be thought of as an *effective temperature* : the plasma begins effectively rarefied in gravitational potential wells, as gravity compresses the fluid and pressure resists, a rarefaction becomes a compression and rarefaction again. The first peak in fig.2.3(a) corresponds to the mode that is caught in its first compression at recombination. The second peak at roughly half the wavelength corresponds to the mode that went through a full cycle of compression and rarefaction during recombination[5].

Region 2 corresponds to the wavelengths smaller than the sound horizon during radiation domination. This is the region where the harmonic oscillator idealization we presented above takes place: indeed metric fluctuations have already decayed (allowing us to neglect gravitational source terms) and $R \ll 1$ during radiation domination.

5 We will use this terminology of the compression and rarefaction phase inside initially overdense regions but one should bear in mind that there are an equal number of initially underdense regions with the opposite phase.

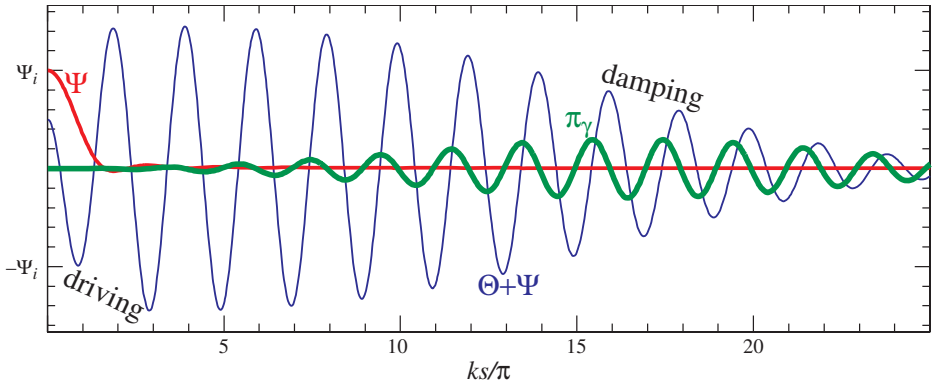

Figure 2.4: Plot from Hu and Dodelson (2002). The decay of the potential Ψ drives the oscillator in the radiation dominated epoch. Diffusion generates viscosity π_γ, i.e. a quadrupole moment in the temperature, which damps oscillations and generates polarization. Plotted here is the numerical solution to (2.9) for a mode with wavelength much smaller than the sound horizon at decoupling, $ks_* \gg 1$.

Region 3 refers to wavelength smaller than the sound horizon during the intermediate stage between the time of equality and the decoupling one. In this region, metric perturbations have decayed but R is not negligible any more. The eq.(2.9) is still an oscillator equation containing a friction term. The solution corresponds to damped oscillations.

It is worth asking what physically causes this damping: when the energy density of non-relativistic baryons takes over, the inertia to compression of photon-baryon fluid increases so that it is hard for the pressure terms to overcome it. Thus baryons lower the sound speed, enhance the amplitude of the oscillations and shift the equilibrium point to $\Theta_0 = -(1+R)\Psi$ (see fig. 2.3(b)). The classical mechanics analogue is that of a spring with a mass $m = 1 + R$ in a constant gravitational field: for the same initial conditions, by increasing the mass the oscillator fall further in the gravitational field with larger amplitude oscillations and a shifted zero-point, breaking the symmetry of the oscillations. In the same manner, the extra-gravity provided by baryons enhances only the compressional phase into the potential well of the oscillations, every other peak and for cosmological model they correspond to the odd peaks.

Region 4 corresponds to modes with smaller wavelength than the diffusion scale in the photon-baryon fluid. At early time in the tightly-coupled limit the photon mean free path is very small, since the rate of collisions is very high, thus all the cosmological scales are well above this length. However, at decoupling the diffusion length suddenly increases encompassing most of the sub-sound-horizon modes. In this regime the oscillator equation is not descriptive at all, since the photon-baryon fluid cannot be described as a perfect fluid. Perturbations, whose wavelength is smaller than λ_d get strongly damped because photon diffusion tends to smooth and average out any small-scale perturbations and imperfections in the fluid such as shear viscosity and heat conduction arise. A non-vanishing anisotropic stress is

directly proportional to the quadrupole moment of the photon temperature distribution, π_γ. A quadrupole moment is established by a gradient in v_γ as photons from "neighbouring" temperature crests meet at trough. By defining the differential optical depth $\dot{\tau} = -\Gamma$, we have that $\pi_\gamma \sim 2(kv_\gamma/\dot{\tau})$, (we will see the leading role of π_γ in the generation of CMB polarization anisotropies in sect.2.2). Viscosity and conduction appear in (2.9) as damping terms and we expect the inhomogeneities to be damped by an exponential factor of order $e^{-k^2\eta/\dot{\tau}}$. Numerical integration show that the damping scale is of order $k_d s_* \approx 10$ leading to a substantial supression of the oscillations beyond the third peak.

2.1.3 *From inhomogeneities to anisotropies*

The most accurate map of temperature anisotropy to date is shown in fig.2.1 and it was observed by Planck satellite. It represents the map of anisotropies seen today from out peculiar position in the Universe and it can be expressed mathematically as:

$$\frac{\delta T}{T}(\hat{n}) = \Theta(\eta, \mathbf{o}, -\hat{n}),$$

since along the line of sight direction $\hat{n}$ photons propagate towards $-\hat{n}$.

We now relate the perturbation in *any* point in the last-scattering surface to what we observe at *any* direction $\hat{n}$. This can be done by means of the line-of-sight integration of the Boltzmann eq. (2.6).

We firstly start computing the total derivative of the product function $\mathcal{F}(\eta, \mathbf{x}, \hat{n}) = e^{-\tau(\eta)}(\Theta(\eta, \mathbf{x}, \hat{n}) + \Psi(\eta, \mathbf{x}))$ along the trajectory of photons travelling from last scattering surface to an observer placed on the Earth. The total derivative of $\mathcal{F}$ is:

$$\frac{d}{d\eta}\mathcal{F}(\eta, \mathbf{x}, \hat{n}) = \mathcal{F}' + \hat{n} \cdot \nabla\mathcal{F},$$

where the derivative $\frac{dn_i}{d\eta} = 0$ because photons travel in straight line in an unperturbed Universe.Therefore, we can explicitly write:

$$\frac{d}{d\eta}\left[e^{-\tau}(\Theta + \Psi)\right] = e^{-\tau}\left((\Theta' + \Psi') + \hat{n} \cdot \nabla(\Theta + \Psi)\right) - \tau' e^{-\tau}(\Theta + \Psi).$$

Notice that the left hand side of the (2.6) equals the first bracket in the r.h.s. of the previous equation; moreover, since $\Gamma = -\tau'$, we get:

$$\frac{d}{d\eta}\left[e^{-\tau}(\Theta + \Psi)\right] = -\tau' e^{-\tau}(\Theta_0 + \Psi + \hat{n} \cdot \mathbf{v}_b) + e^{-\tau}(\Phi' + \Psi').$$

We therefore integrate this relation along the line of sight, $\hat{n}$ starting from early time before recombination such that $e^{-\tau(\eta_{ini})} \simeq 0$ till the present time (by definition $e^{-\tau(\eta_0)=1}$, yielding to:

$$(\Theta + \Psi)\,|_{obs} = \int_{\eta_{ini}}^{\eta_0} d\eta\,\left[g((\Theta_0 + \Psi + \hat{n} \cdot \mathbf{v}_b) + e^{-\tau}(\Phi' + \Psi'\right], \tag{2.11}$$

where the notation $|_{obs}$ means evaluated at observer location, along this line of sight, i. e. at coordinates $(\eta_0, \mathbf{o}, \hat{n})$. The (2.11) further simplifies by assuming the *instantaneous decoupling approximation*: claiming that all the photons decoupled at η_{dec}, implying that the visibility function becomes a Dirac delta, $g \simeq \delta_D(\eta - \eta_{dec})$ and $e^{-\tau}$ a Heaviside function. In this limit (2.11) reds:

$$(\Theta + \Psi)\,|_{obs} = (\Theta_0 + \Psi)\,|_{dec} + (\hat{n} \cdot \mathbf{v}_b)\,|_{dec} + \int_{\eta_{dec}}^{\eta_0} d\eta(\Phi' + \Psi'),$$

where $|_{dec}$ means evaluated at last scattering surface, i. e. $(\eta_{dec}, -r_{dec}\hat{n}, \hat{n})$ (r_{dec} is the comoving radius at decoupling). Let us analyse its r.h.s. term by term starting from the first one: the temperature anisotropy measured by an observer today obviously accounts for the intrinsic temperature anisotropy $\Theta_0\,|_{dec}$ at the decoupling seen in that direction. However, the gravitational term Ψ acts as a "blue or red shifter" of photons travelling along gravitational potential fluctuations affecting the intrinsic anisotropy. This is usually known as *Sachs-Wolfe* (SW) effect.

The second term is related to the correction to the temperature coming from the usual Doppler effect, this correction in fact involves the projection of photon-baryon fluid velocity along the line of sight.

The last term accounts for the variations of gravitational potentials during time: the amount of blueshifts and redshifts experienced by photons going through a potential well do not compensate if in the meanwhile Ψ changes : the well gets deeper between the time at which photons enter and leave the well. This is the case when a changes of dominant species happens in the Universe. Similar effects related to $\Phi' \neq 0$ caused by dilation effects. Both are usually referred to as *Integrated Sachs-Wolfe* (ISW) effect.

Finally, we can neglect the gravitational term in the left hand side since it is a negligible *isotropic* correction to the observed anisotropies.

Similarly we can derive the behaviour for the variable $\Theta_\ell(\eta, k)$ in Fourier and harmonic space. The calculations can be found in Seljak and Zaldarriaga (1996); Zaldarriaga and Harari (1995), we quote the final result, in the instantaneous decoupling approximation, showing a tight similarity to the real space counterpart:

$$\begin{aligned}\Theta_\ell(\eta_0, k) \simeq\ & [\Theta_0(\eta_{dec}, k) + \Psi(\eta_{dec}, k)]\, j_\ell(k(\eta_0 - \eta_{dec})) \\ & + 3\Theta_1(\eta_{dec}, k)\frac{dj(x)_\ell}{dx}\,|_{k(\eta_0 - \eta_{dec})} \\ & + \int_{\eta_{dec}}^{\eta_0} d\eta(\Phi' + \Psi')j_\ell(k(\eta_0 - \eta)),\end{aligned} \tag{2.12}$$

where we exploited the dipole relation $v_b \simeq 3i\Theta_1$ and $j_\ell(x)$ is the spherical Bessel function. From (2.12) we see that, to solve for the anisotropies today, we must know the monopole, the dipole and the potential at the time of recombination plus the ISW correction if the potentials are time dependent. We stress here that the Bessel function determines how much anisotropy on

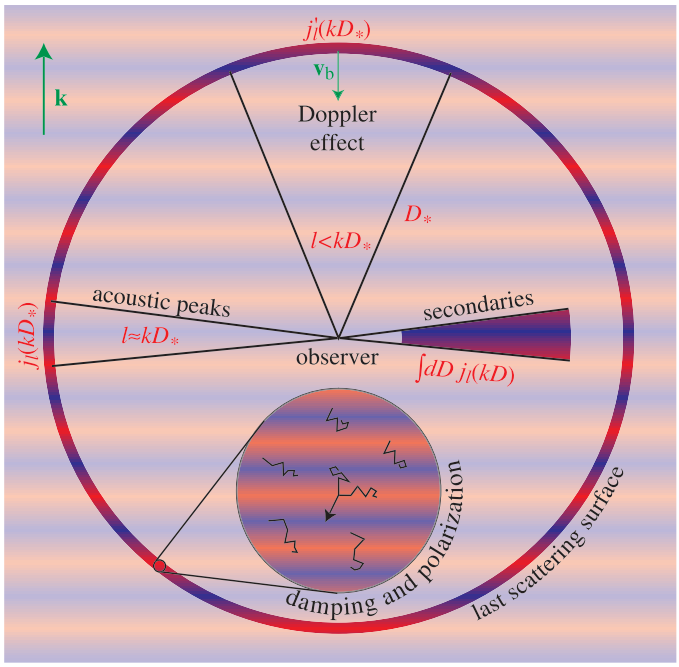

Figure 2.5: CMB anisotropies can be thought of as the line-of-sight projection of various sources of plane wave temperature and polarization fluctuations: the acoustic effective temperature and velocity or Doppler effect. Secondary contributions (such as SZ effect and reionization) differ in that the region over which they contribute is thick compared with the last scattering surface at recombination. The plot is from Hu and Dodelson (2002).

a given angular scale $\theta = \pi/\ell$ is contributed by a plane wave with wave number k. For large value of ℓ, i. e. small angular scales, j_ℓ is very peaked around $x = k(\eta_0 - \eta_{dec}) \simeq \ell$, meaning that $\Theta_\ell \approx 0$ elsewhere. An oscillating inhomogeneity with wavelength k at recombination appears as an angular anisotropy at the scale $\theta = \pi/\ell$ where the Bessel function peaks. More explicitly, if one consider the angular diameter distance, d_A of a physical wavelength $\lambda \sim \pi a/k$, we get an angular scale for a given wavelength as seen from the last scattering surface:

$$\theta = \frac{\lambda}{d_A(a_{dec})} = \frac{\pi a_{dec}}{k}\frac{1}{a_{dec}(\eta_0 - \eta_{dec})},$$

where we assume a flat Universe for the angular distance for sake of simplicity. In particular, we have seen that oscillating inhomogeneities follow a harmonic relation: $k_n = n\pi/s_*$ so that for $n = 1$ we have:

$$\ell_a = \frac{\pi(\eta_0 - \eta_{dec})}{s_*} \sim \frac{\pi\eta_0}{\eta_{dec}} \approx 200,$$

where we approximate $s_* \sim \eta_{dec} \ll \eta_0$ and in a flat matter dominated Universe $\eta(z) \propto (1+z)^{1/2}$. The higher multipoles $\ell_n = n\ell_a$ correspond to a coherent series of acoustic peaks whose first element gives a measure of the angular scale of the sound horizon at recombination $\sim 2°$.

2.1.4 *Spherical Harmonics decomposition*

Since the temperature anisotropies we observe today appears as a field defined in every point in the celestial sphere, they can be expanded in the *Spherical Harmonic domain*:

$$\Theta(\eta, \mathbf{o}, -\hat{n}) = \sum_{\ell=0}^{\infty} \sum_{m=-\ell}^{\ell} a_{\ell,m} Y_{\ell m}(\hat{n}).$$

By means of the Legendre expansion of Θ (2.5) and some basic relation between the Legendre polynomials and spherical harmonics it is possible to relate the $a_{\ell m}$ coefficient to the Θ_ℓ as:

$$a_{\ell m} = (-i)^\ell \int \frac{d^3\mathbf{k}}{2\pi^2} Y_{\ell m}(\hat{k}) \Theta_\ell(\eta_0, \mathbf{k}),$$

where $\hat{k} = \mathbf{k}/k$ denotes the unit vector. Since in sect.1.9 we assume Gaussian perturbations produced at the time of inflation as initial conditions for linear perturbation theory, it follows that both Θ_ℓ and $a_{\ell m}$ are Gaussian random variables, i. e. they are defined by their variance. We have seen the variance to be related to the correlation function and consecutively to the power spectrum of Θ_ℓ. This is further linked to the primordial curvature power spectrum $P_\mathcal{R}$:

$$\langle a_{\ell m} a_{\ell' m'} \rangle = \delta_{\ell\ell'} \delta_{mm'} C_\ell \tag{2.13}$$

with

$$C_\ell = \frac{1}{2\pi^2} \int \frac{dk}{k} |\Theta_\ell(\eta_0, k)|^2 P_\mathcal{R}(k). \tag{2.14}$$

Where $\delta_{\ell\ell'}$ is the Kronecker symbol, which nullifies $\langle a_{\ell m} a_{\ell' m'} \rangle$ for $\ell \neq \ell'$ and $m \neq m'$. The fact that the quantity C_ℓ is function of ℓ but not of m is a consequence of statistical isotropy, remember that we did something similar in Fourier space: power spectra are function of k not of $\mathbf{k}$. The C_ℓ is called the *angular* power spectrum of temperature anisotropies and it encodes the variance information concerning a given cosmological model generating a corresponding CMB map.

At this point it is worth thinking about the meaning of the averaging symbol $\langle \dots \rangle$ in (2.13). It is an ensemble average meant to be computed over many realization, i. e. in this context many realizations of the Universe, all obeying to the same cosmological model, encoded in the C_ℓs . However, what we really observe is only one realization: our Universe itself. Thus, CMB maps allow us to measure only one value for each $a_{\ell m}$ and their variance is not expected to be equal to C_ℓ ; even if we know the right cosmological model, they would scatter around the true value C_ℓ . This intrinsic and unavoidable scattering limits the possibility of finding the best theory matching the observations, though we can considerably reduce the

scattering by noticing that at a given ℓ there are $2\ell+1$ values over which is possible to average $|a_{\ell m}|^2$, since it does not depend on m. The best estimator of underlying C_ℓs is thus:

$$\hat{C}_\ell := \frac{1}{2\ell+1} \sum_{-\ell \leqslant m \leqslant \ell} |a_{\ell m}|^2.$$

By performing ensemble averages, one can easily show that this is an unbiased and minimum variance estimator:

$$\langle \hat{C}_\ell \rangle = C_\ell \qquad \langle (\hat{C}_\ell - C_\ell) \rangle = \frac{2}{2\ell+1} C_\ell^2,$$

where the variance is called as *sample* or *cosmic variance* and it can be seen as a theoretical error: it is not possible to reconstruct the underlying model with infinite precision or infinite precise observations. This is dramatically limiting the low ℓ part of the spectrum where the scattering is larger and the true underlying C_ℓs will always be poorly known. The power spectrum is usually displayed as the power per logarithmic interval in multipole, i. e.

$$D_\ell = \frac{\ell(\ell+1)}{2\pi} C_\ell \tag{2.15}$$

2.1.5 *The Angular Power Spectrum of Temperature Anisotropies*

We have now all the mathematical tools to understand how the terms contributing in Θ_ℓ in (2.12) manifest at the power spectrum level in eq.(2.14).

A. The SW term encodes the sum $\Theta_0 + \Psi$, where Ψ is a negligible term for all the modes that are in sub-Hubble regimes, since metric perturbations decay quickly as they cross the horizon, the sum therefore reduce to $\Theta_{0,\mathrm{obs}} \simeq \Theta_{0,\mathrm{dec}}$ for all these modes that should present peaks corresponding to the harmonics of the horizon scale at decoupling. On the contrary at the super-horizon scales modes are frozen and they are related to metric perturbations, thus since Bessel function is peaked around $k \simeq \ell/(\eta_0 - \eta_{\mathrm{dec}})$ we have that:

$$C_{\ell<100}^{SW} \sim [\Theta_0(\eta_{\mathrm{dec}}, k) + \Psi(\eta_{\mathrm{dec}}, k)]^2 \, P_{\mathcal{R}}(k),$$

corresponding to a flat and roughly constant contribution mostly at lower multipoles, i. e. scales larger than the horizon at decoupling (see the magenta solid line in fig.2.6). It is interesting to ask ourselves why we do not see the power spectrum to be zero in correspondence of the "zeroes" of the monopole acoustic oscillations. This is due to the fact that the zeroes are smoothed out by many modes which contribute to anisotropy on a given angular scale, changing the zeroes to troughs at the C_ℓs level.

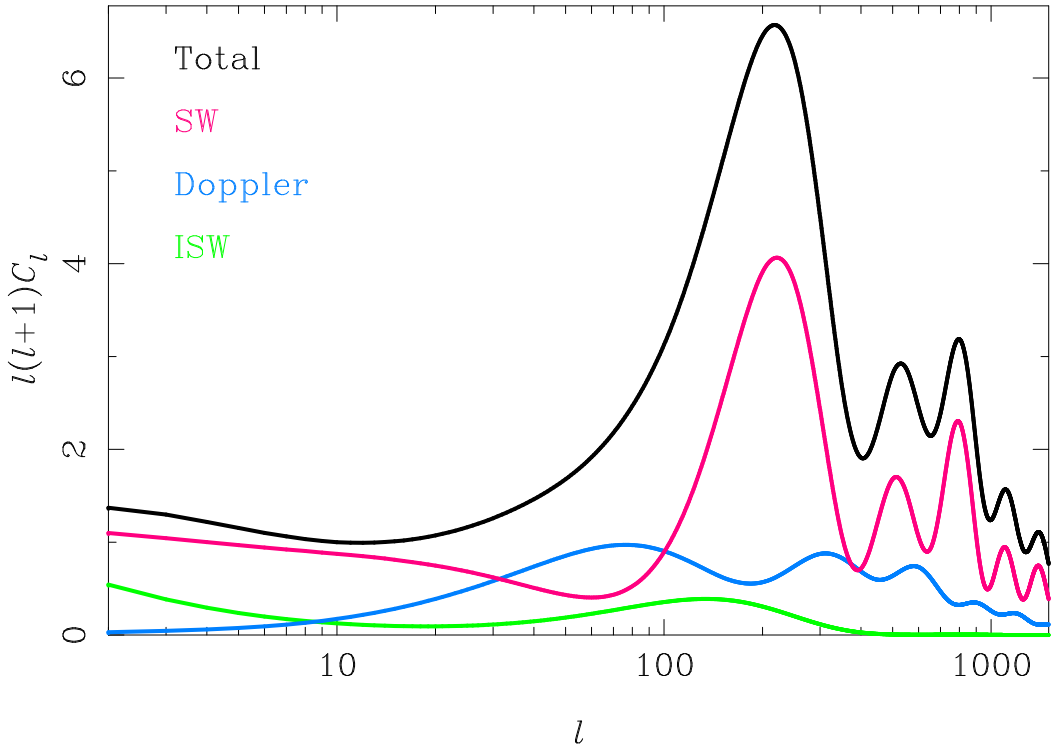

Figure 2.6: Contribution of the various terms in eq. (2.12) to the temperature-anisotropy power spectrum from adiabatic initial conditions coming from evolution of the potential along the line of sight (Challinor & Peiris, 2009). The units of the spectrum are arbitrary.

b. The Doppler contribution is related to the dipole term, which can be qualitatively approximated by the time derivative of the monopole $\Theta_0'(\eta_{dec}, k)$. This contribution is smaller than the monopole, out of phase with it on smaller scales and null for scales above the horizon as there are no oscillation and significant dynamics at those scales. The overall effect, as depicted in fig.2.6 by the cyan line, is to raise the SW term and fill further the troughs.

c. Most of the contribution to ISW comes from the time of matter-radiation equality, where the potentials changed due to the change of species driving the dynamics. The transition, in fact, is not abrupt and even for $a_{eq} \sim 10^{-4}$, an early ISW (EISW) can lasts up to the recombination since it takes some time for sub-sound-horizon metric fluctuations to freeze around a constant value and affects mainly the scales around the sound-horizon peak $\ell \approx 200$. However, during the Λ dominated regime, the equation of state changes again, so metric fluctuations vary on all scales as in the time of equality (as known as Late ISW (LISW)) appearing as a tilt to the low multipoles of power spectrum, being the latter an obvious example of secondary CMB anisotropies.

In fig.2.6 one can appreciate the series of acoustic peaks predicted at the end of sect.2.1.3. Moreover, due to the shift of zero-point oscillations given bythe baryon loading $-(1+R)\Psi$ for Θ_0, there is an asymmetry between the first few odd peaks and the even ones so that Odd peaks are enhanced by the baryon loading.

Finally, the overall amplitude of the peaks is suppressed at larger multipoles by the diffusion damping. The envelope decays exponentially as $e^{-(\ell/\ell_d)^2}$ where ℓ_d is the multipole related to the diffusion scale.

2.2 POLARIZATION ANISOTROPIES

What we have seen in the previous section is the behaviour and the evolution of scalar perturbations: the density inhomogeneities in the large scale structure of the Universe or the temperature anisotropies in the CMB that relate to the scalar perturbations generated by the inflaton field. Scalar perturbations leaves a signature even in the linear polarization of the CMB due to the presence of the dissipation terms in the acoustic oscillations at recombination (fig.2.4).

The process responsible to produce polarization is the Thomson scattering between photons and electrons. whose cross section depends on polarization as (Chandrasekhar, 1960):

$$\frac{d\sigma_T}{d\Omega} \propto |\hat{\epsilon} \cdot \hat{\epsilon}'|^2,$$

where $\hat{\epsilon}(\hat{\epsilon}')$ are the incident (scattered) polarization directions. As a qualitative description, the incident light "shakes" an electron in the direction of its electric field vector $\mathbf{E}$, or polarization $\hat{\epsilon}'$, causing it to radiate with an

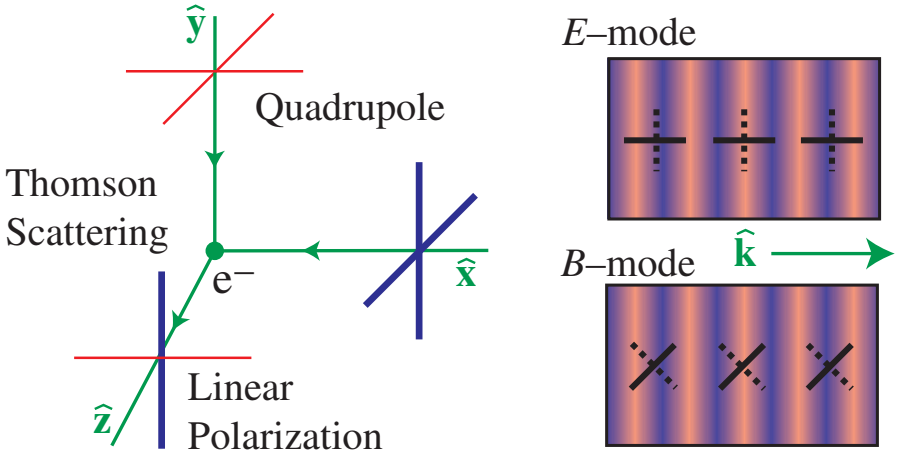

Figure 2.7: Plots from Hu and Dodelson (2002). Thomson scattering of radiation with a quadrupole anisotropy generates linear polarization. Blue colors (thick lines) represent hot and red colors (thin lines) cold radiation. The component of the polarization that is parallel or perpendicular to the wavevector **k** is called the E-mode and the one at 45° angles is called the B-mode.

outgoing polarization parallel to that direction. However, since the outgoing polarization $\hat{e}$ must be orthogonal to the outgoing direction, incoming radiation (polarized parallel to the outgoing direction) cannot scatter and it leaves only one polarization state.

One can wonder if an isotropic radiation field, such as the monopole, is able to produce polarization[6]. If we have radiation coming from two directions (as in fig.2.7) $x-$ and $y-$, having equal intensity in both directions leads to unpolarized radiation. The same holds if the radiation field is a dipole. So that, to produce polarization, it is necessary that an anisotropic radiation field possesses at least a quadrupolar anisotropy.

In fact, as sketched in fig.2.7 the hotter (colder) radiation incident from the $x-$ ($y-$) direction produces higher (lower) intensity along the $y-$ ($x-$) axis of the outgoing wave. Therefore, the intensity of the outgoing wave is larger along $y-$axis than along the $x-$axis yielding the outgoing radiation to be polarized.

The monopole and dipole Θ_0 and Θ_1 are of the same order of magnitude at recombination, but their oscillations are $\pi/2$ out of phase. However, the quadrupole coming from photon dissipation is of order $\pi_\gamma k\Theta_1/\dot{\tau}$ (see fig.2.4) and since Θ_1 is out of phase with the monopole, the polarization peaks should also be out of phase with the temperature peaks.

However, one may wonder whether tensor perturbations may take a role in shaping the CMB polarization, in particular: are they able to generate quadrupolar perturbations ?

6 Notice that electron scattering of a completely unpolarized incident wave produces a scattered wave with some degree of polarization, depending on the angle with respect the incident direction(Rybicki & Lightman, 1979).

Let us start from the Boltzmann equation for tensorial modes in the CMB temperature anisotropies:

$$\Theta^{(T)\prime} + ik\mu\Theta^{(T)} = -h' - \tau'\left(\Theta^{(T)} - \frac{1}{10}\Theta_0^{(T)}\right) \tag{2.16}$$

and polarization anisotropies:

$$\Theta_P^{(T)\prime} + ik\mu\Theta_P^{(T)} = -\tau'\left(\Theta_P^{(T)} - \frac{1}{10}\Theta_{P0}^{(T)}\right) \tag{2.17}$$

The only external source is the metric tensor perturbation and evolves accordingly to the Einstein equations as:

$$h'' + 2\frac{a'}{a}h' + k^2 h = 0.$$

In order to obtain the polarization anisotropy for a mode $\mathbf{k}$, we can define the initial conditions and then evolve Θ_P as we have done in the previous section for Θ; the power spectra coming from tensorial perturbations can be defined very similarly to (2.14) as:

$$C_\ell^{(T)} = \frac{1}{2\pi^2}\int \frac{dk}{k}|\Theta_\ell^{(T)}(\eta_0, k)|^2 P_h(k), \tag{2.18}$$

and

$$C_{P\ell}^{(T)} = \frac{1}{2\pi^2}\int \frac{dk}{k}|\Theta_{P\ell}^{(T)}(\eta_0, k)|^2 P_h(k). \tag{2.19}$$

Tensor perturbations can be thought as a stochastic background of gravitational waves propagating through the spacetime since the inflation. Moreover, since they are sources of quadrupolar distortions in the spacetime, they provide a further source of polarization to the CMB. Thus,being able to observe the CMB polarization coming from tensorial perturbations is a very powerful and feasible way to probe the inflationary Universe.

2.2.1 *The Stokes Parameters*

In order to proceed further we need to introduce the *Stokes parameters* formalism that describes locally the polarization field. A monochromatic wave propagating along the $z-$ direction is expressed by its physical components, along $x-$ and $y-$ axis:

$$E_x = E_{0x}\cos(\omega t - \phi_x), \qquad E_y = E_{0y}\cos(\omega t - \phi_y),$$

where $E_{0x,0y}$ and $\phi_{x,y}$ are respectively amplitudes and phase angle in the direction perpendicular to the propagation one. These equations describe the motion of the electric field's tip in the $x-y$ plane. These are the most general expression for an *elliptically polarized* wave. When the motion of the tip follows a (counter)clockwise rotation for an observer that is facing

toward the incoming wave, the wave is said to have *(positive) negative helicity*. If $E_{0x} = E_{0y}$ and $\phi_x - \phi_y = \pi/2$ we have a *circularly polarized wave*. Whereas if $\phi_x = \phi_y$ the wave is *linearly polarized*.

The four parameter $E_{0x,0y}$ and $\phi_{x,y}$ can be expressed in a set of more useful parameters, known as *Stokes Parameters*, which are defined by equations:

$$\begin{aligned} I &= E_{0x}^2 + E_{0y}^2, \\ Q &= E_{0x}^2 - E_{0y}^2, \\ U &= 2E_{0x}E_{0y}\cos(\phi_x - \phi_y), \\ V &= 2E_{0x}E_{0y}\sin(\phi_x - \phi_y). \end{aligned} \tag{2.20}$$

The parameter I measures the relative intensity of the wave. The parameter Q gives the preponderance of x—linear polarization over y—linear polarization, while U quantifies the same along axes rotated by $45°$. Finally, V is the parameter that encodes circular polarization commonly ignored in cosmology, since Thomson scattering is not expected to produce circular polarization; the presence of primordial magnetic field at recombination could generate a small component of circular polarization.

2.2.2 *The E and B modes*

Being temperature a scalar quantity, it is invariant under rotation in the plane perpendicular to direction $\hat{n}$. We would like to treat CMB linear polarization by means of some invariant quantities independent on the observer position.

Unfortunately, the Q, U Stokes parameter are not invariant because they are connected to the polarization vector field as they are defined in eqs.(2.20). If one considers a planar rotation R of an angle ψ around the direction of observation $\hat{n}$, the unitary vectors of the axes coordinates $\hat{x}$ and $\hat{y}$ and coefficients $E_{0x,y}$ are transformed as:

$$\begin{aligned} \hat{x}' &= \cos\psi\ \hat{x} + \sin\psi\ \hat{y} \\ \hat{y}' &= -\sin\psi\ \hat{x} + \cos\psi\ \hat{y}, \end{aligned}$$

and similarly the components:

$$\begin{aligned} E'_{0x} &= \cos\psi\ E_{0x} + \sin\psi\ E_{0y} \\ E'_{0y} &= -\sin\psi\ E_{0x} + \cos\psi\ E_{0y}. \end{aligned}$$

For the Stokes parameters this implies that:

$$I' = I, \tag{2.21}$$

$$\begin{aligned} Q' &= Q\cos 2\psi + U\sin 2\psi, \\ U' &= -Q\sin 2\psi + U\cos 2\psi. \end{aligned} \tag{2.22}$$

Thus, Q and U are two quantities that, under a coordinate rotation $x_i = \mathcal{R}_i^k x'_k$, transforms as $P_{ij} = R_i^k P'_{kh} \mathcal{R}_j^h$, where:

$$P_{ij} = \begin{pmatrix} Q & U \\ U & -Q \end{pmatrix}. \tag{2.23}$$

More explicitly, $\mathcal{P}_{ij}$ is a symmetric trace-less 2×2 tensor or equivalently a spin-2 field χ with components (Q, U). We can construct two quantities from the Stokes Q and U parameters:

$$(Q \pm iU)'(\hat{n}) = e^{\mp 2i\psi}(Q \pm iU)(\hat{n}),$$

and we may expand both the quantities in the appropriate spin-weighted basis[7]

$$\begin{aligned}(Q + iU)(\hat{n}) &= \sum_{\ell m} a_{2,\ell m}\, {}_2Y_{\ell m}(\hat{n}) \\ (Q - iU)(\hat{n}) &= \sum_{\ell m} a_{-2,\ell m}\, {}_{-2}Y_{\ell m}(\hat{n}).\end{aligned} \tag{2.24}$$

Q and U are defined at each direction $\hat{n}$ with respect to the spherical coordinate system $(\hat{e}_\theta, \hat{e}_\phi)$. By using the first equation in (A.5), one can show that the expansion coefficients for the polarization variables satisfy $a^*_{-2,\ell m} = a_{2,\ell -m}$. We note that it is more convenient to deal with spin-0 quantities as they are rotationally invariant. Moreover, it is meaningless to deal with power spectra computed from observer dependent quantities as the Stokes parameters.

An important property of spin-s functions ${}_sf(\theta, \phi)$, is the called *spin raising (lowering) operator* $\eth$ ($\bar{\eth}$), i. e. with the property of raising (lowering) the spin-weight of a function,

$$\begin{aligned}(\eth\, {}_sf)' &= e^{-i(s+1)\psi}\, \eth\, {}_sf \\ (\bar{\eth}\, {}_sf)' &= e^{-i(s-1)\psi}\, \bar{\eth}\, {}_sf.\end{aligned}$$

Their explicit expressions are given in appendix A. Thus, one can get spin-0 quantities by using these operators $\eth$ and $\bar{\eth}$. Indeed, by acting twice with $\eth$, $\bar{\eth}$ on $Q \pm iU$ in equation (2.24) we have that:

$$\begin{aligned}\bar{\eth}^{\,2}(Q + iU)(\hat{n}) &= \sum_{\ell m} \left[\frac{(\ell+2)!}{(\ell-2)!}\right]^{1/2} a_{2,\ell m} Y_{\ell m}(\hat{n}) \\ \eth^{\,2}(Q - iU)(\hat{n}) &= \sum_{\ell m} \left[\frac{(\ell+2)!}{(\ell-2)!}\right]^{1/2} a_{-2,\ell m} Y_{\ell m}(\hat{n}).\end{aligned}$$

7 See appendix A for the definition of the spin-weighted basis.

The expressions for the expansion coefficients are

$$\begin{aligned} a_{2,\ell m} &= \int d\Omega \; {}_2Y^*_{\ell m}(\hat{n})(Q+iU)(\hat{n}) \\ &= \left[\frac{(\ell+2)!}{(\ell-2)!}\right]^{-1/2} \int d\Omega \; Y^*_{\ell m}(\hat{n}) \, \bar{\eth}^{\,2}(Q+iU)(\hat{n}) \\ a_{-2,\ell m} &= \int d\Omega \; {}_{-2}Y^*_{\ell m}(\hat{n})(Q-iU)(\hat{n}) \\ &= \left[\frac{(\ell+2)!}{(\ell-2)!}\right]^{-1/2} \int d\Omega \; Y^*_{\ell m}(\hat{n}) \, \eth^{\,2}(Q-iU)(\hat{n}). \end{aligned} \tag{2.25}$$

Therefore, instead of $a_{\pm 2,\ell m}$ it is more convenient to introduce a linear combination of both,

$$\begin{aligned} a_{E,\ell m} &= -(a_{2,\ell m} + a_{-2,\ell m})/2 \\ a_{B,\ell m} &= i(a_{2,\ell m} - a_{-2,\ell m})/2, \end{aligned} \tag{2.26}$$

from which, we can define two quantities in real space,

$$\begin{aligned} E(\hat{n}) &= \sum_{\ell,m} a_{E,\ell m} \, Y_{\ell m}(\hat{n}) \\ B(\hat{n}) &= \sum_{\ell,m} a_{B,\ell m} \, Y_{\ell m}(\hat{n}). \end{aligned} \tag{2.27}$$

They can be visualized as maps and as a result $E(\hat{n})$ and $B(\hat{n})$ are invariant under rotations.

It is interesting to analyse the behaviour of E and B under a parity transformation: i. e. a transformation that reverses the sign of the $\vec{x}$ coordinates but leave the others unchanged. In spherical coordinates, this results in changing only the sign of azimut angle ϕ. Under this transformation $\hat{e}'_\phi = -\hat{e}_\phi$ and $\hat{e}'_\theta = \hat{e}_\theta$, hence the Stokes parameters transform as $Q'(\hat{n}') = Q(\hat{n})$ and $U'(\hat{n}') = -U(\hat{n})$. With the aid of equation (A.2) we can show that

$$\begin{aligned} \bar{\eth}^{\,2}(Q+iU)'(\hat{n}') &= \eth^{\,2}(Q-iU)(\hat{n}) \\ \eth^{\,2}(Q-iU)'(\hat{n}') &= \bar{\eth}^{\,2}(Q+iU)(\hat{n}), \end{aligned}$$

so that by means of eqs. (2.25), (2.26) and (2.27),

$$\begin{aligned} E'(\hat{n}') &= E(\hat{n}) \\ B'(\hat{n}') &= -B(\hat{n}). \end{aligned}$$

The two new variables behave differently: E is invariant under parity transformations, whilst B is not. This explain why the choice of the two letter since they remind the analogy with electric and magnetic fields (see fig.2.7).

In conclusion, to characterize the statistics of CMB polarization perturbations only three power spectra are needed: E, B and the cross correlation

between T and E. The cross correlation between B and E or B and T vanishes because B has the opposite parity to T or E. Under the assumption of Gaussianity, the power spectra are defined by the rotationally invariant quantities that hereafter we call respectively E and B modes, in the same fashion as (2.13):

$$\begin{aligned}
\langle a^*_{E,\ell'm'} a_{E,\ell m}\rangle &= C_\ell^{EE}\delta_{\ell'\ell}\delta_{m'm}\\
\langle a^*_{B,\ell'm'} a_{B,\ell m}\rangle &= C_\ell^{BB}\delta_{\ell'\ell}\delta_{m'm}\\
\langle a^*_{T,\ell'm'} a_{E,\ell m}\rangle &= C_\ell^{TE}\delta_{\ell'\ell}\delta_{m'm}\\
\langle a^*_{B,\ell'm'} a_{E,\ell m}\rangle &= \langle a^*_{B,\ell'm'} a_{T,\ell m}\rangle = 0,
\end{aligned}$$

from which descend the observed quantities as

$$\begin{aligned}
C_\ell^{EE} &= \frac{1}{2\ell+1}\sum_m |a^*_{E,\ell m} a_{E,\ell m}|\\
C_\ell^{BB} &= \frac{1}{2\ell+1}\sum_m |a^*_{B,\ell m} a_{B,\ell m}|\\
C_\ell^{TE} &= \frac{1}{2\ell+1}\sum_m |a^*_{T,\ell m} a_{E,\ell m}|.
\end{aligned}$$

Hereafter we refer the power spectrum coming from the CMB temperature anisotropies (defined in (2.14)) as C_ℓ^{TT}.

Spectra for both scalar and tensor perturbations are shown in fig.2.8 left and right panels. One of the striking features of the tensor power spectra is that they all peak at $\ell \sim 100$ which is roughly the scale of the horizon at decoupling and on smaller scales they decay rapidly. This is expected since tensor perturbations are damped once they enter the horizon. Unfortunately, they are always sub-dominant in the TT, TE, EE power spectrum: there is no way to measure them separately from the scalar ones. However, there is a unique *observational window* at $\ell < 200$ in the BB power spectra. Indeed B-modes are not expected to be generated by scalar perturbations at low multipoles[8] and we should be able to observe the recombination peak at $\ell = 100$ whose amplitude depends on the tensor-to-scalar ratio r. Actually, r is a *free* parameter of the theory and at the time of writing, only upper limits have been set on it. We will dedicate the next chapter for a wider discussion about this topic.

An other interesting feature is the different oscillation phases between T and E: they are out of phase. This is due to the phase shift between the monopole and the quadrupole, which are the main contributors respectively for the T and E power spectra. Furthermore, the expected small amplitude of the quadrupole is reflected in the amplitude of CMB polarization smaller than the CMB temperature, at the percentage level, i. e. 4 orders of magnitude in terms of power spectrum.

8 We discuss in the sect.2.4 the lensing of E modes which leaks into B mode at large multipoles.

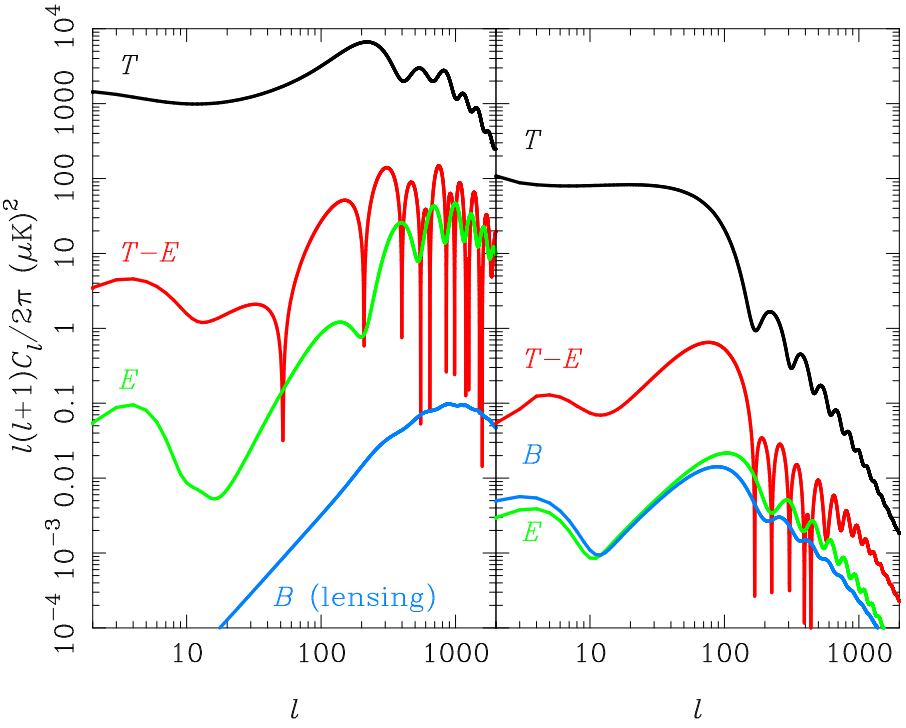

Figure 2.8: Figure from Hu and Dodelson (2002). (Left) CMB power spectra generated by scalar perturbations; (right) spectra generated by tensor perturbation, notice in this figure that tensor perturbations decay rapidly once they enter the horizon. A tensor-to-scalar ratio $r = 0.2$ is considered.

Finally, one could notice in fig.2.7 that at large angular scales $\ell < 10$ there is a 'bump', called *reionization bump*. This contribution to C_ℓ^{EE} and C_ℓ^{BB} is due to the photon emitted at last scattering that scattered when the intergalactic medium reionized at $z_{reion} \lesssim 5$. Re-scattering erases scalar fluctuations below the horizon scales at the time of recombination and weakly regenerates them at larger scales. The effect is so large that, despite cosmic variance, τ_{reio} can be well measured using polarization data as we will see in the next chapter.

2.3 THE RELATION WITH COSMOLOGICAL PARAMETERS

The CMB power spectra provide a very powerful tool to infer the value of several cosmological parameters. Since the CMB observables are mostly a projection of conditions on the last-scattering surface, parameters can have an influence either through the acoustic physics of the pre-recombination plasma or through the angular diameter distance to last scattering, d_A as it controls the projection of linear distances at recombination to observed angular scales on the sky.

As we summarized in table 1.1, we can consider the minimal amount of six free parameters of the ΛCDM model. The other cosmological parameters as Ω_Λ can be inferred from a combination of them.

We now consider their main effect onto CMB power spectra.

A. We have seen that the position of the first peak at $\ell \approx 200$ corresponds to the most typical scale (the sound horizon) acting as a standard ruler placed at the angular distance from recombination. The former is related to the evolution prior to recombination: Ω_c, Ω_b (which governs the sound speed as a function of a). The latter depends on the expansion and the geometry of the Universe after decoupling, H_0 and Ω_c.

B. The relative amplitude of odd and even peaks is related to the baryon loading term $-R\Psi$ in the SW effect: this is strictly related to Ω_b (see fig.2.9 (top)). Since the sound speed as well as the sound horizon get reduced, this effect shifts the acoustic peaks in temperature and polarization spectra to smaller scales (larger ℓ).

C. The value of Ω_c shifts the time of equality and affects both the EISW and the amplitude of all peaks (changing the duration of time from equality to decoupling, controls how many acoustic oscillations are damped by the presence of baryons). Moreover, it changes into the equality time, may affect the overall peak scales (see the bottom panel of fig.2.9). Thus, larger values of Ω_c shift the acoustic peaks rightward to smaller scales since the perturbation related to the peaks enter the horizon earlier and this is why we observe this effect even in TE end EE power spectra.

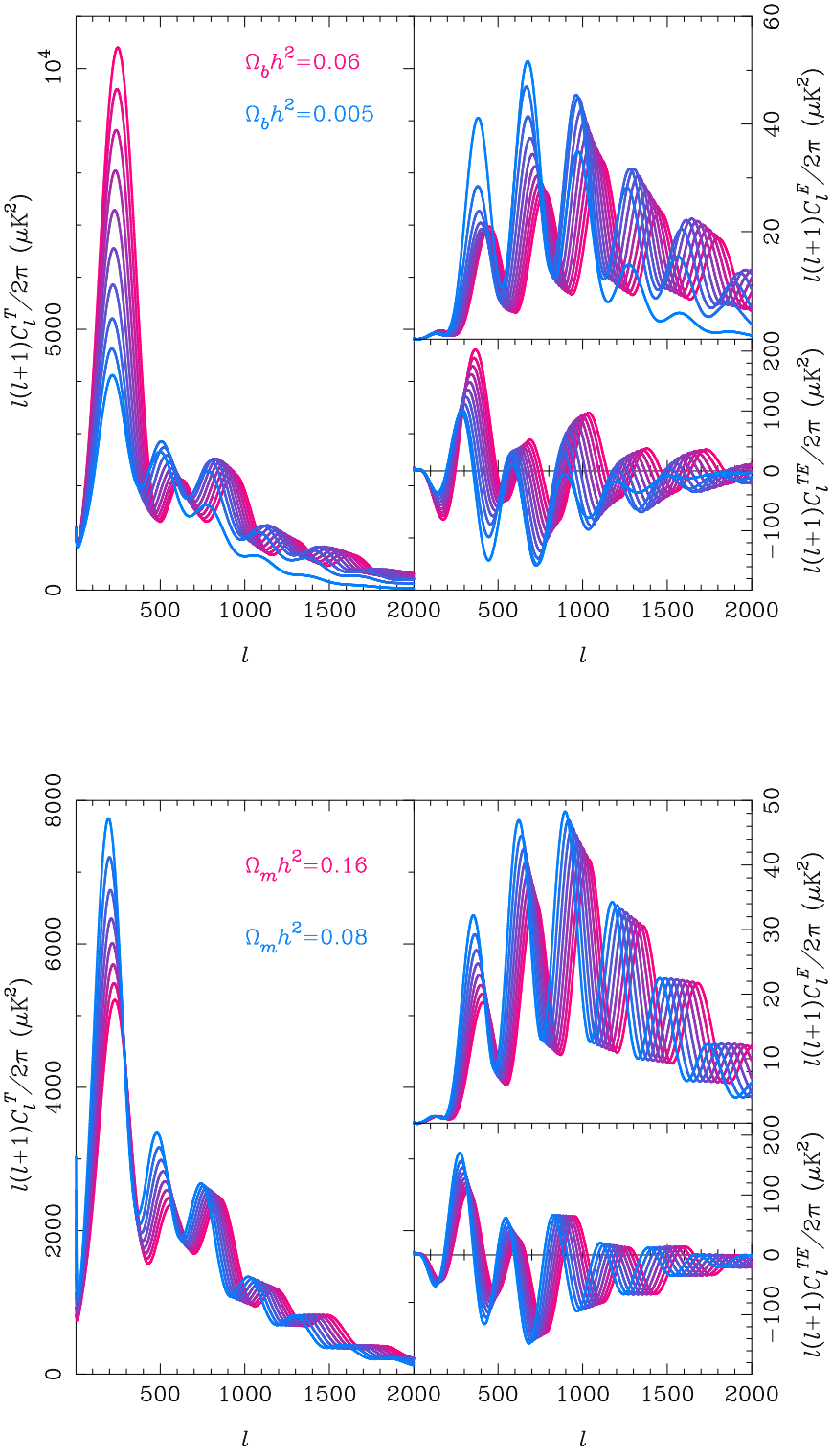

Figure 2.9: Variation of C_l^T (left), C_l^E (top right) and C_l^{TE} (bottom right) as $\Omega_b h^2$ is varied with fixed $\Omega_c h^2$ (top) and as $\Omega_m h^2$ is varied at fixed $\Omega_b h^2$ (bottom). For the latter the angular diameter distance to last scattering has been held fixed (figures from Challinor and Peiris (2009)). All models assume flat curvature.

D. The diffusion damping near recombination controls the envelope of the peaks, it depends on the ratio of damping scale at decoupling by the angular distance to decoupling. The former is related to the Thomson scattering rate Γ before decoupling depending on Ω_c (for the value of η at equality) and on Ω_b (for the ionization fraction as a function of a). The angular distance as the item A depends on H_0 and Ω_c. An increase in the number density of electrons in the plasma (by means of Ω_b) reduces the amount of diffusion damping so that smaller amount of diffusion damping are related to larger Ω_b (see the C_ℓ^{TT} in fig.2.9 (top)). On larger scales instead, where tight-coupling still holds approximately, this reduction decreases the quadrupole anisotropy around recombination (the reduction in the plasma bulk velocity also contributes the same way) and the polarization is reduced as in fig.2.9 (top). Larger Ω_b values imply larger reductions in the amplitude of polarization power spectra.

E. The overall amplitude obviously depends on that of the primordial spectrum A_s as well as the overall slope does on the tilt n_s.

F. The LISW tilts the SW plateau at smaller ℓs. The effects is more enhanced as Ω_Λ gets larger values (see fig.2.10).

The dependence of C_l^T on the curvature fraction, Ω_K and dark energy density in ΛCDM models is illustrated in fig. 2.10. Both parameters principally affect the anisotropies through d_A, by simply shifting the peaks either leftward or rightward. At large scales the LISW effect plays a key role. To disentangle both these effects which are degenerate in CMB power spectra (as known as *geometric degeneracy*) one may exploit some other external datasets. This can be easily understood since the angular scale of a ruler in closed or open curvature geometry is respectively larger or smaller than the one in a Euclidean geometry. This reflects into a rigid leftward (rightward) displacement of the peaks as the Universe curvature is negative (positive). The combination of more than one ruler, in addition to the CMB scales, may break degeneracy and help in discriminating these models.

Finally, neutrino oscillations imply that at least two flavours are massive. The minimum mass of the heaviest eigenstate is $\approx 0.05\,\mathrm{eV}$. At this level, neutrinos are relativistic at recombination and their effect on the dynamics of the primordial plasma are indistinguishable from massless neutrinos. However, if neutrino mass exceeds $\approx 0.6\,\mathrm{eV}$, a neutrino becomes non-relativistic at recombination. At this mass, the eigenstates must be very nearly degenerate and the total (summed) neutrino mass is therefore $\sum_\nu m_\nu \approx 1.8\,\mathrm{eV}$. This sets a rough limit on the determination of masses from the primary CMB anisotropies and is close to the limit $\sum_\nu m_\nu < 1.3\,\mathrm{eV}$ from the five-year WMAP data (Komatsu et al., 2009). Even with minimal masses, two of the neutrino eigenstates are non-relativistic today therefore affecting the measurements of d_A and suppress the late-time growth of structure on scales small enough that the neutrinos cannot cluster.

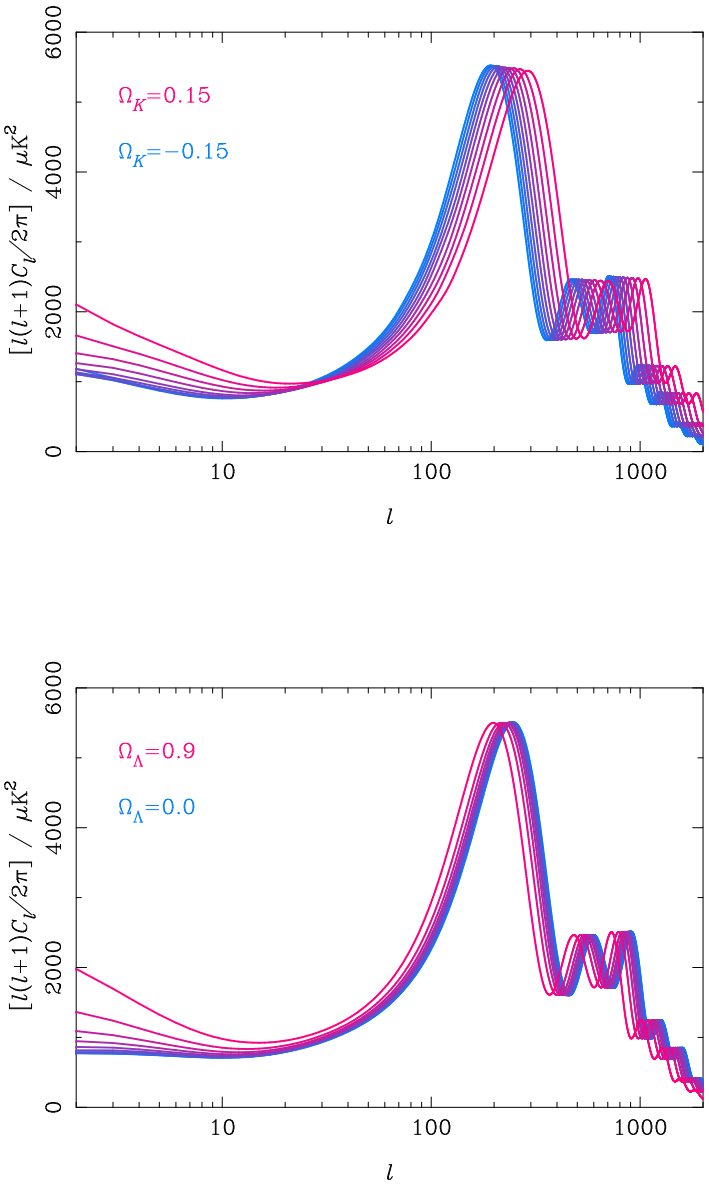

Figure 2.10: Variation of C_l^T with spatial curvature (top) and dark energy density (bottom). In both cases, $\Omega_b h^2$ and $\Omega_c h^2$ are fixed and the dark energy model is a cosmological constant (figures from Challinor and Peiris (2009)).

2.4 GRAVITATIONAL LENSING IN CMB

In the previous Sections, we have focused on the so called primary anisotropies. We consider now the secondary ones, i.e. produced during the path of CMB photons towards us. The most important effect for our purposes is represented by the gravitational lensing, which we describe here.

In 1911, Einstein published a research paper where he claimed an experimental test to the postulates of General relativity:

> Rays of light, passing close to the sun, are deflected by its gravitational field ϕ, so that the angular distance between the sun and a fixed star appearing near to it is apparently increased by nearly a second of arc. [...] the deflection which a light-ray experiences toward the side $\mathbf{n}'$ on any path s is:
>
> $$\alpha = -\frac{1}{c^2}\int \frac{\partial \phi}{\partial n'} ds.$$
>
> As the fixed stars in the parts of the sky near the Sun are visible during total eclipses of the Sun, this consequence of the theory may be compared with experience. [...] It would be a most desirable thing if astronomers would take up the question here raised.

In fact, two independent groups of astronomers led by Crommelin and Eddington , during a Solar Eclipse on May 29, 1919, measured the position of Hyades stars in an open star-cluster lying just behind the Sun with deflection compatible with the one predicted by Einstein. This was one of the striking experimental proof of General Relativity: the presence of mass is able to bend the light rays.

Gravitational lensing has a non negligible effect when we consider the CMB power spectra, especially at small angular scales. Furthermore, in fig.2.8, we omit to describe the solid cyan power spectrum in the left panel. We dedicate the following section to discuss the B-modes generated from the scalar E-modes which are gravitationally lensed and deflected into B-modes by the intervening distribution of matter in the Universe. A very complete review about this topic the one made by Hanson, Challinor, and Lewis (2010).

In order to infer the effect of lensing in the CMB we can restrict our analysis to flat sky (i. e. so small patches that we can approximate them as flat): the effect can be described as a remapping of the *unlensed* CMB, i. e.

$$\tilde{T}(\hat{n}) = T(\hat{n} + \alpha(\hat{n})), \tag{2.28}$$

$$(\tilde{Q} \pm i\tilde{U})(\hat{n}) = (Q \pm iU)(\hat{n} + \alpha(\hat{n})), \tag{2.29}$$

where α is the deflection field as defined by Einstein (1911). It consists of the sum of all the deflections made by matter-lenses along the path from the last scattering surface to us. In a flat Universe, and under the *Born approximation* (that is computing the integral along the unperturbed path) we have:

$$\alpha(\hat{n}) = -2\int_0^{\chi_*} d\chi \frac{f_K(\chi_* - \chi)}{f_K(\chi_*)} \nabla_\perp \Psi(\chi\hat{n}; \eta_0 - \chi),$$

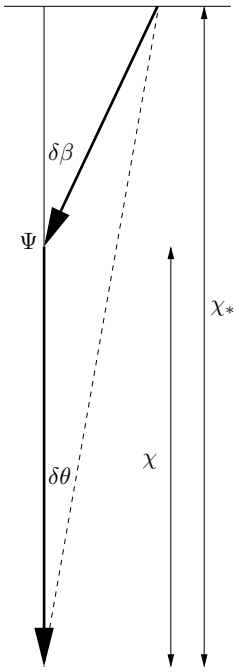

Figure 2.11: Weak lensing geometry for a source at comoving distance χ_* lensed by a potential Ψ at distance χ (Lewis & Challinor, 2006). The lensing deflection by an angle $\delta\beta$ changes the observed angle of the source by an angle $\delta\theta$.

where Ψ is the so called Weyl potential, defined as a combination of the potentials in the Newton gauge $\Psi = (\Psi_N + \Phi_N)/2$ [9], χ_* is the comoving distance to last scattering and the gradient $\nabla_\perp$is computed in a plane orthogonal to the line of sight and can be extended to the covariant derivative on the sphere as $\nabla_\perp = [1/f_K(\chi)]\,\nabla_{\hat{n}}$.

In fig.2.11 gravitational lensing in presence of a Weyl potential is sketched. General Relativity specifically only enters through the relation between the Weyl potential and the stress-energy tensor as usual via the Einstein equation (1.6) and can be seen as a Poisson equation

$$\left(\Delta + \frac{3K}{a^2}\right)\Psi = 4\pi G(\delta\rho + \Pi) \approx 4\pi G\delta\rho, \tag{2.30}$$

where the last approximation holds since the anisotropic stress tensor is small where the gravitational lensing mostly contributes in matter and dark energy domination eras. The result in (2.30) is remarkable since connects directly the Weyl potential to the matter perturbation.

We assume the large scale structure of the Universe made by several potential wells, each giving a contribution to the observed deflection angle:

$$\alpha^{pw}(\hat{n}) = 4\left(\frac{\chi_* - \chi}{\chi_*}\right)\Psi^{pw}(\chi\hat{n}),$$

being $\Psi^{pw}(\chi\hat{n})$ the potential at closest approach. Nearby lenses have the largest contribution since the geometric factor is larger at small redshift.

9 Assuming that anisotropic stresses vanish.

As usual, we consider the potentials at scales as large as the horizon to be nearly scale-invariant, whereas they become small on smaller scales. We therefore need to consider two kinds of lensing perturbations: from the largest observable scales $\chi_* \sim 14$Gpc where there is only one very large lens, down to smaller scales $\sim 300\,$Mpc from which descend most of the lenses along the line of sight, $14000/300 \sim 50$ contributing to the lensing deflection. The size of each deflection is set by the Newtonian potentials, which have variance $(2.7 \times 10^{-5})^2$ per unit log range in scale, so typical deflections have $|\alpha| \sim 1 \times 10^{-4}$rad. Considering each lens independently, the total r.m.s. deflection should therefore be $\sim 50^{1/2}\, 10^{-4} \sim 2$ arcmin.

Approximating the light path as the unperturbed line of sight and expressing α as an angular gradient related to the projected gradient as $\nabla_\perp = 1/\chi\nabla$, we can define a lensing potential $\psi(\hat{n})$ so that

$$\alpha(\hat{n}) = \nabla\psi(\hat{n}),$$

where the derivative has to be taken with respect to the position on the sky. This definition allows us to bring out the gradient from the integral and define the lensing potential as the line of sight integral:

$$\psi(\hat{n}) = -2\int_0^{\chi_*} d\chi \frac{f_K(\chi_* - \chi)}{f_K(\chi_*) f_K(\chi)} \Psi(\chi\hat{n}; \eta_0 - \chi).$$

For CMB analysis we can approximate recombination as instantaneous so that we have a single source plane at $\chi = \chi_*$, and consider all the effects coming from late time sources to be projected into a single 2D map of the lensing potential on the sphere containing all the required informations. Moreover, we can assume a flat Universe, so that $f_K(\chi) = \chi$.

For a Gaussian lensing potential the power spectrum encodes all the statistical informations to fully describe the lensing in the CMB. We can define the angular correlation function of the lensing potential as

$$\begin{aligned}\langle \psi(\hat{n})\psi(\hat{n}')\rangle =& 16\pi \sum_{\ell\ell' mm'} \int_0^{\chi_*} d\chi \int_0^{\chi_*} d\chi' \frac{(\chi_* - \chi)}{\chi_*\chi} \frac{(\chi_* - \chi')}{\chi_*\chi'} \times \\ & \times \int \frac{dk}{k} j_\ell(k\chi) j_{\ell'}(k\chi') P_\Psi(k; \eta, \eta') Y_{\ell m}(\hat{n}) Y^*_{\ell' m'}(\hat{n}') \delta_{\ell\ell'} \delta_{mm'}.\end{aligned}$$

Moreover, ψ can be expanded in spherical harmonics as in (2.13) so that:

$$\begin{aligned}&\psi(\hat{n}) = \sum_{\ell m} \psi_{\ell m} Y_{\ell m}(\hat{n}), \\ &\langle \psi_{\ell m} \psi_{\ell' m'} \rangle = \delta_{\ell\ell'} \delta_{mm'} C^\psi_\ell, \\ &C^\psi_\ell = 16\pi \int \frac{dk}{k} \int_0^{\chi_*} d\chi \int_0^{\chi_*} d\chi' P_\Psi(k; \eta_0 - \chi, \eta_0 - \chi') j_\ell(k\chi) j_{\ell'}(k\chi') \frac{(\chi_* - \chi)}{\chi_*\chi} \frac{(\chi_* - \chi')}{\chi_*\chi'}\end{aligned}$$

We can link the Weyl potential to the primordial comoving curvature perturbations via the transfer function, i. e.

$$\Psi(k, \eta) = T_\Psi(k, \eta)\mathcal{R}(k),$$

so that:

$$C_\ell^\psi = 16\pi \int \frac{dk}{k} P_{\mathcal{R}}(k) \left[\int_0^{\chi_*} d\chi T_\Psi(k, \eta_0 - \chi) j_\ell(k\chi) \left(\frac{\chi_* - \chi'}{\chi_* \chi'} \right) \right]^2 . \tag{2.31}$$

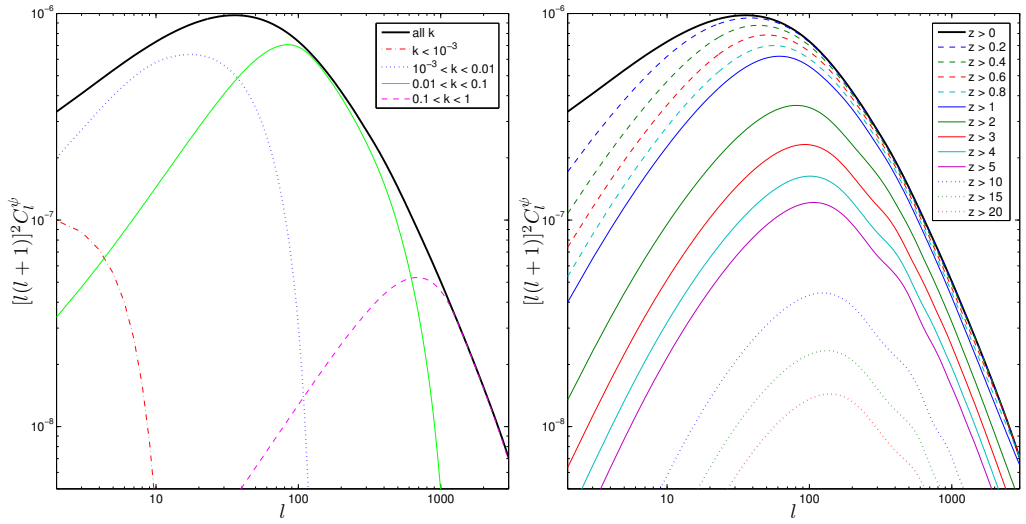

Figure 2.12: The lensing potential power spectrum contribution coming from (left) several wave number bins and from (right) sources at increasing redshifts from (Lewis & Challinor, 2006).

It is interesting to see the contributions to the lensing potential power spectrum at increasing redshift and in terms of wave numbers, both are shown in fig.2.12, respectively in the (right) and (left) panel. We can notice that nearby low redshift potentials contribute to the large scale lensing, though it is sensible to EISW and LISW contribution at these scales. This effects con be emphasized since the cross correlation of CMB temperature power spectrum with the one of the lensing potential is significant up to $\ell = 60$ where C_ℓ^ψ peaks.

Measuring C_ℓ^ψ is therefore a very powerful way to study not only the primordial curvature power spectrum but also the one of density perturbations Δ_m^2, whose measures are usually biased if one consider only the *luminous* matter, as galaxies. In fact, by means of eq.(2.30) we get:

$$P_\Psi(k, \eta) = \frac{9\Omega_c^2(\eta) H^4(\eta)}{8\pi^2} \frac{\Delta_m^2(k, \eta)}{k}.$$

2.4.1 *Lensing of CMB Temperature*

To study the properties of the lensed CMB analytically it is useful to Taylor expand the (2.28) as:

$$\begin{aligned} \tilde{T}(\hat{n}) &= T(\hat{n} + \alpha(\hat{n})) \\ &= T(\hat{n}) + \alpha^i \nabla_i T(\hat{n}) + \frac{1}{2} \alpha^i \alpha^j \nabla_i \nabla_j T(\hat{n}) + \dots \end{aligned} \tag{2.32}$$

If we stop at the first-order and consider the Fourier expansion:

$$\left[\alpha^i \nabla_i T(\hat{n})\right](\mathbf{l}) = \left[\nabla^i \psi \nabla_i T(\hat{n})\right](\mathbf{l}) = -\int \frac{d^2\mathbf{L}}{2\pi} \mathbf{L}\cdot(\mathbf{l}-\mathbf{L})\psi(\mathbf{L})T(\mathbf{l}-\mathbf{L}), \quad (2.33)$$

i. e. a mode $\psi(\mathbf{L})$ is coupled to the unlensed CMB at wave vector $\mathbf{l}-\mathbf{L}$ into the observed CMB at wave vector $\mathbf{l}$. Fixed lenses introduce off-diagonal components into the covariance matrix of the observed CMB, with a characteristic spacing of $\delta\ell = 50$ so that

$$\langle \tilde{T}(\mathbf{l}_1)\tilde{T}(\mathbf{l}_2)\rangle_{CMB} = \frac{1}{2\pi}\psi(\mathbf{l}_1+\mathbf{l}_2)\cdot\left[\mathbf{l}_1 C_{\ell_1}^{TT} + \mathbf{l}_2 C_{\ell_2}^{TT}\right] \text{ with } \mathbf{l}_2 \neq \mathbf{l}_1,$$

where $\langle\ldots\rangle_{CMB}$ is estimated over an ensemble of CMB fluctuations and large scales of the lensing potential induce correlations between CMB modes on smaller scales. However, the Taylor expansion does not hold any more if one wants to compute the lensed power spectrum at the percentage precision level.

Although one of the effect on lensing is to slightly modify the CMB fluctuations toward a non-Gaussian field, the lensed CMB power spectrum can be still useful for comparing model and observations. By simplifying a bit the expansion in (2.32), we can write

$$\tilde{T}(\mathbf{l}) = T(\mathbf{l}) + \delta T(\mathbf{l}) + \delta^2 T(\mathbf{l}) + \ldots$$

where δ denotes the order of the lensing potential. The angular power spectrum to the lowest order in C_ℓ^ψ follows from:

$$C_\ell^{\tilde{T}\tilde{T}}\delta(\mathbf{l}-\mathbf{l}') \approx C_\ell^{TT}\delta(\mathbf{l}-\mathbf{l}') + \langle\delta T(\mathbf{l})\delta T^*(\mathbf{l}')\rangle + \langle T(\mathbf{l})\delta^2 T^*(\mathbf{l}')\rangle + \langle\delta^2 T(\mathbf{l})T^*(\mathbf{l}')\rangle.$$

Notice that we have already explicitly written an expression for $\delta T(\mathbf{l})$ in (2.33), similarly we have for $\delta^2 T(\mathbf{l})$:

$$\delta^2 T(\mathbf{l}) = -\frac{1}{2}\int\frac{d^2\mathbf{l}_1}{2\pi}\int\frac{d^2\mathbf{l}_2}{2\pi}\mathbf{l}_1\cdot(\mathbf{l}_1+\mathbf{l}_2-\mathbf{l})\mathbf{l}_1\cdot\mathbf{l}_2\, T(\mathbf{l}_1)\,\psi(\mathbf{l}_2)\psi^*(\mathbf{l}_1+\mathbf{l}_2-\mathbf{l}),$$

assuming the statistics from an isotropic Gaussian random field for both $T(\mathbf{l})$ and $\psi(\mathbf{l})$, we get:

$$\langle T(\mathbf{l})\delta^2 T^*(\mathbf{l}')\rangle + \langle\delta^2 T(\mathbf{l})T^*(\mathbf{l}')\rangle = -\ell^2 R^\psi C_\ell^{TT}\delta(\mathbf{l}-\mathbf{l}'),$$

$$\langle\delta T(\mathbf{l})\delta T^*(\mathbf{l}')\rangle = \delta(\mathbf{l}-\mathbf{l}')\int\frac{d^2\mathbf{L}}{(2\pi)^2}\left[\mathbf{L}\cdot(\mathbf{l}-\mathbf{L})\right]^2 C_{|\mathbf{L}-\mathbf{l}|}^\psi C_L^{TT},$$

$$\text{with } R^\psi \equiv \frac{1}{2}\langle|\nabla\psi|^2\rangle = \frac{1}{4\pi}\int\frac{d\ell}{\ell}\ell^4 C_\ell^\psi \sim 3\times10^{-7}.$$

Putting all these relations together we find an expression for the lensed temperature power spectrum (to first order in C_ℓ^ψ):

$$C_\ell^{\tilde{T}\tilde{T}} = (1-\ell^2 R^\psi)C_\ell^{TT} + \int\frac{d^2\mathbf{l}'}{(2\pi)^2}\left[\mathbf{l}'\cdot(\mathbf{l}-\mathbf{l}')\right]^2 C_{|\mathbf{l}-\mathbf{l}'|}^\psi C_{l'}^{TT} \quad (2.34)$$

The second term is a convolution of the unlensed temperature power spectrum with the lensing potential one. It smooths out the main acoustic peaks in the unlensed power spectrum with a characteristic kernel width of $\delta\ell \approx 50$. On the contrary at smaller scales, where the diffusion damping acts in reducing sensibly the power spectrum, the lensing adds $\sim 10\%$ of power to the unlensed CMB at $\ell > 2000$ where a non -negligible contribution comes from modes $\ell' \ll \ell$, see fig.2.13. At this regime of scales we can approximate (2.34) as:

$$C_\ell^{\tilde{T}\tilde{T}} \approx C_\ell^\psi \int \frac{d^2\mathbf{l}'}{(2\pi)^2}(\mathbf{l}\cdot\mathbf{l}')C_{l'}^{TT} \approx \ell^2 C_\ell^\psi \int \frac{dl'}{l'}\frac{(l')^4 C_{l'}^{TT}}{4\pi} \approx \ell^2 C_\ell^\psi R^T, \tag{2.35}$$

where R^T is defined similarly as R^ψ, and is half the mean-squared gradient of the unlensed CMB.

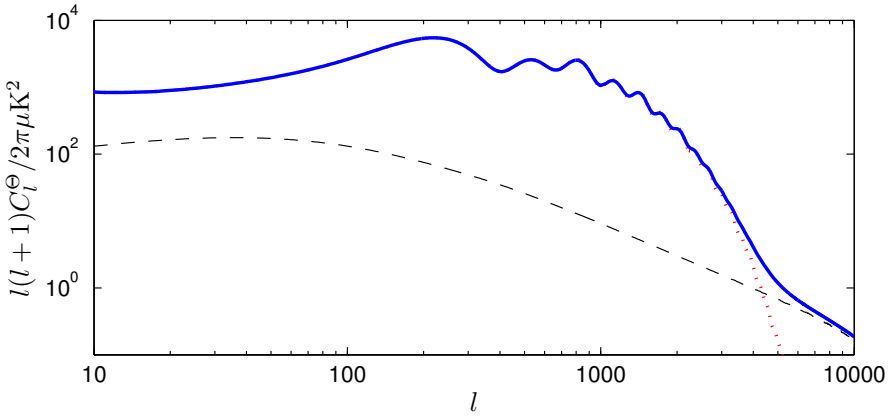

Figure 2.13: The lensed (solid) and unlensed (dotted) temperature power spectrum (Lewis & Challinor, 2006), as well as the small scale approximation (eq. (2.35)).

2.4.2 *Lensing of CMB Polarization*

Let us consider now the lensing in the polarization CMB field with the flat sky assumption we made as in the previous section, so that in terms of E and B modes we can write the Fourier modes as a function of the polarization tensor:

$$[E(\mathbf{l}) \pm iB(\mathbf{l})] = -\int \frac{d^2(\mathbf{x}}{2\pi}[Q \pm iU]e^{\mp 2i\xi_l}e^{-i\mathbf{l}\cdot\mathbf{x}}, \tag{2.36}$$

where ξ_l is the angle between $\mathbf{l}$ and x-axis.

For simplicity, we assume no primordial B-modes, so that $B(\mathbf{l}) = 0$. The computation for polarization lensed power spectra is very similar to the one we sketched above for the temperature one. At the lowest order in C_ℓ^ψ :

$$C_\ell^{\tilde{T}\tilde{E}} = (1-\ell^2 R^\psi) C_\ell^{TE} + \int \frac{d^2\mathbf{l}'}{(2\pi)^2} \left[\mathbf{l}'\cdot(\mathbf{l}-\mathbf{l}')\right]^2 C^\psi_{|\mathbf{l}-\mathbf{l}'|} C^{TE}_{l'} \cos\left[2(\xi_{\mathbf{l}'}-\xi_{\mathbf{l}})\right] \quad (2.37)$$

$$C_\ell^{\tilde{E}\tilde{E}} = (1-\ell^2 R^\psi) C_\ell^{EE} + \int \frac{d^2\mathbf{l}'}{(2\pi)^2} \left[\mathbf{l}'\cdot(\mathbf{l}-\mathbf{l}')\right]^2 C^\psi_{|\mathbf{l}-\mathbf{l}'|} C^{EE}_{l'} \cos^2\left[2(\xi_{\mathbf{l}'}-\xi_{\mathbf{l}})\right] \quad (2.38)$$

$$C_\ell^{\tilde{B}\tilde{B}} = \int \frac{d^2\mathbf{l}'}{(2\pi)^2} \left[\mathbf{l}'\cdot(\mathbf{l}-\mathbf{l}')\right]^2 C^\psi_{|\mathbf{l}-\mathbf{l}'|} C^{EE}_{l'} \sin^2\left[2(\xi_{\mathbf{l}'}-\xi_{\mathbf{l}})\right]. \quad (2.39)$$

The lensing of EE and TE power spectra produces very similar effects as the TT one (fig.2.14), it blurs the peaks and shifts the power into the damping tail. As one can note from fig.2.14 (a) the peaks blurring is more evident in EE than in TT since the oscillations are sharper, leading to a larger fractional variations ($\sim 30\%$) around the acoustic peaks. At small angular scales $\ell \gg 3000$, for $\ell' \ll \ell$ we can approximate EE spectrum as in (2.35):

$$C_\ell^{\tilde{E}\tilde{E}} \approx C_\ell^\psi \int \frac{d^2\mathbf{l}'}{(2\pi)^2} (\mathbf{l}\cdot\mathbf{l}') C^{EE}_{l'} \cos^2\left[2(\xi_{\mathbf{l}'}-\xi_{\mathbf{l}})\right] \approx \frac{1}{2}\ell^2 C_\ell^\psi R^E. \quad (2.40)$$

Moreover, as we have already seen, lensing of E-modes causes power to leak into B-modes and this represents an issue for measuring primordial B-modes at lower multipoles. Since EE peaks around $\ell \sim 1000$, for $\ell \ll 1000$ we can approximate eq.(2.39), since $|\mathbf{l}'| \gg |\mathbf{l}|$

$$C_\ell^{\tilde{B}\tilde{B}} \approx \int \frac{d^2\mathbf{l}'}{(2\pi)^2} |\mathbf{l}'|^2 C^\psi_{l'} C^{EE}_{l'} \sin^2\left[2(\xi_{\mathbf{l}'}-\xi_{\mathbf{l}})\right] \approx \frac{1}{4\pi}\int \frac{dl'}{l'} (l')^4 C^\psi_{l'} (l')^2 C^{EE}_{l'}. \quad (2.41)$$

This quantity does not depend on ℓ, it is constant to a value $C_\ell^{\tilde{B}\tilde{B}} \approx 2\times 10^{-6}\,\mu K^2$ for any ℓ and acts as a white-noise spectrum of B-modes. Indeed, in fig.2.15 we can notice that lensing B-modes behave as a white-noise spectrum for $\ell < 100$, since they have an ℓ^2 dependence coming from the pre-factor $\ell(\ell+1)/2\pi$.

2.5 LENSING POTENTIAL RECONSTRUCTION

Before closing this chapter we discuss here the common methodology to reconstruct the lensing potential from CMB lensed maps which adopted the formalism for small sky patches (where the flat approximation holds, Hu and Okamoto (2002)), whereas the approximation for full sky was presented in a follow up paper (Okamoto & Hu, 2003). At the time in which this Thesis has been written, the flat sky approximation has been valid, since the reconstruction has been achieved in small patches, e. g. see Ade et al. (2014b), so

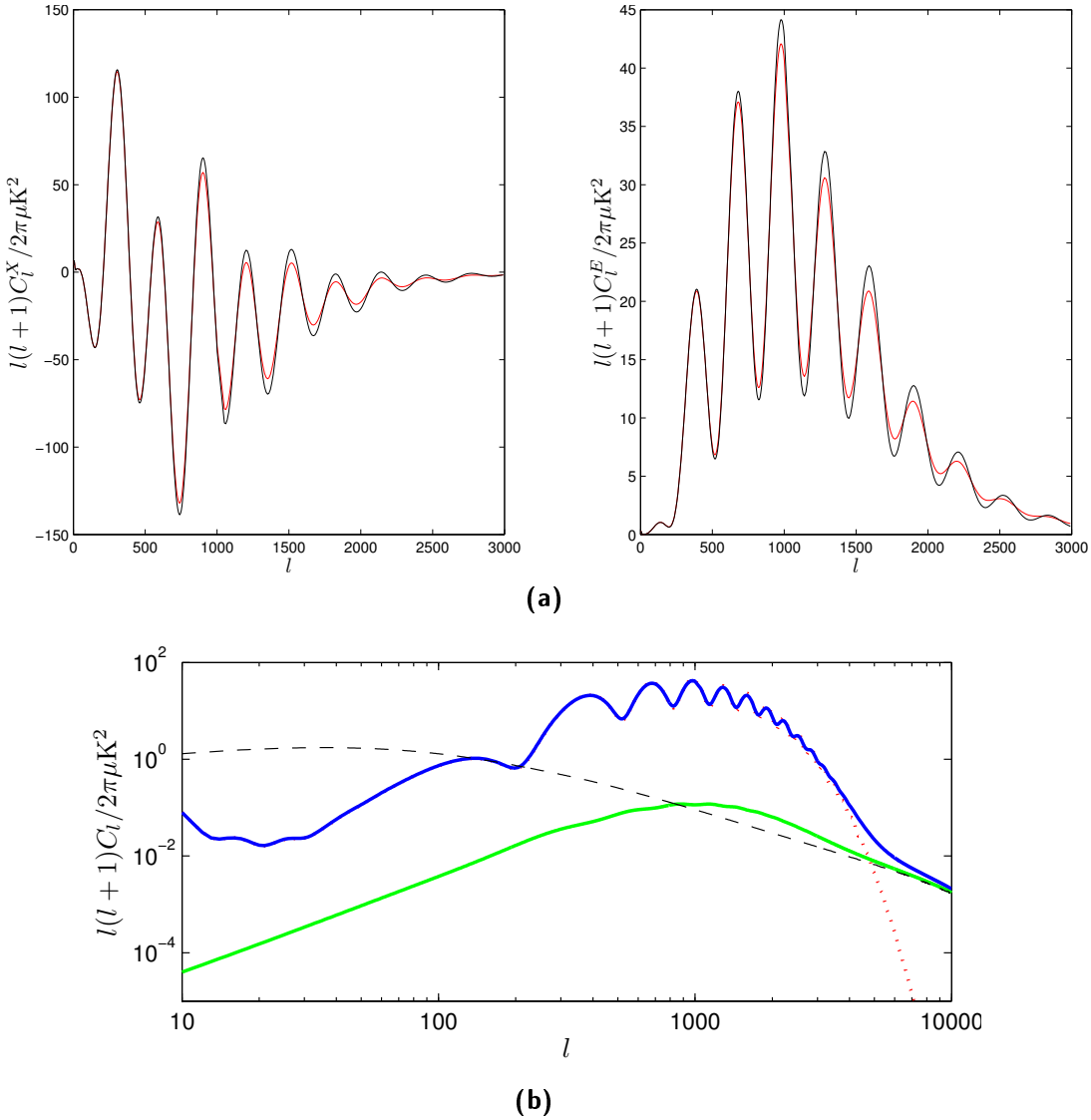

Figure 2.14: (a) (solid black) The unlensed TE and EE power spectra compared to the (solid red) smoother lensed ones (from Lewis and Challinor (2006)).(b) The lensed EE (solid blue) and lensed BB (solid green) power spectra as compared to the unlensed E power spectrum (red dotted). The small scale approximation in (2.40) is the dashed line.

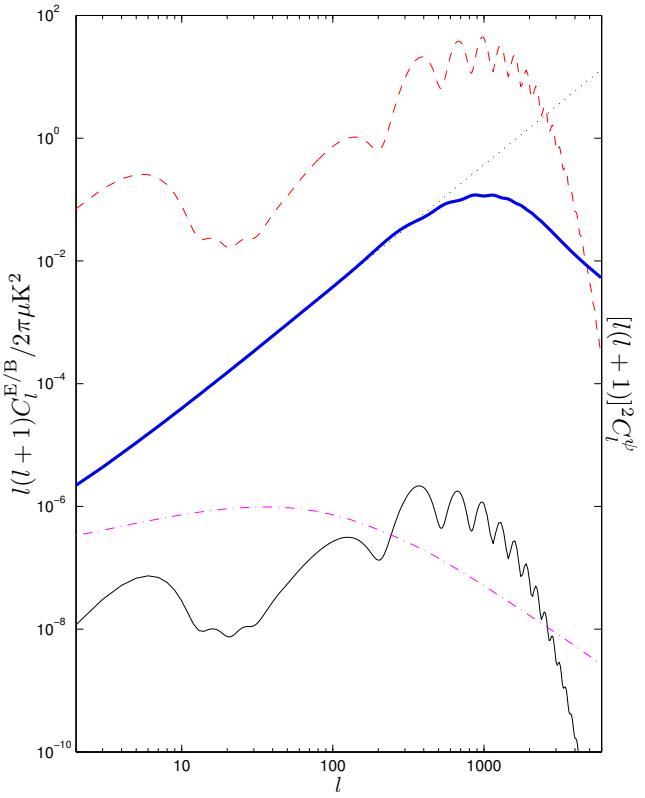

Figure 2.15: The unlensed E-mode power spectrum (dashed),the lensing deflection power spectrum (dot-dashed) and the contribution to the large-scale lensed B-mode power spectrum from each $\log \ell$ given by half their product(solid thin). The dotted line comes from the large-scale white-noise approximation (2.41) which is consistent to the full numerical result (solid-thick) up to $\ell \sim 500$. Figure from Lewis and Challinor (2006).

that we can decompose the temperature, polarization and potential fields in the harmonic domain as :

$$\begin{aligned} T(\hat{n}) &= \int \frac{d^2l}{(2\pi)^2} T(\mathbf{l}) e^{i\mathbf{l}\cdot\hat{n}} \\ (Q \pm iU)(\hat{n}) &= -\int \frac{d^2l}{(2\pi)^2} \left[E(\mathbf{l}) \pm B(\mathbf{l})\right] e^{\pm 2i\xi_l} e^{i\mathbf{l}\cdot\hat{n}} \\ \psi(\hat{n}) &= \int \frac{d^2l}{(2\pi)^2} \psi(\mathbf{l}) e^{i\mathbf{l}\cdot\hat{n}}. \end{aligned}$$

Lensing changes the Fourier moments by

$$\begin{aligned} \delta T(\mathbf{l}) &= \int \frac{d^2l'}{(2\pi)^2} \tilde{T}(\mathbf{l}') W(\mathbf{l}', \mathbf{L}), \\ \delta E(\mathbf{l}) &= \int \frac{d^2l'}{(2\pi)^2} \left[\tilde{E}(\mathbf{l}') \cos(2(\xi_{l'} - \xi_l) - \tilde{B}(\mathbf{l}') \sin(2(\xi_{l'} - \xi_l)\right] W(\mathbf{l}', \mathbf{L}), \\ \delta B(\mathbf{l}) &= \int \frac{d^2l'}{(2\pi)^2} \left[\tilde{B}(\mathbf{l}') \cos(2(\xi_{l'} - \xi_l) + \tilde{E}(\mathbf{l}') \sin(2(\xi_{l'} - \xi_l)\right] W(\mathbf{l}', \mathbf{L}), \end{aligned} \tag{2.42}$$

where $W(\mathbf{l}, \mathbf{L}) = -(\mathbf{l} \cdot \mathbf{L})\psi(\mathbf{L})$. From eq. (2.42), one can notice that lensing mixes and correlate the Fourier modes across a range defined by the power in the deflection field C_ℓ^{dd}[10].

Since the statistical properties of the unlensed fields are all encoded in the power spectra, we can express the ones of the observed temperature and polarization fields by averaging over an ensemble of realization of temperature and polarization fields with a fixed lensing field. The two point correlation function of the modes takes the form:

$$\begin{aligned} \langle \tilde{X}_\mathbf{l} \tilde{Y}_{\mathbf{l}'} \rangle_{CMB} \simeq & \langle X_\mathbf{l} Y_{\mathbf{l}'} \rangle_{CMB} + \langle \delta X_\mathbf{l} Y_{\mathbf{l}'} \rangle_{CMB} + \langle X_\mathbf{l} \delta Y_{\mathbf{l}'} \rangle_{CMB} = \\ & = f_{XY}(\mathbf{l}, \mathbf{l}') \psi_{XY}(\mathbf{L}). \end{aligned} \tag{2.43}$$

The correlation function returns the value of the deflection potential weighted by the proportionality constant $f_{XY}(\mathbf{l}, \mathbf{l}')$ which depends only on the unlensed CMB power spectra. These correlation functions cannot be used to reconstruct the deflection potential since ψ is statistically isotropic, so that the ensemble average $\langle \psi \rangle = 0$. However, eq. (2.43) suggests that an appropriate average over pairs of multipole moments can be an appropriate estimator the deflection field by defining the weighting as:

$$d_{XY}(\mathbf{L}) = \frac{A_{XY}}{L} \int \frac{d^2l_1}{(2\pi)^2} X(\mathbf{l}_1) Y(\mathbf{l}_2) F_{XY}(\mathbf{l}_1, \mathbf{l}_2), \tag{2.44}$$

with $\mathbf{l}_2 = \mathbf{L} - \mathbf{l}_1$ and the normalization factor

$$A_{XY}(L) = L^2 \left[\int \frac{d^2l_1}{(2\pi)^2} f_{XY}(\mathbf{l}_1, \mathbf{l}_2) F_{XY}(\mathbf{l}_1, \mathbf{l}_2) \right]^{-1}$$

10 Notice that in this section we slightly changed the notation, to be closer to the literature. Hereafter, we refer to the deflection field with $d(\hat{n})$, instead of α, so that $d = \nabla\psi$.

is chosen to satisfy

$$\langle d_{XY}(\mathbf{L})\rangle_{CMB} = d(\mathbf{L}) \equiv L\psi(\mathbf{L}).$$

In correspondence to the 3! choice of X, Y combining T, E, B, there are six estimators, though the combination $XY = BB$ which has vanishing signal-to-noise due to the faintness of primordial gravitational wave perturbations reduces the number of estimators to five. F_{XY} can be optimized in such a way that the estimator in (5.4) minimizes the variance $\langle d^*_{XY} d_{XY}\rangle$:

$$F_{XY}(\mathbf{l}_1, \mathbf{l}_2) = \frac{C^{YY}_{l_1} C^{XX}_{l_2} f_{XY}(\mathbf{l}_1, \mathbf{l}_2) - C^{XY}_{l_1} C^{XY}_{l_2} f_{XY}(\mathbf{l}_2, \mathbf{l}_1)}{C^{XX}_{l_1} C^{YY}_{l_2} C^{YY}_{l_1} C^{XX}_{l_2} - (C^{XY}_{l_1} C^{XY}_{l_2})^2}. \tag{2.45}$$

Notice that the weighting filters F_{XY} get simplified if $X = Y$:

$$F_X(\mathbf{l}_1, \mathbf{l}_2) \to \frac{f_X(\mathbf{l}_1, \mathbf{l}_2)}{2 C^{XX}_{l_1} C^{XX}_{l_2}},$$

and if $C^{XY}_l = 0$, as in the case of TB, EB,

$$F_{XY}(\mathbf{l}_1, \mathbf{l}_2) \to \frac{f_{XY}(\mathbf{l}_1, \mathbf{l}_2)}{C^{XX}_{l_1} C^{YY}_{l_2}}.$$

The noise properties of two estimators for two different ρ, σ choices of X, Y, are shown in fig.2.16 and in general one can combine all the $d_{\rho\sigma}$ into a minimum variance coaddition d_{MV} . For current experiments d_{MV} is dominated by the combinations involving temperature, TT in particular. However, as the sensitivity of the experiments improve, polarization will play a progressively more important role for the minimum variance estimator, being mostly dominated by EB (Hu & Okamoto, 2002).

2.6 OTHER SECONDARIES ANISOTROPIES

There is a variety of secondary effects on the CMB, in addition to the LISW and reionization discussed previously in this Chapter. We list here the most important ones, leaving the complete description to the quoted references. One of the most important is Sunyaev-Zel'dovich (SZ) effect which can be either *thermal* (tSZ, Sunyaev and Zeldovich (1980)) or *kinetic* (kSZ, Hand et al. (2012)). The former is due to scattering of photons from hot electrons in galaxy clusters and it can smear the power on small scales. However, this signal has a frequency dependence different than the CMB one and hence it can in principle easily be distinguished. The kSZ effect arises when the scattering of photons with electrons happens in a bulk flow of a non-linear perturbation with respect to the CMB. Essentially it is a Doppler term related to electron velocity projected along the line of sight. Both give rise to a percent uncertainty at large multipoles $\ell = 2000$, and they are expected to be significantly correlated. For polarization, the kSZ is negligible and one

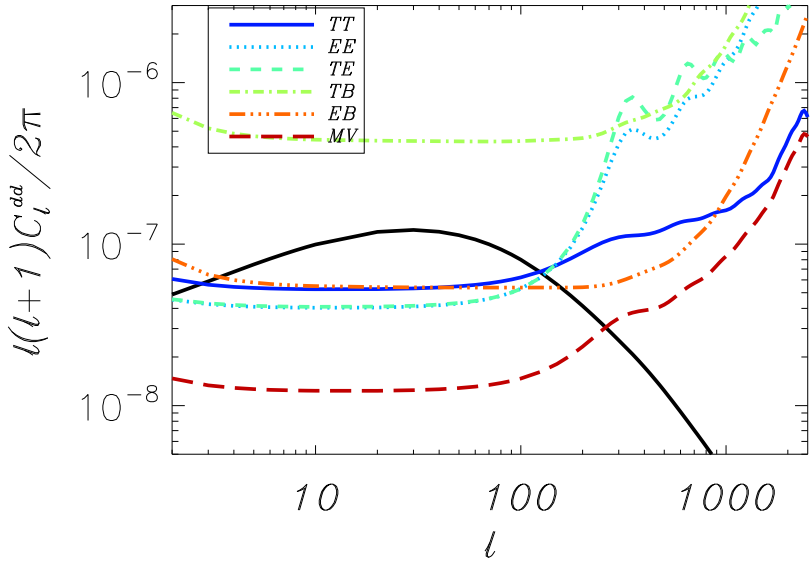

Figure 2.16: The solid black curve is the deflection angle power spectrum C_ℓ^{dd}. The noise in lensing-reconstruction from the quadratic optimal estimator given the nominal sensitivity of Polarbear experiment (see chapter 4) for different estimators: TT (solid dark blue), EE (dot light blue), TE (dashed green), TB (dot-dash yellow), EB (double-dot-dash orange) and minimum variance (MV) (dashed dark red). For Polarbear sensitivity and angular resolution, the lowest-noise estimator is one of the EE and TE estimators depending on the angular size (Miller et al., 2009).

has to deal only with lensing, further details may be found in the review article Kitayama (2014).

Finally, another secondary and non-linear contribution comes from the Rees-Sciama effect (Rees & Sciama, 1968), a sort of LISW anisotropy generated by photons going through potential wells evolving because of non-linear growth or bulk motion.

3

STATUS OF CMB MEASUREMENTS

> Voir.[...] Voilà pourquoi, sans doute, l'histoire du Monde vivant se ramène à l' élaboration d'yeux toujours plus parfaits au sein d'un Cosmos où il est possible de discerner toujours davantage. [...] Chercher à voir plus et mieux n'est donc pas une fantaisie, une curiosité, un luxe. Voir ou périr. [1]
>
> — Pierre Teilhard de Chardin

In this chapter we present the latest CMB measurements obtained with several experiments, both ground based telescope and space satellites aimed at observing CMB temperature and polarization anisotropies. As we briefly discussed in previous chapters, after the detection of COBE of large scale temperature anisotropies (at angular resolution of $\sim 7^\circ$), many other experiments observed the first acoustic peaks in the range $30 < \ell < 600$; among those we quote MAXIMA (Hanany et al., 2000) and BOOMERANG (de Bernardis et al., 2000).

Polarization anisotropies have been observed for the first time by the ground based experiment Degree Angular Scale Interferometer (DASI) at frequencies $20 - 36$ GHz (Kovac et al., 2002). The WMAP satellite, then, observed them with a wider range of frequencies ($20 - 90$ GHz) and in a full sky survey the polarization at the microwave regimes (Hinshaw et al., 2013; Page et al., 2007). Planck provided the latest measurements of temperature anisotropies (Planck Collaboration, Ade, Aghanim, Arnaud, Ashdown, et al., 2016) with a better sensitivity and frequencies spanning in the millimeter and sub-millimeter regimes ($30 - 857$ GHz). In the last decade several ground based experiments have been proposed and deployed, mostly in the Antarctica, as the Background Imaging of Cosmic Extragalactic Polarization (BICEP) (Barkats et al., 2014) and South Pole Telescope (SPT, Story

1 "Seeing.[...] That is probably why the history of the living world can be reduced to the elaboration of ever more perfect eyes at the heart of a Cosmos where it is always possible to discern more. [...] To try to see more and to see better is not, therefore, just a fantasy, curiosity, or a luxury. See or perish.", P. T. de Chardin, Le Phénomène humain, 1947.

et al. (2013)), and in the Atacama Desert (Chile), like Polarbear (Ade et al., 2014) and Atacama Cosmology Telescope (ACT, Das et al. (2014)); moreover, several balloon experiments (as the E and B EXperiment (EBEX) (Reichborn-Kjennerud et al., 2010) and SPIDER (Filippini et al., 2010)) flew recently some years ago. The TT, EE, TE, BB and lensing power spectra in fig.3.1 were obtained by combining the data of all the experiments listed above.

One can notice how well the theoretical TT power spectrum is constrained (shown as a black solid line in fig.3.1(a)) by the temperature data of Planck, ACT and SPT experiments. At large angular scales (unaccessible for ground based telescopes), the Planck data represent a very good fit for the standard ΛCDM 6 parameter model discussed in Chapter1, whereas the high resolution and high sensitivity data of ACT and SPT allow to probe the damping tail ($\ell \sim 4000$). By combining temperature and polarization data (EE and TE power spectra, respectively fig.3.1(d) and (c)) it is possible to obtain the measurements in Table 1.1, at the end of Chapter1, are reported the latest values from Planck temperature and polarization measurements (Planck Collaboration, Ade, Aghanim, Arnaud, Ashdown, et al., 2016).

Planck measurements allowed to reconstruct very well the CMB lensing power spectrum (fig.3.1 (b)). These measurements are very useful since they can break the geometrical degeneracy in the estimation of Ω_Λ and Ω_K since closed geometries predict larger power in the lensing potential (Stompor & Efstathiou, 1999). Thus, they can be independently constrained: $\Omega_K = 0.0096 \pm 0.01$ and $\Omega_\Lambda = 0.67 \pm 0.027$ (Planck Collaboration, Ade, Aghanim, Arnaud, Ashdown, et al., 2016).

Over the last 3 years lensing B-modes have been for the first time measured by Polarbear Collaboration (Ade et al., 2014). Experiments are characterising the lensing B-mode power spectra with increasing accuracy in the multipole interval $600 < \ell < 3000$: see the recent results from The POLARBEAR Collaboration et al. (2017), ACTpol Louis et al. (2016), SPTpol Keisler et al. (2015) showed that the required detector accuracy to better constrain lensing B-modes has been reached.

Observing larger angular scales from the ground is not easy since atmosphere and systematics can induce correlations into the signal on the same scales. Furthermore, at lower multipoles the Galactic contamination has to be taken into account, as we will discuss in the following.

3.1 THE BICEP2-PLANCK CASE

Page et al. (2007) presented the WMAP polarization measurements showed significant levels of polarized foreground emission due to both Galactic synchrotron radiation and thermal dust emission. We will discuss their main features and physical properties later in this Chapter, while in this Section, we discuss their most important role in the first claim, subsequently withdrawn because of them, of detection of B-modes from cosmological Gravitational Waves. The quoted WMAP results showed that they dominate at $\ell < 50$ which is the entire multipole interval accessible by WMAP; the for-

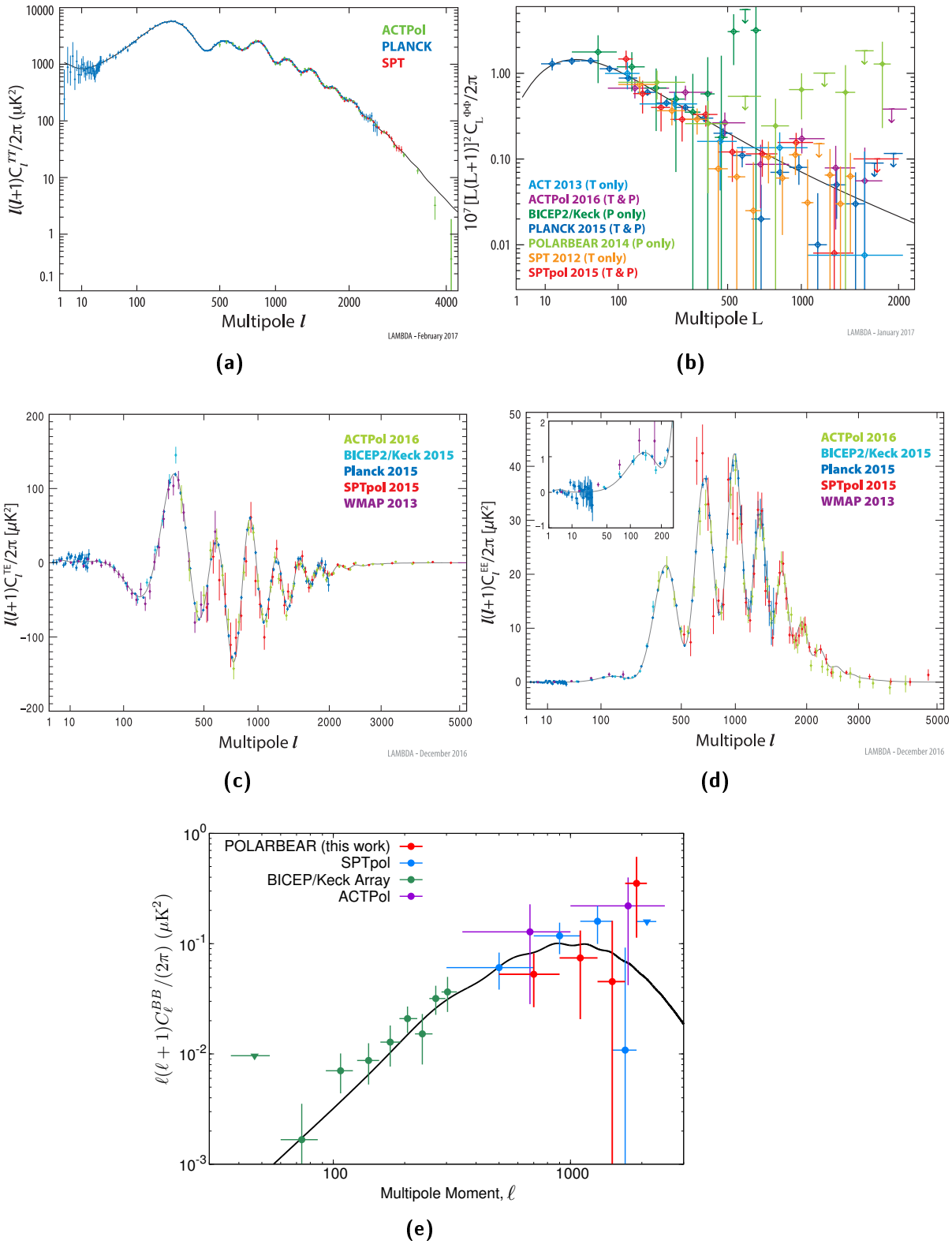

Figure 3.1: Current measurements of CMB and lensing power spectra from the LAMBDA web site. The best-fit ΛCDM theoretical spectrum fitted from Planck TT and low-ℓ polarization data is plotted.The error bars show ±1σ uncertainties. References are quoted in the text.

mer being important at low frequencies $\nu \lesssim 40$GHz, while the latter starts to emerge at frequencies larger than ~ 90 GHz due to their physical properties, which we will discuss later. Even if a large Galactic mask is applied (cutting 30% of the sky), the high Galactic latitude rms of polarized foreground emission, averaged over large angular scales $\ell = 4 - 6$, ranges from 5μK at 22GHz to 0.6μK at 61 GHz. For comparison, the levels of CMB polarization for a ΛCDM model assuming a tensor-to-scalar ratio $r = 0.3$ are 0.3μK and 0.1μK respectively for E and B-mode polarization. Therefore, it has been clear that in order to measure B-modes in CMB polarization, the Galactic diffuse foregrounds emission must be taken into account.

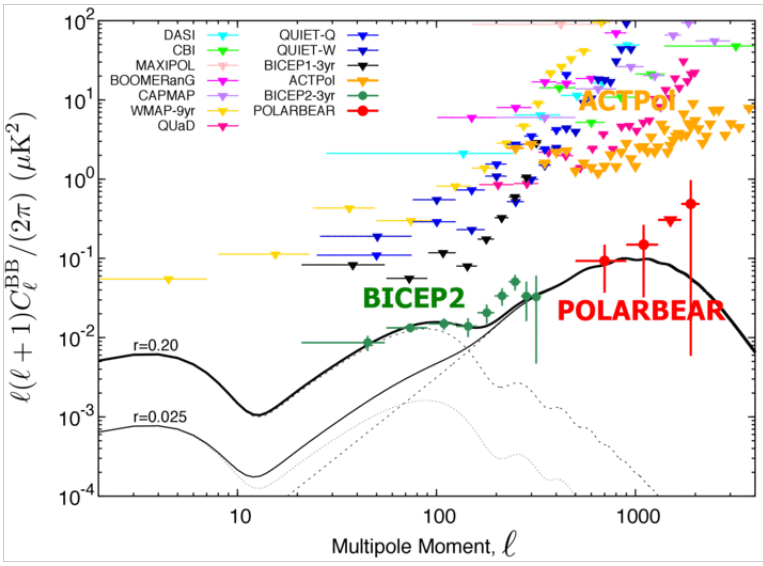

Figure 3.2: B-modes power spectrum measurements reported by the BICEP2 publication (BICEP2 Collaboration et al., 2014). The green filled circles show the detected excess with 1σ error bars.

In May 2014, the BICEP collaboration held a press-release stating that they observed at 150 GHz an excess B-mode power over the lensed ΛCDM expectation at a significance of 5σ (BICEP2 Collaboration et al., 2014). They observed a wide patch, 1% of the sky, close to the South Galactic Pole, centred in $(l, b) = (316°, -59°)$, collecting over 590 daily scans from early 2010 until late 2012 . They classified the excess signal in fig.3.2 as *astrophysical* since the effects of systematics contamination (through jackknife tests and simulations based on calibration) were estimated to be smaller. Neither synchrotron nor thermal dust were found to be comparable to the excess since the observation patch is chosen in a region where the Galactic foregrounds were thought to be quite low, an order of magnitude cleaner than the average at $b > -50°$ level. By cross-correlating with the WMAP at 23 GHz (as a monitor for synchrotron) and considering several dust models they found that the total contribution from diffuse foregrounds would be corresponding to $r \leqslant 0.01$. Roughly an order of magnitude smaller of what they have measured, i.e. $r = 0.20^{+0.07}_{-0.05}$. their conclusion was that this signal should have been related to primordial fluctuations!

After a couple of months later, the Planck collaboration reported measurements from the frequency channel most sensitive to polarization at 353 GHz (aimed at monitoring the dust polarized emission, (Planck Collaboration, Adam, Ade, Aghanim, Arnaud, et al., 2016)). They found that at high Galactic latitudes the polarization fraction is higher than at latitudes closer to the Galactic plane, as expected because of smaller cancellation produced by the shorter column density along the line of sight.

In fig.3.3 the power spectra of EE and BB computed with increasing masking of the sky show that: *even in the faintest dust-emitting regions there are no "clean" windows where primordial CMB* B*-mode polarization could be measured without subtraction of dust emission.* These findings confirm earlier conservative expectations on the diffuse foreground emission levels (Baccigalupi, 2003).

The Planck Collaboration further investigated the level of dust polarization in the BICEP2 field: by extrapolating the Planck 353 GHz data to 150 GHz, the dust BB power spectrum in the range $40 < \ell < 120$ was found at the very same magnitude as the excess reported by BICEP2. The large uncertainties are due to the extrapolation to 150 GHz of the instrumental noise and foreground parameters as shown in fig.3.4.

These conclusions were further extended to all patches far away from the Galactic plane as shown in fig.3.5, by quantifying the dust contamination detected at 353 GHz and extrapolated at 150 GHz. The estimates were then compared with the value of the CMB B-modes $D^{BB}_{\ell=80}$ at a reference value of $r = 1$, being $6.71 \times 10^{-2} \mu K^2$; defining a new "dust induced" r_d parameter. therefore one can express the estimated power in units denoted with r_d. Since the CMB primordial tensor B-mode power is directly proportional with the tensor-to-scalar ratio r, a value of $r_d = 0.1$ would mean that the expected contamination from dust at $\ell = 80$ equals the amplitude of the CMB primordial power spectrum D^{BB}_{ℓ} for $r = 0.1$.

These estimates have been computed in 352 400 deg^2 patches and projected position in the sky along with uncertainty $\sigma(r_d)$. The latter are at the same order of r_d and in 5 cases yield to negative values though consistent with $r_d = 0$ at 1σ.

The Planck Collaboration, Adam, Ade, Aghanim, Arnaud, et al. (2016) concluded that a very accurate assessment of the dust contribution to the B-mode power measured by the BICEP2 experiment would have required a *dedicated joint analysis with Planck*, in order to take into account all the *pertinent observational details of the two data sets, such as masking, filtering, and colour corrections*.

As a result, the joint analysis revealed a 150×353 GHz cross-correlation in B modes at high significance finding strong evidence for dust and no statistically significant evidence for tensor modes.

The latest result (as shown by green filled circles in fig.3.1 (e)) come from combining the 95 GHz data from the Keck Array with 353 GHz Planck and 150 GHz BICEP2 (BICEP2 Collaboration et al., 2016) and yield to the upper limits: $r < 0.07$ at 95% confidence level.

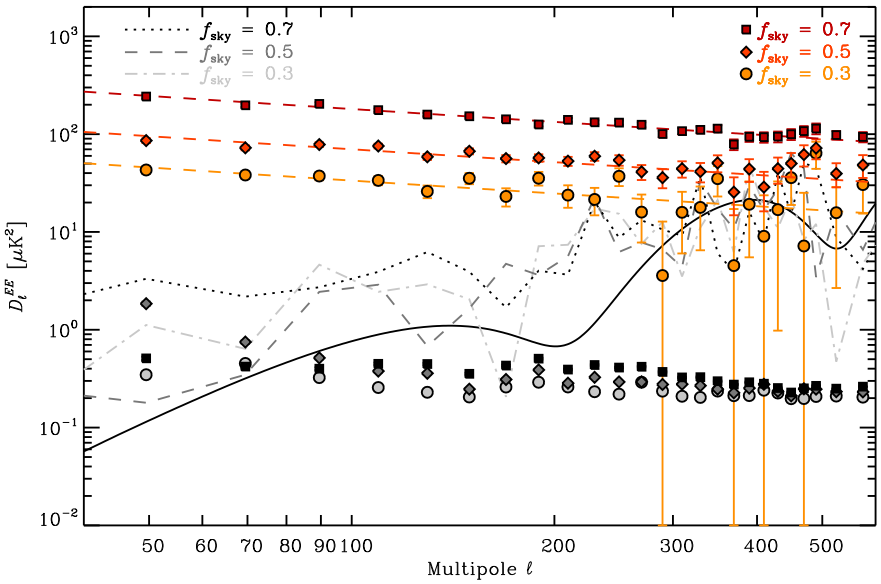

(a)

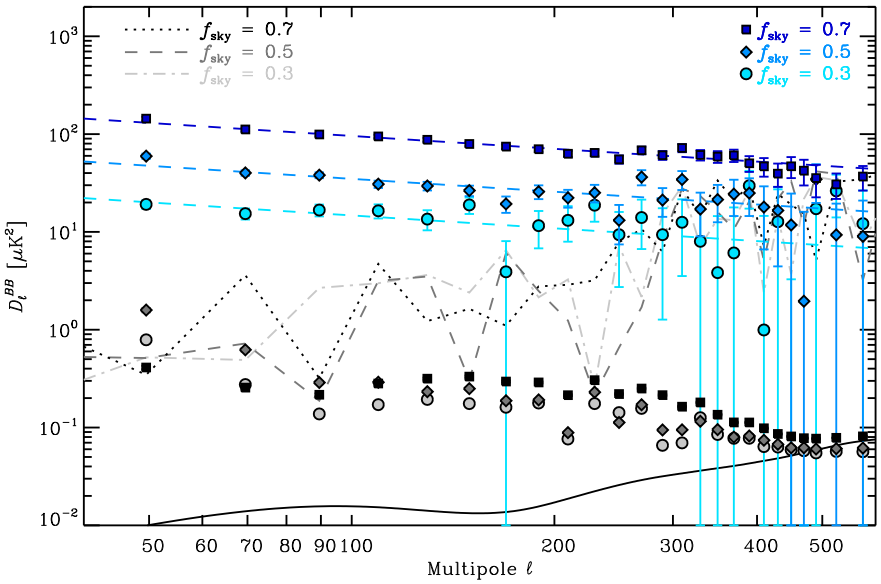

(b)

Figure 3.3: Planck 353 GHz (red, top) and (blue, bottom) power spectra (in μK) computed on three regions having $f_{sky} = 0.3$(circles, lightest), $f_{sky} = 0.5$ (diamonds, medium) and $f_{sky} = 0.7$ (squares, darkest), from (Planck Collaboration, Adam, Ade, Aghanim, Arnaud, et al., 2016). The uncertainties shown are $\pm 1\sigma$. The best-fit power laws in ℓ are given for each spectrum as a dashed line of the corresponding colour. The Planck Collaboration, Ade, P. A. R., et al. (2014) best-fit CMB model based on temperature anisotropies, with a tensor amplitude fixed at $r = 0.2$ are shown as solid black lines; the rise for $\ell > 200$ is from the lensing contribution. In the lower parts of each panel, the global estimates of the power spectra of the systematic effects are shown in different shades of grey, with the same symbols to identify the three regions. Finally, absolute values of the null-test spectra from the cross-spectra computed by splitting in two sub sets the whole dataset, are represented as dashed-dotted, dashed, and dotted grey lines for the three sky area.

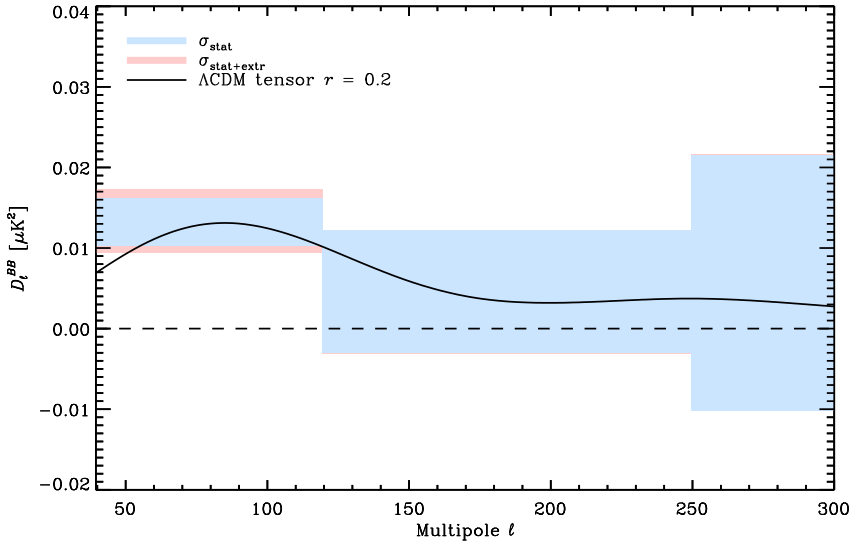

Figure 3.4: Planck 353 GHz angular power spectrum computed on the BICEP2 patch and extrapolated to 150 GHz, from (Planck Collaboration, Adam, Ade, Aghanim, Arnaud, et al., 2016). The shaded boxes represent the 1σ uncertainties: blue for the statistical uncertainties from noise; red adding in quadrature the uncertainty due to the extrapolation from 353 to 150 GHz. The Planck Collaboration, Ade, P. A. R., et al. (2014) best-fit ΛCDM expectation and the corresponding $r = 0.2$ tensor B modes is plotted as a black line.

Similar analysis related to synchrotron by Krachmalnicoff, Baccigalupi, Aumont, Bersanelli, and Mennella (2016), showed that it is not possible to exclude the presence of synchrotron contamination to B modes at the level required to measure a gravitational wave signal with $r \simeq 0.01$ at frequencies $\leqslant 150$ GHz.

All the ground based CMB experiments should therefore optimize the frequency coverage, the integration time and coverage area so as to have a similar S/N level for the CMB and dust. They could exploit the Planck 353 GHz data[2] to remove the dust emission via foreground cleaning and separate all the astrophysical components by means of multi-frequency data-analysis (the so-called *component separation*). However, the accuracy of such cleaning is limited by Planck noise, not appropriate for B-mode foreground cleaning.

Summary, all the coming and future developments of CMB experiments are planned to increase the sensitivity of CMB channels ($100 - 150$ GHz) and add frequency channels both at high and lower frequencies to monitor the polarized Galactic emission respectively from dust and synchrotron.

3.2 ASTROPHYSICAL FOREGROUNDS FOR B-MODE OBSERVATIONS

The list of foregrounds in the microwave band is long and includes anything in space that might come between us and radiation left over from the Big

2 The Planck data are publicly available at the Planck Legacy Archive.

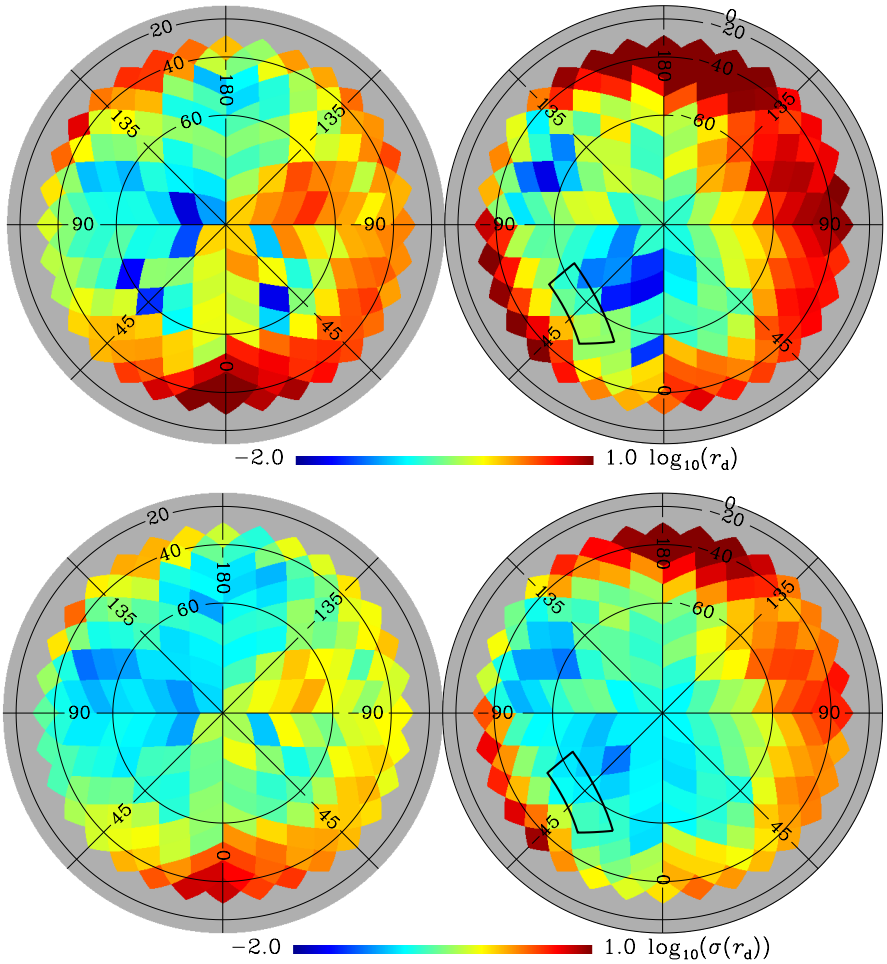

Figure 3.5: Orthographic projection of D_ℓ amplitude at $\ell = 80$ computed from the Planck 353 GHz data extrapolated to 150 GHz, and normalized bu the CMB expectation for tensor-to-scalar ratio $r = 1$, from (Planck Collaboration, Adam, Ade, Aghanim, Arnaud, et al., 2016). The coulours represent the estimated contamination from dust in terms of the logarithm of the absolute value of r_d (see details in Sect.3.1 for this definition) within $400^{\circ 2}$ patches. (top) The northern (southern) Galactic polar caps is on the left (right).(bottom) associated uncertainty $\sigma(r_d)$. The thick black contour outlines the BICEP2 field region.

Bang. Thermal dust, synchrotron radiation which we anticipated in a few crucial aspects above, and molecular rotational lines emissions contribute up to regions far from the Galactic plane. At small angular scales, one has to take into account the further presence of extragalactic foregrounds: radio sources, star forming galaxies and clusters of galaxies (generating SZ effect, see sect.2.6).

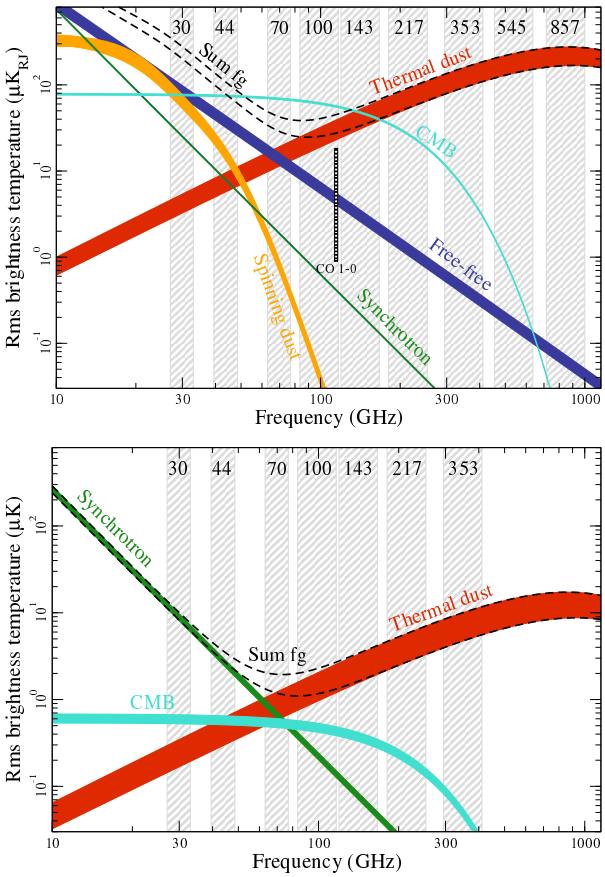

Figure 3.6: Brightness temperature (top) and polarization (bottom) rms as a function of frequency of astrophysical components observed by Planck, from (Planck Collaboration, Adam, R., et al., 2016). For temperature, each component is smoothed to an angular resolution of 1° FWHM, and the lower and upper edges of each line are defined by masks covering 81 and 93% of the sky, respectively. For polarization, the corresponding smoothing scale is 40′ for $f_{sky} = 73$ and 93%. Note that foreground rms values decrease nearly monotonically with f_{sky}, whereas CMB rms does not.

The intensity of these components vary across the sky, but the relative amplitudes are fairly typical. At very high frequencies (above 100 GHz), dust dominates, while at lower frequencies synchrotron and free free become important. The former arises from the interaction of cosmic rays with the Galactic magnetic field; the latter is produced by bremsstrahlung in hot HII regions. At low frequencies there is mounting evidence for an Anomalous Microwave Emission (AME) due to spinning dust grains (Planck Collaboration et al., 2011).

In fig.3.6 (top) the rms of the *brightness temperature*[3] of all these components are shown as functions of frequency, with different spectral dependency. Moreover, at $70-120$ GHz there is a window where CMB is expected to be dominant with respect to the other components (Planck Collaboration, Adam, R., et al., 2016).

Unfortunately, the situation is sensibly different when we consider polarization (fig. 3.6 bottom panel): both synchrotron and dust dominate at any frequency, though the minimum of both polarized emission is at $\nu \sim 100$ GHz and free-free and AME are essentially unpolarized (upper limits of a few percent (Planck Collaboration, Adam, R., et al., 2016)). Hence, knowing very well synchrotron and dust is remarkable not only to determine the level of contamination to CMB polarization, but also to trace magnetic field over the entire volume of the Galaxy. We describe both aspects in the next sections, 3.2.2 and 3.2.1, while in Chapter 6 we address the contamination induced by polarization of molecular rotational lines.

3.2.1 *Thermal Dust emission*

Regions of the sky containing a small amount of stars are apparent to any observer looking at the Milky Way from a dark site. These regions are especially conspicuous in the Southern hemisphere where one sees the utter darkness across Centaurus and Sagittarius. William Herschel regarded these regions as curious voids in the distribution of stars. In the early 20th century, detailed studies by Trumpler (1934) convincingly demonstrated that interstellar dust was responsible. Starlight passing through a dusty medium is subject to both absorption and scattering. Both processes are wavelength-dependent, resulting in an apparent reddening of the light. The combination of these effects is termed *extinction*.

Advances in infra-red astronomy have improved our understanding of interstellar dust. The starlight energy heats the dust which re-radiates at a lower energy ($\lambda > 100, \mu m$). Approximately 20% of the energy from starlight in our Galaxy is reprocessed in this way by interstellar dust.

Besides attenuating starlight, dust grains are known to polarize that light. The basic explanation is that a large scale Galactic magnetic field induces alignment of elongated dust grains. Starlight polarization measures the pro-

3 Brightness temperature is commonly defined for radio sources as the equivalent temperature that a black body would need in order to emit the observed intensity. Since we are in the Rayleigh-Jeans regime of frequencies, we can approximate it as :

$$T_b = \frac{c^2}{2\nu^2 k_B} I_\nu,$$

where T_b is usually measured in K_{RJ}. Thermodynamic temperature (referred K_{CMB}) and brightness temperature are related via the following relation:

$$K_{RJ} = K_{CMB} \frac{x^2 e^x}{(e^x - 1)^2}, \text{with } x = \frac{h\nu}{kT_0}.$$

jection of the direction of polarization on the plane of the sky. However, these polarization measures are affected by extinction, giving often ambiguous results for denser dust clouds. On the other hand, sub-mm polarization is free from opacity effects. Thus, by measuring the degree of polarization, one can infer dust density in dusty regions.

One expects polarization only if the dust grains are non-spherical and have a preferential axis of alignment. The magnetic moments of the dust grains will preferentially align with the ambient magnetic field. As these aligned grains rotate, they emit polarized radiation. Therefore, a more accurate knowledge of dust polarization is necessary not only to disentangle it from CMB measurements but also because it represents a new, essentially unexplored, means to study interstellar dust and the physical processes that couple dust grains and their alignment with local physical conditions.

Thermal dust emission has been mapped over the full sky in several bands by the Planck satellite (Planck Collaboration, Adam, R., et al., 2016), who released intensity and polarization maps after been processed by component separation, see fig.3.7 (bottom). In the left bottom panel is shown the polarization amplitude defined as

$$P = \sqrt{Q^2 + U^2}, \tag{3.1}$$

whereas in the right bottom panel is the polarization angle:

$$\psi = \frac{1}{2} \arctan\left(\frac{U}{Q}\right). \tag{3.2}$$

The *degree of polarization*, or *polarization fraction*, is defined by the ration of polarization by intensity amplitudes:

$$f_p = \frac{P}{I}. \tag{3.3}$$

As it is depicted in fig.3.6, thermal dust follows approximately a *grey body emission*, i. e. a body which does not absorb all incident radiation and emits less than a black body. It is characterized by an emissivity $\epsilon < 1$, such that the flux energy irradiated is

$$j = \epsilon \sigma_B T^4,$$

where σ_B is the Stephan-Boltzmann constant. However, remind that a black body has $\epsilon = 1$. Total dust emission is modelled as

$$I_\nu \propto \nu^{\beta_d} B_\nu(T),$$

where $B_\nu(T)$ is the Planck function at temperature T, so that the brightness temperature of a grey body can be written as

$$T_{b,grey} \propto \frac{\nu^{\beta_d+1}}{e^{h\nu/kT_d} - 1}, \tag{3.4}$$

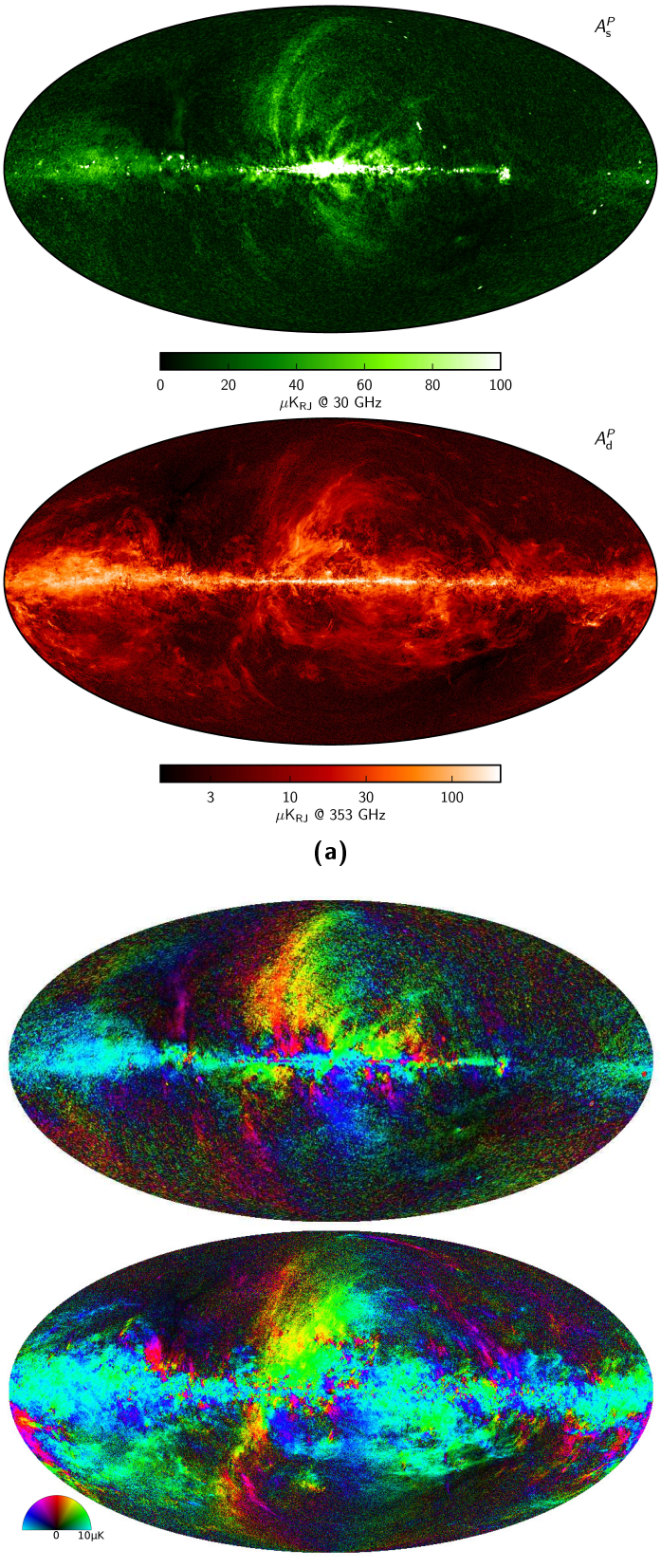

Figure 3.7: Planck polarization amplitude A^P (a) and polarization angle ψ maps (b) for synchrotron (top) and dust (bottom) emissions. Synchrotron emission is shown at 30 GHz, smoothed to an angular resolution of $40'$, while thermal dust emission at 353 GHz is smoothed to $10'$. In panel (b) light blue and red colours indicate polarization angles aligned with meridians and parallels (respectively $\psi = 0, 90$ deg) while yellow and purple indicate angles rotated by -45 and $+45$ degrees with respect to the local meridian.

where T_d is a typical temperature $T_d = 19.6$.K, $\beta_d = 1.51 \pm 0.01$ for intensity and $\beta_d = 1.59 \pm 0.02$ for polarization determined by recent Planck observation (Planck Collaboration, Adam, R., et al., 2016).

These steep values have implications for the composition of dust grain suggesting mostly emission from silicate such as $MgO{\cdot}SiO_2$ at temperatures of about 10 K.

3.2.2 *Synchrotron emission*

Synchrotron emission arises mostly from the acceleration of cosmic ray electrons in magnetic fields present in our own Galaxy. At small scales Type Ib and Type II supernova remnants are the source of magnetic fields, whereas at larger scales the Galactic magnetic field is expected from the shearing effect of differential rotation of Milky Way. As one can notice in fig.3.7 (top), most of the high-latitude polarized emission is associated with distinct large-scale loops and spurs. Synchrotron emission arises from two types of sources: electrons trapped in the magnetic fields of discrete supernova remnants and diffuse emission from cosmic ray electrons spread throughout the Galaxy. In a supernova remnant the magnetic field is typically $\sim$ 75 μG, whilst the diffuse Galactic magnetic field is an order of magnitude fainter,$1 - 5$ μG.

The energy spectrum of cosmic ray electrons is expressed as a relativistic electron number density distribution $N(E) \sim E^{-p}$. Since $N(E)$ varies across the Galaxy, as well as the magnetic field, B, the resulting synchrotron emission can be characterized by a wide range of spectral behaviours, so that the observed morphology and spectral parameters of synchrotron sky maps will change substantially with frequency and with the line of sight.

Optically thin synchrotron emission is described by a power-law, whose spectral index, α, is related to the electron-energy distribution index, p, by $\alpha = -(p+3)/2$.

Discrete supernova remnants have a spectral index of $\alpha \sim -0.5$ (i.e. $p \sim 2$) in the few GHz radio range and contribute only $\sim$ 10% of the total synchrotron emission of the Galaxy at 1.5 GHz (Biermann, 1976), despite the enhanced magnetic field strength. More than 90% of the observed synchrotron emission arises from a diffuse component with a direction-dependent spectral index that generally lies in the range $-1.1 < \alpha < -0.5$ (that is $2.0 < p < 3.2$, Lisenfeld and Völk (2000)).

If synchrotron flux density scales as a power law also the equivalent brightness temperature follows a power-law with index β_s, namely:

$$T_b \propto \nu^{-\beta_s} \tag{3.5}$$

where $2.5 < \beta_s < 3.1$ and it still holds: $\beta_s = -(p+3)/2$.

Synchrotron emission is also accompanied by *self-absorption*, i. e. a photon emitted by synchrotron radiation of interacting with a charge and being absorbed by it. This happens where the synchrotron emission is optically

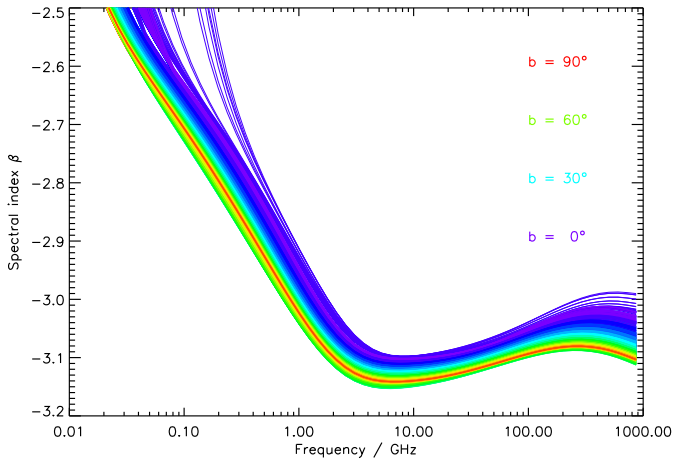

Figure 3.8: Local estimates of synchrotron spectral index for a sample of pixels, from Planck Collaboration, Ade, P. A. R., Aghanim, N., Alves, M. I. R., et al. (2016). The spectra are colour-coded by Galactic latitude: spectra at low latitudes show strong low-frequency curvature.

thick (especially at low frequencies), and does not depend on the value of p, and in the optically thick regime, it goes as $T \sim \nu^{5/2}$.

Synchrotron emission from a single charge results in an elliptically polarized wave. However, for any reasonable distribution of particle that varies smoothly with pitch angle (the angle between magnetic field and the velocity of the particle), the elliptical component will cancel out, as emission cones will contribute equally from both sides of the line of sight. Thus the radiation will be partially linearly polarized (Rybicki & Lightman, 1979). In the absence of non-uniform magnetic fields, the polarization fraction f_p is related to the spectral index p, or β_s as:

$$f = \frac{p+1}{p+\frac{7}{3}} = \frac{(3\beta_s+3)}{(3\beta_s+1)} \sim 0.7. \tag{3.6}$$

This value is almost never observed since non-uniform magnetic field directions along line of sight might generally reduce the degree of observed polarization to $< 20\%$.

Fig.3.7 (top) shows the synchrotron emission as observed by Planck at 30 GHz after component separation. In Planck Collaboration, Ade, P. A. R., Aghanim, N., Alves, M. I. R., et al. (2016), measurements of synchrotron spectral index on several patches and at different frequencies show a weak dependence on the frequencies $d\beta_s/d\ln\nu \approx -0.13$ at around 1 GHz (see fig.3.8), being roughly constant to $\beta_s \approx 3.1$ at higher frequencies. The synchrotron intensity is connected to the total magnetic field strength, while its polarization fraction gives information about the field structure on both global and local scales.

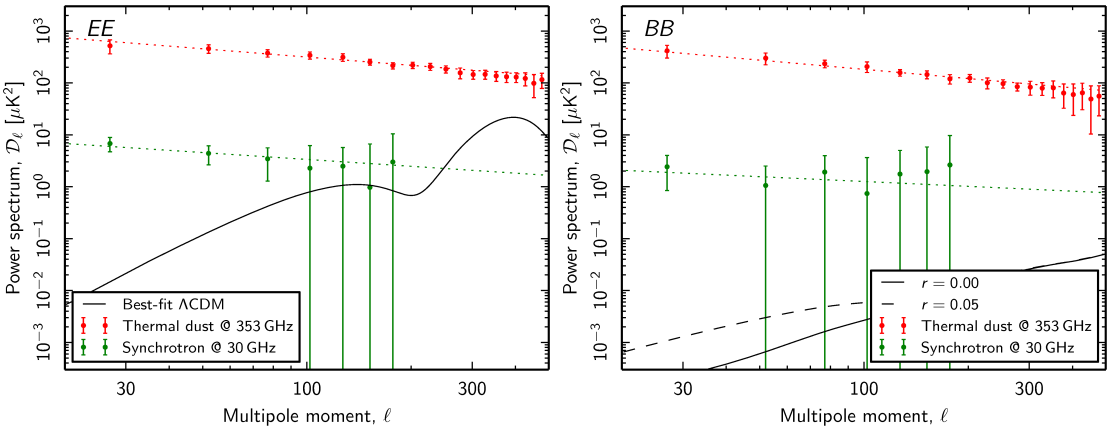

Figure 3.9: EE (left) and BB (right) power spectra for polarized synchrotron at 30 GHz and thermal dust emission (at 353 GHz),evaluated within a total effective sky fraction of 73% of the sky from Planck Collaboration, Adam, R., et al. (2016). The dashed lines show the best-fit power-law models to each case, and the solid black lines shows the best-fit ΛCDM power spectrum as fitted to temperature observation only (Planck Collaboration, Ade, Aghanim, Arnaud, Ashdown, et al., 2016). The dashed black line in the BB panel shows the spectrum for a model with a tensor-to-scalar ratio fof $r = 0.05$.

3.2.3 *Synchrotron and thermal dust angular power spectra*

As it has been shown in fig.3.3 the EE and BB power spectra of dust emission can be very well approximated by a power-law:

$$D_\ell = A \left(\frac{\ell}{80}\right)^{\alpha_\ell}.$$

Earlier, Page et al. (2007) found that even synchrotron power spectrum shows a similar dependency on ℓ.

In Planck Collaboration, Adam, R., et al. (2016), best fit values of the two parameters A and α_ℓ were obtained for both synchrotron and dust in a region including 73% of the sky; the power spectra are shown in fig.3.9 as dotted lines: for EE (left panel) $\alpha_\ell^{dust} = -0.53 \pm 0.02$ and $\alpha_\ell^{sync} = -0.44 \pm 0.07$, whereas for BB (right panel)$\alpha_\ell^{dust} = -0.59 \pm 0.02$ and $\alpha_\ell^{sync} = -0.31 \pm 0.13$. Though the synchrotron uncertainties are relatively larger, (because of the lower signal-to-noise ratio of the channel at 30 GHz compared to 353 GHz one) these models can be exploited to estimate the total foreground level as a function of both multipole moment and frequency.

Moreover, one of the most interesting results (Planck Collaboration, Ade, P. A. R., Aghanim, N., Arnaud, M., et al., 2016) is represented by the asymmetry between the B- and E-modes, with a power ratio of $BB/EE = 0.59 \pm 0.01$, indicating the presence of significant filamentary structures on intermediate angular scales. Similar findings regard the synchrotron emission, with an even stronger asymmetry of $BB/EE = 0.34 \pm 0.07$, implying that polarized synchrotron emission appears to be more aligned along filamen-

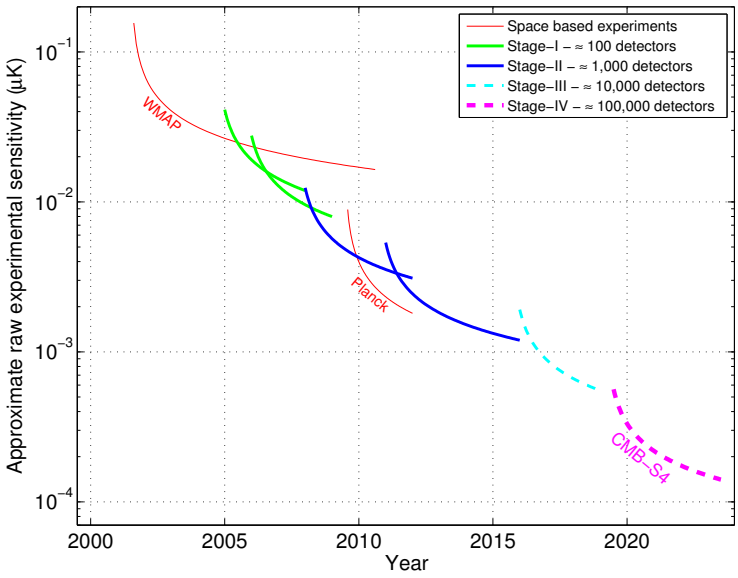

Figure 3.10: The evolution of sensitivity of CMB experiments, scaling with the total number of bolometers. Ground-based CMB experiments are classified into Stages. Courtesy of Julian Borril.

tary structures than thermal dust. Finally, it is remarkable to notice that the cross-spectra between the WMAP and Planck synchrotron data and the dust as observed by Planck 353 GHz have been measured (Choi & Page, 2015), showing, on scales of tens of degrees, a positive signal corresponding to 20%. This is expected, and will be further scrutinized in the future, because of the underlying Galactic magnetic field activating polarization for both dust and synchrotron.

3.3 THE FUTURE: FROM STAGE-2 TO STAGE-4

As shown in fig.3.10, in the last two decades the CMB measurements have increased sensitivity following a scaling given by *Moore's Law*, doubling every 2 years (Abazajian et al., 2016). Several requirements have to be fulfilled to maintain this scaling:

A. more focal plane pixels are needed to increase sensitivity;

B. multiple telescopes to field the hundreds of thousands of polarization detectors;

C. large fractions of the sky has to be observed to get ($\ell \sim 20$) and measure the B-mode recombination bump;

D. smaller angular scales are needed for de-lensing the inflationary B modes, to constrain the total mass of neutrinos Σm_ν, and investigate dark energy equation of state;

e. multi-band polarization measurements are required to distinguish the primordial polarized signals from the Galactic polarized foregrounds via component separation algorithms.

To take advantage of the best atmospheric conditions, the South Pole and the Chilean Atacama sites are baselined, with the possibility of adding a new northern site to increase sky coverage to the entire sky not contaminated by Galactic foregrounds.

As one can state from fig.3.10, the scaling shows a sequence made by transitions of several *stages*, each related to the sensitivity: e. g. WMAP sensitivity is comparable to ground based experiments encoding < 100 detectors and we can call them Stage-1 experiments. However, the number of detector employed, to date, by ground based experiments is $\sim 1,000 - 5,000$, i. e. representing the Stage-2 actual sensitivity achieved with CMB experiments. Furthermore, fig.3.10 shows expectations for upcoming Stage-3 experiments, characterized by order $10,000$ detectors and the projection for a Stage-4 (the so-called CMB S4, (Abazajian et al., 2016)) experiment with order 100,000 detectors: the ultimate step for a B-mode detection from ground based telescopes.

CMB-S4 science goals requires sensitivity of order 1 µKarcmin over roughly half of the sky and order of 500,000 CMB-sensitive detectors for a four-year survey (fig.3.10).

This is the context where we mostly contributed since the beginning of the work outlined in this PhD thesis: within the EBEX and Polarbear collaborations, we have been part of the team estimating the contribution of foregrounds in the second season of Polarbear data (Chapter4) and contributed to the design of the coming Polarbear II detectors (Stage-3) by forecasting and modelling the molecular rotational line emission (Chapter 6). Finally, we implemented and tested a package aimed at producing CMB intensity and polarization maps (containing a very large number of pixels,as required in the third item of the above CMB S4 list) with an affordable and computationally cheap methodology will be presented in Chapter 5.

Part II

DATA-ANALYSIS FOR CMB EXPERIMENTS

We present the research studies carried on during the PhD in the following chapters. First, we describe the Polarbear experiment, as it constitutes the framework where most of the work presented here was exploited, since May 2014. In the following, we will focus on specific aspects of the mentioned contribution, specifically map-making techniques, and foreground modeling.

4

THE POLARBEAR EXPERIMENT

> The personal observation and the direct examination increase the capability of recalling and distinguishing facts and of identifying objects. [...] There is a major advantage and incentive in collecting data than in simply reading books.
>
> Al Biruni, 1030

4.1 OVERVIEW OF THE EXPERIMENT

In this Chapter we will briefly describe the Polarbear experiment and the recent results reported in the collaboration paper, The POLARBEAR Collaboration et al. (2017) (sect.4.8.5). The experiment makes use of a millimeter-wave polarimeter to observe maps of the CMB temperature and polarization anisotropies. Observations began in January 2012. After having validated the instrument performances, scientific observations of the CMB started in June 2012. The telescope is located at the James Ax Observatory at an elevation of 5190 m in the Atacama Desert in Chile. This choice was due to the fact that median precipitable water vapour (PWV) is very low, about 1mm corresponding to a sky brightness in the observation band (150 GHz) of 12K at an elevation angle of 60° (Ade et al., 2014).

Polarbear aimed at characterizing the CMB B-mode polarization at large and small angular scales. Its geographical location allows to achieve more than half-sky coverage. Its first two seasons of data were targeted on small patches ($5° \times 5°$) to quickly achieve a very high sensitivity levels. This strategy was designed to characterize the gravitational lensing signal.

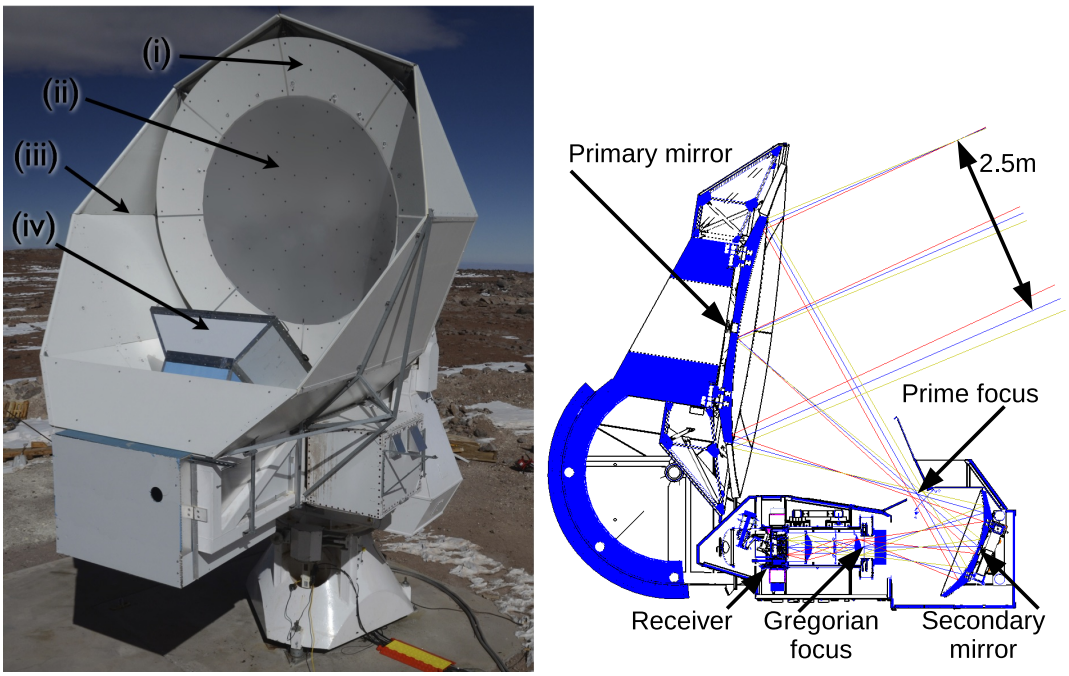

Figure 4.1: (a) Ray tracing scheme of the optics of the telescope cross-section. (b) The Huan Tran Telescope fully assembled at the James Ax observatory in Chile. (i) Primary guard ring. (ii) Monolithic precision primary mirror. (iii) Comoving shields (iv) Primary focus baffle. From (Kermish et al., 2012).

4.1.1 *The Huan Tran Telescope*

The Polarbear experiment is made by the Huan Tran Telescope (HTT) composed by two reflectors coupled to a cryogenic receiver. The HTT mirrors are in an off-axis Gregorian configuration satisfying the Mizuguchi-Dragone condition. This particular design provides a low cross-polarization and astigmatism over the diffraction limited field of view (Dragone, 1978; Mizugutch, Akagawa, & Yokoi, 1976) and it has two focuses: the prime focus and the Gregorian focus (as shown in fig.4.1)

The primary mirror is an off-axis paraboloid comprised of a central panel with 50 µm rms surface accuracy and eight lower precision outer panel segments. The aperture projected along boresight is an ellipse with a 3.5 m minor axis (2.5 m for the central panel). As it is shown in fig.4.1 (b), a 4K stop in the receiver creates a 2.5 m primary illumination pattern on only the central monolithic panel, giving a beam size of 3.5 FWHM. To avoid radiation coming from the ground and the telescope structure, an outer panel avoids the *spillover light* (i. e. radiation coming directly to the receivers) to be filled mainly by radiation coming from the sky. The combination of several baffles (shown in fig.4.1 (b)) and an additional absorptive shielding (1 m in radius) above the primary mirror, allow to reduce the side lobe contribution.

The telescope optics, cryogenics, receiver and electronics are installed on a mount that provides control of telescope pointing in azimuth and elevation.

PATCH	R.A	DECL.	EFFECTIVE AREA
RA4.5	$4^h40^m12^s$	$-45°$	$7.0\,\mathrm{deg}^2$
RA12	$11^h53^m0^s$	$-0.5°$	$8.7\,\mathrm{deg}^2$
RA23	$23^h1^m48^s$	$-32°\,48'$	$8.8\,\mathrm{deg}^2$

Table 4.1: The three Polarbear patches.

4.1.2 *The receiver and the focal plane*

In order to achieve the required instrumental sensitivity, the Polarbear focal plane is cooled down to 250 mK so that thermal carrier noise in the detectors is smaller than the photon noise (set by the quantum fluctuations in the photon arrival rate). This cryogenic cooling is achieved by a closed-cycle refrigeration.

The cryogenic receiver is shown in fig.4.2(a) and hosts a cold half-wave plate (HWP), re-imaging optics, aperture stop, and a focal plane of 637 dual-polarization pixels (i. e. 1274 detectors) with a 2.4° diameter field of view.

The detector array is composed of 7 individual wafers, each of which is a hexagon 80 mm across (Arnold et al., 2012). Once radiation gets into a wafer pixel, it is then coupled from free space to a superconducting Niobium micro-strip wave guide by means of a dual-polarization antenna and a contacting dielectric lenslet (fig.4.2). The design band is centred at 148 GHz with 26% fractional integrated bandwidth. The spectral bandpass of each detector in a pixel is determined by three-pole micro-strip filters, the power transmitted through each filter is deposited on a superconducting transition-edge sensor (TES) bolometer. Each TES bolometer is biased with an AC voltage to keep it at the superconducting temperature, so that when the optical power changes on a transition bolometer, it creates a compensating change in electrical current, measured using frequency-domain multiplexed superconducting quantum interference device (SQUID) ammeters.

4.1.3 *The scanning strategy*

Polarbear observed three CMB fields (summarized in table 4.1) during the first and second season, each one visible for 6 to 8 hours per day. The location of the patches is shown in fig. 4.3 overplotted with a map at 857 GHz from Planck (Planck HFI Core Team et al., 2011) to emphasize the Galactic dust contribution, and their choice was motivated to minimize foreground contribution, by their overall daily visibility and to overlap with other surveys, (RA23 and RA12 observations have been cross-correlated with *Herschel*-Atlas ones, see subsect. 4.8.2). Polarbear observes each patch continuously for up to eight hours while the patch is above the minimum observing elevation (40°) and rises to a maximum elevation angle of 80°. To optimize

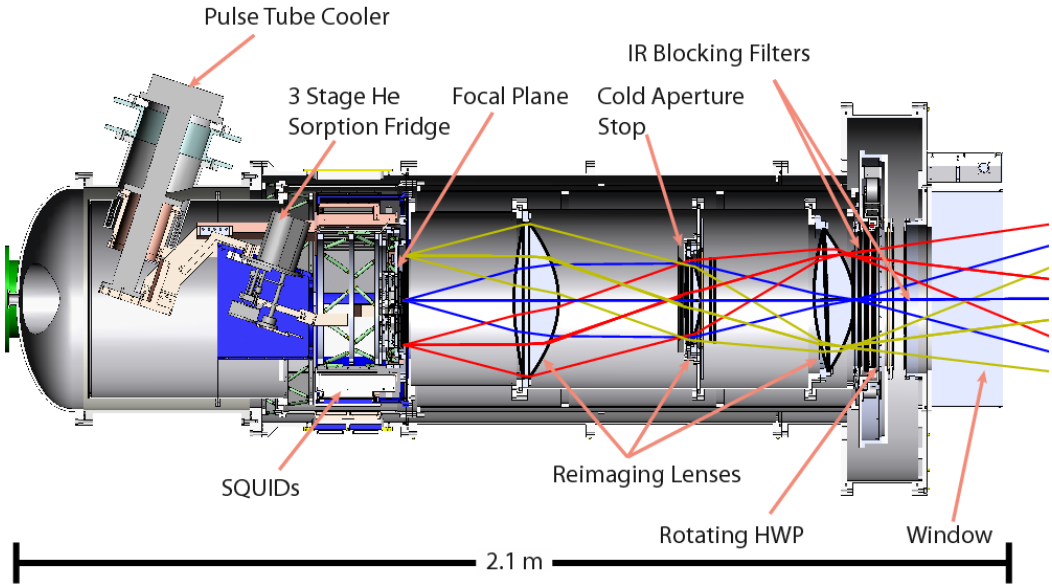

(a)

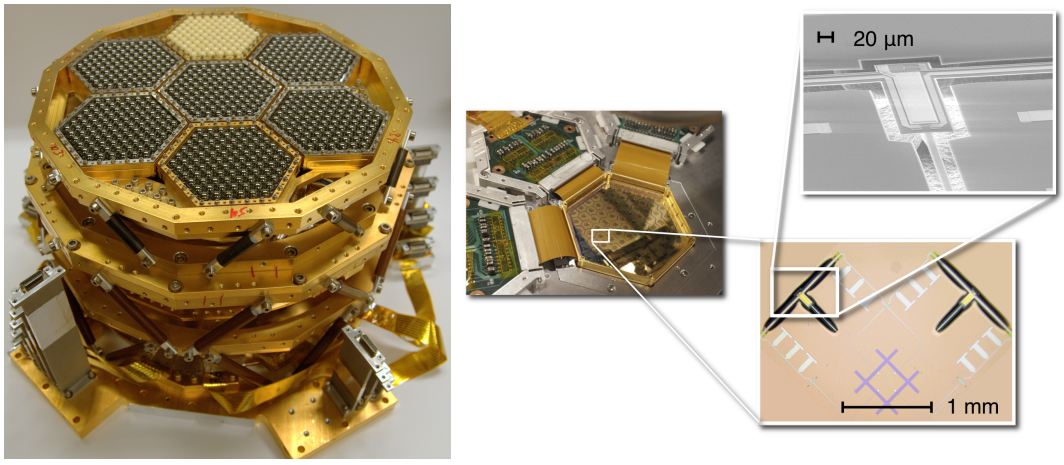

(b)

Figure 4.2: (a) Cross-section of Polarbear receiver. (b) The Polarbear focal plane showing the support structure and the mK wiring. The center panel shows the back of a wafer with the lenslet ends, visible around of the hexagonal support; the right inset shows an orthogonal pair of antennas, the microstrips (the microstrip filters are also visible) and the two bolometers. The top-right panel zooms on the thermally isolated island of the bolometer. From (Kermish et al., 2012).

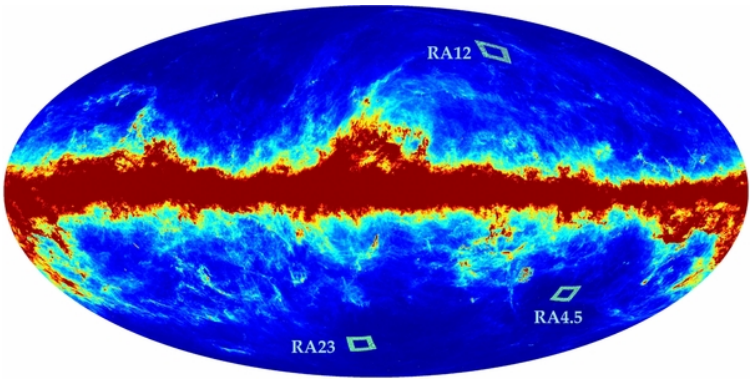

Figure 4.3: Polarbear observation patches

sensitivity and ensure a linear response, the detectors are re-biased every hour. Between two re-bias the detector gain is estimated (see sect.4.2).

The observations are divided into constant elevation scans (CESs) during which the telescope scans back and forth $\sim 3°$ in azimuth at a speed of $0.7°s^{-1}$ and at constant elevation (hereafter, we commonly refer to each azimuthal sweep as a *subscan*). After approximately 15 minutes, when the patch has moved out of the field of view, the telescope moves the elevation and azimuth toward the new coordinates of the patch. Each CES is made of about 200 constant-velocity subscans, and about 36% of a CES sample is discarded to avoid having data acquired while the telescope accelerates, i. e. at the "telescope turning points" between two consecutive subscans. Another important feature is that observations with constant elevation allows scan-synchronous systematics, as the ground pick-up which has to be removed from the maps, by means of filtering operations (see the next sect. 4.3).

Observations included astrophysical sources sources as well, to be used as *on-sky* calibrators. Tau A, radio source in the Crab Nebula, was used to calibrate the polarization angle of the detectors as described in sect. 4.2. Jupiter and Saturn were also observed in the patches and they were used for characterizing the angular beam of the experiment and the detector gain.

4.1.4 *Instrument performances*

The expected sensitivity of an experiment is commonly referred in terms of Noise Equivalent Temperatures (NETs) of the detectors, obtained by considering the nominal design value and the atmospheric loading in the Atacama; they are commonly measured in terms of $\mu K\sqrt{s}$. By means the total observation efficiency and the detector yield (i. e. the average number of detectors for which a good calibration has been achieved), it is then possible to get an estimate of the map depth. Assuming 70% of detector yield, 18% of observation efficiency, $f_{sky} = 1.6\%$ from the three patches, we expect to have $480\,\mu K\sqrt{s}$, corresponding to $6.3\,\mu K$ arcmin and $8.9\,\mu K$ arcmin respectively for temperature and polarization map depths. The measurements averaged across the first season of observations will be discussed in

sect.4.8.3 and the measured sensitivity was slightly worse than the expected value 550μK $\sqrt{s}$. However, after two season of data (see sect.4.8.5) the resulting polarization white-noise levels achieved encompassed the expectations: 7, 6 and 5 μK arcmin respectively for RA4.5, RA12,RA23 .

4.2 CALIBRATION

Before processing the data for map-making and power spectrum estimation, four quantities of the instrument have to be very well characterized: the pointing, the detector gain, the polarization angle and the effective beam of the instrument, since the combined effect of all of them could result into a significant contamination if not taken into account.

POINTING. To estimate maps, we need to know where each detector was pointing as a function of time. We determine the pointing model by means of extended and point-like millimeter sources selected from known source catalogues to span in a wide range in azimuth and elevation occurring several times per week during the observations. The source positions, obtained by the best-fit of the pointing model, are recovered with an accuracy of $27 \div 30''$.

GAIN. The time ordered data (TOD) recorded by each bolometer are detected as an electrical flowing in the detector. However, to convert the measured current into CMB temperature units, a characterization of the responsivity of the detector, or the gain, is required. An array of astrophysical and ground-based calibrators are used to measure the gain; they can be defined as *relative* and *absolute* calibrators. The latter is determined by means of the CMB C_ℓ^{TT} power spectrum, whereas for the former a combination of the internal thermal source and Saturn observations have been used. The relative calibration can be summarized in three steps: the first step involves observations of a chopped thermal source (at 700 °C, known as the *stimulator*) visible through a small hole in the secondary mirror and the the observed flux from Saturn. Then, the polarized emission of the stimulator further rotated by HWP has to be corrected by means of an angle-dependent template by considering observations of several astrophysical sources at different HWP angles. Finally, the stimulator and Saturn observations are combined to calculate the relative gain for each detector. This is a remarkable process since a miscalibration of relative gain can result in systematic leakage of CMB temperature to polarization.

BEAM. Dedicated observations of Jupiter and Saturn were used to estimate the beam map and its effective window function B_ℓ. The main lobes of the beam, are well approximated by a Gaussian core having $3'.5 \pm 0'.1$ FWHM plus a diffraction tail asymptotically decaying as $1/\theta^3$ where θ is the radial coordinate of the beam profile. By comparing the B_ℓ power derived from the best fit profile model and the one from the

Jupiter maps we get less than 1.5% differences in all the considered ℓ range. The median beam ellipticity measured across the array is 5% and the median difference in the ellipticity measured for two channels in the focal plane pixel is 1.6%. The relative beam ellipticity and orientation of the ellipses mainly contribute to the Intensity-to-Polarization leakage which has to be taken under control.

POLARIZATION ANGLE. The relative detector polarization angles is determined by observing Tau A for roughly 30 minutes every day. Each detector TOD is then fitted to a reference Tau A map provided by Institute of Radio Astronomy in the Millimeter range (IRAM) 30 m telescope (Aumont et al., 2010) convolved with the Polarbear Jupiter-based beam and pointing information. The estimated individual-pixel angular uncertainty in each wafer is 1.2°. This uncertainty level can produce relevant E- to B-modes leakage. To further improve the accuracy in the global instrument polarization angle, it is possible to calibrate it by nulling the C_ℓ^{EB} cross spectrum (Keating, Shimon, & Yadav, 2013), expected to be exactly zero within the cosmic variance from parity constraints: so that a measured non-zero EB spectrum can be produced by a miscalibration of the polarization angle. The model for the measured EB power described in (Keating et al., 2013) simplifies to $C_\ell^{EB} \simeq \pm 2\Delta\psi(C_\ell^{EE} - C_\ell^{BB})$, where $\pm$ depends on the convention adopted for the polarization angle. $\Delta\psi$ is best fitted by the measured EB spectrum and its value can be used to remove the leaked EE power from BB spectrum, to be equal to $4\Delta\psi^2 C_\ell^{EE}$.

4.3 FROM TIME-ORDERED DATA TO MAPS

4.3.1 *Low-level data processing*

We describe the process of huge data compression which is performed by CMB data-analysis allowing to go from the timestream data ($10^{10} \div 10^{11}$) to maps (10^4) and consecutively from maps to angular power spectra. Given a range of angular scales involved in the analysis defined by the width of the patch and the beam resolution, it is possible to convert it into a range of frequencies of the time domain data by means of the telescope scan speed (ω measured in rad/s). So that, a multipole order ℓ_f is related to a frequency f via $\ell_f \sim 2\pi f/\omega$. For Polarbear scanning at $0.7°s^{-1}$ speed, the science band frequencies is $\sim 1 - 4$ Hz, corresponding to $500 < \ell < 2100$. Since the sampling frequency of Polarbear data is 190 Hz (to which a multipole scale $\ell \sim 10^4$, well beyond the science band, corresponds) the data need to be firstly downsampled by a factor of six lower frequency to 31.8 Hz.

The stimulator phase is very useful because it allows to measure both the detector gain and the time constant for each single stimulator scan, where the source is switched-on and a chopper modulates the radiation coming to the focal plane as a square wave. The time scan length can be ideally decom-

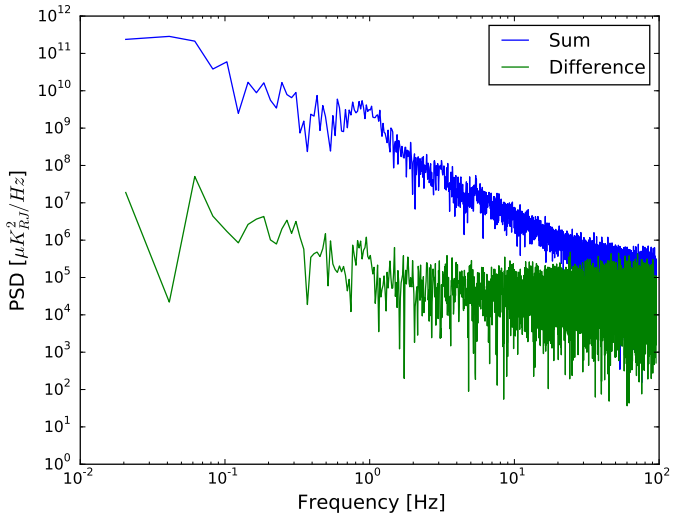

Figure 4.4: Power Spectral Density of summing and differencing the signal acquired by a detector pairs during 1 CES.

posed into several chunks where the chopping frequency ω_c is constant. For each of these chunks, the detector gain g_{ω_c} is fitted as a modulated electromagnetic wave:

$$d(t) = A\cos(\omega_c t) + B\sin(\omega_c t) \approx g_{\omega_c} e^{i\omega_c t}, \tag{4.1}$$

where in (4.1) the phase information is assumed to be null. g_{ω_c} is then fitted as $g_{\omega_c} = \sqrt{|A|^2 + |B|^2}$. Since a bolometer records a modulation of the incoming power P as an RC circuit we get a differential equation for the detector transfer function of the circuit T:

$$C\frac{dT(t)}{dt} = -GT(t) + P(t),$$

where C is the heat capacity of the bolometer and G its thermal conductivity.

In the Fourier domain, we can compute the transfer function of the circuit:

$$\tilde{\tau}(\omega) = \frac{\tilde{P}(\omega)/G}{1 + i\omega\tau} \equiv \frac{g_\omega}{1 + i\omega\tau}, \tag{4.2}$$

where the last equality holds if we assume that the incoming power recorded by the bolometer follows eq.(4.1). Since the Polarbear detectors are not able to measure the phase information, it is only possible to measure the absolute value of the quantity in eq.(4.2), and can fit for the time constants as a function of frequency and the gain. The bolometer optical responses, (expected to be between $1 - 3$ ms) are comparable to the sample rate and small enough that a further deconvolution of these transfer functions is not necessary (Arnold et al., 2012).

Timestreams are noise weighted with a filter which projects three types of low signal-to-noise ratio modes. The first filter involves high-frequencies

which low-pass filters the timestreams to eliminate aliasing of higher frequencies into our science band, since the multipole ℓ corresponding to the Nyquist frequency[1] is well beyond ($\ell = 7950$). The time stream is low-pass filtered at 6 Hz, i. e. $\ell = 3150$.

In the case of ground-based experiments, a correlated $1/f$ power spectrum is expected for the noise:

$$n(f) = \sigma_{det}^2 \left[1 + \left(\frac{f}{f_{knee}}\right)^{\alpha}\right],$$

with f_{knee} of the order of few Hz and σ_{det} is the white noise contribution. The responsible to the $1/f$ power are mainly atmospheric conditions (stability of PWV, wind speed, etc.) or bias effects of the bolometers which may spatially correlate the signal on several detectors. To remove this excess noise at low-frequency (see solid blue line in fig.4.4), a polynomial base is subtracted to the signal of each detector during each CES subscan. Further details about it are reported in the next chapter (sect. 5.7).

Finally, as described in sect4.1.3, the Polarbear scanning strategy is designed to concentrate scan-synchronous signals, as a far sidelobe scanning the ground, into a small number of modes to be easily filtered. Even this contribution has to be removed from the timestream and the methodology, cmmonly referred as *ground filtering* will be described in sect.5.7.

4.3.2 *The two Polarbear map-making pipelines*

Once the relative gain calibration g for a pair of detector is available, one can compute the intensity and polarization timestream by considering the fact that in a focal plane pixel, two timestreams are measured by the orthogonal antennas, the *top* $d_{top}(t)$ and the *bottom* $d_{bot}(t)$ timestreams modelled as:

$$\begin{aligned} d_{top}(t) &= g_{top}\left[I(\hat{n}(t)) + Q(\hat{n}(t)\cos(2\phi(t)) + U(\hat{n}(t)\sin(2\phi(t))\right] \\ d_{bot}(t) &= g_{bot}\left[I(\hat{n}(t)) - Q(\hat{n}(t)\cos(2\phi(t)) - U(\hat{n}(t)\sin(2\phi(t))\right]. \end{aligned}$$

To minimize the filtering operations at the timestream level, we can combine both the TODs such that:

$$d^{+} = \frac{d_{top} + d_{bot}}{2} \tag{4.3}$$

$$d^{-} = \frac{d_{top} - d_{bot}}{2}. \tag{4.4}$$

In fig. 4.4 the power spectral density of both d^{+} and d^{-} samples is shown. Notice in particular that the excess at low frequencies due to $1/f$ noise is minimized by the subtraction of the orthogonal detectors in a pair, since the polarized emission from the major contaminant the atmosphere is very small. This combination allows to disentangle the Stokes intensity signal I,

1 It Is the frequency defined as half of the sampling rate, in our case ~ 95 Hz.

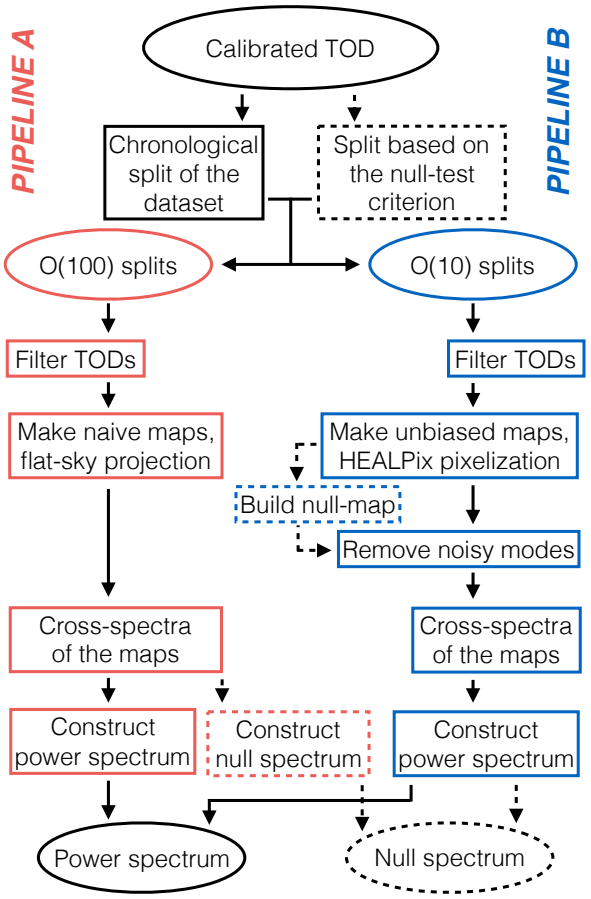

Figure 4.5: Flowchart of Polarbear pipelines from The POLARBEAR Collaboration et al. (2017). The main steps starting from the calibrated TOD and leading to the production of angular cross-spectra are shown with solid boxes and arrows. In addition, extra steps related to the production of null cross-spectra used to assess the quality of the dataset are shown with dashed boxes and arrows.

from the Q, U, in fact we can write two separate data models for polarization and intensity stokes parameters:

$$d_t^+ = A_{tp} I_p + n_t^+ \tag{4.5}$$

$$d_t^- = A_{tp}(\cos(2\phi_t) Q_p + \sin(2\phi_t) U_p) + n_t^-, \tag{4.6}$$

where A_{tp} is called *pointing matrix* and it projects the TOD data sampled at time t to the pixel p in the map, ϕ_t is the polarization angle and n_t^{+-} is the term encoding the noise of a detector pair.

The process of estimating the maps from the time streams (4.5) and (4.6) is called map-making and Polarbear collaboration adopted two independent and algorithmically different pipelines A and B to analyse the data of the first two seasons. The main difference between the two are sketched in the flowchart in fig.4.5. Pipeline A corrects for the filtering process at the power spectrum level resulting in a *biased* map estimator because the filter reduces the power of the signal we want to estimate (Chiang et al., 2010), whereas pipeline B estimates maps by compensating the effect of filtering

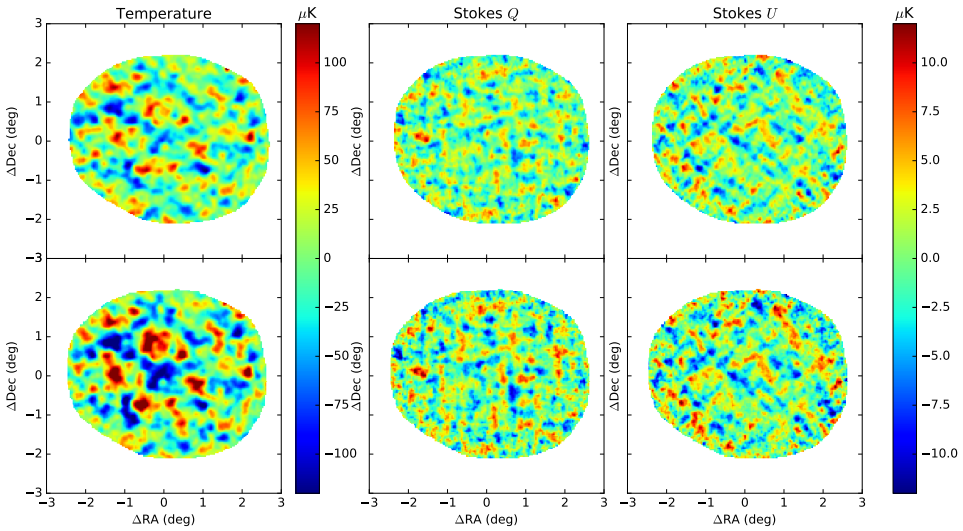

Figure 4.6: Polarbear CMB intensity and polarization sky maps of RA23 in equatorial coordinates from The POLARBEAR Collaboration et al. (2017). The left, center and right panels show temperature anisotropy, Q and U Stokes parameters respectively. The top maps are generated by pipeline A, while the bottom maps are generated by pipeline B. Both sets of he maps are smoothed with a Gaussian filter with 3.5′ FWHM.

and restores the power subtracted out from the signal, so that in this case the estimator is *unbiased* (Tegmark, 1997b). This makes the pipeline B more computationally challenging because it involves an explicit factorization of a dense matrix whose size is given by the number of pixels in the map 5×10^4. Poletti et al. (2016) show that due to the sizes involved, the problem is still affordable by current computing systems if massively parallel routines are conceived and data are distributed across processors.

The two pipelines use a different pixelization scheme. The former projects the time-domain data onto flat sky maps using a cylindrical equal-area projection, with pixels of width 2′. The latter projects the TOD onto curved-sky maps using the Hierarchical Equal Area Latitude Pixelization (`HEALPix`)[2] (`nside=2048`, i. e. pixel width ∼ 1′.7, Górski et al. (2005)). Given the relatively small fraction of sky observed (few degrees across for each Polarbear patch) and the beam of the telescope, the two approaches are equivalent. The maps from both pipelines are shown in fig. 4.6, despite the structures observed are clearly in agreement between the two sets of maps, as expected, the amplitude of the signal is different due to the fact that the two pipelines treat the amplitudes of the modes in the maps differently. However, having two pipelines is very useful since it helps in spotting some unconsidered systematics and makes more robust the results independently obtained.

2 http://healpix.sourceforge.net

We developed and applied to the Polarbear dataset an alternative pipeline for the unbiased estimator which estimates iteratively the maps without involving the direct inversion of the matrix (see Chapter 5).

4.4 POWER SPECTRA ESTIMATION

The power spectra estimation starts to be problematic when one has to deal with small patch observations. First of all, the spherical harmonic are not anymore an orthonormal basis in a partial sky. Secondly different harmonic coefficients are correlated because of the convolution of the sky power and the harmonic representation of the observed patch. According to the MASTER method (Hivon et al., 2002) the observed or *pseudo* power spectra are related to the true ones via

$$\tilde{C}_\ell = \sum_{\ell'} M_{\ell\ell'} F_{\ell'} B_\ell^2 C_{\ell'} + N_\ell, \tag{4.7}$$

where $M_{\ell\ell'}$ is the *mode-mixing matrix* and defines how masking effects correlate with the modes at different angular scales. F_ℓ is known as the *filter transfer function* and represents how the effects of the time domain filtering propagates at the power spectrum level. In the biased formalism it acts as a *debiasing* term correcting for the filter at the power spectrum estimation. B_ℓ is the beam window function and it is related to the Gaussian beamwidth ($\theta_b = FWHM/2\sqrt{2\ln 2}$) as $B_\ell \propto \exp\left(-\theta_b^2 \ell(\ell+1)/2\right)$, N_ℓ is the noise power spectrum.

The transfer filter function F_ℓ is estimated via MC simulations, whose input is a set of $1'$-resolution Gaussian realizations of a $10° \times 10°$ CMB patch. By exploiting the pointing data from observations one gets the TOD from simulated maps, filter them and estimate pseudo-power spectrum. The filter transfer function is then estimated iteratively:

$$F_\ell^n = F_\ell^{n-1} + \frac{\tilde{C}_\ell - \sum_{\ell'} M_{\ell\ell'} F_{\ell'}^{n-1} C_{\ell'} B_\ell^2}{C_\ell B_\ell^2},$$

with $F_\ell^0 = 1$ and convergence is achieved within around 10 iterations. Though being efficient, this methodology introduces an additional dependence of the estimated power spectrum on the cosmological model used for the simulations of F_ℓ which ideally should be avoided.

Furthermore, when polarization power spectra are involved in a small patch the situation worsens: in fact the decomposition into E and B modes is not unique anymore (Bunn, Zaldarriaga, Tegmark, & de Oliveira-Costa, 2003; Lewis, Challinor, & Turok, 2001) and the pseudo-spectrum estimator as the one in eq.(4.7) introduces *E-to-B leakage*, so that B pseudo spectra contains spurious power coming from E-modes and as a results the B-mode variance increases. Smith and Zaldarriaga (2007) found a way to minimize this effect via the so-called *pure*-pseudo power spectrum estimator. In the following we will show results of X^{2}PURE package which relies on the implementation of the pure estimator (Grain, Tristram, & Stompor, 2009). X^{2}PURE

optimizes the apodization of the sky mask, adopts a proper analytical correction to the mode mixing matrix in order to minimize the E-to-B leakage and the variance due to noise. In both the Polarbear pipelines the power spectrum estimators are based on the pure -pseudo C_ℓ technique despite they differ in a few aspects. X^2PURE approach has been used by the Polarbear unbiased pipeline and it has the further positive aspect that it does not need to compute the filter transfer function.

4.5 DATA VALIDATION AND SYSTEMATICS

The total observation time for the two seasons and the three CMB patches is 4700 hours, corresponding to 33% of the total calendar time available. 60% of this time, 2800 out 4700 hours, pass all the three steps of data quality checks. The first requirement is to have a successful measurement of the detector gains for each CES. Second, data based on bad weather conditions, incomplete observations, hardware glitches, a certain angle between the patch and the Sun or the Moon, are discarded. The third step goes further and consists in defining the subscans, and among them identifying the bad ones as listed in the intermediate step.

Several systematics effects have been considered to investigate instrumental effects:

1. uncertainty in the instrument polarization angle and in relative pixel polarization angles,
2. uncertainty in instrument boresight pointing model,
3. differential pointing between the two detectors in a pixel,
4. the drift of the gains between two consecutive thermal source calibrator measurements,
5. relative gain calibration uncertainty between the two detectors in a pixel,
6. crosstalk in the multiplexed read out,
7. differential beam size and differential beam ellipticity.

All of these effects were analyzed using signal-only simulations to highlight the effect of the specific uncertainty on C_ℓ^{BB} and they are shown in fig. 4.8(a).

We considered $12° \times 12°$ maps $3''$ resolution pixels by generating several realizations of the theoretical unlensed ΛCDM spectra convolved with the symmetric Polarbear beam window function, B_ℓ. The realizations contain all the CMB power spectra but the BB ones. Maps are therefore scanned with the actual Polarbear scanning strategy and the instrumental effect to be considered is injected into the simulated samples of data directly: the I, Q, U are the outputs of the simulations and the power spectra of these

maps are then estimated using the X^2PURE method. As a result of this framework, any non-zero C_ℓ^{EB} or C_ℓ^{BB} power is spurious and a measurement of the instrumental systematic effect.

We adopted this approach to estimate the systematics of deconvolving the time stream by the time constant of the detector, which is neglected since the bolometer optical responses are comparable to the sample rate. We scanned with the Polarbear scanning strategy a CMB map with only E-modes and check whether deconvolving the time stream by the detector time constant may produce some effect into the B-modes power spectrum . As it is shown in fig.4.7, it is reasonable to neglect this systematic effect, if

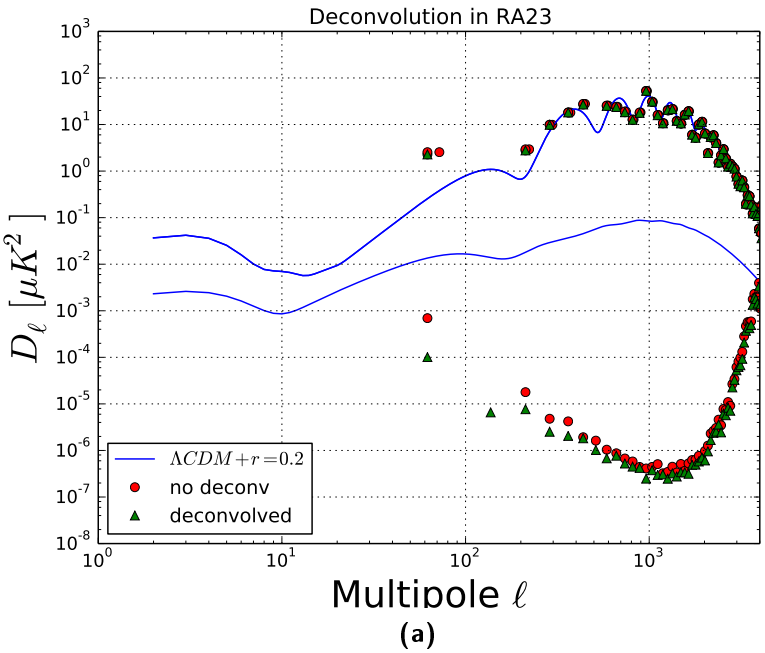

Figure 4.7: (a) E and B Power spectra computed from simulated timestream (not) deconvolved by the time constant of the detector with green triangles (red circles). Notice that the simulation maps scanned to compute the timestreams does not contain any B-modes. As a reference, we overplot the E-modes from ΛCDM and $r = 0.2$ B-modes.

compared to the lensing B-mode power.

The PolarBear collaboration has adopted a blind approach to data analysis. That means that the main observables are not inspected until the data pass quality tests defined beforehand. Therefore, before unblinding the data a suite of null tests is performed to evaluate the calibration, data-selection criteria, and some unknown systematic errors. Several splits of data have been chosen in order to be sensitive to various sources of systematics contamination or miscalibration. The null estimator is at the power spectrum level and is defined by the *binned null* power spectrum $\hat{C}_b^{null}$. For each null power spectrum bin b we calculate the statistics $\chi_{null}(b) = \hat{C}_b^{null}/\sigma_b$, with σ_b given by a MC-based estimation of the corresponding standard deviation, and $\chi^2_{null}(b)$. Whereas $\chi_{null}(b)$ is sensitive to systematic contam-

ination in the null spectra, $\chi^2_{null}(b)$ is more sensitive to the outlier bins. The Probability-To-Exceed (PTE) distribution is then computed from of the χ^2_{null} by bin, spectrum and null-test. Each of these sets of PTEs is required to be consistent with a uniform distribution by means of a Kolmogorov-Smirnov test, requiring a p-value (i. e. probability of observing deviation from uniformity larger than that which is observed igven the hypothsesis of uniformity) to be greater or equal than 5%. For both the first and the second season of Polarbear data, these distributions are consistent with a uniform distribution from zero to one.

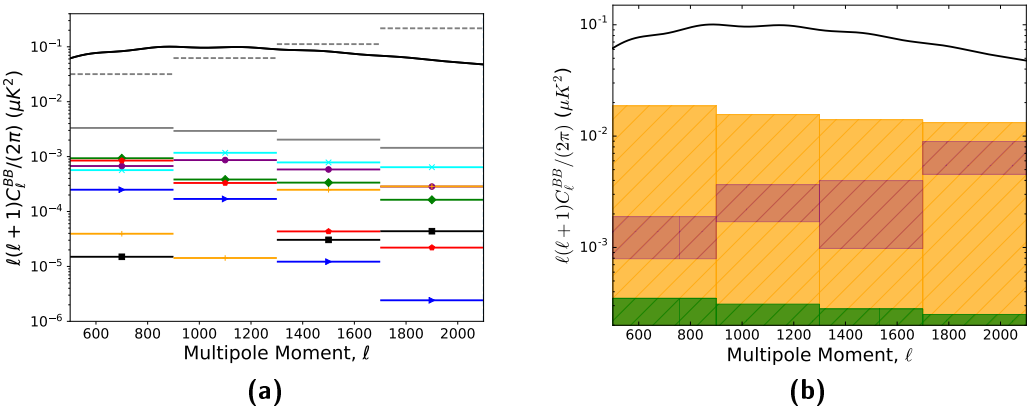

Figure 4.8: (a) Estimated levels or upper bounds on instrumental systematic uncertainties, from The POLARBEAR Collaboration et al. (2017), in the four bins of the C_ℓ^{BB} power spectra, as described in sect. 4.2. Individual effects (solid colors) and their combination (solid horizontal grey line) are displayed: combined uncertainty in instrument polarization angle and relative pixel polarization angles after self-calibration (purple circle), combined uncertainty in instrument boresight pointing model and differential pointing between the two detectors in a pixel (cyan cross), the drift of the gains between two consecutive thermal source calibrator measurements (red star), relative gain-calibration uncertainty between the two detectors in a pixel (green diamond), crosstalk in the multiplexed readout (blue arrow), differential beam shape (orange plus), and differential beam ellipticity (black square). For comparison we display the binned statistical uncertainty the theoretical Planck ΛCDM lensing B-mode spectrum (solid black line). (b) Estimated foreground contributions to D_ℓ^{BB} at 68.3% confidence intervals in the multipole range $500 \leqslant \ell \leqslant 2100$ from The POLARBEAR Collaboration et al. (2017): the upper limits on polarized Galactic foregrounds, synchrotron (green shaded area) and thermal dust (orange shaded area), and the combined radio and dusty power (purple box). As it can be seen, the foreground contributions are small, although not completely negligible.For comparison, a theoretical Planck ΛCDM spectrum (solid black line) is shown.

4.6 POLARIZATION MODULATION AND THE HALF-WAVE PLATE

The presence of low-frequency $1/f$ noise degrades the sensitivity of large aperture experiments and impedes to accurately measure degree-scale B-modes.

Polarization modulation using a Continuously Rotating Half-Wave Plate (CRHWP) is a well-known technique to reduce the impact of both $1/f$ noise and instrumental systematic errors. The CRHWP at the entrance of the Polarbear receiver (exactly at the Gregorian focus,see fig.4.2(b)) is a 3.1mm thick single crystal disk of A-plane sapphire. The presence of CRHWP thus mitigates the instrumental systematic effects: because of the birefringent properties of this crystal and by rotating the polarization angle to which the detectors are sensitive, it is possible to measure the modulated polarization signal in a frequency band, where the detector sensitivity is dominated by white noise (that is limited by the photon noise). Additionally, the CRHWP enables a detector, sensitive to a single linear polarization state, to measure both Q and U Stokes parameters. It also eases requirements on the levels of instrumental and cross-polarization and allow such systematic errors to be better characterized and corrected later in the data analysis step.

During part of the first season, the HWP did not rotate continuously but it wad stepped everyday by an angle of 11.25 degrees. However, for the third Polarbear season of data, it was instead installed a CRHWP at the prime focus and its performances have been described by Takakura et al. (2017). We show that observations using a CRHWP show a mitigation of $1/f$ noise and have smaller systematics uncertainties than methods that take the difference between orthogonal detectors, eq. (4.6). Therefore, the CRHWP has the potential to be one of the essential tools for the next-generation CMB-S4 experiments.

4.7 FOREGROUND ESTIMATES

Though Galactic foregrounds are expected to be sub-dominant with respect to the lensing B-modes at arcminute scales, we assess limits on their contribution to Polarbear observations.

For assessing the thermal dust contamination we put the publicly available Planck sky map at 353 GHz as a tracer of polarized emission from thermal dust. To avoid noise bias in the computation of spectra, we calculate cross-spectra using half-mission jacknife splits using the X^2PURE power spectrum estimator. The statistical errors have been evaluated by means of white noise MC simulations, using the pixel-pixel noise covariance matrices of the input maps. Unfortunately, the small sizes of Polarbear patches and the Planck noise level at the small angular scales at high Galactic latitudes prevented to estimate B-mode spectra directly in the regions considered. Therefore, in order to provide an upper limit on the amplitude of thermal dust, we compute power spectra on larger circular regions, within a 10° radius, centred on the observed patches.

FOREGROUNDS	Expected power in $D_\ell^{BB}(10^{-4}\,\mu K)$			
	$\ell = 500$–900	900–1300	1300–1700	1700–2100
Galactic dust	63.5 ± 123.3	53.6 ± 102.4	48.8 ± 91.4	46.9 ± 85.1
Galactic synchrotron	1.4 ± 2.1	1.2 ± 1.9	1.1 ± 1.7	1.0 ± 1.5

Table 4.2: Expected foreground power in D_ℓ^{BB} from The POLARBEAR Collaboration et al. (2017). The total central value (uncertainty) on the final line is the linear (quadrature) sum of the individual foreground powers.Note that reported values for Galactic dust and synchrotron are upper limits and we have no detection of dust contamination nor of synchrotron contamination in our observed fields.

We extrapolated the measured amplitude of the spectra at $\ell \simeq 80$ (a multipole bin between 60 and 99) in these regions to higher multipoles by applying the power law scaling $D_\ell \propto \ell^{\alpha_d}$, as defined in 3.2.3. We then scale the Planck measurements to the Polarbear frequency assuming a modified blackbody spectral dependence for the thermal dust as in eq.(3.4), assuming for T_d, β_d and their parameter uncertainties the ones obtained by Planck Collaboration, Adam, R., et al. (2016) and described in sec.3.2.1.

For the extrapolation in frequency we take into account both the Planck and the Polarbear frequency band passes, and for the extrapolation in ℓ we consider the actual Polarbear band power window function. To account for the fact that we are measuring the foreground amplitude on larger regions, we include in the error budget the Gaussian approximation of the signal sample variance evaluated for the actual sky area of the Polarbear patches.

A similar procedure has been used to estimate the amplitude of polarized synchrotron emission. We computed power spectra for synchrotron B-modes by cross-correlating the Planck Low Frequency Instrument 30 GHz map at the effective frequency of 28.4 GHz (Planck Collaboration, Adam, Ade, Aghanim, Akrami, et al., 2016) with the WMAP -K map at a frequency of 22.8 GHz (Hinshaw et al., 2013). Spectra are computed on the same circular regions of 10° radius. The measured amplitude at $\ell \simeq 80$ is rescaled in frequency considering a power-law frequency dependence with $\beta_s = -3.12 \pm 0.02$ (Fuskeland, Wehus, Eriksen, & Næss, 2014) and in multipole considering $D_\ell \propto \ell^{\alpha_s}$ with $\alpha_s = -0.31 \pm 0.13$ (Planck Collaboration, Adam, R., et al., 2016). Synchrotron and Dust extrapolated uncertainties are shown in fig.4.8(b) and the value are reported in table4.2.

4.8 RESULTS FROM THE FIRST AND SECOND SEASONS OF DATA

With the data collected during the first season (2012-2013), four papers were published. Recently, the publication including second season observations,

conducted from 2013 to 2014, came out. Here, we will briefly describe the main findings of all of the Polarbear publications so far.

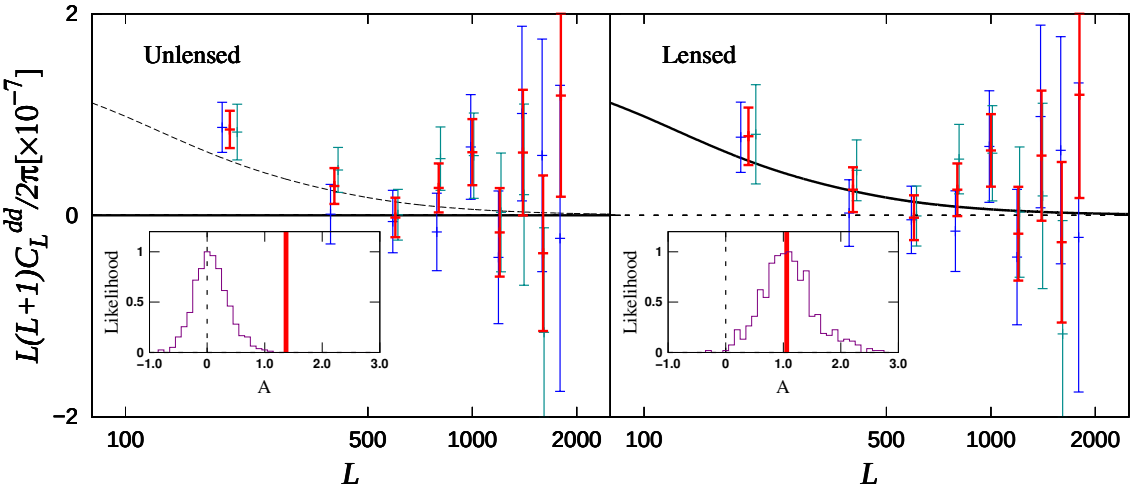

Figure 4.9: Polarization lensing power spectra co-added from Polarbear patches and two estimators are shown in red from Ade et al. (2014). The lensing signal predicted by the ΛCDM model is shown as the dashed black curve in the left panel and the solid black curve in the right panel, respectively. The lensing power spectrum estimated with $\langle EEEB \rangle$ is in blue and the one estimated with $\langle EBEB \rangle$ in dark green. *Left:* A 4.2σ rejection of the null hypothesis of no lensing indicating a lensing amplitude $A = 1.37 \pm 0.30 \pm 0.13$ where the errors are statistical and systematic respectively (normalized to the fiducial ΛCDM value). Right: The same data, assuming the existence of gravitational lensing to calculate error bars, including cosmic variance. In this case, the lensing amplitude is measured as $A = 1.06 \pm 0.47^{+0.35}_{-0.31}$, corresponding to 54% uncertainty on the C_L^{dd} power spectrum. The histograms of the amplitudes A from 500 unlensed and lensed simulations are shown in the inset boxes.

4.8.1 *Measurement of the CMB Polarization Lensing Power Spectrum with the POLARBEAR experiment*

Ade et al. (2014) reported the first direct evidence for polarization lensing based on CMB observations, by means of the four-point correlations estimator (see eq.(2.44)) of even- and odd-parity E- and B-mode polarization mapped over $\sim 30\,\mathrm{deg}^2$ of the sky patches of Polarbear experiment. These data were analyzed using the Polarbear blind analysis framework and checked for spurious systematic contamination using null tests and simulations. As shown in fig.4.9, polarization lensing and lensing B-modes have been found at a 4.2σ significance.

4.8.2 *Evidence for Gravitational Lensing of the CMB Polarization from Cross-Correlation with the CIB*

Ade et al. (2014a) reconstructed the gravitational lensing signal from CMB polarization from Polarbear experiment and cross-correlate it with CIB maps from the Herschel satellite (Eales et al., 2010). This choice is justified by the fact that high correlation between the CMB lensing and CIB fields was found, with a maximal correlation coefficient of ~ 80% observed at a CIB wavelength of approximately ~ 500µm (Holder et al., 2013).

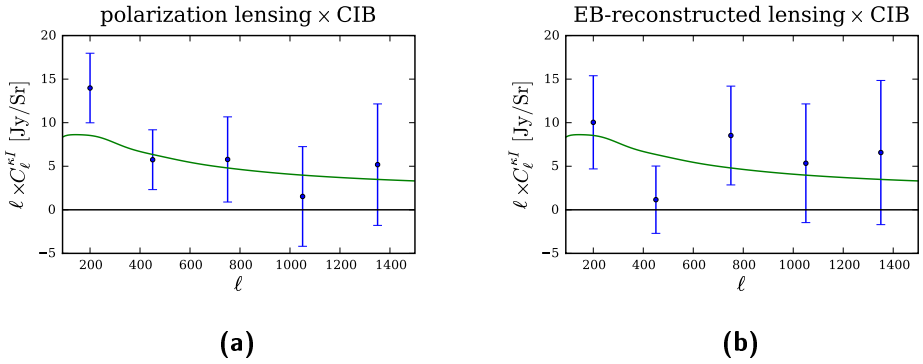

Figure 4.10: Cross-power spectra of CMB polarization lensing and the 500µm Herschel CIB flux. (a) the minimum variance combination of all polarization lensing measurements cross-correlated with the Herschel maps. (b) the cross power of EB reconstructed lensing with the Herschel maps; constructed from the EB estimator.

Given the definition of the estimators EE and EB as in eq.(2.44), they calculated a noisy map of the lensing *convergence* field (defined as $\kappa = -\nabla d/2$) which is then cross-correlated with the Herschel CIB maps. The multipole scale considered in the polarization maps ranged from 500 to 2700 to be sure that the noise is effectively white and systematics from beam and foregrounds are sub-dominant. The predicted cross-power spectrum (solid green in fig.4.10) estimator is given by:

$$C_\ell^{\kappa I} = \int \frac{dz H(z)}{\eta^2(z)} W^\kappa(z) W^I(z) P(k = \ell/\eta(z), z),$$

where $P(k, z)$ is the matter power spectrum, $W^I(z)$ is proportional to the redshift origin of the CIB signal dI/dz and W^κ is the CMB lensing kernel. The cross powers of polarization lensing and the CIB Herschel maps have been measured on the two Polarbear patches (RA12 and RA23), with lensing derived from both the EB and EE estimators. From the co-added combination of all four polarized lensing-cross powers (two estimators on two maps), shown in the left panel of fig. 4.10, they get a minimum variance combination for gravitational lensing in CMB polarization found at a statistical significance of 4.0σ. The two cross-power spectra involving the EB estimator have been similarly co-added to calculate a cross-power corresponding

to a measurement of B-mode polarization. The right panel of fig. 4.10 shows the evidence for the presence of a lensing B-mode signal at a significance of 2.3σ. This work on polarization lensing, via the robust cross-correlation channel, not only reinforced Polarbear auto-correlation measurements, but also represented one of the early steps towards establishing CMB polarization lensing as a new powerful observable to probe structure formation and cosmological expansion in cosmology.

4.8.3 *A Measurement of the CMB B-Mode Polarization Power Spectrum at Sub-Degree Scales with Polarbear*

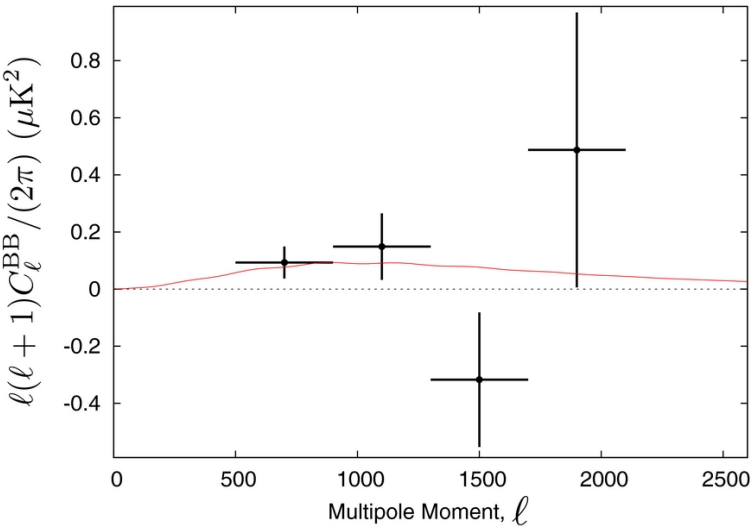

Figure 4.11: Binned C_ℓ^{BB} spectrum measured using Polarbear data from all the three patches (~ 25 deg^2) from Ade et al. (2014b). A theoretical ΛCDM from WMAP 9 years of data C_ℓ^{BB} spectrum with $A_L = 1$ is shown in solid black. The uncertainty shown for the band powers is the diagonal of the band power covariance matrix, including beam covariance.

Ade et al. (2014b) reported one of the first measurements of B-mode polarization power spectrum from the first season (2012-2013) of Polarbear data. The measurement covers the angular multipole range $500 < \ell < 2100$ and is based on observations onto the three patches listed in table 4.1. Including both systematic and statistical uncertainties (whose estimation is described in sect.4.2) the hypothesis of no B-mode polarization power from gravitational lensing is rejected at 97.2% confidence. The band powers are consistent with the standard cosmological model (see fig. 4.11) and, by fitting a single lensing amplitude parameter, A_L to the measured band powers, they got $A_L = 1.12 \pm 0.61(\mathrm{stat})^{+0.04}_{-0.12}(\mathrm{sys}) \pm 0.07(\mathrm{multi})$, where $A_L = 1$ is the fiducial WMAP-9 ΛCDM value. In this expression, "stat" refers to the statistical uncertainty, "sys" to the systematic uncertainty and astrophysical foregrounds, and "multi" to the calibration uncertainties that have a multiplicative effect on the measured amplitude A_L. This represents the first

measurement of lensing B-mode power fully obtained from CMB polarization maps.

4.8.4 *Polarbear constraints on cosmic birefringence and primordial magnetic fields*

In addition to probing inflation and the large scale matter distribution, precision measurements of the CMB B-modes represent competitive new tests for testing a variety of exotic physics: e. g. B-modes can be used to constrain Primordial Magnetic Fields (PMFs) and parity-violating physics. Magnetic fields exists in all gravitationally bound structures in the Universe, and to explain the micro-Gauss fields observed in galaxies, PMF seeds are required over a scale of a few Mpc, (the usual parameter is B_{1Mpc}). In Ade et al. (2015) we focus on both, because both lead to *birefringence*, i.e., a rotation of polarization converting E-modes into B-modes. B-modes generated by parity-violating processes can be compared to those generated by a PMF via the Faraday rotation, so that the strength of the parity-violating interaction can be quantified by an equivalent primordial magnetic field level.

Anisotropic cosmic birefringence adds a phase factor $e^{\pm 2i\alpha(\hat{n})}$ to the underlying CMB polarization representing the *anisotropic rotation field*, so that the observed Stokes parameters transform as

$$(Q \pm iU) = (\tilde{Q} \pm i\tilde{U})(\hat{n})e^{\pm 2i\alpha(\hat{n})},$$

where we labelled by the tilde, $\sim$, quantities expected from theory. Taylor expanding the CMB polarization, decomposed into E- and B-modes to first order in α, reveals that the off-diagonal elements of the two-point correlation function are proportional to the rotation field. A quadratic estimator can be thus defined as:

$$\alpha_{EB}(\mathbf{L}) = A_{EB}(L)\int \frac{d^2l}{(2\pi)^2} E(\mathbf{l})B(\mathbf{l}')\frac{2\tilde{C}_l^{EE}\cos 2\phi_{l'l}}{C_l^{EE}C_l^{BB}},$$

where as usual $\mathbf{L}, \mathbf{l}, \mathbf{l}'$ are coordinates in Fourier space with $\mathbf{L} = \mathbf{l} + \mathbf{l}'$, $\phi_{l'l}$ is the angular separation between $\mathbf{l}'$ and $\mathbf{l}$, C_ℓ^{EE} and C_ℓ^{BB} are the observed power spectra including experimental noise and A_{EB} is a normalization factor ensuring the estimator of the rotation power spectrum to be unbiased (Yadav, Biswas, Su, & Zaldarriaga, 2009). The rotation power spectrum is derived from a four-point correlation of E and B via

$$\langle \alpha^*_{EB}(\mathbf{L})\alpha_{EB}(\mathbf{L}')\rangle \simeq (2\pi)^2\delta(\mathbf{L}-\mathbf{L}')(C_L^{\alpha\alpha} + N^{(0)}_{EB}(L) + \text{higher-order terms}), \quad (4.8)$$

with $N^{(0)}$ being the Gaussian contribution to the four-point function.

In fig. 4.12 we show the anisotropic cosmic birefringence power spectrum reconstructed using the quadratic estimator from data in the three Polarbear patches, as well as the co-added spectrum. The measurement is consistent with zero and we do not detect any anisotropic rotation signal.

This non-detection translates into a 95% confidence level upper limit of $B_{1Mpc} < 93$ nG on the amplitude of an equivalent primordial magnetic field

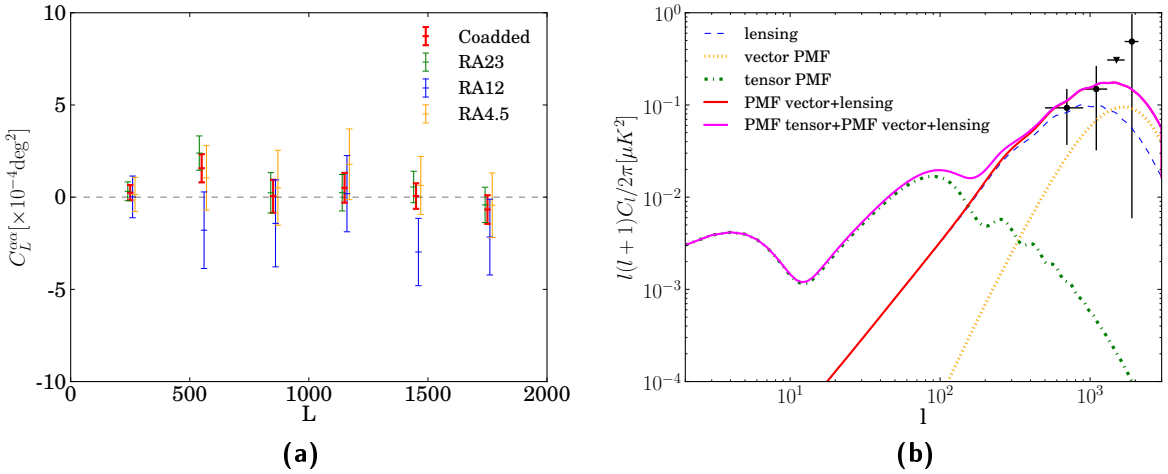

Figure 4.12: (a) The anisotropic cosmic rotation power spectra from Polarbear first-season data in three patches. The spectrum of an individual patch is indicated by the green (RA23), blue (RA12) and orange (RA4.5) colors. The coadded (red) power spectrum is consistent with zero. (b) B-mode polarization power spectrum sourced by a scale-invariant PMF.The passive tensor mode (green), the compensated vector mode (orange), the gravitational lensing contribution (blue) and the combinations of the lensing and vector B modes (red) and all the three components (magenta) are shown. The PMF contribution is based on $B_{1\mathrm{Mpc}} = 2.5$ nG. The data points are from Ade et al. (2014b).

inclusive of systematic uncertainties. This four-point correlation constraint on Faraday rotation is about 15 times tighter than the upper limit of 1380 nG inferred by Planck Collaboration, Ade, Aghanim, Arnaud, Arroja, et al. (2016a).

As shown in fig. 4.12 there are two potentially observable frequency independent contributions to B-mode spectrum sourced by the stress-energy from a nearly scale-invariant PMF. A *passive* tensor mode generated by PMF before neutrino decoupling is practically indistinguishable from the inflationary tensorial B-modes (see the dot-dashed green line in fig. 4.12). The second contribution comes from vector modes, as shown by the dotted orange line in fig. 4.12 and peaks around $\ell \sim 1700$, with power proportional to $B^4_{1\mathrm{Mpc}}$. Using the POLARBEAR measurements of the B-mode power spectrum (Ade et al., 2014b), we set at a 95% confidence level the upper limit of $B_{1\mathrm{Mpc}} < 3.9$ nG.

4.8.5 *A measurement of the CMB B-mode polarization power spectrum at sub-degree scales from 2 years of Polarbear data*

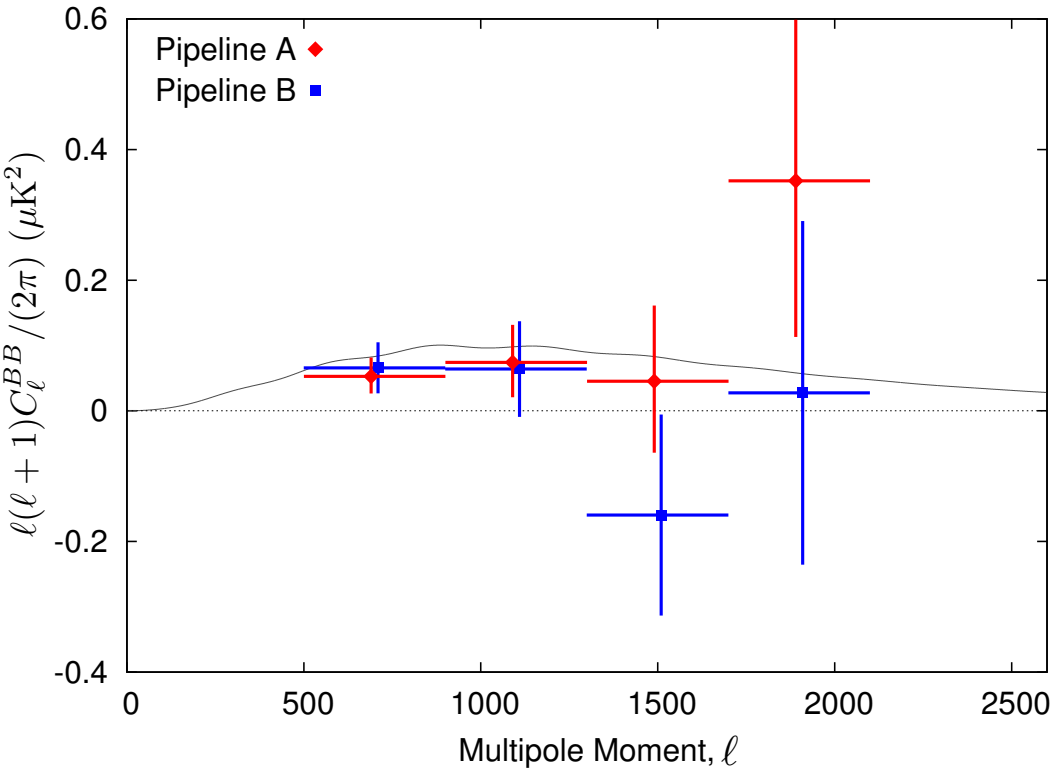

Figure 4.13: Polarbear B-mode angular power spectrum from the two-season datasets , from The POLARBEAR Collaboration et al. (2017). Red diamonds (blue squares) show the measured band powers from pipeline A (B) described in sect.4.3. The plotted error bars correspond to the 68.3% confidence intervals of the statistical uncertainty only. The black curve is a theoretical Planck 2015 ΛCDM lensing B-mode spectrum shown for comparison.

Finally, by exploiting the same data analysis pipeline described in the previous sections of this chapter, in The POLARBEAR Collaboration et al. (2017) we report an improved measurement of the CMB B-mode polarization power spectrum by adding new data collected during the second season of observations (2013-2014) to the re-analyzed data from the first season (2012-2013) in the range of angular multipoles $500 \leqslant \ell \leqslant 2100$. The null hypothesis of *no B-mode polarization* is rejected at a confidence of 3.1σ including both statistical and systematic uncertainties. We test the consistency of the measured B-modes with the ΛCDM framework by fitting for a single lensing amplitude parameter A_L relative to the Planck best-fit model prediction. We obtain $A_L = 0.60^{+0.26}_{0.24}(\text{stat})^{+0.00}_{0.04}(\text{inst}) \pm 0.14(\text{foreground}) \pm 0.04(\text{multi})$, where $A_L = 1$ is the fiducial ΛCDM value, with uncertainties estimated as described in previous sections (4.5, 4.7). Lensing extraction, as well as cross-correlation studies, similar to those published from the analysis of the first year of data, are in progress.

4.9 THE FUTURE DEPLOYMENTS: THE SIMONS ARRAY AND SIMONS OBSERVATORY

The first two Polarbear seasons concentrated on characterizing the lensing of B-modes and have been very well exploited for a wide variety of other cosmological quantities of interests to date. In May 2014 the third campaign of Polarbear observations started focusing mostly on a larger patch whose effective area is 700deg^2 with a sensitivity of $15\,\mu\text{K}\,\text{arcmin}$. This region corresponds to the one observed by BICEP2 experiment and it is observable for about 14 hours from Chile locations. Finally, as anticipated in sect.4.6 the CRHWP is operating at 2 Hz allowing to reduce the $1/f$ noise and does not worsen the beam systematics. The third season wide patch observations of Polarbear acts as a *pathfinder* to reach larger and larger angular scales to better constrain the primordial B-modes.

In order to achieve this goal the road map for Polarbear experiment provides not only an expansion of the focal plane increasing the number of detectors (Polarbear-2 phase, Inoue et al. (2016)) but also a deployment of 2 further HTT-like telescopes at James Ax observatory, constituting an *array* of three telescopes, which will be called the *Simons Array* (SA, Arnold et al. (2014); Stebor et al. (2016); Suzuki et al. (2016)). Moreover, in spring 2016 the Polarbear and ACT collaborations will merge into the Simons Observatory[3], whose perspective is an intermediate step (an array of multi-telescope CMB experiments in the Atacama desert) toward the CMB-S4 (see sect.3.3).

The Polarbear-2 receiver is mounted on the focal plane of a telescope with same design as the HTT. The Polarbear-2 focal plane contains 7 modules (shown in fig.4.14) each module having 271 dual linear polarized pixels simultaneously able to detect CMB radiation at 95 and 150 GHz bands each of them sensitive to the two orthogonal polarization states independently

3 simonsobservatory.org

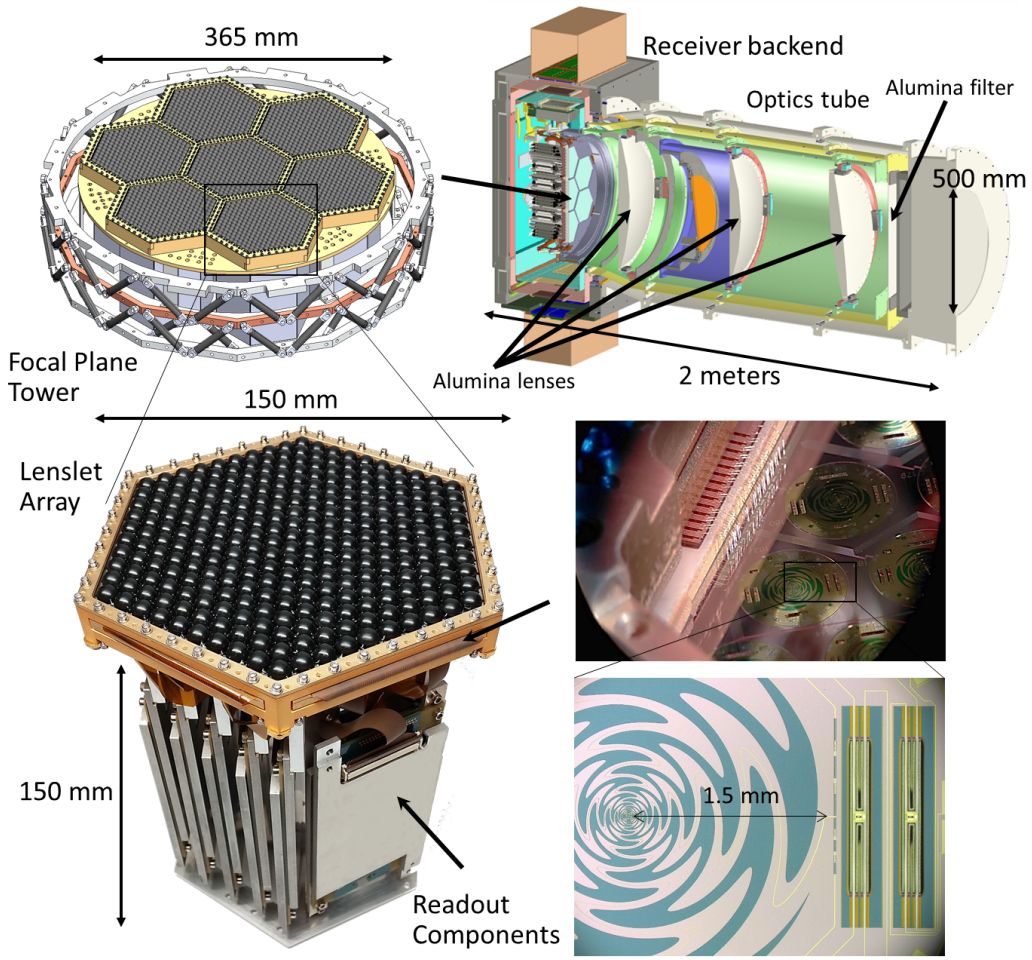

Figure 4.14: The Polarbear-2 receiver in CAD drawing (upper right) and a CAD drawing of the focal plane tower (upper left) from Suzuki et al. (2016). Photograph of a detector module (bottom left), which consists of a detector wafer, lenslet wafer and cryogenic readout electronics. The Sinusoidal circular structure is a broadband antenna. Large rectangular structures are TES bolometers (bottom right).

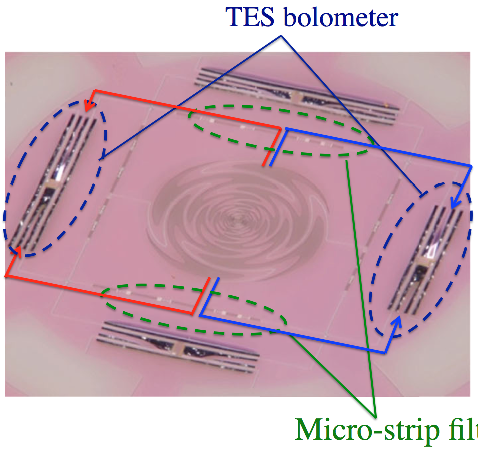

Figure 4.15: The sinuous antenna sensitive to 95 and 150 GHz band from Stebor et al. (2016). The microstrip filter separates the signal between 150 and 95 GHz. The separated signals are then detected by TES bolometers.

(2 TES bolometers), accounting for 1897 pixels and 7588 bolometers (4 per each pixel). This result can be achieved by slightly expanding the sizes of the focal plane thanks to the so called sinuous antenna technology enabling to couple a broad range of frequencies to the microstrip lines. The two frequencies can then be selected by microstrip filters (fig. 4.15) and redirected to different frequency bolometers. The target NET of each detector is $360\,\mu K\sqrt{s}$. Total array NET of each frequency is $5.8\mu K\,\sqrt{s}$ for both the frequency channels. The beam size slightly changes for the 95 GHz channel to be $5.2'$. The receiver is already deployed and ready to be installed into the HTT telescope by the fall of 2017.

The Simons Array will consist of three cryogenic receivers each featuring multifrequency bolometer arrays mounted onto separate 3.5m telescopes. The twin HTT have been assembled in the summer of 2016 at the site and, at the time of writing , one of them is ready to host the receiver (fig.4.16 (top)).

Two of the three HTT receivers will be identical to Polarbear-2, whereas the third receiver will cover 220 and 270 GHz bands. The receivers are expected to be deployed in 2018. In total SA will account for $\sim 20,000$ detectors, 7588, 7588,3794 and 3794 respectively for 95, 150, 220 and 270 GHz. The expected sensitivity of the Simons Array in its final configuration is $360\,\mu K\sqrt{s}$ in the 95 GHz band, $360\,\mu K\sqrt{s}$ in the 150 GHz band, $979\,\mu K\sqrt{s}$ in the 220 GHz band and $1095\,\mu K\sqrt{s}$ in the 270 GHz band. The combination of high sensitivity, multi-frequency coverage and large sky area will allow SA to produce high quality polarization CMB maps. The Simons Array will be able to constrain r to uncertainties $\sigma(r) = 4 \times 10^{-3}$ when considering statistical noise alone, and $\sigma(r) = 6 \times 1o^{-3}$ at $r = 0.1$ when foregrounds are cleaned as depicted in bottom panel of fig.4.16. It will further constrain the sum of neutrino masses to 40 meV (at 1σ) when combined with galaxy surveys.

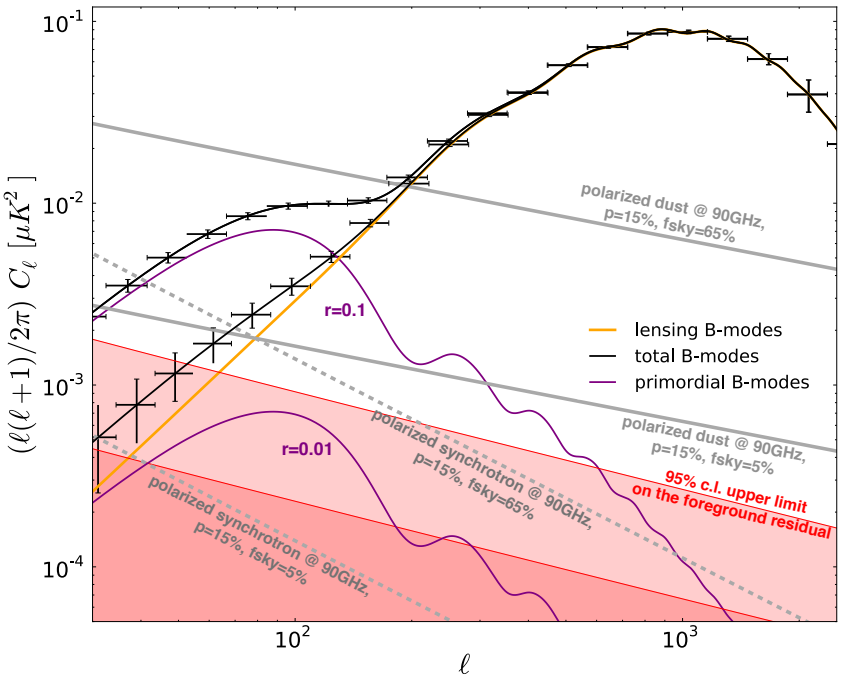

Figure 4.16: (top) A photograph of SA at James Ax taken in March, 2017. (bottom) Forecasts from Errard et al. (2016) given the expected sensitivity of SA. In grey power spectrum of (solid) thermal dust (dashed) synchrotron observed with different fraction of sky. The red shaded area represents the residuals of foregrounds (at 2σ confidence level) after the foreground cleaning procedure.

5

ITERATIVE SOLVERS FOR CMB MAP-MAKING

> In science, answers are not just as important as questions. [...] The recent developments of science offer an interesting lesson in how to put questions.
>
> Fred Hoyle

As discussed in the previous chapter, (sect. 4.3) Polarbear exploited two different approaches in the map-making process. In this framework, we focused on the so called unbiased estimators of CMB map-making, i. e. the estimator adopted by the Polarbear pipeline B. The methodology of this pipeline has been described by Poletti et al. (2016) and it is based in an explicit factorisation and inversion of a matrix (Borrill, 1999; Stompor et al., 2002; Tegmark, 1997a). Therefore, the only limitation is the computational complexity of matrix inversion, i. e. $\mathcal{O}(N_p^3)$, with N_p being the number of pixels in the map. As small regions of the sky ($f_{sky} \approx 0.1\%$) are concerned, this approach is extremely successful to yield unbiased maps within reasonable computational times by distributing data among several processing elements and exploiting scalable high performance routines as in Poletti et al. (2016).

However, the future ground experiments (CMB-S4 and SO) are expected to observe larger and larger patches, involving larger N_p, to reach deep measurements of larger angular scales with arcminute resolution beams.

An alternative to the explicit inversion approach is represented by iterative methods (Doré, Teyssier, Bouchet, Vibert, & Prunet, 2001; Oh, Spergel, & Hinshaw, 1999; Wright, 1996). They involve algorithms within the class of the *Krylov* methods (Golub & Van Loan, 1996) and they are aimed at iteratively solving the map-making equation, whose only computational complexity is due to large matrix-vector products. As we will describe in

sect.5.2, they bypass the matrix inversion issue and they do not even need to store the whole system matrix in the memory.

To date, many CMB iterative solvers are based on the *Conjugate Gradient* (CG) method: in this chapter we apply a methodology recently proposed by Szydlarski, Grigori, and Stompor (2014) to reconstruct the maps from both simulated and realistic Polarbear datasets. This work has been part of the research project of the Master in High Performance Computing program we attained in December 2016.

5.1 THE MAP-MAKING PROBLEM

In sect.4.3 we quickly described the two different pipelines adopted by Polarbear, without adding further details about the biased and unbiased estimators. We address them in more detail here.

The input data of map-making procedure is the calibrated TODs collected in one time-domain vector d of size N_t encoding all measurements performed during a certain lapse of time by all the detectors of a CMB experiment. As one may expect the measurement can be easily modelled as the sum of an astrophysical signal s_t plus the instrumental noise of the detector itself n_t. Furthermore, a certain pixel of the sky will have been observed as many times as the telescope pointing direction intercepts that pixel. These informations are fully encoded into the pointing matrix A_{tp} (a sparse and tall $N_t \times N_p$ matrix). The data model can be written as:

$$d_t = s_t + n_t = A_{tp} s_p + n_t, \tag{5.1}$$

with s_p being the map, represented as a vector in the pixel domain. The structure of the pointing matrix can be quite complex since it involves the scanning strategy of a CMB experiment and it can be block-sparse or sparse depending whether the detectors are sensitive or not to the polarization. In the former case, the data model can be generalized as the combination of the three *Stokes parameters* I_p, Q_p, U_p in the p-th pixel observed at time t:

$$d_t = I_{p_t} + Q_{p_t} \cos(2\phi_t) + U_{p_t} \sin(2\phi_t) + n_t, \tag{5.2}$$

with ϕ_t being the angle of the detector projected onto the sky coordinates at time t. Therefore, the pointing matrix has three non zero entries per row and s_p becomes an array encoding three maps related to the three Stokes parameter mqps,$s_p = (I_p, Q_p, U_p)$. Notice that the two models in (4.5) and (4.6) can be easily seen as particular cases of (5.2). We can write (5.2) in a compact way as

$$d = As + n, \tag{5.3}$$

where we further assume the noise vector to be *white*, i. e. a Gaussian vector, $\langle n \rangle = 0$ and defined by the noise covariance matrix N.

The Generalized Least Squares (GLS) solution to the general data model in (5.3) yields to an *unbiased* estimator (Tegmark, 1997b) for any choice

of a positive definite matrix M. The GLS solution can be derived from a minimization problem of a quadratic form $\mathcal{Q}(s) = (As - d)^\dagger M(As - d)$, i. e.

$$\frac{\partial \mathcal{Q}}{\partial s} = 0 \Leftrightarrow A^\dagger M(As - d) = 0,$$

from which we can define the unbiased estimator as

$$\hat{s} = (A^\dagger MA)^{-1} A^\dagger Md. \tag{5.4}$$

It is straightforward to understand why this estimator in (5.4) is unbiased, since $\langle d \rangle = As$ and the noise is white:

$$\langle \hat{s} \rangle = (A^\dagger MA)^{-1} A^\dagger M \langle d \rangle = s.$$

The covariance of this estimator can be written as:

$$\begin{aligned} \Sigma =& \langle (\hat{s} - s)(\hat{s} - s)^\dagger \rangle = (A^\dagger MA)^{-1} (A^\dagger M \langle nn^\dagger \rangle MA)(A^\dagger MA)^{-1} \\ =& (A^\dagger MA)^{-1} (A^\dagger M \mathcal{N} MA)(A^\dagger MA)^{-1}. \end{aligned} \tag{5.5}$$

Since we assumed above the noise to be Gaussian distributed, the likelihood function takes the form:

$$\begin{aligned} -2 \ln \mathcal{L}(s) \equiv& n^\dagger \mathcal{N}^{-1} n \\ =& (As - d)^\dagger \mathcal{N}^{-1} (As - d) + \text{const}. \end{aligned}$$

With a little of algebra and by changing the value of the constant we can express the likelihood as:

$$\begin{aligned} & -2 \ln \mathcal{L}(s) = \\ &= \left(((A^\dagger \mathcal{N}^{-1} A)^{-1} A^\dagger \mathcal{N}^{-1} d - s) \right)^\dagger A^\dagger \mathcal{N}^{-1} A \left(((A^\dagger \mathcal{N}^{-1} A)^{-1} A^\dagger \mathcal{N}^{-1} d - s) \right) + \text{const}. \end{aligned}$$

The likelihood gets a minimum when

$$\hat{s} = (A^\dagger \mathcal{N}^{-1} A)^{-1} A^\dagger \mathcal{N}^{-1} d,$$

so that our estimator (5.4) is also *minimum variance* if $M = \mathcal{N}^{-1}$ and Σ further simplifies to

$$\Sigma = (A^\dagger \mathcal{N}^{-1} A)^{-1}.$$

As discussed in sec.4.3, usually the raw TODs need to be filtered in order to remove from them some unwanted signal which is not astrophysical as the ground pickup, the atmosphere or detector correlation typically arising at low frequencies and present a very large variance component (see fig.4.4). Such signals in the time-domain are usually discarded and filtered out.

Although the template of the unwanted signal, T, is well known and can be modelled, the amplitude y at each time is unknown: what a filtering

operation usually does, is setting to zero the amplitude of the timestream component parallel to T, i. e.

$$d' = (\mathbb{1} - T(T^\dagger T)^{-1}T^\dagger)d = F_T d \text{ and } F_T T = 0, \tag{5.6}$$

so that $d' \cdot T_i = 0$, where T_i encodes an arbitrary number of templates collected as columns of a *template matrix*, T. The most general form of the filtering operator is expressed in terms of a full-rank weight matrix,M:

$$d' = (M - MT(T^\dagger MT)^{-1}T^\dagger M)d = F_T d. \tag{5.7}$$

Several CMB data analysis pipelines (BICEP2 Collaboration et al., 2014; Planck Collaboration, Ade, P. A. R., et al., 2014) adopted a *simplified approach* by applying sequentially different typologies of filters. The drawback of this approach is that two different templates T_1 and T_2 are not orthogonal, thus their respective template matrices do not commute:

$$\begin{aligned} F_1F_2 =& \mathbb{1} - T_1T_1^\dagger - T_2T_2^\dagger + T_1(T_1^\dagger T_2)^{-1}T_2^\dagger \neq \\ \neq& \mathbb{1} - T_1T_1^\dagger - T_2T_2^\dagger + T_2(T_2^\dagger T_1)^{-1}T_1^\dagger = F_2F_1, \end{aligned}$$

where we assumed the templates to be normalized $T_i^\dagger T_i = 1$. Moreover, if T_2 satisfies $F_1F_2T_2 = 0$, this does not imply $F_2F_1T_2 = 0$ since the product F_1T_2 introduce extra-components such that $F_2F_1T_2 = -T_2T_2^\dagger T_1 + T_1(T_1^\dagger T_2)^{-1}T_2^\dagger T_1 \neq 0$. The remedy, obviously, is to further orthogonalize the template matrix as

$$\tilde{T} = T(T^\dagger T)^{-1/2},$$

where the number of columns of $\tilde{T}$ may be smaller than the T ones since some template could be linearly dependent. For further insights about the filter orthogonalization, see Poletti et al. (2016).

With the definition of F_T in (5.7) it is possible to generalize (5.4)

$$\hat{s}_u = (A^\dagger F_T A)^{-1}A^\dagger F_T d. \tag{5.8}$$

Notice that the filtering operator does not change the properties of the estimator in (5.8). It is still unbiased,

$$\begin{aligned} \hat{s} =& s + (A^\dagger F_T A)^{-1}A^\dagger F_T n, \\ \langle \hat{s} - s \rangle =& \langle (A^\dagger F A)^{-1}A^\dagger F n \rangle = 0, \end{aligned}$$

and if we consider $M = \mathcal{N}^{-1}$, it is minimum variance:

$$\Sigma = (A^\dagger F A)^{-1}(A^\dagger F \mathcal{N} F A)(A^\dagger F A)^{-1} = (A^\dagger F A)^{-1},$$

since

$$F\mathcal{N}F = FM^{-1}F = F.$$

The estimator in (5.8) is the one adopted by Polarbear in the pipeline B (Poletti et al., 2016) and the most expensive part is to compute and invert the matrix $A^\dagger F_T A$, where the filter operator F_T is defined as:

$$F_T = \mathbb{1} - \tilde{T}\tilde{T}^\dagger,$$

where $\tilde{T}$ is the orthonormalized template matrix.

Chiang et al. (2010) proposed an alternative approach that estimate a biased map by means of the following estimator:

$$\hat{s}_b = (A^\dagger M A)^{-1} A^\dagger F_T d, \tag{5.9}$$

where all the TOD components parallel to the templates are discarded by means of F_T and $(A^\dagger M A)^{-1}$ does not restore the power subtracted by filtering. The bias left by the estimator (5.9) is:

$$\langle \hat{s} - s \rangle = \left((A^\dagger M A)^{-1} A^\dagger F - \mathbb{1} \right) s,$$

and is not null in general.

Moreover, if one consider M as a diagonal matrix[1] the required computational time dramatically gets reduced. This approach is so attractive that pipelines of different CMB experiments adopted it, thanks to the fact that it is cheap in terms of computational cost and time although it is biased. However, the bias requires to be evaluated by Monte Carlo simulations and it is corrected at the power spectrum level, see sect. 4.4.

5.2 THE PRECONDITIONED CONJUGATE GRADIENT SOLVER

By looking at (5.8), it is worth noticing that we can rewrite it as a linear system:

$$\begin{aligned} \left(A^\dagger F A \right) \hat{s} &= A^\dagger F d, \\ &\Downarrow \\ \mathcal{A} x &= b, && (5.10) \\ \text{where } \mathcal{A} &= A^\dagger F A, && (5.11) \\ \text{and } b &= A^\dagger F d, && (5.12) \end{aligned}$$

with $\mathcal{A}$ Symmetric and Positive Definite (SPD).

The CG algorithm is particularly attractive for large sparse systems since it references the system matrix $\mathcal{A}$ only through its multiplication of a vector. This algorithm is based on the idea of a minimization of the following functional:

$$f(x) = \frac{1}{2} x^\dagger \mathcal{A} x - b x,$$

1 This is the case for the following analysis.

and one can easily notice that finding the minimum of this functional,i. e. $\nabla f = 0$,is equivalent to solve (5.10).

The minimization is carried out by generating a succession of search directions, p_k called *conjugate gradients*, each one computed from the evaluation of the residual vector at each stage, defined as

$$r^{(k)} = b - Ax^{(k)}.$$

The solution at the k-th step, $x^{(k)}$, is obtained from the solution at the previous step by adding p_k such that the convergence to the true solution is ensured with the lowest number of iterations. In facts, the CG exploits the sequence of conjugate gradients requiring them to be $\mathcal{A}$-orthogonal (or $\mathcal{A}$-conjugate), that is $\forall k \geqslant 0$, $(\mathcal{A}p_j)^\dagger p_{k+1} = 0$, $j = 0, 1, \ldots, k$. So that the solution $x^{(k+1)}$ is constructed in the space orthogonal to the one spanned from the previous k directions p_k. Usually at the first iteration p_0 is defined from the r.h.s. , i. e.$p_0 = b/ \parallel b \parallel_{\mathcal{A}}{}^2$, the approximate solution is $x_0 = (p_0^\dagger b)p_0$. The next direction is then chosen to be $r_0 = b - \mathcal{A}x_0$ and p_1 is defined by removing the component of r_0 parallel to p_0 and by normalising it. The iterative process is stopped when the residual norm is smaller than a fixed tolerance: $\parallel r^{(k)} \parallel < \epsilon_{tol}$. The CG algorithm is further described in Appendix B.

The convergence rate of the CG depends on the condition number κ[3] of $\mathcal{A}$. It can be shown that after k iterations of CG,

$$\parallel x - x^{(k)} \parallel_{\mathcal{A}} \leqslant 2 \parallel x - x^{(0)} \parallel_{\mathcal{A}} \left(\frac{\sqrt{\kappa} - 1}{\sqrt{\kappa} + 1} \right)^k, \tag{5.13}$$

where x is the true solution to (5.10) (Golub & Van Loan, 1996).

To reduce the condition number of the system matrix, it is very useful to apply a *preconditioner* matrix M_P to the linear system such that the preconditioned matrix $M_P A$ is closer to $\mathbb{1}$ and presents a smaller condition number (or a more clustered eigenspectrum). In this case the CG converges within a smaller number of iterations. This algorithm is usually referred as *Preconditioned Conjugate Gradient* (PCG)[4] and it solves the following linear system:

$$M_P \mathcal{A} x = M_P b. \tag{5.14}$$

5.3 THE DEGENERACIES FOR CMB GROUND-BASED EXPERIMENTS

A ground-based CMB experiment, scanning the sky with a focal plane encoding thousands of polarization sensitive pixels, has seldom to cope with

2 The $\mathcal{A}$-norm,$\| \cdot \|_{\mathcal{A}}$, of a vector v is defined as

$$\parallel v \parallel_{\mathcal{A}} = \sqrt{v^\dagger \mathcal{A} v}.$$

3 The condition number κ of a matrix is the ratio of the largest to the smallest eigenvalue of the matrix.

4 For a full description of the algorithm please see Appendix B.

both atmospheric and ground emissions, which have to be filtered out in the time domain. However, this kind of filters introduce degeneracies between a certain sky signal $\tilde{s}$ and the amplitude of a certain template amplitude $\tilde{y}$. This results into the impossibility to reconstruct that sky component when the template $\tilde{y}$ is filtered out, since $A\tilde{s} = T\tilde{y}$ and $A^\dagger F A\tilde{s} = A^\dagger F T\tilde{y} = 0$. Moreover, this degeneracy generates a singularity in the eigenspectrum of $A^\dagger F A$ and it therefore increases the condition number κ.

When the map-making problem involves the explicit inversion of the system matrix, such degeneracies prevent the inversion process and a further step to regularize the inversion is needed. The regularization helps in determining which modes can be retained and which ones are singular. The identification of the singular modes is extremely useful because they generate the null space of $\mathcal{A}$, and it is possible to invert it in the subspace orthogonal to the null space (Poletti et al., 2016). A very similar approach, will be presented in sect.5.5.

5.3.1 *Low-frequency correlations*

Although in the previous sections we assumed uncorrelated noise, this is of course an idealization which cannot always be generalized: correlations between different detectors induced by instrumental noise as well as atmospheric emission emerge especially at low frequency, showing a typical signature of the so-called $1/f$ noise. As a consequence, it is not accurate to approximate the noise covariance matrix as diagonal,on the contrary it is a very dense matrix and its inversion is computationally unfeasible. Filtering these low-frequency modes would result in removing both noise and signal long term trends present in the TODs, whose signal-to-noise ratio is usually very low. The temporal template resembling these long trend modes is well approximated by an arbitrary linear combination of piece-wise low order polynomials. Thus, the resulting residual noise

$$w = n - Bx$$

is expected to better resemble a white noise sample (with a nearly diagonal covariance matrix) than the time domain noise n. B is the template matrix and x is the amplitude of the corresponding templates. The Matrix B needs to account for the correlated B_{corr} and uncorrelated B_{uncorr} contributions as well as x is split in the amplitude of all the correlated and uncorrelated time domain modes x_{corr} and x_{uncorr}. As discussed in the previous section, we are discarding all the sky modes $\tilde{s}$ with projection in the time domain $A\tilde{s}$ parallel to a template-like mode. One of the unconstrained modes for ground-based observation is the global offset of the map since the offset of the time stream is always filtered.

When two CESs do not present common pixels, the offsets of both TODs are poorly constrained. As a results, the effect in map domain of filtering the long term trend of the TODs manifests as a poorly constrained long mode in declination.

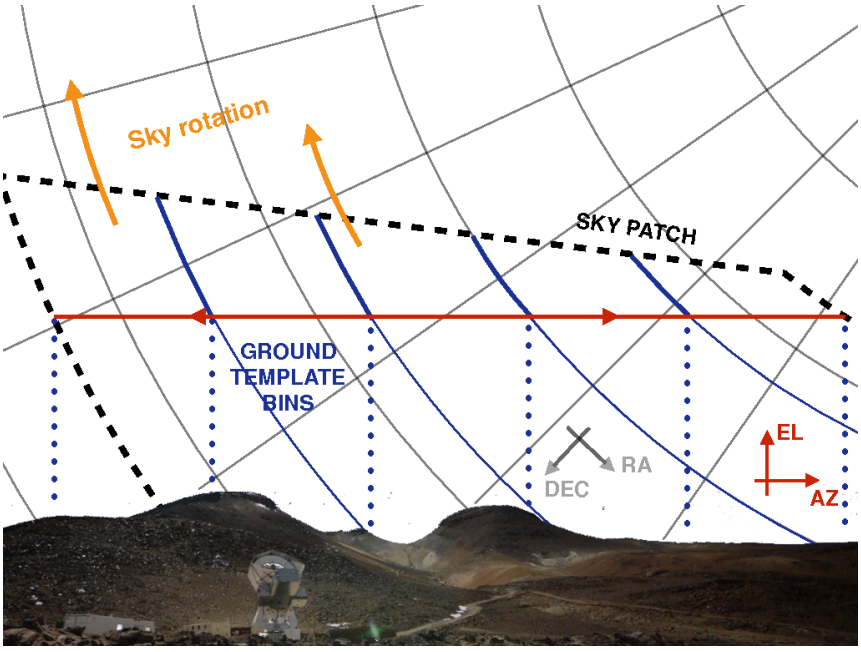

Figure 5.1: Illustration of the binning in azimuth associated to the ground pickup filtering and the Polarbear scanning strategy at constant elevation scans (red line). Regions of sky delimited by blue dotted lines represent the area observed in correspondence of each ground template bin. From Poletti et al. (2016).

5.3.2 *Ground pickup*

Though ground-based experiments are designed to have very low side lobes of the beam, the signal from the ground is not negligible compared to the CMB one. It is straightforward to figure out the ground signal collected by each detector at a certain constant elevation as a one-dimensional map depending on the azimuth, discretized by bins.

For sake of simplicity in this section, we assume no other contribution to be present, the TOD data can be written as:

$$d = As + Gg + n.$$

Intuitively, we can think the second term as the ground template map g projected to the time domain by means of the "projection matrix" G, each of its column representing a specific azimuthal bins of a specific detector at a given CES. The columns have 1 in correspondence of the measurement performed by a specific detector during a specific CES collecting the ground signal related to a given azimuth, and zero elsewhere.

Even in this case, the net effect of ground filtering on one detector measurements results in unconstrained modes in correspondence of different azimuthal bins, as illustrated in fig. 5.1. This is the case in particular for ground-based experiments far from the Earth Poles. In fact, two different ground bins relate to different sky areas and will be disjoint since both present a different ground pickup amplitude. These degeneracies can be

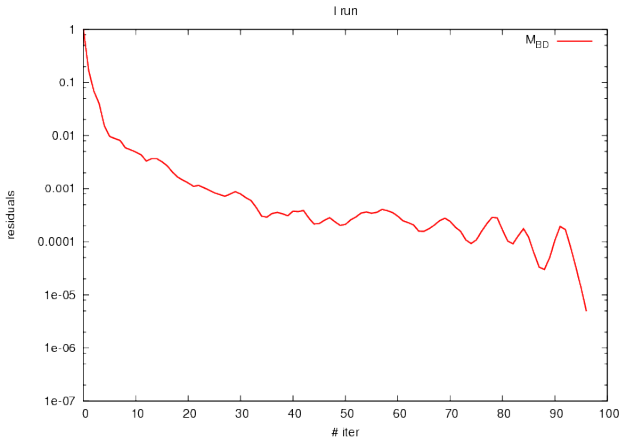

Figure 5.2: Residual norms at each iteration step, by preconditioning with the M_{BD}. The run encode 1 hour of simulated intensity-only Polarbear data with polynomial filtering only (see further details in next sect.5.9.1)

broken when combining data coming from several detectors, but only if the two azimuthal bins are respectively shifted so that the corresponding sky patches will be shifted as well and include pixels from two adjacent patches.

5.4 THE JACOBI PRECONDITIONER

From (5.4) we can easily define a preconditioner as:

$$M_P \equiv M_{BD} = (A^\dagger M A)^{-1}, \tag{5.15}$$

where M the weight matrix as in (5.24). M_{BD} is commonly referred as the *Jacobi Preconditioner* since, in absence of time domain filtering, it exactly coincides to $\mathcal{A}^{-1}$. Given the sparsity structure of the pointing matrix A, one could easily realize that M_{BD} is block diagonal and the sizes of each block is equal to the number of the Stokes parameters we are taking into account in the analysis. This is why we will refer to it in the following sections as the *block-diagonal* preconditioner.

The effect of Jacobi preconditioners onto the eigenspectrum of $\mathcal{A}$ results in a net shift of the larger eigenvalues towards the unity. This results on a decrease of the condition number as far as singular eigenvalues are not concerned. Unfortunately, as discussed in the end of the previous section, in the case of ground based experiments matrix $\mathcal{A}$ has very small eigenvalues with *low-energy* content. On the other hand, they have a very high content in terms of noise which hinders the convergence of PCG by generating a *low-mode plateau* that prevents to get lower thresholds, see fig.5.2.

5.5 TWO-LEVEL PRECONDITIONERS

An alternative preconditioner may be found among the class of the so called *Deflation* preconditioners that have proven to be successful in presence of

few isolated extremal eigenvalues. They act as de-projectors from the so called *deflation subspace*, $\mathcal{Z}$. This subspace is generated by r linearly independent eigenvectors that are related to the smallest eigenvalues and constitute the columns of the *deflation* matrix Z. The projection onto the deflation subspace may be defined as:

$$R = \mathbb{1} - \mathcal{A}Z(Z^\dagger \mathcal{A} Z)^{-1} Z^\dagger. \tag{5.16}$$

The projector R is orthogonal to any vector $\forall w \in \mathcal{Z}$ since $R\mathcal{A}Z = 0$.

On the other hand, being $\mathcal{A}$ SPD, one can build the orthogonal complement $\mathcal{Y}$, such that $\mathcal{Y} \oplus \mathcal{Z}$ and $y^\dagger z = 0$ for any $y \in \mathcal{Y}$ and $z \in \mathcal{Z}$. The natural choice for a basis of $\mathcal{Y}$ is given by all the remaining larger eigenvectors of $\mathcal{A}$, Y, such that $\mathcal{Y} = span\{Y\}$. For all of these Y, orthogonal to the deflation subspace, it holds that $R\mathcal{A}Y = \lambda RY = \lambda Y$.

In the exact precision algebra, R would be a very efficient preconditioner, as for each steps of an iterative CG-like solver would be orthogonal to the null space of the $R\mathcal{A}$. However, we deal in a finite precision arithmetic and the zero eigenvalues are often as bothersome as the small ones due to the numerical precision of the machine.

The solution to this issue is combining this deflation preconditioner with another one. This is the reason why we refer it as *two-level* preconditioner. Following Szydlarski et al. (2014) we combined it to the standard Jacobi preconditioner:

$$\begin{aligned} M_{2l} =& M_{BD} R + Z E^{-1} Z^\dagger \\ =& M_{BD}(\mathbb{1} - \mathcal{A}Z(Z^\dagger \mathcal{A} Z)^{-1} Z^\dagger) + Z E^{-1} Z^\dagger. \end{aligned} \tag{5.17}$$

The dimension of deflation subspace, is given by $dim(\mathcal{Z}) = r$ and since $r \ll N_p$, it is very easy to invert the *coarse* operator $E = (Z^\dagger \mathcal{A} Z)$. Moreover, as $\mathcal{A}$ is SPD, so is E. We note that this new preconditioner defined above fixes the issue of dealing with zero eigenvalues by rescaling all the null eigenvalues of $R\mathcal{A}$ to one:

$$M_{2l}\mathcal{A}Z = Z. \tag{5.18}$$

Since what we stated above, M_{2l} acts onto a vector $y \in \mathcal{Y}$ as the M_{BD} does

$$M_{2l}\mathcal{A}y = M_{BD}\mathcal{A}y.$$

Therefore, if we define $\mathcal{Z}$ as the deflation subspace generated by the eigenvectors related to the smallest eigenvalues of our system matrix $\mathcal{A}$, the two-level preconditioner shifts both the small and large eigenvalues of $\mathcal{A}$ close to one. Thus, when M_{2l} is applied to the system matrix $\mathcal{A}$, we can represent the product $M_{2l}\mathcal{A}$ as a two block matrix. The first block is related to the deflation subspace and from (5.18) we have that:

$$M_{2l}Az = z, \ \forall z \in \mathcal{Z}.$$

The second block is identified by the component of the solution belonging to $\mathcal{Y}$, where it is possible to run the PCG and gets fast convergence. Indeed in

this subspace the matrix $M_{BD}\mathcal{A} \sim \mathbb{1}$ and the PCG algorithm converges faster since it has a smaller condition number $\mathcal{O}(10)$ (due to the considerations made at the end 5.4).

As a results, the PCG with M_{2l} is expected to achieve the PCG tolerance within a smaller number of iterations with respect to the M_{BD}.

Finally in order to build the deflation subspace it is not necessary to compute the whole eigenspectrum of $\mathcal{A}$ it is enough to rely with *approximations* of the eigenvectors related to the smallest eigenvalues computed by means of the *Arnoldi algorithm*.

5.5.1 *The Arnoldi Algorithm*

The *Krylov* subspace algorithms are based upon the structure of a sequence of vectors naturally produced by the power method, a class of those, namely the Minimal Residuals (MINRES) and the Generalized Minimal Residual (GMRES) methods (Golub & Van Loan, 1996) rely on the Arnoldi algorithm.

Our aim is to find an approximation to the eigenvalues of a matrix B of a generic linear system with r.h.s. b:

$$Bx = b. \tag{5.19}$$

The Arnoldi algorithm is an algorithm aimed at solving a linear system by projecting the system matrix onto a convenient Krylov subspace generated by the first m vectors:

$$\mathcal{K}_m(B, b) = span\{b, Bb, B^2b, \ldots, B^{m-1}b\}, \tag{5.20}$$

and the algorithm steps are summarized in Algorithm 1.

Algorithm 1 Basic Arnoldi Algorithm

Require: : r_0, $w_1 = r_0 / \parallel r_0 \parallel$
1: **for** $j = 1 \rightarrow m$ **do**
2: **for** $i = 1 \rightarrow j$ **do**
3: $h_{i,j} = (Bw_j, w_i)$
4: **end for**
5: $v_j = Bw_j - \sum_{i=1}^{j} h_{i,j} w_i$
6: $h_{j+1,j} = \parallel v_j \parallel$
7: $w_{j+1} = v_j / h_{j+1,j}$
8: **end for**

Hence, the output of the Arnoldi algorithm is an orthonormal basis $W^{(m)} = (w_1|w_2|\ldots|w_m)$ (called the *Arnoldi vectors*), together with a set of scalars $h_{i,j}$ (with $i, j = 1, \ldots, m$ and $i \leqslant j + 1$) plus an extra-coefficient $h_{m+1,m}$. The former set of coefficients are the elements of an upper Hessenberg matrix H_m with non-negative subdiagonal elements and is commonly referred as a *m-step Arnoldi Factorization* of B. If B is Hermitian then H_m is symmetric, real

and tridiagonal and the vectors (columns of $W^{(m)}$) of the Arnoldi basis are called *Lanczos vectors*. B and H_m are intimately related via:

$$BW^{(m)} = W^{(m)}H_m + h_{m+1,m}w_{m+1}e_m^\dagger, \tag{5.21}$$

where e_m is a $1 \times m$ unit vector with 1 on the m-th component.

In other words, H_m is the projection of B onto the subspace generated by the Arnoldi basis $W^{(m)}$ within an error given by $\tilde{W}_m = h_{m+1,m}w_{m+1}e_m^\dagger$. The iteration loop ends when this error term gets smaller than a certain threshold ϵ_{tol}.

Eq. (5.21) is remarkable, since connects the eigenpairs of B to the ones of H_m. Let us consider an eigenpair of H_m, (λ_i, y_i):

$$H_m y_i = \lambda_i y_i,$$

then the vector $v_i = W^{(m)}y_i$ satisfies

$$\| Bv_i - \lambda_i v_i \| = \| (BW^{(m)} - W^{(m)}H_m)v_i \| = \| \tilde{W}_m v_i \| . \tag{5.22}$$

I. e. the eigenpairs of H_m are approximations of the eigenpairs of B within an error given by $\tilde{W}_{m+1}$. They are the so called *Ritz eigenpairs* and they are very easy to compute since the size of H_m is $\lesssim \mathcal{O}(100)$. For a typical CMB dataset this is the order of Arnoldi iterations required to encompass a tolerance $\epsilon_{tol} \sim 10^{-6}$.

5.6 BUILDING THE DEFLATION SUBSPACE

Given the definitions of the two-level preconditioner made in 5.5, we apply the Arnoldi algorithm to the matrix $B = M_{BD}\mathcal{A}$. We select the first r eigenpairs whose eigenvalues are smaller than a certain threshold ϵ_λ. We build the orthonormal basis of the deflation subspace $\mathcal{Z}$ with these selected r eigenvectors Z_D and construct the two-level preconditioner with them as columns of Z. Obviously, the size of the deflation subspace increases by considering larger threshold values ϵ_λ and we have found that a deflation subspace with size ranging between 5 and 20 $\epsilon_\lambda < 0.01 \div 0.1$ performs better; further tests will be presented in sect. 5.10.

The Ritz eigenvectorscan be projected in the sky as maps and they peculiarly appear as long modes across the sky patch. As we commented in sect.5.3 modes propagating along the declination direction are related to the degeneracies due to ground filtering. Whereas modes propagating in the RA direction present more frequent oscillations and they are related to degeneracies introduced by the time domain polynomial filtering (the larger is the order of polynomials filtered out the more emphasized is the amplitude of the modes).

The very same features have been remarkably observed in the nearly degenerate mode eigenvectors by Poletti et al. (2016), see fig.5.3. Nevertheless the eigenvectors in the bottom panel of fig.5.3 come from the eigendecomposition of $A^\dagger FA$

$$\mathcal{A} = A^\dagger FA = V\mathrm{diag}(e)V^\dagger,$$

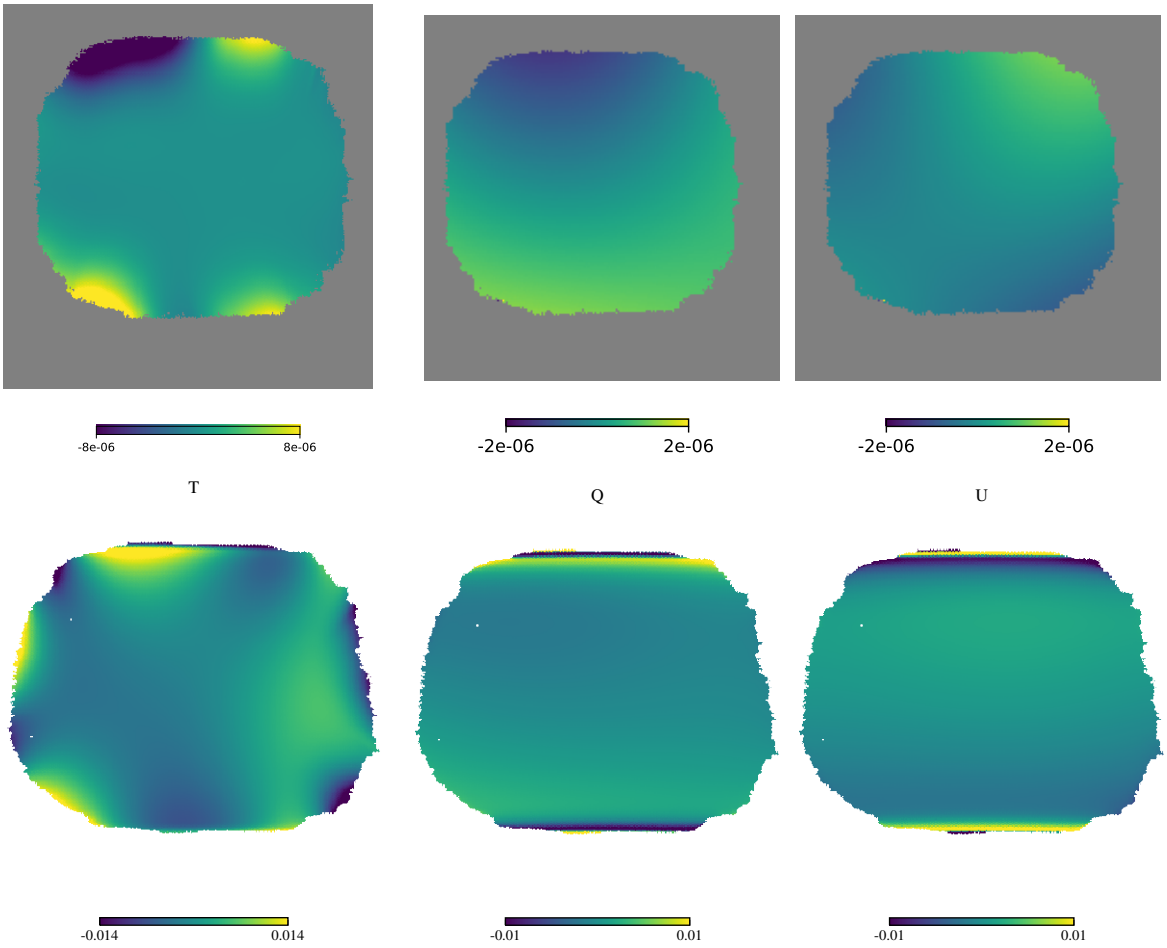

Figure 5.3: (top) In left (middle and right) panel the Ritz eigenvectors related to the smallest degenerate mode for temperature (Q and U) data set, from Puglisi et al. (in prep.). Notice that in order to emphasize the features the color scale boundaries have been saturated. (bottom) Eigenvectors of nearly degenerate modes from (Poletti et al., 2016, fig.10) as in the top panel. Notice that for polarization both the maps involves horizontal features at the high and low declination ends of the patch . This is mostly due to ground pickup removal. For intensity, effects from high order polynomial filtering are more significant with respect to polarization. Notice the prominent features at the boundaries at intermediate declinations and a more complex long mode.

which slightly differs from $\mathcal{A}$ since F in this case encodes a further orthogonalization of polynomial and ground filters.

5.7 THE POLARBEAR DATA MODEL

In sect.4.3 we have derived the two sets of time streams, obtained by summing and differencing the signal coming from each pair of bolometers, respectively (4.5) and (4.6), in order to disentangle total intensity and polarization signals without any loss of accuracy.

Since we apply the proposed methodology of this chapter to simulated Polarbear data on the RA23 patch, the two seasons of observations are divided in $N_{CES} = 6219$ CES, each one composed by ~ 120 subscans usually observed by ~ 220 pairs of bolometers. Each CES lasts 15 minutes and since samples are down-sampled from 190 to 31.8 Hz, their number per detector is $N_t^{CES} \sim 27000$. The TODs d^+ and d^- can be thus expressed as:

$$d^{\pm} = A^{\pm} s_{T/QU} + G^d g^{\pm} + B^{\pm} x^{\pm} + w^{\pm}, \tag{5.23}$$

where $A^{\pm}$, $g^{\pm}$, $x^{\pm}$, $w^{\pm}$ are analogously defined as $d^{\pm}$ in (4.3) and (4.4). The matrix $B^{\pm}$ encode the time domain filtering and can be expressed in terms of B_{corr} and B_{uncorr}. In this analysis B_{corr} contains four templates of the Legendre polynomials up to the third order and B_{uncorr} the ones till the first one. The columns of B_{corr} and B_{uncorr} are linearly dependent and we can define B^+ as $B^+ \equiv B_{corr}$. On the other hand, $B^- \equiv B_{uncorr}$. This filtering is applied within each subscan of a given CES so that the number of polynomial templates per CES and detector pair is $N_{subscan} \times N_{poly} \sim 480\,(240)$, since $N_{poly} = 4(2)$ depending if one considers the sum or the difference time stream. The ground term is the same for summed and differenced data, and its number of columns is the same as the number of azimuthal bins (~ 100 since each bin is $0.08°$ wide) and the number of rows depends on the number of samples N_t^{CES} in a given CES. $w^{\pm}$ are the *white noise* terms, which can differ for each CES and each pair of bolometers. Both are respectively evaluated as the inverse of the average of power spectral density of the time streams $d^{\pm}$ between 1.04 and 3.13 Hz. $w^{\pm}$ populate the weight matrix which is assumed to be block diagonal, each block corresponding to the noise weight of the i-th detector pair within the c-th CES:

$$M^{\pm}_{c,i} = w^{\pm}_{c,i} \mathbb{1}. \tag{5.24}$$

In the following analysis, both ground F_G and polynomial F_B filters defined as in (5.7) with $T = G, B$ have been applied sequentially to the data. However, since the filters are orthogonal only internally, the matrix $A^\dagger F_G F_B A$ is not symmetric as it is required by the CG algorithm. We encompass this issue, by defining

$$F \equiv F_G F_B,$$

and exploiting the following properties:

$$F_B^\dagger = F_B,$$
$$F_G^\dagger = F_G$$

and

$$F^\dagger F = F_B F_G F_G F_B = F_B F_G F_B$$

where for the first equality we make use of the definition in (5.6) for F_B and F_G and for the last equality we exploited the property of idempotence of F_G, (being all the filter operators defined in (5.6) *projectors*). Two categories of filters have been combined in such a way that the system matrix of the unbiased estimator is symmetric:

$$(FA)^\dagger FA = A^\dagger F^\dagger FA \equiv A^\dagger F_B F_G F_B A = A^\dagger \bar{F} A, \tag{5.25}$$

where the operator $\bar{F} = F_B F_G F_B$ encodes all the filtering and weighting operations when applied to a time-domain vector.

In this fashion, we recover a similar expression for the unbiased estimator as in (5.8), with $\bar{F}$ instead of simply F:

$$\hat{s} = (A^\dagger F A)^{-1} A^\dagger F d, \tag{5.26}$$

The definition of observed pixels is performed prior to the map-making procedure. At first, we identify as ill conditioned, those pixels whose 2-by-2 block of $A^\dagger M A$ matrix presents a condition number larger than 10^3. We, finally, consider the samples related to pixels commonly observed within a group of daily CESs in order to have enough redundancy to disentangle the Q, U polarization signals.

This yields to maps of $\sim 4 \times 10^4$ pixels following the HEALPix scheme, with the gridding parameter set to `nside=2048`.

5.8 IMPLEMENTATION

We have developed a `Python` module[5] aimed at producing maps by means of iterative solvers whose application can be either real or simulated Polarbear data. Indeed it is implemented to be well interfaced to the outputs of the low-level data processing Polarbear pipeline. These routines calibrate the data and perform the data cuts by including the definition of the subscans and the preprocessed vector coincides to the one in the r.h.s. of (5.4).

Finally, the data model is the one assumed in (5.23) and it is consistent with the other Polarbear map-making pipelines (sect.4.3).

For all the validation tests and the full season runs we exploited the supercomputing resources at our disposal at SISSA and at National Energy Research Scientific Computing Center (NERSC-Berkeley)[6]:

5 https://github.com/giuspugl/COSMOMAP2, for the documentation go to http://giuspugl.github.io/cosmomap.

6 http://www.nersc.gov/users/computational-systems/edison/ .

ULYSSES (SISSA): 10^3 computing nodes, 20 *Intel Xeon "Ivy Bridge"* cores per node (each has a clock rate 2.8 GHz), 160 GB per node;

EDISON (NERSC): 5,586 computing node, 12 *Intel Xeon "Ivy Bridge"* cores per node (each has 2 threads with a clock rate 2.4 GHz), 128 GB per node;

CORI KNL (NERSC): 9,688 computing node, 68 *Intel Xeon Phi "Knights Landing"* cores per node (with a clock rate 1.4 GHz), 96 GB per node.

In particular, all the full season runs have to be run at Nersc facilities since the Polarbear data are stored there.

To build the pointing matrix A for the case of d^+ timestream the vector encoding the index of the observed pixel is needed. For d^-, a further time-domain vector is required to store the values of the polarization angle for any time sample. Moreover, the sines and the cosines of the polarization angle have been precomputed and stored into the memory. For both the sum and difference timestreams, the vector encoding which azimuthal bin has been observed at each time sample and needed to initialize the ground pickup filtering.

The weights for each detector pairs are precomputed both for summed and differenced data during a CES as the inverse of the average of PSD of the real data taken within the Polarbear science band.

Every matrix involved in computing the estimator (5.26), namely A,$A^\dagger$, F_B, F_G, $\mathcal{N}^{-1}$, M_{BD}, M_{2l} does not need to be fully stored in the memory, they are all implemented as *linear operators* and (by means of the Python module `linop`): it is enough to implement the product of each matrix onto a generic vector. In particular, since most of the time is spent during the filtering products involving $\sim 3N_t^2$ operations (here we recall that $F = F_P F_G F_P$ from (5.25)), we capitalize by developing a fast implementation for the time-domain operations.

We summarize the implementation in few steps:

A. Whenever the operator $\mathcal{A}$ is applied to a pixel domain vector, it involves sequentially the application of A, F_B, F_G, F_B, and $A^\dagger$.

B. Being the application of F_B the slowest requiring to compute the Legendre polynomial basis within each subscan, it is implemented by following a *multithreading* paradigm, so that a series of instructions, to be consecutively executed, forks into a specified number of threads and the instructions are then run concurrently. By choosing to split the computation of F_B through ~ 4 threads we got a speed up of a factor 4 when compared to the serial execution;

C. in order to construct the M_{2l} preconditioner, Ritz eigenvectors of $M_{BD}\mathcal{A}$ are selected from the eigenvalues smaller than ϵ_λ. The matrices $\mathcal{A}Z$, E and E^{-1} are precomputed and stored in memory. The inversion is performed either with an LU decomposition or an eigen-decomposition.

Given the size of the deflation subspace ($r \lesssim 20$) these operations are computationally cheap;

D. During each iteration of the iterative solver, the application of the preconditioner to a pixel-domain vector is needed.

5.8.1 *Parallelism*

In order to process a full season of Polarbear observations (meaning a 10^{11} samples per TOD), the solver does not process the full dataset at once: data need to be distributed among processors. We adopted the so called *divide-and-conquer* approach that breaks down a very huge problem into a number of sub-problems of the same type, so that each processing element solves iteratively the linear system for one daily map. We thus split the data set into roughly 250 groups of maps usually each one encoding $20 \div 30$ CESs processed by each cpu. No communication among processors is needed and each processor run twice and produces two maps.

However, groups of daily CESs involve several time-domain and map-domain arrays to be kept in memory during the execution and not all the processors within a NERSC node can be exploited since the memory limit within a node is easily saturated when data of only 2-3 groups of daily maps are loaded. Though this represents a limitation when short and massively parallel runs are to be preferred, we kept using the divide-and-conquer approach since it was adopted by the Polarbear iterative map-maker in the following we focus on a comparison between the standard preconditioner and the two-level one applied on the same amount of data.

5.9 VALIDATION OF THE CODE WITH SIGNAL ONLY SIMULATIONS

End-to-end comparison are usually performed in order to validate a code, thus we simulate TODs from known input TQU CMB only maps. The input maps shown in fig.5.4 are produced by means of the `synfast` routine of the HEALPix package (Górski et al., 2005) which reads as an input one realization of CMB power spectra computed with the CAMB package (Lewis, Challinor, & Lasenby, 2000) assuming the Planck best fit cosmological parameters (Planck Collaboration, Ade, Aghanim, Arnaud, Ashdown, et al., 2016). The input map is scanned with Polarbear pointing and polarization angle informations coming from the two season of observations onto RA23 observations.

We then run the iterative solvers on several combination of data to compute the reconstructed map and compare it to the input one. In particular since we know the exact solution, signal only simulations are useful to quantify the error associated to the reconstructed map at each iteration step, i. e.

$$\| e^{(k)} \| = \| x - x^{(k)} \|,$$

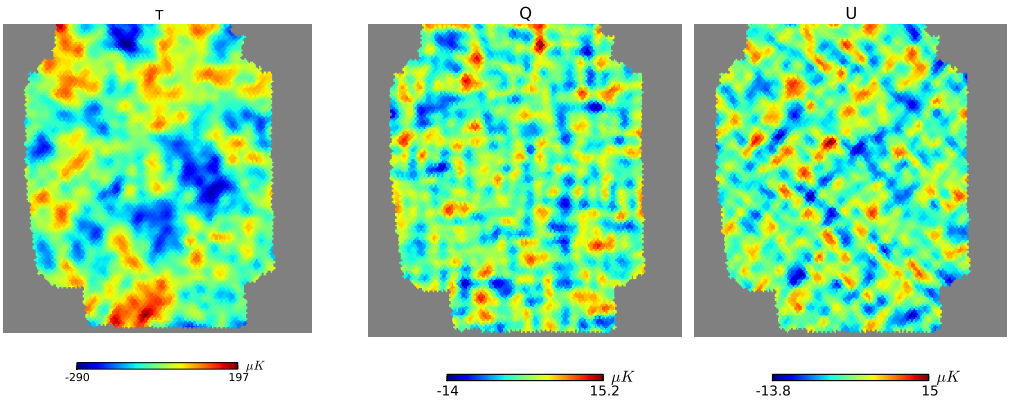

Figure 5.4: Input CMB maps used for the simulating the dataset, from Puglisi et al. (in prep.).

where x is the true solution to the linear system and $x^{(k)}$ is the solution at the k-th iteration.

5.9.1 *Application to 1 h of simulated data*

We consider a small sub set of data encoding 1 h of observations, namely 4 CESs. This case encodes $N_p \sim 10^4$ and $N_t \sim 2 \times 10^7$.

As one of the first implementation checks, we considered the linear system built from (5.4), and preconditioned with the Jacobi preconditioner M_{BD}. The PCG converges within one iteration as expected since in absence of filters M_{BD} is exactly defined as $\mathcal{A}^{-1}$, see eq.(5.15).

Subsequently, we gradually complicate the linear system by filtering the data with the Legendre polynomials as described in sect.5.3.1 and 5.7. The Arnoldi algorithm took $\sim$ 50 iterations[7] to converge within a tolerance of 10^{-6}. 14 approximated eigenvalues have been found smaller than 0.2, so that the deflation subspace is built with $r = 14$ Ritz eigenvectors.

In total, each run performed in one Ulysses node, took less than $\sim$ 10 minutes and even accounting for the time required for running the Arnoldi algorithm, the runs with the two-level preconditioner ended with half of the time spent by the block-diagonal one. Fig.5.5 shows the residuals at each PCG iteration step for the Jacobi and two-level preconditioners respectively in red and green.

It is remarkable to state that the performances for the two-level preconditioner (green solid line in right panel) do not change if a larger number of pixels are involved, but as expected on the condition number of the preconditioned matrix. Indeed, this is the case when the solver involves polarization maps: the number of pixel doubles with respect to the case of temperature only data. By looking at the performances of M_{BD} in fig.5.5

7 This value may change if the timestream increases.

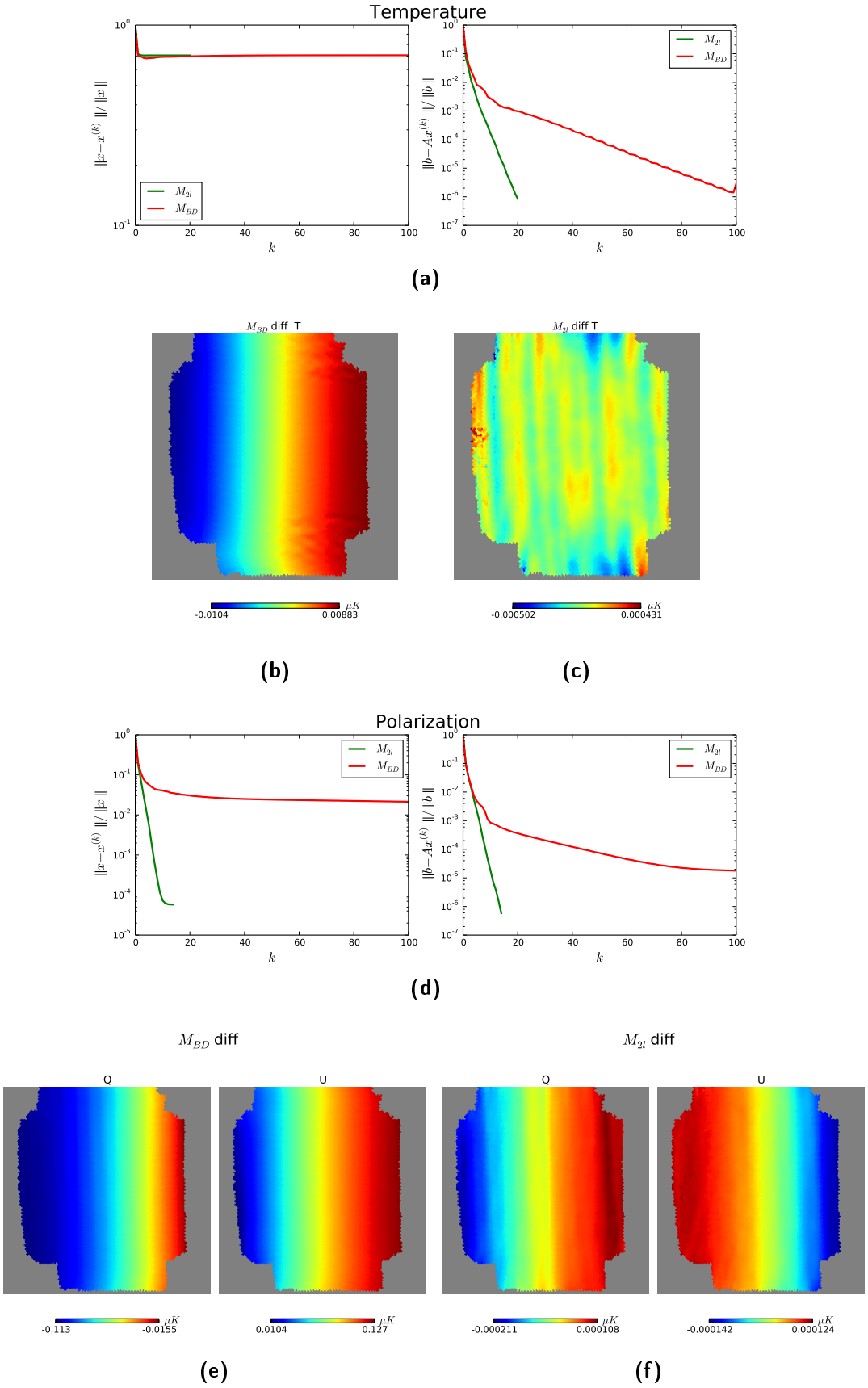

Figure 5.5: Signal only PCG runs with a simple polynomial filtering solving for temperature and polarization, from Puglisi et al. (in prep.). The plots show error (left panel) and residual norms (right panel) as a function of iteration steps (solid red) for M_{BD}, (solid green) for M_{2l} (panels a and d). Also, the difference (input - output) maps for cases preconditioned by M_{BD} and M_{2l} respectively are shown in panel b and f.

(red solid line in right panel), both cases do not converge and we observe the very well known convergence plateau behaviour. Vice versa, regardless the number of pixels involved, the M_{2l} converges within 20 iterations for both cases.

In the left panels of fig.5.5 the performances in terms of the error norms are plotted. At a first inspection, they can be misleading since they look to be soon saturated at the first iteration steps. This is mainly due to the modes (appearing as a long wave mode) of the input map which are not constrained by the solver and prevent the error norms to go further beyond the value ~ 0.7. In facts, as expected both the difference maps (input - reconstructed maps), shown in fig.5.5, present a long mode across the whole patch. Both preconditioners M_{BD} and M_{2l} successfully reconstructed the maps respectively with 10^{-4} and 10^{-6} relative errors. In particular, we achieve the smallest difference with Q and U maps reconstructed with M_{2l}.

Finally, we test the realistic case where both ground and polynomial filters are combined so that $\mathcal{A} = (A^{\dagger} F_B F_G F_B A)$.

As shown in fig.5.6, the situation changes since we observe a convergence plateau even in the M_{2l} residuals, though roughly one order of magnitude lower than the M_{BD} ones. In the following analysis, this feature is quite common even when real data are involved and it is mainly due to the fact that the presence of both ground and polynomial filters results in an increase of the condition number of $\mathcal{A}$.

At this point, one may argue that there is no gain in the execution time since accounting for the time of running both the Arnoldi algorithm and the PCG with M_{2l} is larger than the execution of a PCG using simply the Jacobi preconditioner. In fact, this is the case: by profiling both runs, the PCG took $\sim$ 15 minutes for both methodologies, whereas the Arnoldi algorithm took $\sim$ 8 minutes. This is quite expected since the Arnoldi algorithm encodes a number of applications of $\mathcal{A}$ to the Arnoldi basis that increases at each iteration step. Hence, this could not be an issue if it might be possible to compute the deflation subspace *a priori* by running only once the Arnoldi algorithm.

Finally, a common feature shared by all the difference maps shown in figg. 5.5, 5.6 is the close similarity to the long-mode maps shown in fig. 5.3. The interpretation to that is quite straightforward: the PCG converges more hardly to the modes related to the singular eigenvalues of $\mathcal{A}$ appearing as long modes in the maps.

5.9.2 *Application to 1 day of simulated data*

As we discussed in sect. 5.8, we run the PCG considering several groups of observations, each one processing independently groups of daily maps made by 27 CESs, i. e. $N_t \sim 10^9$ and $N_p \sim 4 \times 10^4$. Hereafter, we focus the following analysis onto polarization data and and a group of data encoding 27 CES is referred with the acronym RHS, being the r.h.s. vector of the linear system in (5.10).

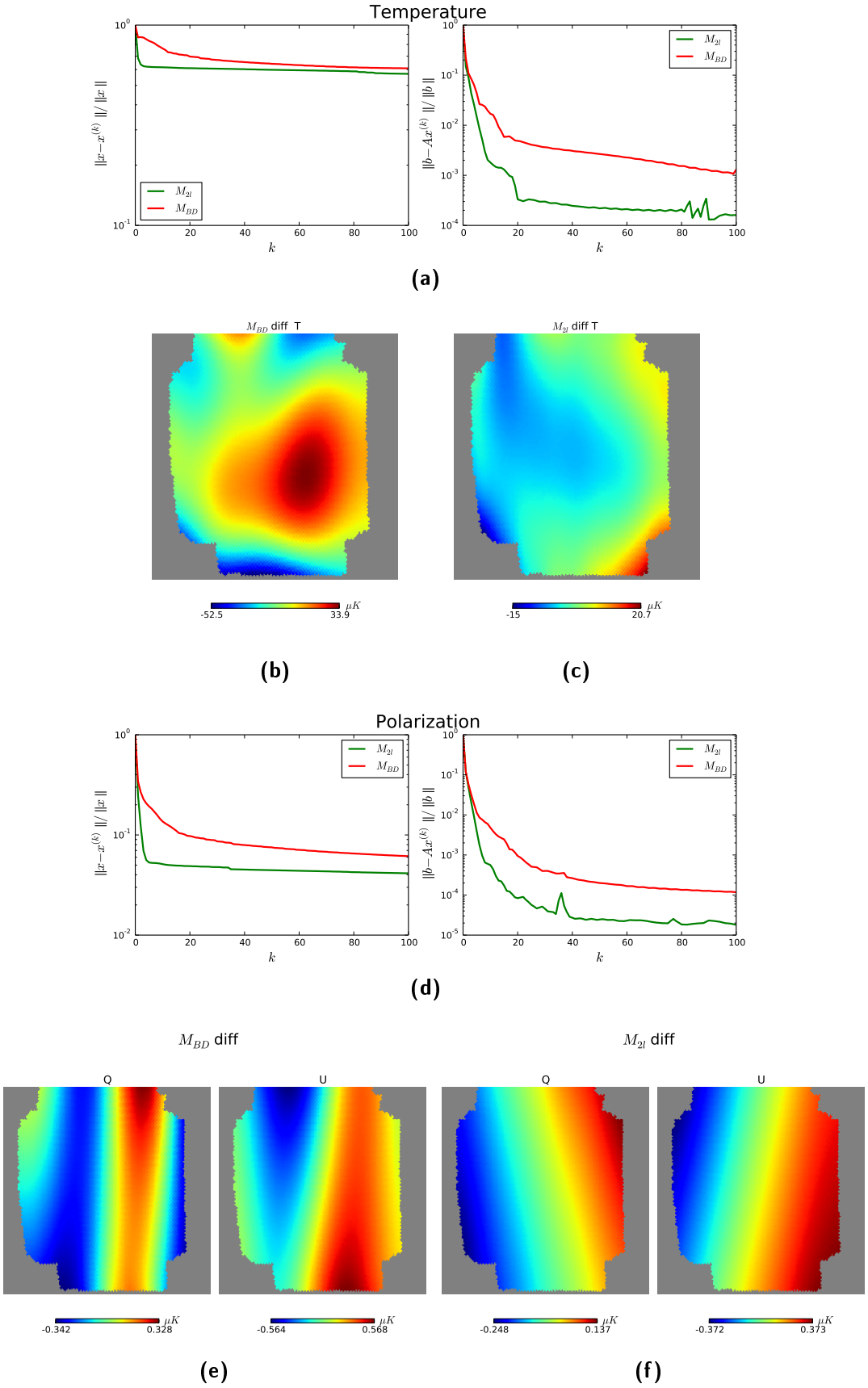

Figure 5.6: Signal only PCG runs with a realistic filtering, encoding the sequential application of $F_B F_G F_B$ for both temperature and polarization runs, from Puglisi et al. (in prep.). As in fig.5.5, the plots show error (left panel) and residual norms (right panel) as a function of iteration steps (solid red) for M_{BD}, (solid green) for M_{2l}.

For the runs involving M_{2l} we approached its construction in the following ways.

1. **The "Active" approach**: the Ritz eigenpairs are computed for each RHS and the eigenvectors related to the eigenvalues smaller than $\epsilon_\lambda = 0.02$ are retained for the deflation subspace. Given this threshold, the M_{2l} is built by means of 4/6 eigenvectors.

2. **The "Lazy" approach**: the Ritz eigenpairs are computed only for one day of data and 6 eigenvectors are selected as in the "active" approach. The M_{2l} built from this eigenvector basis is then applied to all the rest of the data set.

Obviously, the "active" approach is more time consuming than the "lazy" one: 30% of the whole execution time is spent within the Arnoldi algorithm, needing $\sim 50 \div 70$ iterations to achieve the tolerance 10^{-6}. On the other hand, we strongly gain both in terms of accuracy of the reconstructed map since we get one order of magnitude smaller residuals norm (see fig.5.7), and in terms of performances, since for same cases it may converge within a smaller amount of iterations, as in the bottom left panel of fig.5.7. Furthermore, since the Ritz eigenvectors are written into disk, they can be re-used for Monte-Carlo noise simulations.

On the contrary, the "lazy" case could gain in terms of solution accuracy only in the cases where the deflation basis is very representative of the whole dataset. If this is not the case, we do not observe any improvements with respect to M_{BD}, as shown in fig. 5.7 by the solid blue line.

To have better statistics of the `mdd` applied in the lazy case we applied it to the whole Polarbear simulated data set. We set the PCG tolerance to 10^{-7} and ran the PCG with both the preconditioners. Moreover, if the PCG does not get the tolerance within 150 steps we stop the run and flag it as `unconverged`. We perform the runs at the Edison system since the whole data of Polarbear collaboration have been stored at NERSC and distribute the dataset across 100 processors. Each processor performs 2 PCG runs (3 hours are required for each run), and the cpu time (quantified in cpu hours, cpuh) for running each PCG solver on the whole data set is 600 cpuh.

All runs converged within 150 iterations and are summarized in tab.5.2 and 5.1 and in fig.5.8. By looking at the PCG execution time and the iteration steps with M_{2l} we observe a slight improvement of a speed up factor 1.5 compared to the M_{BD} values. This is an interesting result since it confirmed the expectations that the degeneracies introduced by the smallest eigenvalues observed in one day of signal only data share roughly the same eigenspectrum as for the other days.

However, one can quest whether it is possible to improve these performances and compute *a priori* a better deflation subspace due to this redundancy among all the RHSs. In order to answer this question, two kind of options have been tested for the following cases.

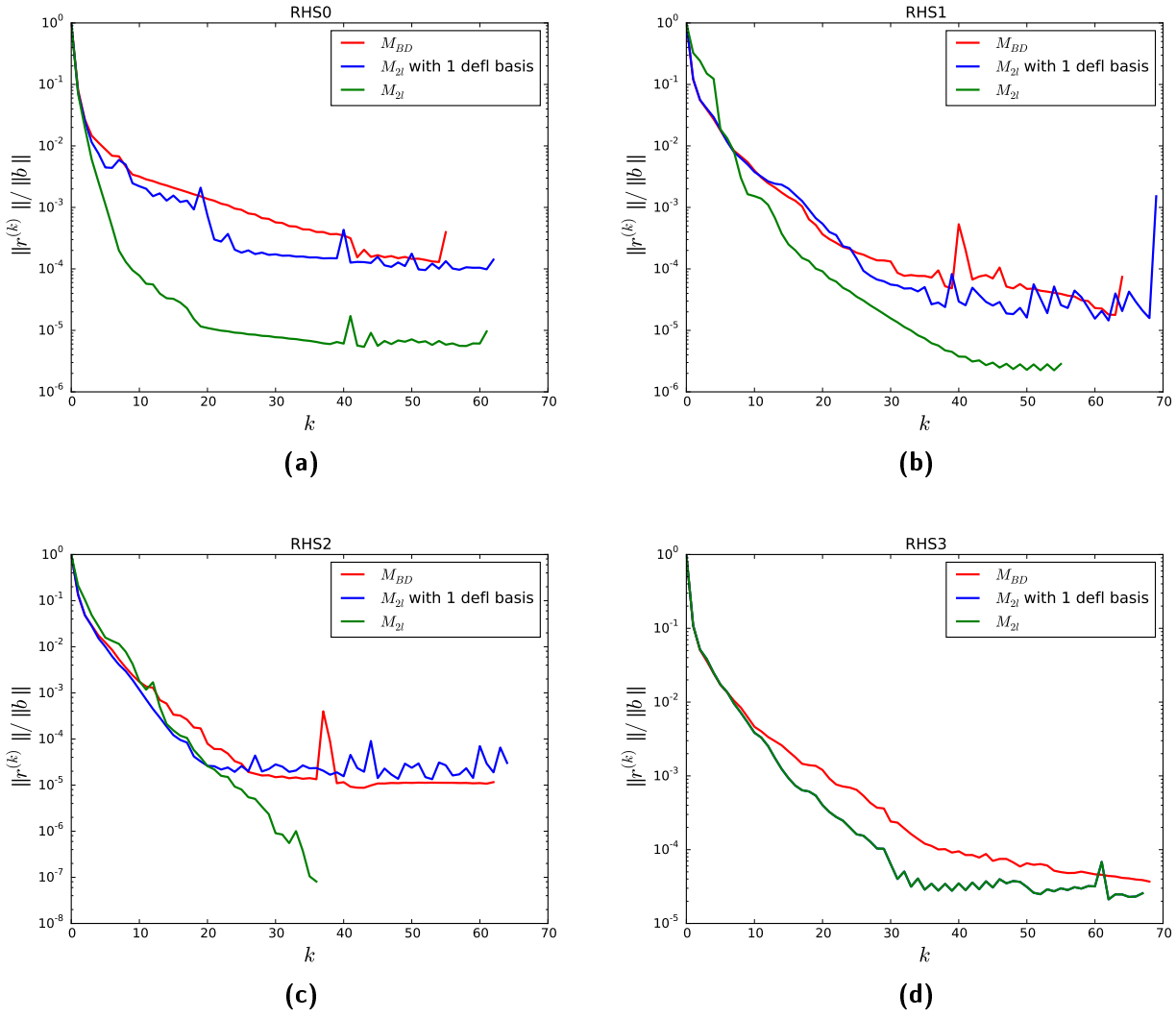

Figure 5.7: Runs encoding signal only RHS (solid red) residuals in terms of iteration steps for M_{BD}; (solid blue) residuals for M_{2l} computed with one deflation basis, whereas (solid green) residuals w/ M_{2l} computed for each RHS, usually 4 eigenvectors are selected with a threshold smaller than 0.02. From Puglisi et al. (in prep.).

1. Precompute several deflation bases from ($\leqslant 10$) different RHSs, collect them into columns of a matrix Z_{all} and find among all columns the ones containing *more than* 80% *of energy* via a *Singular Value Decomposition* (see Appendix C) of Z_{all}. The selected columns constitute a more representative deflation basis. The M_{2l} built with it is then applied on the whole data set and the results are shown in Appendix C. They indicate a factor of 2 less cpu time and iterations.

2. We can increase the size of time samples, namely 3 more CESs per group, so that each processor reconstructs a 3-day map. This test has been applied to real data and will be discussed in subsect. 5.10.1.

	PCG execution time [min]	Iteration steps	$\| r^k \| / \| b \| (\times 10^{-8})$
M_{BD}	6.5	32	5.8
M_{2l}	4.3	20	6.1

Table 5.1: Median values of PCG runs with the Jacobi and the two level preconditioner.

	PCG execution time [min]	Iteration steps	$\| r^k \| / \| b \| (\times 10^{-8})$
M_{BD}	402.3 ± 113.2	32.3 ± 6.4	6.1 ± 2.2
M_{2l}	283.7 ± 134.5	22.8 ± 11.1	6.4 ± 1.9

Table 5.2: Mean and standard deviation of PCG runs with the Jacobi and the two level preconditioner.

5.10 APPLICATION TO THE TWO-SEASON POLARBEAR DATA

Once we have validated the pipelines, and checked the performances on signal only data, the next step is to apply this methodology to the real noisy data. As a first attempt, we choose to run the PCG onto the usual data split (each RHS encodes by 27 CESs). As in the previous section, two different cases related to M_{2l} have been considered: the lazy one where M_{2l} is built from one precomputed Ritz eigenvector basis and the active one where the deflation basis is computed for each RHS.

In order to choose the eigenvalue threshold we did several convergence tests with ϵ_λ ranging from 10^{-2} to 0.5. As expected, by increasing the threshold, more and more Ritz eigenvectors are selected so that the size of the deflation subspace increases as well (as a reference look at table 5.3). As a result of these tests we find that the size of the deflation subspace at a given threshold is the same for different RHSs, implying that the eigenvalues of the different matrices $\mathcal{A}$ (each one related to a certain RHS) follow the same distribution. This is a remarkable results in support of our hypothesis that

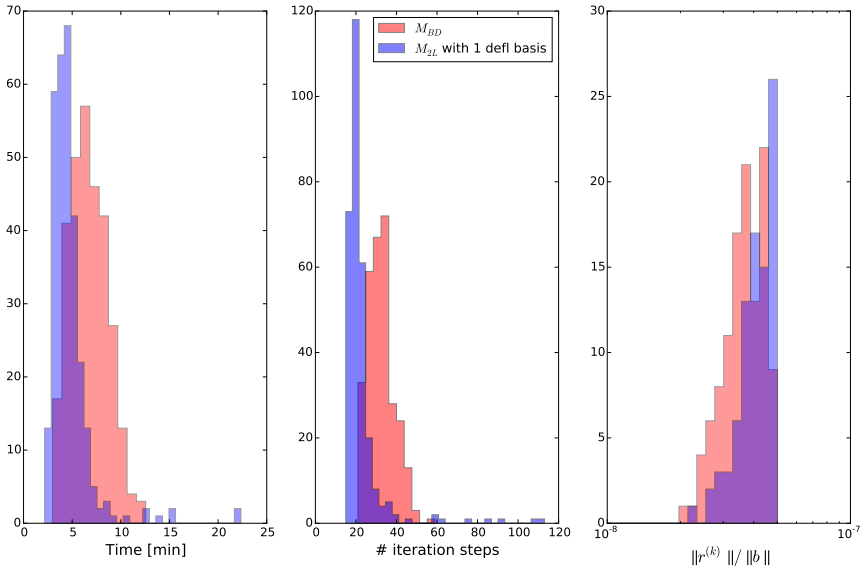

Figure 5.8: Normed histograms of (left) PCG execution time, (middle) total iteration steps, (right) norm of the residuals for the M_{BD} (red) and the M_{2l} (blue) preconditioners. From Puglisi et al. (in prep.).

the degeneracies in different days of observations are very similar, so that the same number of eigenvalues falls within a given bin, even if their amplitude may slightly change. A further remarkable result is that *the larger is the size of the deflation subspace, the steeper is the descending line of the residual norms as a function of iteration steps*. This is a feature shared among most the tests shown in fig. 5.9: they all do not cross a tolerance of $10^{-4} \div 10^{-5}$, nonetheless they hit the plateau after a different number of iterations. Hence, we choose $\epsilon_\lambda = 0.2$ and selected selected 14 eigenvectors to construct the two-level preconditioner.

ϵ_λ	$\dim(\mathcal{Z})$
0.01	3
0.02	4
0.06	8
0.15	12
0.5	21

Table 5.3: The size of the deflation subspace as a function of eigenvalue thresholds

.

Looking at fig.5.10 and fig.5.11, two facts can be appreciated: (i) running with M_{2l} in the lazy approach is very similar to the M_{BD} runs in terms of performances and accuracy of the solutions; (ii) vice versa the performances achieved by M_{2l} with the active approach are sensibly better; the norm of residuals are usually 1-2 orders of magnitude smaller (compare green and

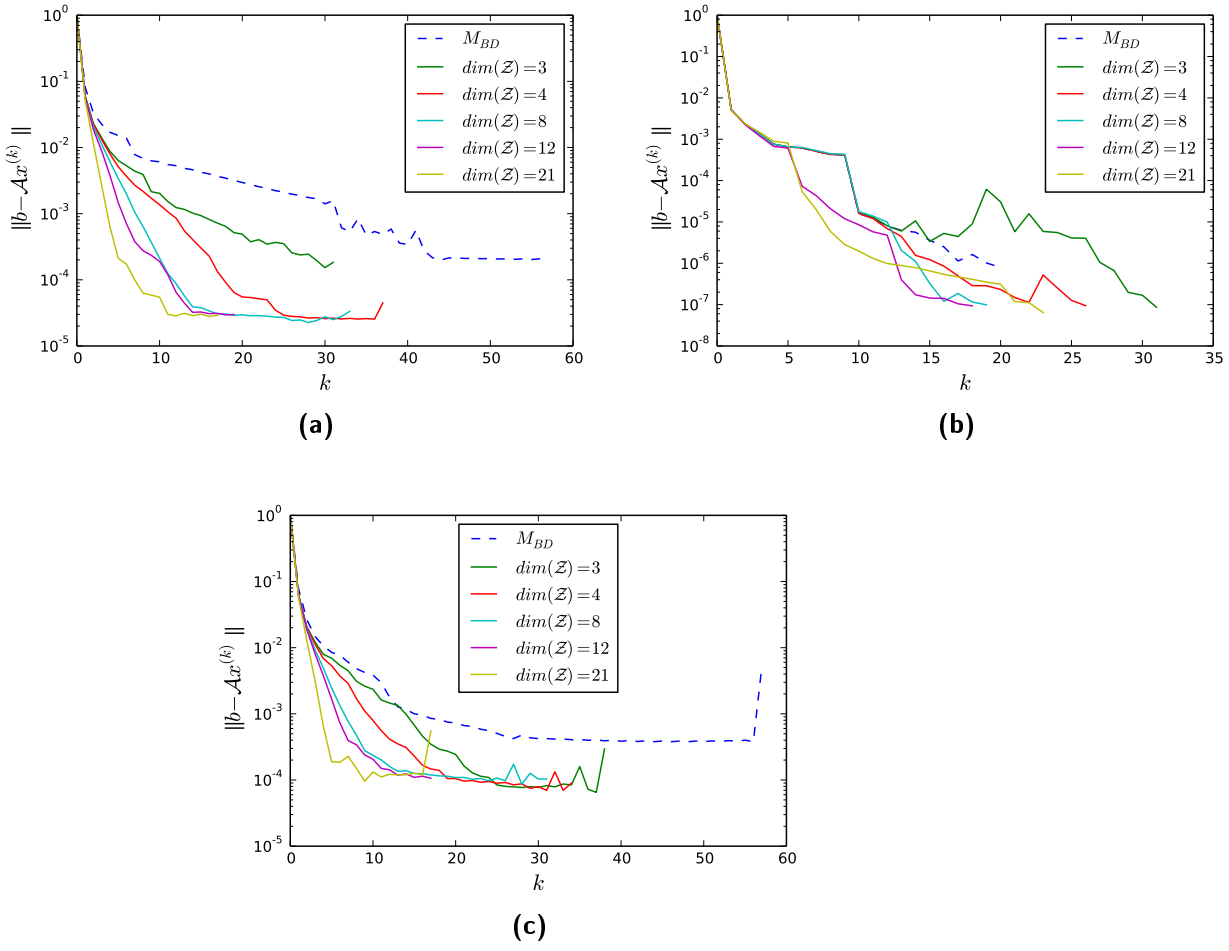

Figure 5.9: Residual norms for different choices of deflation subspace size (solid). As a reference the residuals of M_{BD} are added with dashed line. From Puglisi et al. (in prep.).

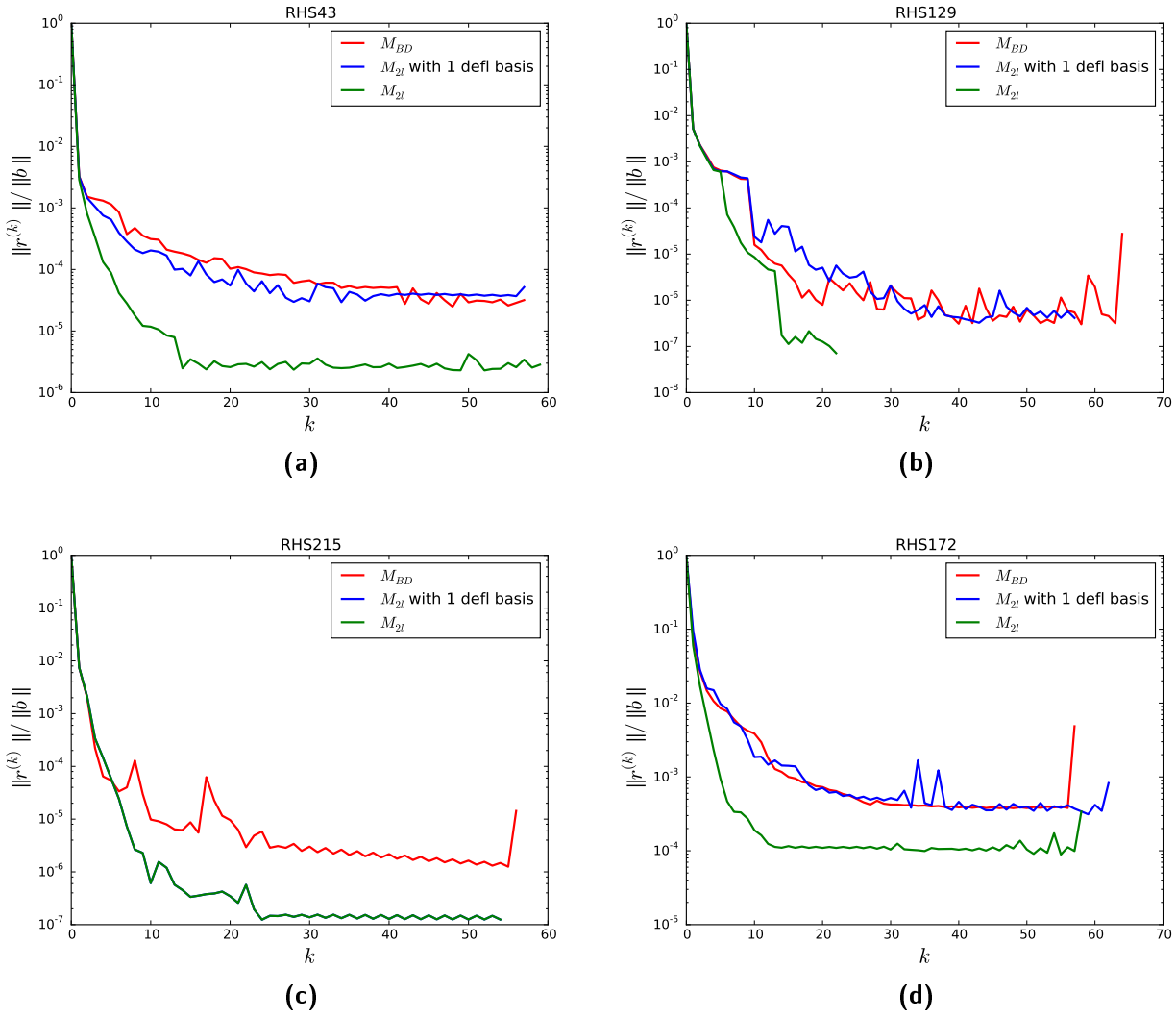

Figure 5.10: Runs encoding real data RHS (solid red) residuals in terms of iteration steps for M_{BD}; (solid blue) residuals for M_{2l} computed with one deflation basis, whereas (solid green) residuals with M_{2l} computed for each RHS, usually 14 eigenvectors are selected with a threshold smaller than 0.2. In panel (c) the blue and green lines overlap, since the two eigenvectors bases are the same. From Puglisi et al. (in prep.).

red lines in fig.5.10) and more than 50% of the runs get the PCG tolerance with less than 20 iterations, which is a factor ~ 3 smaller than the runs with the M_{BD}. To be more quantitative, we summarized in table 5.4 the number of converged runs to a PCG tolerance 10^{-4} and the total cpu time and we see that running the Arnoldi algorithm for each RHS requires ~ 50% larger computational cost, i. e. 22 kcpuh, for a run encoding all the RA23 dataset. In fact, the Arnoldi algorithm needs 50/60 iterations to get a tolerance of $\epsilon_{tol} = 10^{-8}$, chosen from a trade off between the Arnoldi threshold and cpu time. We remind that if a higher ϵ_{tol} is set the approximated eigenvectors are coarser.

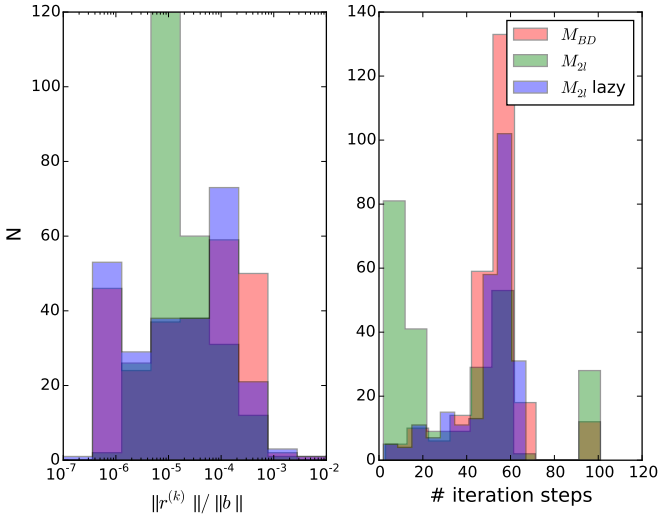

Figure 5.11: Histograms comparing PCG runs with 27 CESs tolerance 10^{-4}, (red) with M_{BD}, (green) with M_{2l} computed for each RHS, (blue) with M_{2l} built from one RHS and applied to all the data set. From Puglisi et al. (in prep.).

On the other hand, the results related to the M_{2l} lazy approach are not as good as the ones we observed in the signal-only data runs (fig.5.8). This could be somehow expected since the real data include noise, or extra correlation from some unfiltered signal. In the perspective of building a more representative deflation basis we applied the SVD method described in Appendix C to 10 precomputed eigenvector bases and built the M_{2l} from the most representative eigenvectors selected with this methodology and apply this solver to the real data. Unfortunately, no sensitive difference has been observed in this case, therefore we decided to test a different approach including more CESs in each RHS.

5.10.1 *PCG Solvers onto a larger dataset*

When we increase the size of each RHS by considering 3 times more CESs, (e. g. 81 CES per RHS) the first thing to be worried about is the limitation due to the memory sizes within each node. In fact, we considered 81 CESs

Preconditioner	CESs per RHS	Converged runs	Number runs	Number cpus	kcpuh
M_{BD}	27	153	257	130	13.5
M_{2l} active	27	224	257	130	21.8
M_{2l} lazy	27	187	257	130	12.9
M_{BD}	81	23	85	85	19.8
M_{2l} lazy	81	64	85	85	22.3

Table 5.4: Summary of PCG runs applied to Polarbear two seasons of data.

since this value is the maximum one that saturates the memory of Edison nodes. Other remarkable considerations are related to the execution time which in this case took roughly 20 kcpuh, each run lasting for 8 hours. Thus we decided to run the two-level PCG in the lazy approach and stop Arnoldi iterations at a higher tolerance ($\epsilon_{tol} = 10^{-6}$). We considered the same eigenvalue threshold as before ($\epsilon_\lambda = 0.2$) and 14 eigenvectors have been selected. With this new subgroups the number of PCG runs to be performed decreased proportionally by a factor of 3, so that 85 processing elements are requested for processing the whole dataset.

The performances in fig.5.12 show a clear indication that most $\sim 75\%$ of the runs preconditioned with M_{2l} converged within a tolerance of 10^{-4}, whereas for M_{BD} only 30%. Furthermore, more than 15 runs with M_{BD} did not converge within 100 iterations, whilst this number reduces to 2 for the two-level preconditioner. Moreover, the two-level preconditioner behaves as expected since the 20% of M_{2l} runs converged within 50 iterations.

All these features allow us to argue that the deflation basis computed only from a RHS encoding a larger number of samples, can be exploited to build the two-level preconditioner and be applied to the other RHSs. This is the reason why in the runs with 27 CESs per RHS, the two-level preconditioner (in the lazy approach) does not perform as well as in this case.

5.11 THE COADDED UNBIASED MAP FROM TWO SEASONS OF POLARBEAR DATA

Once all the maps $\hat{s}_i$ are obtained independently from all the groups of CESs, they are co-added with the following weighted average:

$$\hat{s} = \left(\sum_i (A^\dagger M A)|_i \right)^{-1} \sum_i (A^\dagger M A)|_i \hat{s}_i, \tag{5.27}$$

with i labelling each of CESs and M is the weight matrix, defined in (5.24). A diagonal element k of each matrix $(A^\dagger M A)_i$ corresponds to the weight associated to pixel k and all the weights can be represented in a map of weights as in fig.5.13(a).

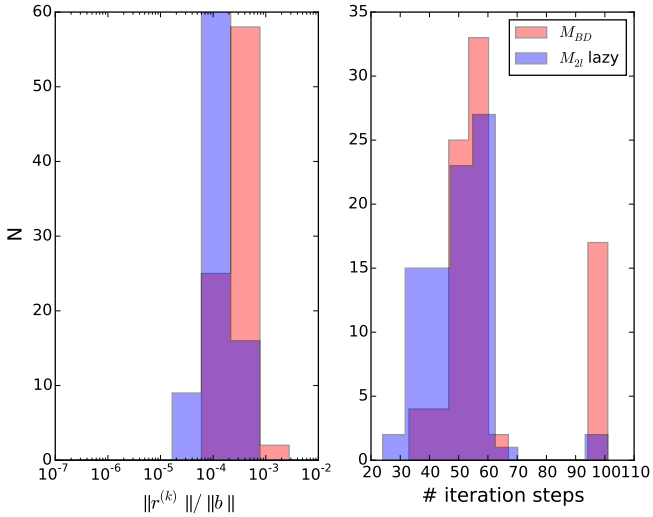

Figure 5.12: Histograms comparing PCG runs with 81 CESs with a tolerance 10^{-4}. From Puglisi et al. (in prep.).

In fig.5.13(b), we show the result of the map co-addition in (5.27) produced from the first two seasons of Polarbear validated dataset onto RA23 patch. The large-scale noisy modes clearly visible in the reconstructed maps are due to the modes which are poorly constrained during the reconstruction process partly because of the small size of the patch and partly because of some degenerate mode present in the PCG solution. Indeed they are remarkably similar to the long modes described in sect.5.6. Both the Q and U maps show two different long modes since as expected the Q and U coadded maps involve the sum of several unconstrained modes which are not symmetric one respect the other. This is the reason why the resulting Q and U maps in fig. reffig:hitcounts look asymmetric. To encompass this issue and for visualisation purposes, we applied a high-pass filter in order to remove the long trend bias from the map. The filter suppresses all the modes in the harmonic space with $\ell < 250$, to be far enough from the Polarbear science band is $500 < \ell < 2100$. Fig. 5.14 shows that we have a robust estimation of Q and U maps in the inner part of the patch (where are the most observed pixels, see fig.5.13(a)). One can easily recognize the horizontal and diagonal pattern respectively on Q and U maps: typical signature of the scalar component of E-modes.

5.12 BEYOND THE PCG: RUNNING WITH GMRES SOLVER

To further investigate the properties and the characteristics of M_{2l} we tested its performances onto a different Krylov solver: the GMRES. Computationally this algorithm is more memory consuming than the PCG, since at k-th iteration it has to retain all the k Arnoldi vectors previously computed to minimize the norm $\| Ax^{(k)} - b \| = \| \tilde{H}_k y_k - W_{k+1}^{\dagger} b \|$, where $\tilde{H}_k$, andW_{k+1} are similarly defined from (5.21). This is the reason why GMRES is com-

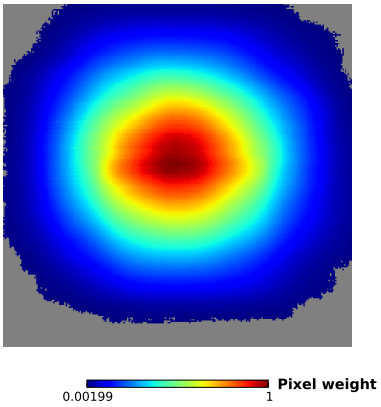

(a)

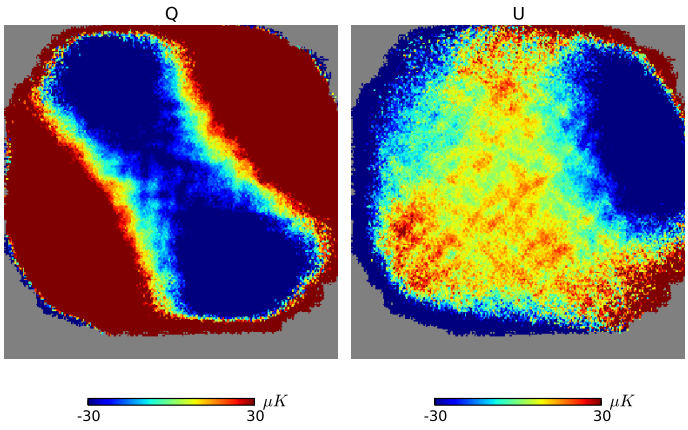

(b)

Figure 5.13: (a) Map of pixel weights of RA23 patch after two seasons of Polarbear observations. (b) The resulting Q and U maps from the coaddition in (5.27). Notice the large-scale noisy modes due to the poorly constrained modes. From Puglisi et al. (in prep.).

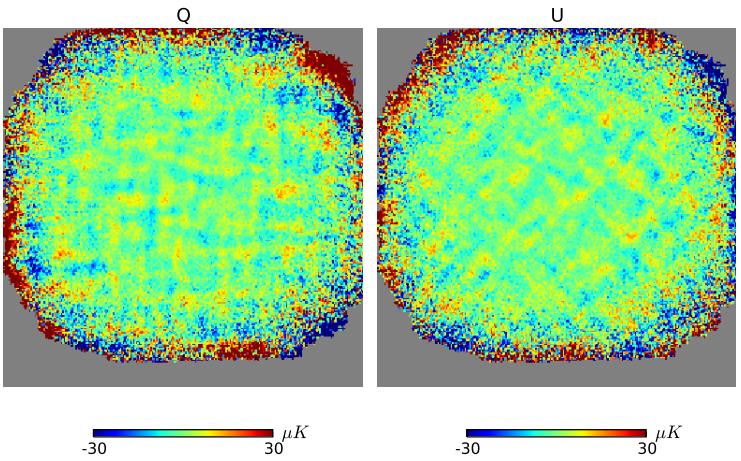

Figure 5.14: Q and U maps after high-pass filter applied to remove the long trend modes present in the coadded maps. From Puglisi et al. (in prep.).

monly restarted after m steps. This algorithm is a generalization of the *Minimal Residual* method and does not assume the system matrix to be SPD.

In this section, we show runs with the GMRES, as preliminary tests to probe different methodologies. We considered three different cases of restarts, $m = 30, 70, 500$ and performed the GMRES run for the daily map linear system preconditioned by M_{BD}, M_{2l}, the latter in both the lazy and active approach. As shown in fig. 5.15(a), the less the GMRES is restarted (i. e. the larger is m), the lower is the level of the convergence plateau. Moreover, in this case we get lower residuals compared to the ones achieved with the PCG. The residuals decrease in a step-wise behaviour (a short plateau then a sudden jump to lower values), which is very typical for the GMRES method. In fact, each of these steps is related to the way the GMRES computation works: it starts focusing around a cluster of eigenvalues refined at each iteration until all the eigenvalues have been very well constrained. The GMRES solver then moves to another eigenvalue cluster, thus we observe subsequently another plateau.

In fig.5.15(b) we show the differences in terms of performances of the M_{BD}(solid thin), M_{2l} active (dot-dashed) and M_{2l} lazy (solid thick). We see that the number of iterations reduced by a factor of 2, when we compare the M_{BD} runs with respect to the M_{2l} ones (dot-dashed). This is somewhat expected, since the Ritz eigenvectors are computed by means of the Arnoldi iterations from which the Hessenberg matrix $\tilde{H}_m$ is computed in the GMRES. In a certain sense, the GMRES benefits twice from the two-level preconditioner, not only because it gets rid of the smallest eigenvalues of $\mathcal{A}$, but also because roughly ~ 50 Arnoldi iterations have been already performed to compute the Ritz eigenvectors. This is clear by looking at the step-wise behaviour of the residuals in fig.5.15(b) since the dot-dashed lines present less steps than the solid thick ones.

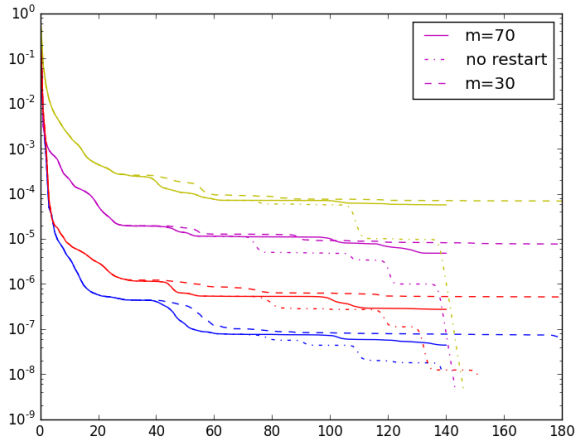

(a)

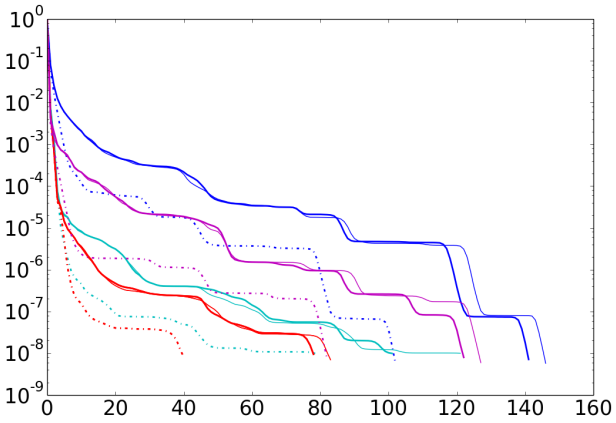

(b)

Figure 5.15: (a) A comparison of Restarted GMRES appplied on 4 RHS, shown are three cases for any choice of restart parameter $m = 30, (70)$ respectively in dashed (solid). We show also the case of unrestarted GMRES (dot-dashed) . (b) Runs of Unrestarted GMRES w/ M_{BD} (solid thin), M_{2l} (dot -dashed), M_{2l} with 1 eigenvector basis applied to all the RHS (solid thick).

5.13 SUMMARY

In this Chapter, we focused on the CMB map-making problem and reconstructed CMB polarization maps from both simulated and real data by means of PCG algorithm. We implemented a pipeline based on a novel class of preconditioners, the two-level preconditioner that relies on projecting out all the modes responsible of hindering the PCG convergence with standard methodologies.

To validate the implementation, end-to-end runs have been performed by means of a data set generated from scanning signal-only map with the pointing and polarization angle informations of the RA23 Polarbear patch. We further applied this methodology to two seasons of data of Polarbear experiment and have found that this proposed methodology converges within less iteration steps (roughly 2 times less with respect to the standard methods) to 2 orders of magnitude lower threshold.

Since the performances of this methodology depends more on the condition number of the system matrix than on the number of pixels, it is really promising for being applied by the forthcoming ground-based CMB experiments, whose observation patches are increasingly getting wider ad wider than the previous ones.

Finally, Given the results obtained with the two-level preconditioner, a massively parallel implementation of the code has to be considered especially to better exploit the computational power available in modern computing systems.

All this is subject of a paper being written in parallel to this Thesis, in preparation of the forthcoming Polarbear Large Patch analysis described in the previous Chapter.

6

CONTAMINATION TO CMB POLARIZATION: A 3D MODEL FOR CO MOLECULAR LINE EMISSION

> In some strange way, any new fact or insight that I may have found has not seemed to me as a "discovery" of mine, but rather something that had always been there and that I had chanced to pick up.
>
> Subrahmanyan Chandrasekhar

In the previous Chapter, the work carried out during the PhD concerning the production of maps in the Polarbear experiment was presented. In this chapter, we present the work that has been recently published in Puglisi, Fabbian, and Baccigalupi (2017). It represents our contribution for the modelization and forecasting of the polarized foreground emission to be exploited in Polarbear and other experiments. It represents the last and missing step in the modelling of the Galactic emission, concerning compact clouds, in addition to the main diffuse foregrounds presented in sect.3.2.

6.1 CARBON MONOXIDE

The Carbon monoxide (CO) molecule is one of the most interesting molecules present in molecular clouds within our Galaxy. Although the most abundant molecule in Galactic molecular clouds is molecular hydrogen (H_2), it is inconvenient to use the emission from that as a tracer because of a low dipole moment making it a very inefficient radiator. We therefore need to resort to alternative techniques for tracing molecular clouds using rotational or vibrational transitions of other molecules such as CO. Observations of CO emission are commonly used to infer the mass of molecular gas in the Milky Way by assuming a linear proportionality between the CO and H_2

densities via the CO-to-H_2 conversion factor, X_{CO}. A commonly accepted value for X_{CO} is 2×10^{20} molecules $\cdot$ cm^{-2} (K km s^{-1})$^{-1}$, although this could vary with position in the Galactic plane, particularly in the outer Galaxy (Balser, Rood, Bania, & Anderson, 2011).

The most intense CO rotational transition lines are the $J = 1 \rightarrow 0$, $2 \rightarrow 1$, $3 \rightarrow 2$ transitions at sub-millimetre wavelengths (115, 230 and 345 GHz respectively). These can usually be observed in optically thick and thermalized regions of the interstellar medium. Traditionally, the observations of standard ^{12}CO emission are complemented by measurements of ^{13}CO lines. Being less abundant (few percent), this isotopologue can be exploited for inferring the dust extinction in nearby clouds and hence providing a better constraint for measuring the H_2 abundance (Bally, Langer, Stark, & Wilson, 1987; Jackson et al., 2006). However, there is growing evidence that ^{13}CO regions could be associated with colder and denser environments, whereas ^{12}CO emission originates from a diffuse component of molecular gas (Roman-Duval et al., 2016).

The spatial distribution of the CO line emission reaches a peak in the inner Galaxy and is mostly concentrated close to or within the spiral arms, in a well-defined ring, the so-called *molecular ring* between about $4-7$ kpc from the Galactic centre. This property is not unique to the Milky Way but is quite common in barred spiral galaxies (see Regan, Sheth, Teuben, and Vogel (2002) for references). The emission in the direction orthogonal to the Galactic plane is confined within a Gaussian slab with roughly 90 pc FWHM in the inner Galaxy getting broader towards the outer Galactic regions, reaching a FWHM of several hundred parsecs outside the solar circle. In the centre of the Galaxy, we can also identify a very dense CO emission zone ,rich in neutral gas and individual stars, stretching out to about 700 light years (ly) from the centre and known as the *Central Molecular Zone*.
Since the 1970s, many CO surveys of the Galactic plane have been carried out with ground-based telescopes, leading to accurate catalogues of molecular clouds (Dame, Hartmann, & Thaddeus, 2001; Mizuno & Fukui, 2004). Usually these surveys have observed a strip of $|b| \lesssim 5$ deg around the Galactic plane. At higher Galactic latitudes ($|b| > 30$ deg), the low opacity regions of both gas and dust, together with a relatively low stellar background which is useful for spotting extinction regions, complicate the observation of CO lines making this very challenging. In fact, only ≈ 100 clouds have been detected so far in these regions.
The Planck satellite team recently released CO emission maps of the lowest rotational lines, $J = 1-0, 2-1, 3-2$ observed in the 100, 217, 353 GHz frequency channels of the HFI (Planck Collaboration, Adam, Ade, Aghanim, Alves, et al., 2016; Planck Collaboration, Ade, Aghanim, Alves, et al., 2014b). These were sensitive enough to map the CO emission even though the widths of these lines are orders of magnitude narrower than the bandwidth of the Planck frequency channels. These single frequency maps have been processed with a dedicated foreground cleaning procedure so as

to isolate this emission. The Planck maps were found to be broadly consistent with the data from other CO surveys (Dame et al., 2001; Heyer & Dame, 2015), although they might still be affected by residual astrophysical emissions and instrumental systematics. In fig. 6.1, we show the so called Type 1 Planck map of the CO $J : 1 - 0$ line (Planck Collaboration, Ade, Aghanim, Alves, et al., 2014b)which will be used in the following.

As we have discussed in the first three chapters of this thesis, many current and future CMB polarization experiments are designed to exploit the faint B-mode signal of CMB polarization as a cosmological probe, in particular to constrain the physics of large scale structure formation or the inflationary mechanism in the early Universe (Hu & White, 1997; Seljak & Zaldarriaga, 1997). As we have discussed in Chapter 3, one of the main challenges in the way of achieving the B-mode signal is the contamination of the primordial CMB signal by diffuse Galactic emission. In this respect, the synchrotron and thermal dust emission are known to be potentially the most dangerous contaminants, because they are intrinsically polarized: appropriate observations, theoretical investigations and modelling of polarized foreground emission at sub-mm frequencies are therefore crucial for the success of future CMB-S4 experiments. However, as these will observe at frequencies overlapping with the CO lines, unresolved CO line emission could significantly contaminate these measurements as well.
CO lines are in fact expected to be polarized at the percent level or below (Goldreich & Kylafis, 1981) because of interaction of the magnetic moment of the molecule with the Galactic magnetic field. This causes the so-called *Zeeman splitting* of the rotational quantum levels J into the magnetic sublevels M which are intrinsically polarized. Moreover, if molecular clouds are somehow anisotropic (e.g when in the presence of expanding or collapsing envelopes in star formation regions) or are asymmetric, population imbalances of the M levels can arise. This leads to different line intensities depending on the directions (parallel or perpendicular to the magnetic field) and to a net linearly polarized emission. Greaves, Holland, Friberg, and Dent (1999) detected polarization in five star-forming regions near to the Galactic Centre while observing the CO lines $J = 2 - 1$, $3 - 2$ and the $J = 2 - 1$ of the isotopologue ^{13}CO. The degree of polarization ranged from 0.5 to 2.5%. Moreover, the deduced magnetic field direction was found to be consistent with previous measurements coming from dust polarimetry, showing that the polarized CO emission could become a sensitive tracer of small-scale Galactic magnetic fields.

In this chapter and in Puglisi et al. (2017), we propose a statistical 3D parametric model of CO molecular cloud emission, in order to forecast the contamination of CMB signal by this, including polarization. Being able to perform statistical simulation of this emission is crucial for assessing the impact of foreground residual uncertainties on cosmological constraints coming from the CMB. In addition, the capability of modeling the Galactic

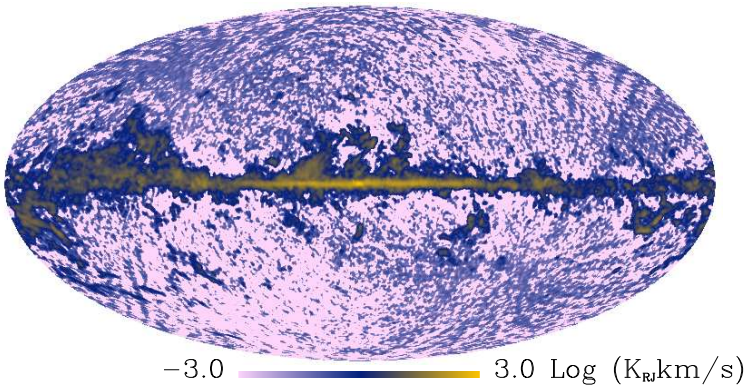

Figure 6.1: Planck CO $1-0$ map (Planck Collaboration, Adam, Ade, Aghanim, Alves, et al., 2016). Note the predominance of instrumental noise in regions far from the Galactic plane. From Puglisi et al. (2017).

foreground emission in its full complexity taking into account line-of-sight effects is becoming necessary in light of the latest experimental results and the expected level of sensitivity for the future experiments (Planck Collaboration et al., 2017; Tassis & Pavlidou, 2015). In sect. 6.2 we present the assumptions made for building the model and the simulation pipeline for its implementation. In sect. 6.3 we describe the methodology for calibrating the CO simulations to match Planck observations. In sect. 6.3.4 we show how the parameters describing molecular cloud distribution shape the angular power spectrum of CO emission. Finally, in sect.6.4 we forecast the expected level of polarized CO contaminations for the CMB B-modes at high Galactic latitudes using our calibrated simulation of sect. 6.3 to infer statistically the emission at high Galactic latitude, where current observations are less reliable.

6.2 BUILDING A STATISTICAL 3D CO EMISSION MODEL

In order to build an accurate description of CO emission in the Galaxy, we collected the most up to date astrophysical data present in the literature concerning the distribution of molecular gas as a function of the Galactic radius (R) and the vertical scale of the Galactic disk (z) as well as of the molecular size and the mass function. The model has been implemented in a Python package named `MCMole3D`[1] which is publicly available, and we present details of it in this Section[2]. The model builds on and extends the method proposed by Ellsworth-Bowers et al. (2015) who conducted a series of analyses distributing statistically a relative large number of molecular cloud objects according to the axisymmetric distribution of H_2 observed in the Galaxy (Wolfire, McKee, Hollenbach, & Tielens, 2003).

1 https://github.com/giuspugl/MCMole3D
2 In the following we will refer to this model as the `MCMole3D` model for the sake of clarity.

6.2.1 *CO cloud spatial distribution*

As mentioned in the introduction, the CO emission is mostly concentrated around the molecular ring. We have considered and implemented two different spatial distributions of the molecular clouds: an axisymmetric *ring-shaped* one and one with 4 spiral arms, as shown in fig. 6.3 (b) and (a) respectively. The first is a simplified model and is parametrized by R_{ring},and σ_{ring} which are the radius and the width of the molecular ring respectively. On the other hand, the spiral arm distribution is in principle closer to the symmetry of our Galaxy and is therefore more directly related to observations. The distribution is described by two more parameters than for the axisymmetric case: the arm width and the spiral arm pitch angle. For the analysis conducted in the following sections, we fixed the value of the pitch angle to be $i \sim -13\,\mathrm{deg}$ following the latest measurements of (Bobylev & Bajkova, 2013; Davis et al., 2012) and fixed the arm half-width to be 340 pc (Vallée, 2014).

Bronfman, Cohen, Alvarez, May, and Thaddeus (1988) found that the vertical profile of the CO emissivity can be optimally described by a Gaussian function of z centred on z_0 and having a half-width $z_{1/2}$ from the Galactic plane at $z = 0$. Both of the parameters z_0 and $z_{1/2}$ are in general functions of the Galactic radius R (see Heyer and Dame (2015) for recent measurements). Since we are interested in the overall distribution of molecular clouds mainly in regions close to the Galactic plane, where data are more reliable, we adopted this parametrization but neglected the effects of the mid-plane displacement z_0 and set it to a constant value $z_0 = 0$, following Delabrouille et al. (2013). The vertical profile is then parametrized just by $z_{1/2}$ and mimics the increase of the vertical thickness scatter that is observed when moving from the inner Galaxy towards the outer regions:

$$z_{1/2}(R) \propto \sigma_z(R) = \sigma_{z,0} \cosh\left(\frac{R}{h_R}\right), \tag{6.1}$$

where $\sigma_{z,0} = 0.1$ and $h_R = 9$ kpc corresponds to the radius where the vertical thickness starts increasing. The half-width $z_{1/2}$ is related to σ_z through the usual relation $z_{1/2} = \sqrt{2\ln 2}\sigma_z$. The final vertical profile is then:

$$z(R) = \frac{1}{\sqrt{2\pi}\sigma_z(R)} \exp\left[-\left(\frac{z}{\sqrt{2}\sigma_z(R)}\right)^2\right]. \tag{6.2}$$

6.2.2 *CO cloud emission*

The key ingredients for modeling the molecular cloud emission are the dimension of the cloud and its typical emissivity. We assume an exponential CO emissivity profile which is a function of the Galactic radius following Heyer and Dame (2015), Roman-Duval et al. (2016):

$$\epsilon_0(R) = \epsilon_c \exp\left(R/R_{em}\right), \tag{6.3}$$

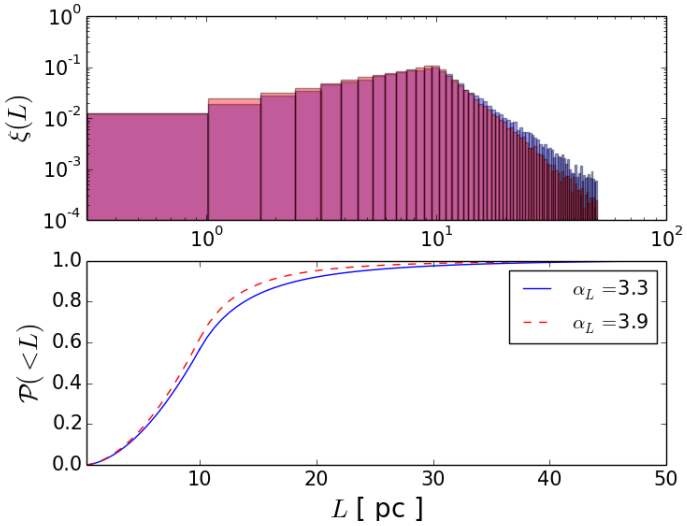

Figure 6.2: (top) Histograms of dN/dL computed by assigning the size of each cloud with the probability function (bottom). The two spectral indices $\alpha_L \approx 3.3\,(3.9)$ refer respectively to clouds in the inner (outer) Galaxy. From Puglisi et al. (2017).

where ϵ_c is the typical emissivity of a particular CO line observed towards the centre of the Galaxy and R_{em} the scale length over which the emissivity profile changes. Clouds observed in the outer Galaxy are in fact dimmer.
We then assume the distribution of cloud size $\xi(L)$ defined by their typical size scale, L_0, the range of sizes $[L_{min}, L_{max}]$ and two power-laws with spectral indices (Roman-Duval, Jackson, Heyer, Rathborne, & Simon, 2010)

$$\xi(L) = \frac{dn}{dL} \propto \begin{cases} L^{0.8} & \text{if } L_{min} < L < L_0, \\ L^{-\alpha_L} & \text{if } L_0 < L < L_{max}, \end{cases} \tag{6.4}$$

with $\alpha_L = 3.3, 3.9$ for clouds inside or outside the solar circle respectively. From the cloud size function $\xi(L)$ we derive the corresponding probability $\mathcal{P}(L)$ of having clouds with sizes smaller than L:

$$\mathcal{P}(< L) = \int_{L_{min}}^{L} dL' \xi(L'). \tag{6.5}$$

The probability functions for different choices of the spectral index α_L are shown in fig. 6.2. We then inverted (6.5) to get the cloud size associated with a given probability $L(p)$. The cloud sizes are drawn from a uniform distribution in $[0, 1]$. The histograms of the sizes generated following this probability function are shown in the top panel of fig. 6.2 and are peaked around the most typical size L_0. In the analysis presented in the following L_0 is considered as a free parameter.
Finally, we assume a spherical shape for each of the simulated molecular clouds once they are projected on the sky. However, we implemented different emissivity profiles that are function of the distance from the cloud

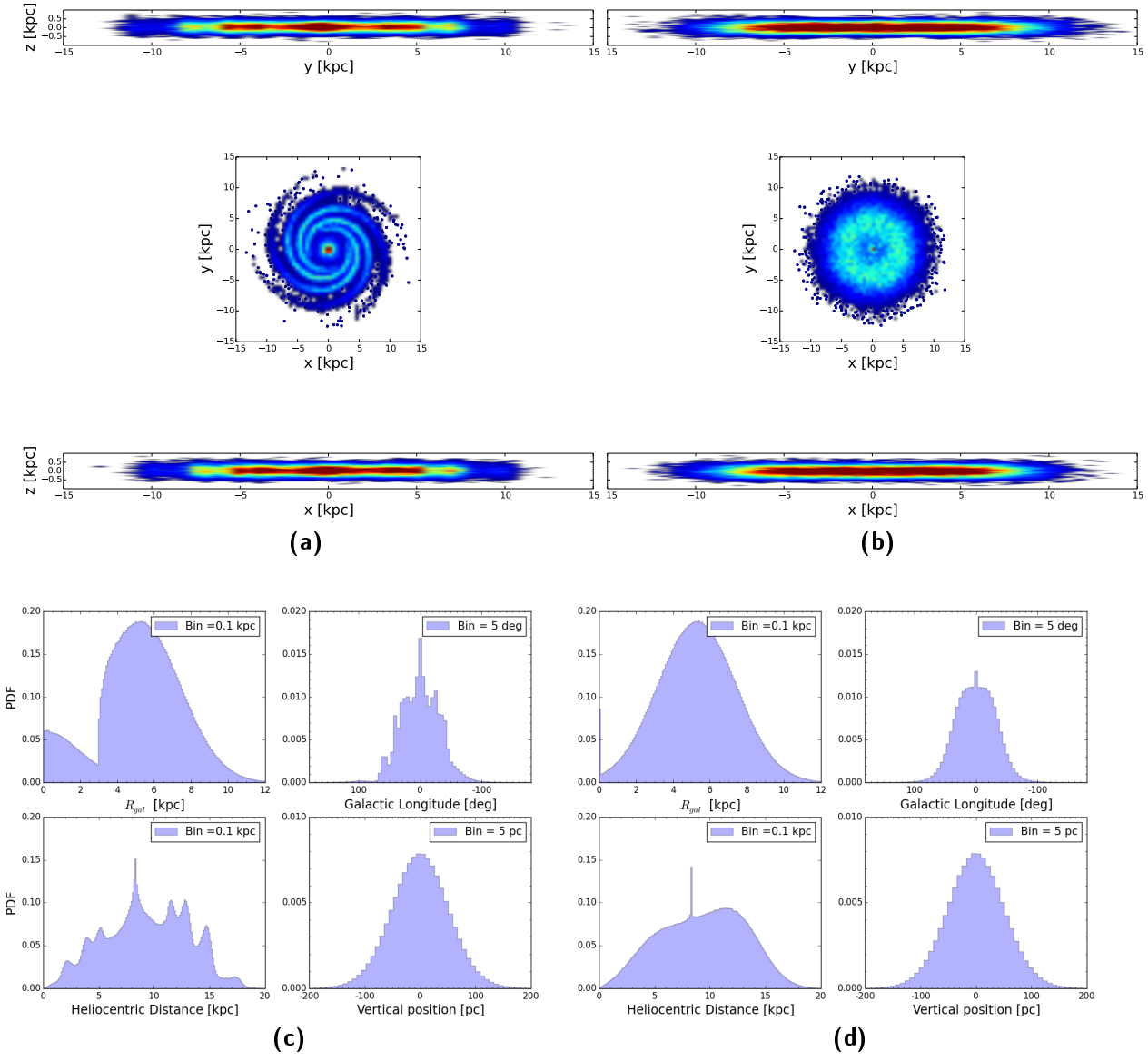

Figure 6.3: Top panels: Density contour plots of an MC galaxy population with 40,000 objects distributed following the (a) `LogSpiral` and (b) `Axisymmetric` distributions. Bottom panels: Probability Density Function (PDF) of 100 MC realizations of 40,000 molecular clouds following the (c) `LogSpiral` and (d) `Axisymmetric` geometry. The latter case is consistent with results in Ellsworth-Bowers et al. (2015). From Puglisi et al. (2017).

`MCMole3D` Default parameters	
N_{clouds}	40,000
R_{ring} [kpc]	5.3
L_{min} [pc]	0.3
L_{max} [pc]	60
$\sigma_{z,0}$ [pc]	100
h_R [kpc]	9
R_{bar} † [kpc]	3
i † [deg]	-12
ϵ_c $[K_{RJ}\,km\,s^{-1}]$	240
R_{em} [kpc]	6.6
L_0 [pc]	[5,50] Default: 20
σ_{ring} [kpc]	[1,5] Default:2.5

Table 6.1: List of parameters used in `MCMole3D` simulations. † only for `LogSpiral`.

center, such as *Gaussian* or *cosine* profiles. These are particularly useful because, by construction, they give zero emissivity at the boundaries[3] and the maximum of the emissivity in the centre of the projected cloud on the sky. This not only mimics a decrease of the emission towards the outer regions of the cloud, where the density decreases, but also allows to minimize numerical artifacts when computing the angular power spectrum of the simulated maps (see sect. 6.3). An abrupt top-hat transition at the boundary of each cloud would in fact cause ringing effects that could bias the estimate of the power spectrum.

6.2.3 *Simulation procedure*

The model outlined in the previous Section enables statistical simulations of CO emission in our Galaxy to be performed for a given set of free parameters Θ^{CO} that can be set by the user:

$$\Theta^{CO} = \{N_{clouds},\ \epsilon_c,\ R_{em},\ R_{ring},\ \sigma_{ring},\ \sigma_{z,0},\ h_R,\ L_{min},\ L_{max},\ L_0\}.$$

The values chosen for our analysis are listed in 6.1.

For each realization of the model, we distribute by default 40,000 clouds within our Galaxy. This number is adopted for consistency with observations when observational cuts are applied (for further details see Ellsworth-Bowers et al. (2015)). The product of each simulation is a map, similar to the one in fig. 6.4, in the HEALPix scheme including all the simulated clouds as

3 For the Gaussian profile, we set σ in order to have the cloud boundaries at 6σ, i.e. where the Gaussian function is zero to numerical precision.

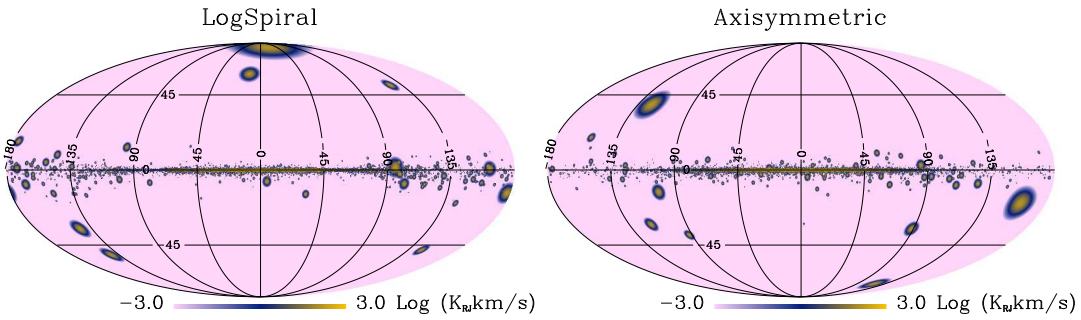

Figure 6.4: Two realizations of CO maps simulated with `MCMole3D` using the distribution parameters given by the values in 6.1. From Puglisi et al. (2017).

seen by an observer placed in the solar system. This map can be smoothed to match the resolution of a specific experiment and/or convolved with a realistic frequency bandwidth. When we compare with the Planck maps described in sect. 6.3, we convolve the simulated maps to the beam resolution of the 100 GHz channel (~ 10 arcmin).
The procedure implemented for each realization is the following.

1. Assign the (R_{gal}, ϕ, z) Galacto-centric positions. In particular:
   - R_{gal} is extracted from a Gaussian distribution defined by the R_{ring} and σ_{ring} parameters. However, the σ_{ring} is large enough to give non-zero probability at $R_{gal} \leqslant 0$. All of the negative values of R_{gal} are either automatically set to $R_{gal} = 0$ (axisymmetric case), or recomputed extracting new positive values from a normal distribution centred at $R = 0$ and with the r.m.s given by the scale of the Galactic bar (spiral-arm case). This choice allows us to circumvent not only the issue of negative values of R_{gal} due to a Gaussian distribution, but also to produce the high emissivity of the Central Molecular zone (see Ellsworth-Bowers et al. (2015) for a similar approach).
   - The z-coordinate is drawn randomly from the distribution in (6.2).
   - The azimuth angle ϕ is computed from a uniform distribution ranging over $[0, 2\pi)$ in the case of the axial symmetry. Conversely, in the case of spiral arms, ϕ follows the *logarithmic spiral* polar equation

     $$\phi(R) = A \log R + B,$$

     where $A = (\tan i)^{-1}$ and $B = -\log R_{bar}$ are, respectively, functions of the mean pitch angle and the starting radius of the spiral arm. In our case we set $i = -12$ deg, $R_{bar} = 3$ kpc.
2. Assign cloud sizes given the probability function $\mathcal{P}(L)$ ((6.5)).
3. Assign emissivities to each cloud from the emissivity profile (see (6.3)).

4. Convert (R_{gal}, ϕ, z) positions into the *heliocentric* coordinate frame $(\ell, b, d_\odot)$.

In fig. 6.3 we show an example of the 3D distribution of the emission as well as the distribution of the location of the simulated clouds using both of the geometries implemented in the package.

6.2.4 *Simulation results*

In fig. 6.4 we show two typical realizations of maps of CO emission for the `Axisymmetric` and `LogSpiral` geometries prior to any smoothing. As we are interested in the statistical properties of the CO emission, we report a few examples of the angular power spectrum C_ℓ corresponding to different distributions of CO emission in fig. 6.5. In the ones shown subsequently the spectra are $\mathcal{D}_\ell$ encoding a normalization factor $\mathcal{D}_\ell = \ell(\ell+1)C_\ell/2\pi$.

We can observe two main features in the morphology of the power spectrum: a bump around $\ell \sim 100$ and a tail at higher ℓ. We interpret both of these features as the projection of the distribution of clouds from a reference frame off-centred (on the solar circle).
The bump reflects the angular scale ($\sim$ 1 deg) related to the clouds which have the most likely size, parametrized by the typical size parameter, L_0, and which are close to the observer. On the other hand, the tail at $\ell \gtrsim 600$ (i.e. the arcminute scale) is related to the distant clouds which lie in the diametrically opposite position with respect to the observer. This is the reason why the effect is shifted to smaller angular scales. The L_0 and σ_{ring} parameters modify the power spectrum in two different ways. For a given typical size, if the width of the molecular ring zone σ_{ring} increases, the peak around $\ell \sim 100$ shifts towards lower multipoles, i.e. larger angular scales, and its amplitude increases proportionally to σ_{ring}, see for instance the bottom right panel in fig. 6.5. This can be interpreted as corresponding to the fact that the larger is σ_{ring}, the more likely it is to have clouds closer to the observer at the solar circle with a typical size given by L_0. On the other hand, if we choose different values for the size parameter (left panels in fig. 6.5) the tail at small angular scales moves downwards and flattens as L_0 increases. Vice versa, if we keep L_0 constant (fig. 6.5 bottom right panel), all of the tails have the same amplitude and an ℓ^2 dependency. In fact, if L_0 is small, the angular correlation of the simulated molecular clouds looks very similar to the one of *point sources* which has *Poissonian* behaviour. Conversely if the typical size increases, the clouds become larger and they behave effectively as a coherent diffuse emission and less as point sources.

Far from the Galactic plane, the shape of the power spectrum is very different. In fig. 6.6 we show an example of the average power spectrum of 100 MC realizations of CO emission at high Galactic latitudes, i.e. $|b| > 30$ deg, for both the `Axisymmetric` and `LogSpiral` geometries. For this run we choose the so-called best fit values for the L_0 and σ_{ring} parameters discussed

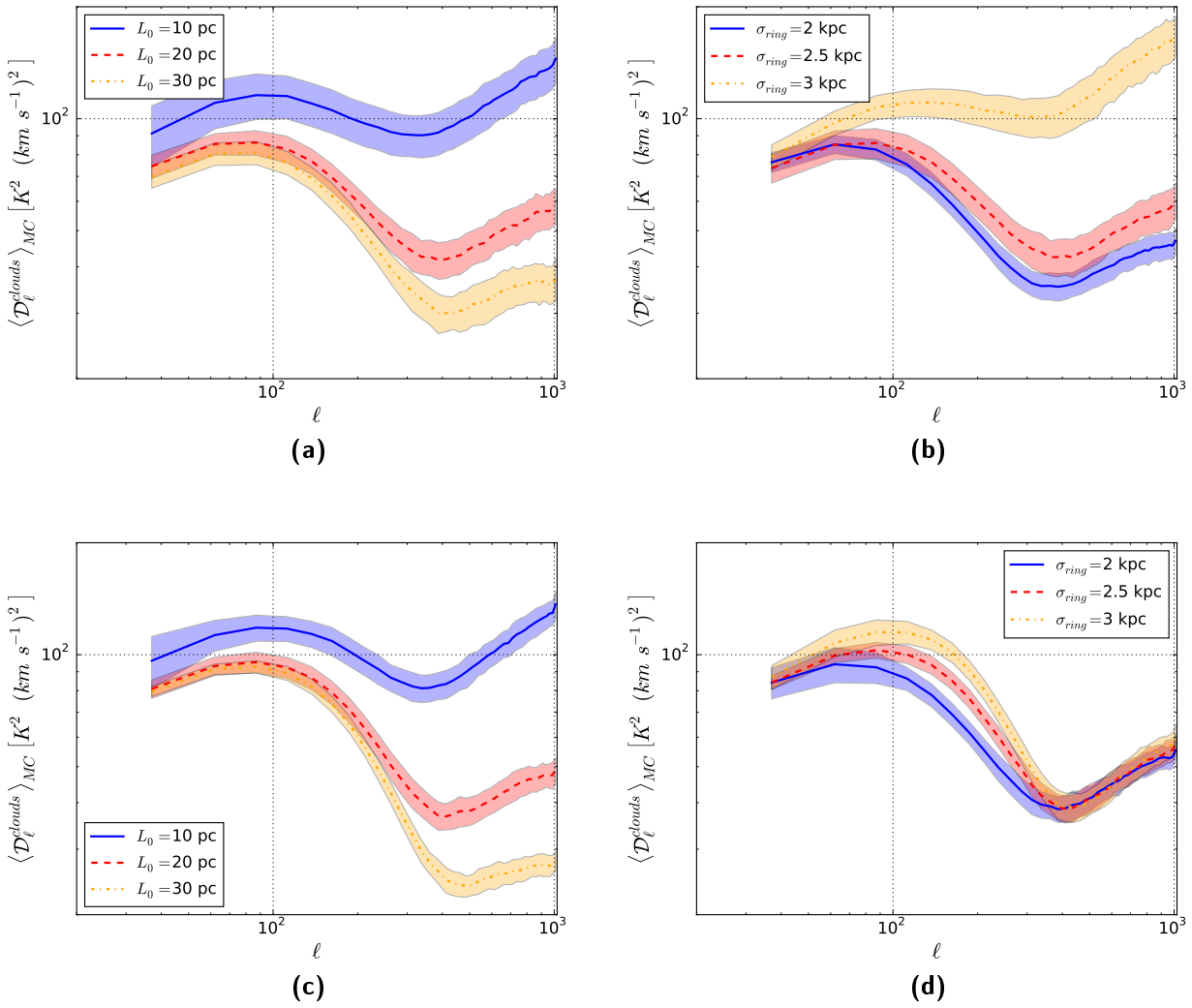

Figure 6.5: Angular power spectra of CO emission in the Galactic plane computed for 100 MC realizations of the `MCMole3D` model assuming different values of its free parameters. The mean value of the simulation is shown by solid, dashed and dot-dashed lines while the shaded area represents the measured variance of the realizations. The top row shows the case of an `Axisymmetric` geometry while the bottom panel displays results for a `LogSpiral` geometry. Results obtained by varying the L_0 ($\sigma_{\mathtt{ring}}$) parameters are shown on the left (right) column. From Puglisi et al. (2017).

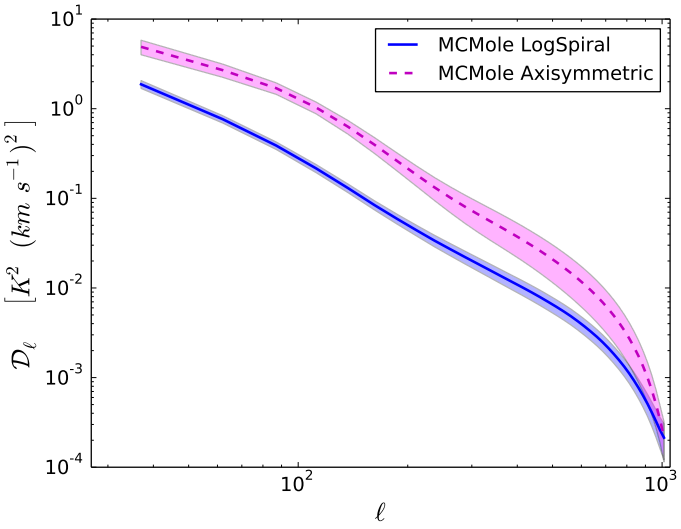

Figure 6.6: Examples of the power spectra of CO emission at high Galactic latitudes (|b| $>$ 30 deg) for `Axisymmetric` and `LogSpiral` geometries. For both the geometries we assumed the best-fit values of the parameters describing the CO distribution presented in sect. 6.3.4. From Puglisi et al. (2017).

later in sect. 6.3.4. In addition to the different shape depending on the assumed geometry, one can notice a significant amplitude difference with respect to the power spectrum at low latitudes. Moreover, this is in contrast with the trend observed in the Galactic plane, where the `LogSpiral` geometry tends to predict a power spectrum of higher amplitude. In both cases, however, the model suppresses the emission in these areas, as shown in fig. 6.4. In the `LogSpiral` case, the probability of finding clouds in regions in between spiral arms is further suppressed and could explain this feature. The emission is dominated by clouds relatively close to the observer for both geometries, and so the angular correlation is mostly significant at large angular scales (of the order of a degree or more) and is damped rapidly at small angular scales.

6.3 COMPARISON WITH PLANCK DATA

6.3.1 *Dataset*

The Planck collaboration released three different kinds of CO molecular line emission maps, described in Planck Collaboration, Ade, Aghanim, Alves, et al. (2014b), Planck Collaboration, Adam, Ade, Aghanim, Alves, et al. (2016). We decided to focus our analysis on the so-called *Type 1* CO maps which have been extracted exploiting differences in the spectral transmission of a given CO emission line in all of the bolometer pairs relative to the same frequency channel. Despite being the noisiest set of maps, *Type 1* are in fact the cleanest maps in terms of contamination coming from other frequency

channels and astrophysical emissions. In addition, they have been obtained at the native resolution of the Planck frequency channels, and so allow full control of the effective beam window function for each map.
For this study we considered in particular the CO $1-0$ line, which has been observed in the 100 GHz channel of the HFI instrument. This channel is in fact the most sensitive to the CO emission in terms of signal-to-noise ratio (SNR) and the 1-0 line is also the one for which we have the most detailed external astrophysical observations. However, the Planck frequency bands were designed to observe the CMB and foreground emissions which gently vary with frequency and, thus, they do not have the spectral resolution required to resolve accurately the CO line emission. To be more quantitative, the Planck spectral response at 100 GHz is roughly 30 GHz, which corresponds to $\sim 8000\,\mathrm{km\,s^{-1}}$, i.e. about 8 orders of magnitude larger than the CO rotational line width (which can be easily approximated as a Dirac delta). Therefore, the CO emission observed by Planck along each line of sight is integrated over the whole channel frequency band. Further details about the spectral response of the HFI instrument can be found in Planck Collaboration, Ade, Aghanim, Armitage-Caplan, et al. (2014).

6.3.2 *Observed CO angular power spectrum*

Since one of the goals of this study is to understand the properties of diffuse CO line emission, we computed the angular power spectrum of the *Type 1* $1-0$ CO map to compare qualitatively the properties of our model with the single realization given by the emission in our Galaxy. We distinguish two regimes of comparison, low Galactic latitudes ($|b| \leqslant 30\,\mathrm{deg}$) and high Galactic latitude ($|b| > 30\,\mathrm{deg}$). While at low Galactic latitudes the signal is observed with high sensitivity, at high latitudes it is substantially affected by noise and by the fact that the emission in this region is faint due to its low density with respect to the Galactic disk.
In fig. 6.7 we show the angular power spectra of the first three CO rotational line maps observed by Planck as well as the expected noise level at both high and low Galactic latitudes computed using a pure power spectrum estimator X^2PURE (Grain et al., 2009). This is a pseudo power spectrum method (Hivon et al., 2002) which corrects the so called E-to-B-modes leakage in the polarization field that arises in the presence of incomplete sky coverage (Bunn et al., 2003; Lewis et al., 2001; Smith & Zaldarriaga, 2007). Although this feature is not strictly relevant for the analysis of this Section, because we are considering the unpolarized component of the signal, it is important for the forecast presented in sect. 6.4. We estimated the noise as the mean of 100 MC Gaussian simulations based on the the diagonal pixel-pixel error covariance included in the Planck maps. One may notice how the noise has a level comparable to that of the CO power spectrum at high Galactic latitude. However, we note that the released *Type 1* maps are obtained from the full mission data from Planck, and not from subsets of the data (e.g. using the so called half-rings or half-mission splits). Thus, it was

not possible to test whether the observed flattening of the power spectrum at large angular scale is due to additional noise correlation not modelled by the Gaussian uncorrelated model discussed above. We notice that, if these maps were present, we could have had an estimate of this correlation using the noise given by the difference between the map auto-spectra and the noise-bias free signal obtained from the cross-spectra of the maps from data subsets. Since even for the $1-0$ line the noise becomes dominant on scales $\ell \approx 20$, we decided to limit the comparison at low Galactic latitude where the signal to noise ratio is very high.
We note that in the following we considered the error bars on the power spectrum as coming from the gaussian part of the variance, i.e., following Hivon et al. (2002)

$$\Delta\tilde{C}_\ell = \sqrt{\frac{2}{\nu}}(C_\ell + N_\ell), \tag{6.6}$$

where ν is the number of degrees of freedom taking into account the finite number of modes going into the power spectrum calculation in each ℓ mode and the effective sky coverage. N_ℓ represents the noise power spectrum and the C_ℓ is the theoretical model describing the CO angular power spectrum with the tilde denoting measured quantities. Since the true CO theoretical power spectrum is unknown, we assumed that $C_\ell + N_\ell = \tilde{C}_\ell$. The Gaussian approximation however underestimates the error bars. The CO field is in fact a highly non-gaussian field with mean different from zero. As such, its variance should contain contributions coming from the expectation value of its 1 and 3 point function in the harmonic domain that are zero in the Gaussian approximation. These terms are difficult to compute and we considered the Gaussian approximation sufficient for the level of accuracy of this study.
As it can be seen in fig. 6.7, all of the power spectra of CO emission at low Galactic latitudes have a broad peak around the multipole $100 \div 300$, i.e. at the ≈ 1 deg angular scale. The signal power starts decreasing up to $\ell \sim 600$ and then grows again at higher ℓ due to the Planck instrumental noise contamination. Such a broad peak suggests that there is a correlated angular scale along the Galactic plane. This can be understood with a quick order of magnitude estimate. If we assume that most of the CO emission is localized at a distance of 4 kpc (in the molecular ring) and molecular clouds have a typical size of 30 pc, we find that each cloud subtends a ~ 0.5 deg area in the sky. This corresponds to a correlated scale in the power spectrum at an ℓ of the order of a few hundred but the detail of this scale depends on the width of the molecular ring zone.

6.3.3 *Galactic plane profile emission comparison*

As a first test we compared the profile of CO emission in the Galactic plane predicted by the model and the one observed in the data. Since we are mostly interested in a comparison as direct as possible with the Planck

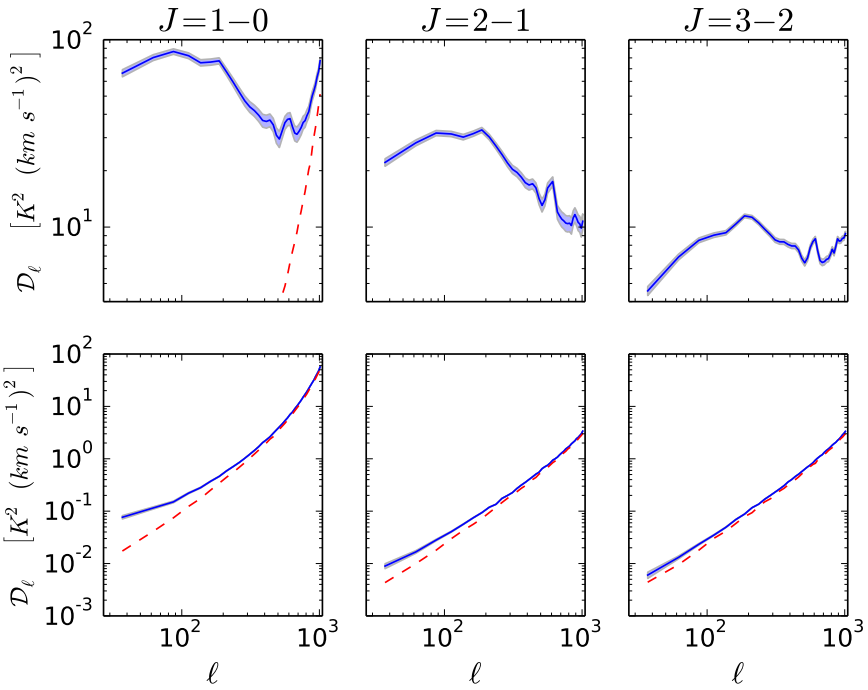

Figure 6.7: CO $1-0$ angular power spectrum (blue solid) estimated from the Planck map at low (top) and high (bottom) Galactic latitudes. The shaded area shows the error bar due to the sample and noise variance. The expected noise level of the maps in the two regions is shown in (red dashed). From Puglisi et al. (2017).

observed data, we convolved the `MCMole3D` maps with a Gaussian beam of 10 arcmin FWHM, corresponding to the nominal resolution of the 100 GHz channel of HFI, prior to any further processing.
In order to compare the data and the simulations, we constrained the total flux of the simulated CO maps with the one observed in the Planck data. This is necessary, otherwise the emission would be directly proportional to the number of clouds distributed in the simulated Galaxy. Such a procedure also breaks possible parameter degeneracies with respect to the amplitude of the simulated power spectra (see next section). Following Bronfman et al. (1988), we therefore computed the integrated flux of the emission along the two Galactic latitudes and longitudes (l, b) defined as

$$I^X(l) = \int db I^X(l, b), \tag{6.7}$$

$$I^X_{tot} = \int dl db I^X(l, b), \tag{6.8}$$

where X refers both to the *model* and to the *observed* CO map. We then rescaled the simulated maps, dividing by the factor f defined as

$$f = \frac{I^{observ}_{tot}}{I^{model}_{tot}}. \tag{6.9}$$

We estimated the integrals in (6.7) and (6.8) by considering a narrow strip of Galactic latitudes within $[-2, 2]$ degrees. We found that the value of f is essentially independent of the width of the Galactic latitude strip used to compute the integrals because most of the emission comes from a very thin layer along the Galactic plane of amplitude $|b| \lesssim 2$ deg.
In fig. 6.8 we show the comparison between $I^{observ}(l)$ and the $I^{model}(l)$ as defined in (6.7) computed as the mean of 100 MC realizations of galaxies populated by molecular clouds for both the `Axisymmetric` and `LogSpiral` models as well as their typical standard deviation. In particular, we chose for these simulations the default parameters in 6.1.

The emission profiles are quite consistent in the regions from which most of the CO emission comes, i.e. in the inner Galaxy, the I and the IV quadrants (longitude in $[-90, 90]$ deg[4]). On the contrary, the emission in the other two quadrants looks to be under-estimated but within the scatter of the simulations. In fact, the observed emissions in both the II and III quadrants come mainly from the closer and more isolated system of clouds. These are actually more difficult to simulate because in that area (at Galactic longitudes $|l| > 100$ deg) the presence of noise starts to be non-negligible (see shaded blue in fig. 6.8).
In addition, we note that the bump in the profile at $l \simeq 60 - 70$ deg, where we see a lack of power in both the `Axisymmetric` and `LogSpiral` cases, corresponds to the complex region of *Cygnus-X*, which contains the very

4 We stress that the definition of quadrants comes from the Galactic coordinates centred on the Sun. The I and IV quadrants are related to the inner Galaxy, while the II and the III ones look at its outer regions.

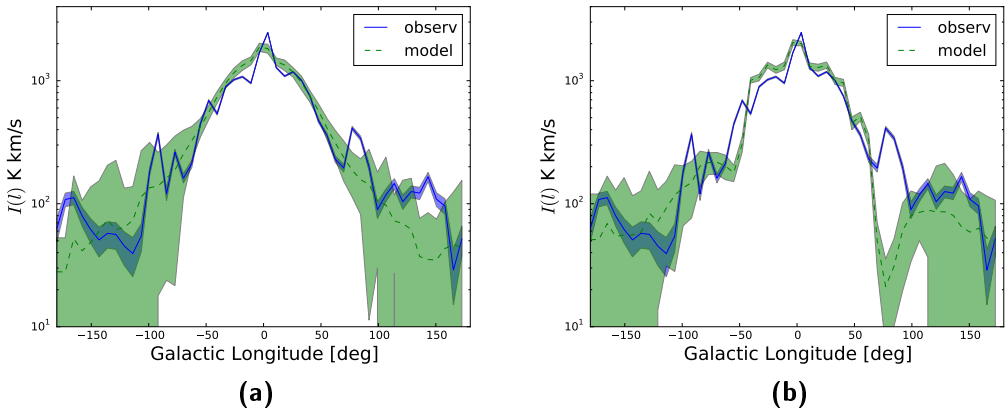

Figure 6.8: Comparison of 100 MC realization of `MCMole3D` simulated Galactic CO emission profiles (dashed green) with Planck observations (solid blue). The average profile integrals defined in (6.7) for the `Axisymmetric` (a) and `LogSpiral` (b) geometries are shown with dashed lines. The shaded area displays the standard deviation of all MCs in each longitude bin (green), or the noise level of Planck (solid blue) estimated from the *Type 1* null map. From Puglisi et al. (2017).

well known X-ray source Cyg-X1, massive protostars and one of the most massive molecular clouds known, $3 \times 10^6 M_\odot$, 1.4 kpc distant from the Sun. Given the assumptions made in sect. 6.2, these large and closer clouds are not easy to simulate with `MCMole3D` especially where they are unlikely to be found, as in inter-spiral arm regions. Despite of this, one can notice an overall qualitative better agreement with observations for the `LogSpiral` model than for the `Axisymmetric` one. The latter reconstructs the global profile very well, but the former contains more peculiar features such us the central spike due to the Central Molecular Zone within the bar, or the complex of clouds at longitudes around $\sim -140, -80, 120$ deg. We will perform a more detailed comparison of the two geometries in the following section and in subsect. 6.3.7.

6.3.4 *Constraining the `MCMole3D` model with Planck data*

After comparing the CO profile emission we checked whether the `MCMole3D` model is capable of reproducing the characteristic shape of the Planck CO angular power spectrum. Given the knowledge we have on the shape of the Milky Way, we decided to adopt the `LogSpiral` geometry as a baseline for this comparison, and to fix the parameters for the specific geometry to the values describing the shape of our Galaxy (see sect. 6.2.3). For sake of completeness we reported the results of the same analysis adopting an `Axisymmetric` geometry in subsect.6.3.7.
We left the typical cloud size L_0 and σ_{ring} (the width of the molecular ring) as free parameters of the model. While the former is directly linked to the

observed angular size of the clouds, the role of the second one is not trivial, especially if we adopt the more realistic 4 spiral arms distribution. Intuitively, it changes the probability of observing more clouds closer to the observer and affects more the amplitude of the power on the larger angular scales.

We defined a large interval, reported in 6.1, where L_0 and σ_{ring} are allowed to vary. Looking at the series of examples reported in fig. 6.5 we can see that suitable parameter ranges which yield power spectra close to the Planck observations are $L_0 = 10 \div 30$ pc and $\sigma_{ring} = 2 \div 3$ kpc. It is interesting to note that these are in agreement with estimates available in the literature (see e.g. (Ellsworth-Bowers et al., 2015; Roman-Duval et al., 2010)).

We then identified a set of values within the intervals just mentioned for which we computed the expected theoretical power spectrum of the specific model. Each theoretical model is defined as the mean of the angular power spectrum of 100 MC realizations of the model computed with `X2PURE`. For each realization of CO distribution we rescaled the total flux following the procedure outlined in the previous section before computing its power spectrum.

Once the expected angular power spectra for each point of the parameter domain had been computed, we built the hyper-surface $\mathcal{F}(\ell; \sigma_{ring}, L_0)$ which for a given set of values (σ_{ring}, L_0) retrieved the model power spectrum, by interpolating it from its value at the closest grid points using splines. We checked that alternative interpolation methods did not impact significantly our results. We then computed the best-fit parameters of the `MCMole3D` model by performing a χ^2 minimization with the Planck CO power spectrum data. For this procedure we introduced a further global normalization parameter A_{CO} to take account of the Planck bandpass effects or other possible miscalibration of the model. These might come either from variations from the scaling laws employed in the model (that are thus not captured by the total flux normalization described earlier), or calibration differences between the Planck data and the surveys used to derive the scaling laws themselves. The bandpass effects tend to decrease the overall amplitude of the simulated signal because each line gets diluted over the width of the Planck frequency band.

Since the theoretical model has been estimated from Monte Carlo simulations, we added linearly to the sample variance error of the Planck data an additional uncertainty budget corresponding to the uncertainty of the mean theoretical power spectrum estimated from MC. We note that when we compute the numerator of the f rescaling factor, we include not only the real flux coming from the CO lines but also an instrumental noise contribution. We therefore estimated the expected noise contribution to f by computing the integral of (6.8) on the Planck error map and found it to be equal to 10%. We propagated this multiplicative uncertainty to the power spectrum level, rescaling the mean theoretical MC error bars by the square of this factor.

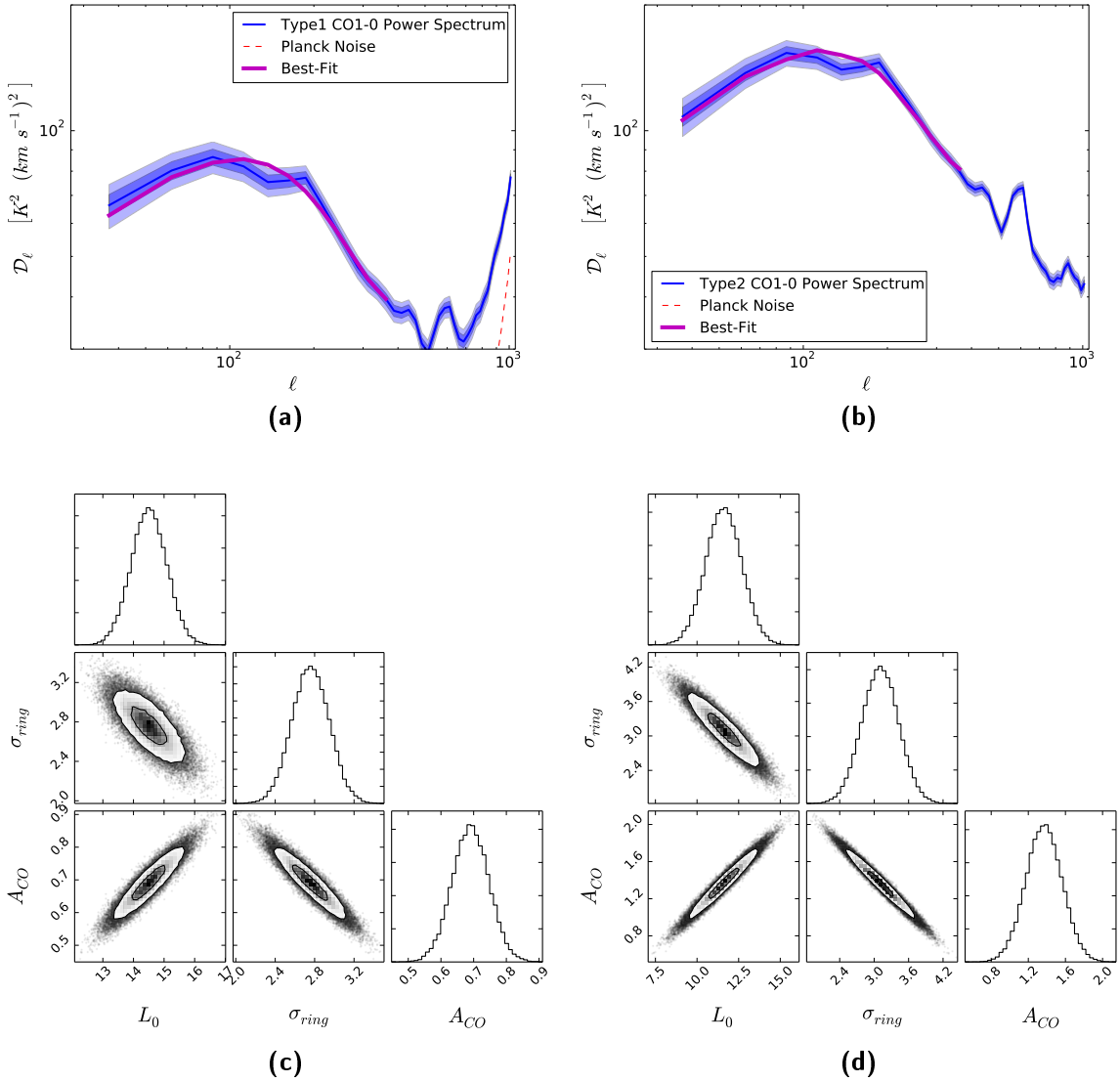

Figure 6.9: Top panels: angular power spectra (solid thin blue) of the Planck *Type 1* (left) and *Type 2* (right) maps. The shaded area correspond to the 1σ (dark blue) and 2σ (light blue) error bars including statistical and systematic uncertainties. The `MCMole3D` model CO angular power spectrum assuming the best-fit parameters of (6.10) is shown in thick solid magenta. The Planck noise power spectrum is shown in red dashed, in the top right panel the noise level is about one order of magnitude smaller than the one in the top left panel. Bottom panels: best-fit parameters of the `MCMole3D` model describing the Planck CO angular power spectrum and their correlations. From Puglisi et al. (2017).

	L_0 [pc]	σ_{ring} [kpc]	A_{CO}	$\tilde{\chi}^2$	*dof*	p-value	$\rho_{L\sigma}$
Type 1	14.50 ± 0.58	2.76 ± 0.19	0.69 ± 0.06	1.48	11	0.13	0.74
Type 2	11.59 ± 1.09	3.11 ± 0.32	1.37 ± 0.19	1.95	11	0.03	0.92

Table 6.2: Summary table of best fit parameters obtained using the two different Planck CO maps.

We limit the range of angular scales involved in the fit to $\ell \leqslant 400$ in order to avoid the regions that display an unusual bump at scales of around $\ell \approx 500$ that is not captured by any realization of our model (see next section). The best-fit parameters are reported in 6.2

$$\begin{aligned} L_0 &= 14.50 \pm 0.58\,\mathrm{pc}, \\ \sigma_{ring} &= 2.76 \pm 0.19\,\mathrm{Kpc}, \\ A_{CO} &= 0.69 \pm 0.06. \end{aligned} \tag{6.10}$$

The values are within the ranges expected from the literature. As it can be seen in fig. 6.9 the power spectrum corresponding to the model with the best fit parameters describes the Planck data reasonably well. The minimum χ^2 obtained by the minimization process gives 1.48 that corresponds to a p-value of 13%. We note, however,that all of the parameters are highly correlated. This is somewhat expected as the larger is σ_{ring}, the closer the clouds get to the observer placed in the solar circle. This effect can be compensated by an overall decrease of the typical size of the molecular cloud as shown in fig. 6.5(d).

Finally, we note that $A_{CO} \lesssim 1$ suggests that, despite the rescaling procedure constraining quite well the overall power spectrum amplitude, the spatial distribution seems to be more complex than the one implemented in the model. This might partially be explained by the fact that we do not model explicitly any realistic bandpass effect of the Planck channel or the finite width of the CO line. Additional sources of signal overestimation could be residual contamination of ^{13}CO 1-0 line or thermal dust in the map or variations of the emissivity profile in (6.3).

6.3.5 *Consistency checks on other maps*

As we anticipated earlier, the Planck collaboration released multiple CO maps extracted using different component separation procedures. We can test the stability of our results by using CO maps derived with these different approaches, in particular the so-called *Type 2* maps. These have been produced exploiting the intensity maps of several frequencies (*multi-channel* approach) to separate the CO emission from the astrophysical and CMB signal (Planck Collaboration, Ade, Aghanim, Alves, et al., 2014b). The maps are smoothed at a common resolution of 15 arcmin and have better S/N ratio

than the *Type 1* ones. However, the CO is extracted by assuming several simplifications which may leak into contamination due to foreground residuals and systematics, as explained in Planck Collaboration, Adam, Ade, Aghanim, Alves, et al. (2016, section 5.5.3).
We repeated the procedure outlined in sect. 6.3.3 and sect.6.3.4 using the *Type 2* $1-0$ map. The values of the best fit parameters are summarized in 6.2 and we show in fig. 6.9 the best-fit model power spectrum together with the power spectrum of *Type 2* map data. We found that the values of A_{CO} obtained for *Type 2* are inconsistent with the one obtained for the *Type 1* maps. However, this discrepancy is consistent with the overall inter calibration difference between the two maps reported in Planck Collaboration, Adam, Ade, Aghanim, Alves, et al. (2016). Such differences are mainly related to a combination of bandpass uncertainties in the Planck observations and presence of a mixture of ^{12}CO and ^{13}CO (emitted at 110 GHz) lines for the *Type 1 maps*. While σ_{ring} is consistent between the two maps, the *Type 2* L_0 parameters are in slight tension at 2.7σ level. The overall correlation of the parameters is increased and the overall agreement between data and the `MCMole3D` mode is reduced although it remains acceptable. We cannot exclude however that this is a sign of additional systematic contamination in the *Type 2* maps.

The Planck collaboration provided maps of the 2-1 line for both of the methods and we could use our model to constrain the relative amplitudes of the lines, while fixing the parameter of the cloud distribution. However, such analysis is challenging and might be biased by the presence of variations of local physical properties of the clouds (opacity and temperature) or by the red or blue shift of the CO line within the Planck bandpass induced by the motion of the clouds themselves (Planck Collaboration, Adam, Ade, Aghanim, Alves, et al., 2016). For these reasons, we decided to restrict our analysis only to the CO $1-0$ line, since it is the one for which the observational data are more robust.

We finally note that the observed angular power spectra of the Planck maps display an oscillatory behaviour at a scale of $\ell \geqslant 400$ with a clear peak at around $\ell \approx 500$. The fact that this feature is present in all of the lines and for all of the CO extraction methods means that it can reasonably be considered as a meaningful physical signature. Because a single cloud population produces an angular power spectrum with a characteristic peak scale, we speculate that this could be the signature of the presence of an additional cloud population with a different typical size or location. However, we decided to leave the investigation of this feature to a future work.

6.3.6 *Comparison with data at high Galactic latitudes*

In fig. 6.10, we compare the Planck CO 1-0 power spectrum at high Galactic latitudes with the average power spectrum of 100 MC realizations of the `MCMole3D` model for the same region of the sky. We assumed for these

runs the best-fit values of the L_0, σ_{ring} parameters reported in (6.10) and a `LogSpiral` distribution.Since the Planck maps at these latitudes are dominated by noise, we subtracted our MC estimates of the noise bias data power spectrum so as to have a better estimate of the signal (blue circles).

As can be observed in fig. 6.10, some discrepancy arises when comparing the power spectrum expected from the simulation of `LogSpiral` `MCMole3D` at high Galactic latitudes with the noise debiased Planck data. This is rather expected because the model has larger uncertainties at high Galactic latitudes than in the Galactic mid-plane (where the best-fit parameters are constrained) given the lack of high sensitivity data. The discrepancy seems to point to an overestimation of the vertical profile parameters $\sigma_{z,0}$ and h_R (see (6.2)) which gives a higher number of clouds close to the observer at high latitude. However, we also point out that, as explained in sect. 6.3.2, the error bars in fig. 6.10 might be underestimated especially at the largest angular scales where we are signal dominated. Therefore, discrepancies of order $\approx 3\sigma$ do not seem unlikely. Since we are mainly interested in using the model to forecast the impact of unresolved CO emission far from the Galactic plane ($|b| > 30$), we investigated whether removing the few high Galactic latitude clouds in the simulation that appear close to the observer would improve the agreement with the Planck data. All of these clouds have, in fact, a flux exceeding the Planck CO map noise in the same sky area and they should have already been detected in real data. We will refer to this specific choice of cut as the High Galactic Latitudes (HGL) cut in the following. The power spectrum of the `MCMole3D` simulated maps obtained after the application of the HGL cut is shown in fig. 6.10. We found that the model, calibrated at low latitudes and after the application of the HGL-cut, agrees very well with the data on the angular scales where the signal slightly dominates, i.e. $\ell \lesssim 80$. We could not extend the comparison to smaller angular scales because the data become noise dominated and the residual increase of power observed on the power spectrum is dominated by a noise bias residual.

6.3.7 *Best-fit with `Axisymmetric` geometry*

In this section, we present the results of the analysis described in sect. 6.3.4 to constraint the CO distribution using the `MCMole3D` model adopting an `Axisymmetric` geometry instead of the `LogSpiral` one. Following the procedure of sect. 6.3.4 we construct a series of $\mathcal{F}(\ell; \sigma_{ring}, L_0)$ hyper-surfaces sampled on an ensemble of specific values of the L_0 and σ_{ring} parameters within the same ranges reported in sect. 6.3.4.
In fig. 6.11 we show the results of the fit of the axisymmetric `MCMole3D` model to the CO power spectrum of the Planck *Type 1* and *Type 2* CO maps in the Galactic plane. We summarize the best-fit values of these parameters in 6.3. As it can be seen from the results of the χ^2 test in tab.6.3 the `Axisymmetric` model does not fit the data satisfactorily. Moreover one of the parameters of the model, the typical cloud size L_0, is in practice uncon-

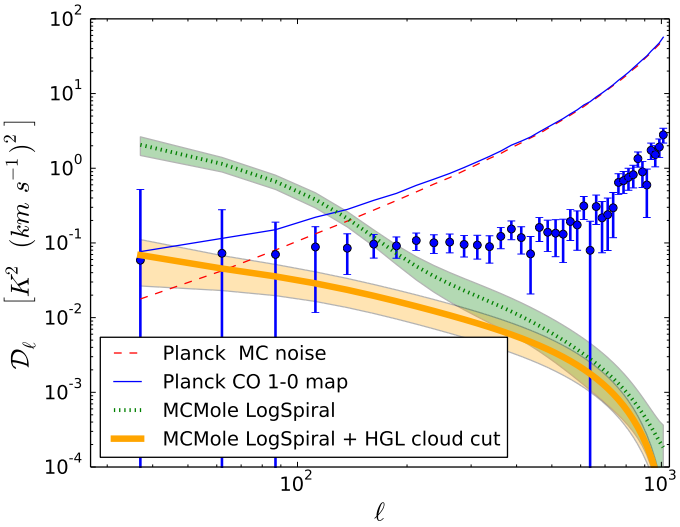

Figure 6.10: CO 1-0 power spectrum at HGL of the `LogSpiral` `MCMole3D` model (dotted green), using the parameters in (6.10). (thick solid orange) We show the power spectrum for the `LogSpiral` geometry, the same parameters in (6.10) and with the HGL-cut of clouds at $|b| > 30$ deg whose flux exceeds the Planck noise. The Planck *Type 1* CO power spectrum before and after noise bias subtraction is shown with the blue solid line and filled circles respectively; the error bars account for both Planck data statistical uncertainties and systematics from the `MCMole3D` simulations. The noise bias is shown with the dashed red line. From Puglisi et al. (2017).

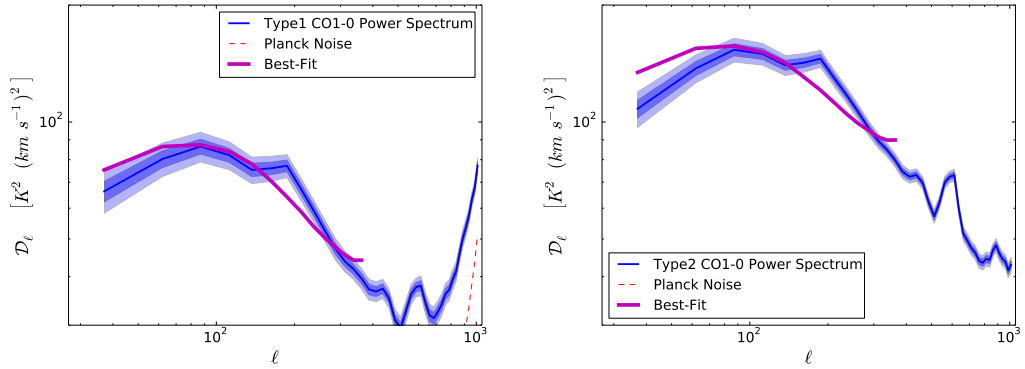

Figure 6.11: Angular power spectra of Planck CO $1-0$ line (blue) for *Type 1* (left) and *Type 2* (right) maps together with the results of the `MCMole3D` best-fit model adopting an `Axisymmetric` geometry (magenta). From Puglisi et al. (2017).

strained. For this reason we decided to adopt the `LogSpiral` geometry as a baseline choice for our forecast presented in sect. 6.4. Nevertheless, we pushed the comparison between the two geometries in the HGL area for sake of completeness.

In fig. 6.12 we show the comparison between the Planck data for *Type 1* maps and the `MCMole3D` axisymmetric best-fit model after the application of the HGL cut described above. The `Axisymmetric` model describes the data similarly to the `LogSpiral` model at the larger scales. The difference in the signal amplitude is in fact less then 30% for angular scales $\ell \lesssim 100$ and the two models are compatible within the error bars. This seems to indicate that in this regime, the details of the CO distribution in the HGL region are mainly affected by the properties of the vertical profile rather than by the geometry of the distribution. Conversely, the difference between the two geometries becomes important at smaller angular scales reaching a level of ≈ 2 at $\ell \approx 1000$.

We finally performed a series of polarized simulations as in subsect. 6.4.2 to estimate the level of contamination to the CMB B-modes power spectrum with the best-fit `Axisymmetric` model and found $r_{CO} \lesssim 0.001$. Moreover, the slope of the BB power spectrum in fig. 6.12 (b) is -2.2 similar to the one computed with the `LogSpiral` geometry.

Because the `LogSpiral` model describes the data both in the high and low galactic latitude area, we consider the upper limit derived with this setup more reliable and the reference estimate for the contamination to the cosmological signal due to the CO polarized emission.

6.4 POLARIZATION FORECASTS

As noted in sect. 6.1, CO lines are polarized and could contaminate sensitive CMB polarization measurements together with other polarized Galactic emission (synchrotron and the thermal dust) at sub-millimeter wavelengths.

	L_0 [pc]	σ_{ring} [kpc]	A_{CO}	$\tilde{\chi}^2$	*dof*	p-value	$\rho_{L\sigma}$
Type 1	19.47 ± 12.68	2.12 ± 0.23	1.00 ± 0.12	7.35	11	0.00	0.99
Type 2	16.24 ± 17.56	2.12 ± 0.30	2.25 ± 0.35	18.08	11	0.00	0.99

Table 6.3: Best-fit parameters for the `Axisymmetric` `MCMole3D` model.

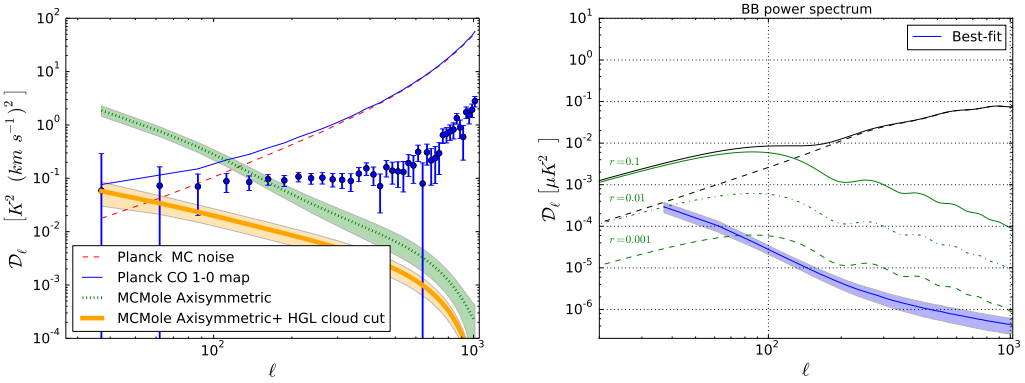

Figure 6.12: Left: CO 1-0 power spectrum at HGL of the `Axisymmetric` `MCMole3D` model (dotted green), for the best-fit parameters reported in tab.6.3. Thick orange solid line shows the power spectrum for the `Axisymmetric` geometry with the HGL-cut applied. The Planck *Type 1* CO power spectrum before and after noise bias subtraction is shown with the blue solid line and dots respectively. The Planck noise bias is shown with the dashed red line. Right: B-mode power spectra of polarized CO emission lines at HGL estimated using the best-fit parameters of the `Axisymmetric` `MCMole3D` model, see fig. 6.16 for a comparison with the `LogSpiral` geometry. From Puglisi et al. (2017).

Future experiments will preferentially perform observations at intermediate and HGL, to minimize contamination from strong Galactic emissions close to the plane. Since CO data at HGL are not sensitive enough to perform accurate studies of this emission, we provide two complementary estimates of the possible contamination from its polarized counterpart to the CMB B-mode power spectrum in this sky region.

6.4.1 *Data-based order of magnitude estimate*

Starting from the measured Planck power spectrum at low Galactic latitudes, one can extrapolate a very conservative value of the CO power spectrum at higher latitudes. Assuming that all of the variance observed in the HGL region is distributed among the angular scales in the same way as in the Galactic plane, we can write

$$C_\ell^{high,CO} = C_\ell^{Gal} \frac{var(high)}{var(Gal)}, \tag{6.11}$$

where the high and Gal denote respectively the regions at high and low Galactic latitudes as shown in fig. 6.13.

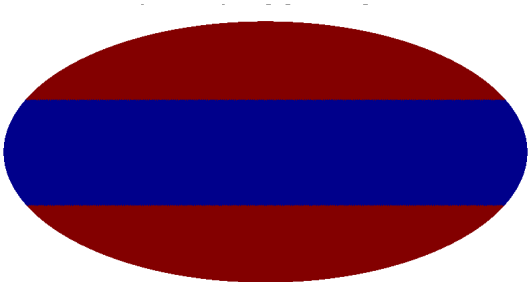

Figure 6.13: Area of the sky denoting $|b| > 30°$ (red) and $|b| < 30°$ (blue) in Galactic coordinates.

This is a somewhat conservative assumption because we know that the bulk of the CO line emission is concentrated close to the Galactic disk and also because it assumes that the Planck noise at HGL is diffuse CO emission. The variance of the Planck CO map is $0.3\,K^2(km\,s^{-1})^2$, at $|b| > 30$ deg, while for $|b| < 30$ deg we get a variance of $193.5\ K^2\ (km\,s^{-1})^2$. The power spectra are thus rescaled with (6.11) and are shown in fig. 6.14.

By looking at fig. 6.14 it is worth to notice that although it is a conservative assumption, the power of the rescaled spectra around the first multipole bins ($\ell < 100$) is in a good agreement with the observed spectrum at HGL. At higher multipoles the predominance of noise prevents us to further probe this regime of scales.

Taking 1% as the polarization fraction, p_{CO}, of the CO emission and an equal power in E and B-modes of polarized CO, we can convert C_ℓ^{COhigh} into its B-mode counterpart as $C_\ell^{COhigh,EE} = C_\ell^{COhigh,BB} = C_\ell^{high,CO} p_{CO}^2/2$. We then apply the conversion factors from Planck Collaboration, Ade, Aghanim,

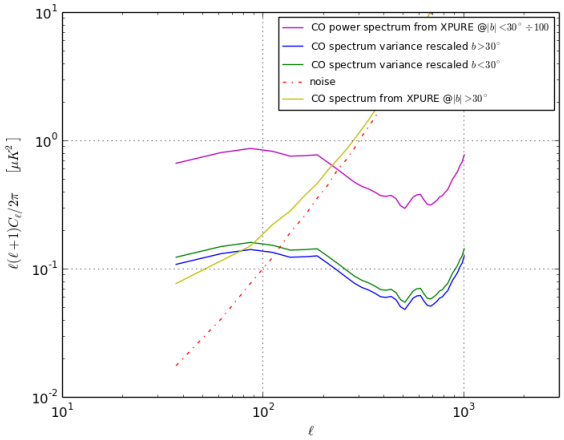

Figure 6.14: Power Spectrum of Planck CO $1-0$ intensity map rescaled with (6.11) to HGL (solid green) and (solid blue) respectively for North and South Galactic latitudes; the CO $1-0$ power spectrum at low Galactic latitudes (divided by 100) is indicated with a magenta line; CO $1-0$ power spectrum at HGL is represented by a yellow line. Notice that the latter is dominated by the noise (red dot-dashed).

Alves, et al. (2014b) to convert the CO power spectrum into thermodynamic units (from $K_{RJ}kms^{-1}$ to μK). We can compare $C_\ell^{COhigh,BB}$ to the amplitude of equivalent cosmological CMB inflationary B-modes with tensor-to-scalar ratio $r = 1$ at $\ell = 80$. In terms of $\mathcal{D}_\ell^{BB}$, this is equal to $\sim 6.67 \times 10^{-2}\mu K^2$ for a fiducial Planck 2015 cosmology. We found that the amplitude of the extrapolated CO B-mode power spectrum is equal to a primordial B-mode signal having $r_{CO} = 0.025$.

6.4.2 *Simulation estimate*

In order to verify and refine the estimate given in the previous Section, we used the model presented in sect. 6.2 to infer the level of contamination from unresolved polarized CO emission. For doing this, we first set the free parameter of the `MCMole3D` model to the best-fit value derived in (6.10).
From the total unpolarized emission in each sky pixel of the simulation, I^{CO}, we can then extract its linearly polarized part by taking into account the global properties of the Galactic magnetic field. Following Delabrouille et al. (2013), Tassis and Pavlidou (2015) the Q and U Stokes parameters of each CO cloud can be related to the unpolarized emission as

$$Q(\hat{n})^{CO} = p_{CO}\, g_d(\hat{n}) I(\hat{n})^{CO} \cos(2\psi(\hat{n})), \tag{6.12}$$

$$U(\hat{n})^{CO} = p_{CO}\, g_d(\hat{n}) I(\hat{n})^{CO} \sin(2\psi(\hat{n})), \tag{6.13}$$

where p_{CO} is the intrinsic polarization fraction of the CO lines, while g_d is the geometric depolarization factor which accounts for the induced depolarization of the light when integrated along the line of sight. The polar-

ization angle ψ describes the orientation of the polarization vector and, for the specific case of Zeeman emission, it is related to the orientation of the component of the Galactic magnetic field orthogonal to the line of sight $B_\perp$. Following the findings of Greaves et al. (1999), we adopted a conservative choice of a constant $p_{CO} = 1\%$ for each molecular cloud of the simulation. Since the polarized emission in molecular clouds is correlated with the polarized dust emission (Crutcher, 2012), we used the g_d and ψ templates for the Galactic dust emission available in the public release of the Planck Sky Model suite[5] (Delabrouille et al., 2013). These have been derived from 3D simulations of the Galactic magnetic field (including both a coherent and a turbulent component) and data of the WMAP satellite.
Since we assumed a constant polarization fraction, the geometrical depolarization effectively induces a change in the polarization fraction as a function of Galactic latitudes, decreasing when moving away from the poles. This effect has already been noticed in Planck observations of thermal dust (Planck Collaboration, Adam, Ade, Aghanim, Alves, et al., 2016), whose polarization fraction increases at high latitudes.
In order to forecast the contamination of unresolved CO polarized emission alone, we apply the HGL-cut as described in subsect.6.3.6 to each realization of the model for consistency.

Once the Q^{CO} and U^{CO} maps have been produced, we computed the angular power spectrum using `X2PURE`.
In fig. 6.16 we show the mean and standard deviation of the B-mode polarization power spectrum extracted from 100 MC realizations of the CO emission following the procedure just outlined. Even though in sect. 6.3.4 we showed that our model tends to slightly overestimate the normalization of the power spectrum, we decided not to apply the best-fit amplitude A_{CO} to the amplitude of the B-mode power spectrum in order to provide the most conservative estimates of the signal.
As could be seen from fig. 6.16, there is a significant dispersion compared to the results of the MC simulations at low Galactic latitudes (see fig. 6.5). This simply reflects the fact that the observations, and hence our model, do not favour the presence of molecular clouds at HGL. Therefore their number can vary significantly between realizations. We repeated this test using the `Axisymmetric` geometry and changing the parameter σ_{ring}. The result is stable with respect to these assumptions. We found that the spatial scaling of the average E and B-mode power spectrum can be approximated by a decreasing power-law $\mathcal{D}_\ell \sim \ell^\alpha$, with $\alpha = -1.78$.
Our simulations suggest that the level of polarized CO emission from unresolved clouds, despite being significantly lower than synchrotron or thermal dust, can nevertheless significantly bias the primordial B-mode signal if not taken into account. The signal concentrates mainly on large angular scales and at $\ell \sim 80$, $\mathcal{D}_\ell = (1.1 \pm 0.8) \times 10^{-4} \mu K^2$ where the uncertainty corresponds to the error in the mean spectra estimated from the 100 MC realizations.

5 http://www.apc.univ-paris7.fr/~delabrou/PSM/psm.html

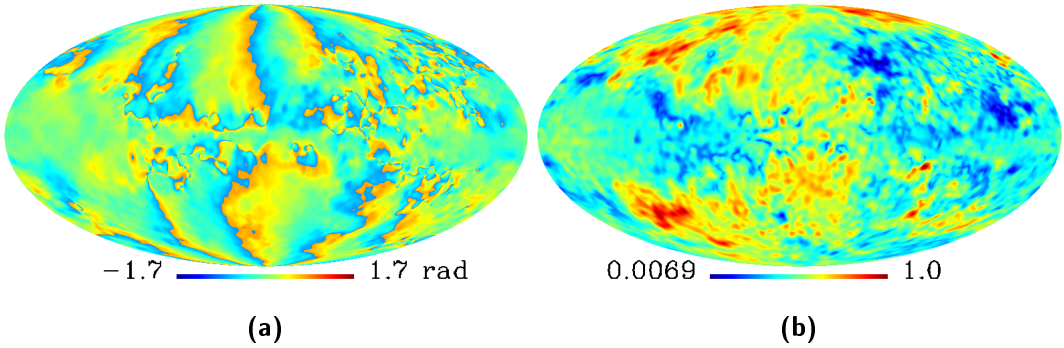

Figure 6.15: (a) Polarization angle and (b) geometrical depolarization maps used for simulating polarized CO emission in Puglisi et al. (2017).

Therefore, the level of contamination is comparable to a primordial B-mode signal induced by tensor perturbations of amplitude $r_{CO} = 0.003 \pm 0.002$, i.e. below the recent upper limit $r < 0.07$ reported by the BICEP2 Collaboration (BICEP2 Collaboration et al., 2016) but higher than the $r = 0.001$ target of upcoming experiments as SA, SO, CMB-S4. The contamination quickly becomes sub-dominant on small angular scales ($\ell \approx 1000$) where the B-modes are mostly sourced by the gravitational lensing.

We finally note that these estimates are conservative since the assumed polarization fraction of 1% of polarized is close to the high end of the polarization fractions observed in CO clouds.

6.5 SUMMARY

In this work we have developed a parametric model for CO molecular line emission which takes account of the CO clouds distribution within our Galaxy in 3D with different geometries, as well as the most recent observational findings concerning their sizes, locations, and emissivity.
Despite most of the observations have so far been confined to the Galactic plane, we have built the model to simulate the emission over the full sky. The code implementing `MCMole3D` is publicly available.
We have compared the results of our simulations with Planck CO data on the map level and statistically (by matching angular power spectra). We found that:

1. the parameters of the size function, L_0, and the width of the Galactic radial distributions σ_{ring} play a key role in shaping the power spectrum;

2. the choice of symmetries in the cloud distribution changes the profile of the integrated emission in the Galactic plane ((6.7)) but not the power spectrum morphology;

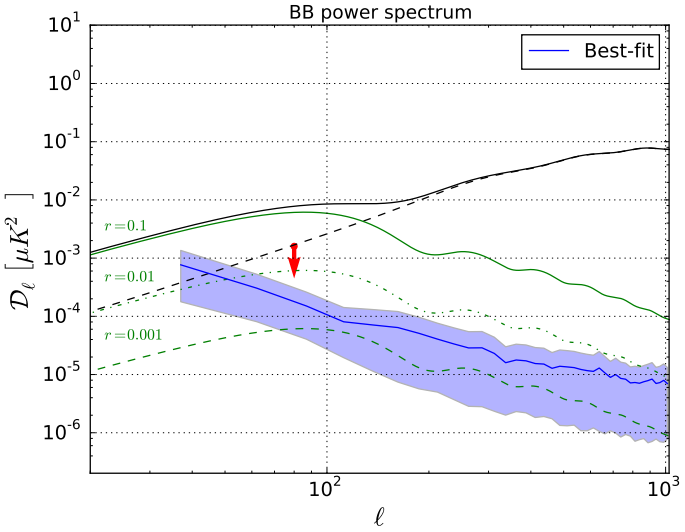

Figure 6.16: B-mode power spectra of polarized CO emission lines at HGL estimated using the best-fit parameters of the `LogSpiral` `MCMole3D` model (see (6.10)). The expected Planck 2015 ΛCDM cosmological signal including the gravitational lensing contribution is shown in black. Potential contributions from inflationary B-modes for tensor-to-scalar ratios of $r = 0.1, 0.01, 0.001$ are shown with solid, dot-dashed and dashed green lines respectively. The red arrow indicates the upper limits obtained in subsect. 6.4.1. From Puglisi et al. (2017).

3. our model is capable of reproducing fairly well the observations at low Galactic latitudes (see fig. 6.8) and the power spectrum at high latitudes (fig. 6.10).

We used our model to fit the Planck observed CO power spectrum and to estimate the most relevant parameters of the CO distribution, such as the typical size of clouds and the thickness of the molecular ring, finding results in agreement with values reported in the literature. The model which we have developed could easily be generalized and extended whenever new data become available. In particular, its accuracy at HGL would greatly benefit from better sub-mm measurements going beyond the Planck sensitivity, as well as from better information about the details of the CO polarization properties.

Finally, we used the best-fit parameters obtained from comparing the `MCMole3D` model with Planck data to forecast the unresolved CO contamination of the CMB B-mode power spectrum at HGL. We conservatively assumed a polarization fraction of $p_{CO} = 1\%$, which corresponds to the high end of those observed at low latitudes,since no polarized CO cloud has yet been observed far from the Galactic plane due to the weakness of this emission.
We found that this signal could mimic a B-mode signal with tensor-to-scalar ratio $0.001 \lesssim r \lesssim 0.025$. This level of contamination is indeed relevant for accurate measurements of CMB B-modes. It should therefore be inspected

further in light of the achievable sensitivities of upcoming and future CMB experiments together with the main diffuse polarized foreground (thermal dust and synchrotron). From the experimental point of view, trying to find dedicated instrumental solution for minimizing the impact of CO emission lines, appears to be particularly indicated in the light of these results.

7

CONCLUSION AND FUTURE OUTLOOK

> The stars know everything,
> So we try to read their minds.
> As distant as they are,
> We choose to whisper in their
> presence.
>
> Charles Simic, *On the Music of the Spheres*

Over the last decades, several experiments have looked into the CMB polarization anisotropies aiming aiming at the discovery of a stochastic background of gravitational waves produced during the inflationary phase. These primordial waves have not been detected yet because of the diffuse polarized emission from our Galaxy at the very same frequencies and several technological challenges to get higher sensitivity in the polarization detectors. In order to achieve this goal, CMB experiments have been conducted by cosmologists from every part of the world: indeed observing the CMB B-mode represents, to date, the ultimate way to probe the Universe at the ultra-high energy regimes ($\sim 10^{16}$ GeV). However, the B-modes generated by gravitational lensing, representing the other, cosmological but non-primordial contribution to B-modes on arcminute scales (gravitational waves produce anisotropy on the degree), have been observed since four years with better and better accuracy and they represent a powerful tool to probe the large scale structure of our Universe.

Since the beginning of the PhD, we have been working with the Polarbear experiment located in the Atacama Desert, which has been observing the sky at sub-millimetric wavelength since 2012. During the first two seasons of observations, Polarbear aimed at characterizing with very high sensitivity the CMB lensing B-modes. Indeed, it was the first experiment that directly measured them (Ade et al., 2014b). Furthermore, Polarbear data have been cross-correlated with the ones from different experiments for measuring the lensing power spectrum and putting constraints on cosmic birefrin-

gence and primordial magnetic fields. To date, Polarbear is completing the third season of data mostly focused on a wider patch to reach larger angular scales to better constrain the primordial B-modes. The data analysis is already ongoing and results are expected to be published in 2018.

In the perspective of collecting high-quality CMB polarization data, the Polarbear focal plane will be expanded and two further telescopes are already deployed, close to the Polarbear site. All will constitute the Simons Array, an array of three telescopes. However, the future of the CMB ground experiments in the Atacama location, i. e. Polarbear and ACT is to merge together into a larger collaboration, the Simons Observatory (SO), to be a pathfinder in the Atacama region towards a future CMB-Stage IV (S4) experiment reaching up to 10^5 detectors and multi-frequency architecture. To date, SO and S4 are among the most promising experiments aiming at capitalizing on the science opportunities offered by high precision and multi-frequency CMB polarization measurements. In one hand the multi-frequency channels will allow us to decouple CMB emission from the other astrophysical components emitting at the sub-millimetric frequencies. So far, data from WMAP and Planck have been exploited by component separation methodologies needed for removing the foreground emissions but the sensitivity of these experiments prevents to go further beyond the latest upper limits which set the contribution to gravitational waves to be 7% or less with respect to the totality of cosmological perturbations. On the other hand, high-sensitivity polarization measurements will allow us to robustly estimate lensing potential maps and measurements of polarization non-gaussianity (Abazajian et al., 2016). For all these purposes it will be crucial to develop advanced map-making procedures in order to minimize both the atmospheric contamination and the anisotropic effects induced by time domain filtering.

In this work, we mainly addressed topics which are related to CMB polarization data analysis: i. e. designing a map-making procedure for large data sets and modelling the polarized Galactic emission of diffuse foregrounds. In Chapter 5 we show our achievements concerning fast maximum likelihood map-making procedure prior to the application to the latest data from Polarbear.

In Chapter 6 we develop one of the very first 3D modeling of Galactic polarized emission, focusing on one of the missing pieces of the current modeling, represented by the Carbon Monoxide emission. We show that we are able to reconstruct the CO emission power spectrum at low Galactic latitudes by means of two parameters. Immediate developments concerning this work are represented by an enhanced parametric analysis, within the limitations of the Planck sensitivity, beyond the two parametric fitting which we adopted in our studies so far. To this regard, the vertical profile parameter $z_{1/2}$ encoding the width of the Gaussian slab of the Galactic plane, could play an important role. Moreover, we can improve the `MCMole3D` model by allowing constrained realizations from Planck or recent CO surveys, implementing different cloud shapes (to date, only spherical clouds

are considered). In particular, the latter is expected to modify the high-ℓ shape of the power spectrum. As a further development along the line of polarized foreground modelling, we are extending the work for CO to extra-Galactic point sources as a contaminant to lensing B-modes in particular.

The unbiased map-making algorithm we have been developing over the last two years, is very promising and can be fully applicable to a typical CMB ground based experiment data set which of course is going to increase both in the time and in the pixel domains as we are going toward the Stage-IV of CMB experiments. As a first step, we are thus planning to apply the unbiased map-making methodology (in Chap.5) to the wide patch data collected during the third season of Polarbear.

This methodology can be further specialized depending on the scanning strategy, noise detector estimation of a given CMB ground-based experiment. I plan to apply it to other data sets of current and forthcoming experiments as the Lite satellite for the studies of B-mode polarization and Inflation from cosmic background Radiation Detection (LiteBIRD) satellite[1], a JAXA led mission.

1 http://litebird.jp/eng/

APPENDIX

A

SPIN-WEIGHTED FUNCTIONS

In this Appendix we review the theory of spin-weighted functions and their expansion in spin-s spherical harmonics. This was used in the main text to make an all-sky expansion of the Q and U Stokes parameters. The main application of these functions in the past was in the theory of gravitational wave radiation for black hole perturbations. Our discussion follows closely that of Goldberg (1967), which is based on the work by Penrose (1967). We refer to these references for a more detailed discussion.

For any given direction on the sphere specified by the angles (θ, ϕ), one can define three orthogonal vectors, one radial and two tangential to the sphere. Let us denote the radial direction vector with $\mathbf{n}$ and the tangential with $\hat{\mathbf{e}}_1$, $\hat{\mathbf{e}}_2$. The latter two are only defined up to a rotation around $\mathbf{n}$.

A function ${}_sf(\theta, \phi)$ defined on the sphere is said to have spin-s if under a right-handed rotation of $(\hat{\mathbf{e}}_1, \hat{\mathbf{e}}_2)$ by an angle ψ it transforms as ${}_sf'(\theta, \phi) = e^{-is\psi}\ {}_sf(\theta, \phi)$. For example, given an arbitrary vector $\mathbf{a}$ on the sphere the quantities $\mathbf{a}\cdot\hat{\mathbf{e}}_1 + i\mathbf{a}\cdot\hat{\mathbf{e}}_2$, $\mathbf{n}\cdot\mathbf{a}$ and $\mathbf{a}\cdot\hat{\mathbf{e}}_1 - i\mathbf{a}\cdot\hat{\mathbf{e}}_2$ have spin 1,0 and -1 respectively.

A scalar field on the sphere can be expanded in spherical harmonics, $Y_{lm}(\theta, \phi)$, which form a complete and orthonormal basis. These functions are not appropriate to expand spin weighted functions with $s \neq 0$.

There exist analogous sets of functions that can be used to expand spin-s functions, the so called spin-s spherical harmonics ${}_sY_{lm}(\theta, \phi)$. These sets

of functions (one set for each particular spin) satisfy the same completeness and orthogonality relations,

$$\begin{aligned} \int_0^{2\pi} d\phi \int_{-1}^{1} d\cos\theta \; {}_sY^*_{l'm'}(\theta,\phi)\; {}_sY_{lm}(\theta,\phi) &= \delta_{l'l}\delta_{m'm} \\ \sum_{lm} \; {}_sY^*_{lm}(\theta,\phi)\; {}_sY_{lm}(\theta',\phi') &= \delta(\phi-\phi')\delta(\cos\theta-\cos\theta'). \end{aligned} \quad (A.1)$$

An important property of spin-s functions is that there exists a spin raising (lowering) operator $\eth$ ($\bar{\eth}$) with the property of raising (lowering) the spin-weight of a function, $(\eth\ {}_sf)' = e^{-i(s+1)\psi}\eth\ {}_sf$, $(\bar{\eth}\ {}_sf)' = e^{-i(s-1)\psi}\bar{\eth}\ {}_sf$. Their explicit expression is given by

$$\begin{aligned} \eth\ {}_sf(\theta,\phi) &= -\sin^s(\theta)\left[\frac{\partial}{\partial\theta} + i\csc(\theta)\frac{\partial}{\partial\phi}\right]\sin^{-s}(\theta)\ {}_sf(\theta,\phi), \\ \bar{\eth}\ {}_sf(\theta,\phi) &= -\sin^{-s}(\theta)\left[\frac{\partial}{\partial\theta} - i\csc(\theta)\frac{\partial}{\partial\phi}\right]\sin^{s}(\theta)\ {}_sf(\theta,\phi). \end{aligned} \quad (A.2)$$

In this work we are mainly interested in polarization, which is a quantity of spin ±2. The $\bar{\eth}$ and $\eth$ operators acting twice on a function ${}_{\pm2}f(\mu,\phi)$ that satisfies $\partial_\phi\ {}_sf = im\ {}_sf$ can be expressed as

$$\begin{aligned} \bar{\eth}^2\ {}_2f(\mu,\phi) &= \left(-\partial\mu + \frac{m}{1-\mu^2}\right)^2\left[(1-\mu^2)\ {}_2f(\mu,\phi)\right], \\ \eth^2\ {}_{-2}f(\mu,\phi) &= \left(-\partial\mu - \frac{m}{1-\mu^2}\right)^2\left[(1-\mu^2)\ {}_{-2}f(\mu,\phi)\right], \end{aligned} \quad (A.3)$$

where $\mu = \cos(\theta)$. With the aid of these operators one can express ${}_sY_{lm}$ in terms of the spin zero spherical harmonics Y_{lm}, which are the usual spherical harmonics,

$$\begin{aligned} {}_sY_{lm} &= \left[\frac{(l-s)!}{(l+s)!}\right]^{\frac{1}{2}}\eth^s Y_{lm} \quad, (0 \leqslant s \leqslant l), \\ {}_sY_{lm} &= \left[\frac{(l+s)!}{(l-s)!}\right]^{\frac{1}{2}}(-1)^s\bar{\eth}^{-s}Y_{lm} \quad, (-l \leqslant s \leqslant 0). \end{aligned} \quad (A.4)$$

The following properties of spin-weighted harmonics are also useful

$$\begin{aligned} {}_sY^*_{lm} &= (-1)^s\ {}_{-s}Y_{l-m}, \\ \eth\ {}_sY_{lm} &= [(l-s)(l+s+1)]^{\frac{1}{2}}\ {}_{s+1}Y_{lm}, \\ \bar{\eth}\ {}_sY_{lm} &= -[(l+s)(l-s+1)]^{\frac{1}{2}}\ {}_{s-1}Y_{lm}, \\ \bar{\eth}\,\eth\ {}_sY_{lm} &= -(l-s)(l+s+1)\ {}_sY_{lm}. \end{aligned} \quad (A.5)$$

Finally, in order to construct a map of polarization one needs an explicit expression for the spin weighted functions:

$$\begin{aligned} {}_sY_{lm}(\hat{n}) &= e^{im\phi}\left[\frac{(l+m)!(l-m)!}{(l+s)!(l-s)!}\frac{2l+1}{4\pi}\right]^{1/2}\sin^{2l}(\theta/2) \\ \times &\sum_r \binom{l-s}{r}\binom{l+s}{r+s-m}(-1)^{l-r-s+m}\cot^{2r+s-m}(\theta/2). \end{aligned} \quad (A.6)$$

B

THE CONJUGATE GRADIENT METHOD

The general idea of iterative methods is to construct a sequence of vectors $x^{(k)}$ such that:

$$\lim_{k\to\infty} x^{(k)} = x,$$

where x is the solution to eq.(5.4). The iterative process is stopped when it is reached a fixed tolerance: $\| x^{(k+1)} - x^{(k)} \| < \epsilon$.

The iterative methods we consider are of the form:

$$\text{given} \quad x^{(0)},\ x^{(k+1)} = Bx^{(k)} + f, \quad k \geqslant 0, \tag{B.1}$$

having denoted B an *iteration matrix*, (depending on A) and g a vector depending on A and the right hand side b. An iterative method of the form (B.1) is *consistent* if both B and g satisfy at the convergence $x = Bx + f$.

B.1 PRECONDITIONED CONJUGATE GRADIENT METHOD

A general way of setting up an iterative method is based on the decomposition of the matrix A of the form $A = M_P - (M_P - A)$, where M_P is a non singular and suitable matrix called *Preconditioner* of A. Hence by applying this decomposition on eq.(5.4), one has

$$Ax = b \Leftrightarrow M_P x = (M_P - A)\, x + b$$

which is of the form (B.1), with

$$B = {M_P}^{-1} (M_P - A) = I - {M_P}^{-1} A \quad \text{and} \quad f = {M_P}^{-1} b.$$

Thus, eq.(B.1) can be written as:

$$\begin{aligned} x^{(k+1)} =& Bx^{(k)} + g \\ =& \left(I - M_P{}^{-1}A\right) x^{(k)} + M_P{}^{-1}b \\ =& x^{(k)} + M_P{}^{-1}r^{(k)}, \end{aligned}$$

$$\Rightarrow x^{(k+1)} - x^{(k)} = M_P{}^{-1}r^{(k)},$$

where $r^{(k)} = b - Ax^{(k)}$ is the *residual* vector at the k-th iteration. We can generalise this method as follows:

$$x^{(k+1)} - x^{(k)} = \alpha_k M_P{}^{-1}r^{(k)} \tag{B.2}$$

where $\alpha_k \neq 0$ is a parameter that improves the convergence of the series $x^{(k)}$ and generally varies during the iterations. The (B.2) is called *dynamic preconditioned Richardson method*. This method requires at each $k+1$-th step the following operations:

- find the *preconditioned residuals*, $z^{(k)}$ by solving the linear system $M_P z^{(k)} = r^{(k)}$;
- compute the acceleration parameter α_k;
- update the solution $x^{(k+1)} = x^{(k)} + \alpha_k z^{(k)}$;
- update the residual $r^{(k+1)} = r^{(k)} - \alpha_k A z^{(k)}$.

In the previous steps one could notice the accelerator parameter, α_k playing a key role through all the iterations. In the special case of symmetric and positive definite matrices one can demonstrate that the optimal choice it is:

$$\alpha_k = \frac{\left(z^{(k)}\right)^T r^{(k)}}{\left(z^{(k)}\right)^T A z^{(k)}}, \quad k \geqslant 0;$$

this method is also called *Preconditioned gradient method*. It is called *gradient* method since to solve the system (5.4) means to solve the minimizer of the following quadratic form:

$$\Phi(y) = \frac{1}{2} y^T A y - y^T b,$$

which is called *energy of the system*. The gradient of Φ is given by

$$\nabla\Phi(y) = \frac{1}{2}\left(A^T + A\right) y - b = Ay - b.$$

Conversely, if $\nabla\Phi(x) = 0$ then x is solution of our linear system.

The method we are dealing with is called *conjugate* gradient method and it is more efficient and effective than the preconditioned gradient method. The

former is fully based on the latter but there is an extra-condition holding during each iteration: *the direction set by the residual vector at each iteration has to be perpendicular with respect to the direction of the previous ones*.

In other words, let $x^{(0)}$ be given (usually 0), from it we compute $r^{(0} = b - Ax^{(0)}$, $z^{(0)} = M_P{}^{-1}r^{(0)}$ and $p^{(0)} = z^{(0)}$, then for $k \geqslant 0$,:

$$\alpha_k = \frac{\left(p^{(k)}\right)^T r^{(k)}}{\left(p^{(k)}\right)^T A p^{(k)}}.$$

Hence, we compute $x^{(k+1)}$, $r^{(k+1)}$, $z^{(k+1)}$ as we did in the previous section and finally to ensure orthogonality between $p^{(k)}$ and $p^{(k+1)}$ we introduce β_k in such a way that:

$$\beta_k = \frac{\left(Ap^{(k)}\right)^T z^{(k+1)}}{\left(Ap^{(k)}\right)^T p^{(k)}}, \tag{B.3}$$

$$p^{(k+1)} = z^{(k+1)} - \beta_k p^{(k)}. \tag{B.4}$$

Finally the error estimation is given by:

$$\| x^{(k)} - x \| \leqslant \frac{2c^k}{1 + 2c^{2k}} \| x^{(0)} - x \| \quad k \geqslant 0 \tag{B.5}$$

where c is defined by the condition number[1]:

$$c = \frac{\sqrt{\kappa(P^{-1}A)} - 1}{\sqrt{\kappa(P^{-1}A)} + 1}.$$

1 $\kappa(P^{-1}A)$ measures how much the output value of the function can change for a small change in the input argument. It is defined as a product of two operator norms: $\kappa(A) = \| A^{-1} \| \cdot \| A \|$

C

FINDING A MORE REPRESENTATIVE BASIS WITH LOW RANK APPROXIMATION

At the end of sect. 5.9.2, we have seen that the PCG converges more quickly if the linear system is preconditioned by a two-level preconditioner. This is due to the fact that we reduce the condition number by means of this class of preconditioners and hence less iteration steps are needed to converge. However, it is not convenient to compute for any RHS the deflation subspace (the procedure involves the Arnoldi algorithm which takes time due to the number of iterations needed).

This is the reason why in sect.5.9.2 we did not compute the deflation basis for each RHS but we did only once and then we used it as the basis to all the RHS of the full Polarbear dataset.

Although we get improvements in terms of iteration steps and execution time, we wonder if it is possible to compute a more representative deflation subspace whose basis *better* approximates properties encoded in several RHSs.

This kind of issues in numerical analysis are approached via the *Low Rank Approximation* or the *Proper Orthogonal Decomposition* and usually involve the *Singular Value Decomposition* of a matrix. They are aimed at extracting a basis encoding characteristics from the system of interest. Generally speaking, these methods give a *good* approximation with substantially lower dimensions.

C.1 LOW RANK APPROXIMATION OF A MATRIX

For any matrix R of rank r it is always possible to decompose it via a SVD (Golub & Van Loan, 1996):

Theorem 1 (SVD Theorem). *If* $R \in \mathbb{R}^{m\times n}$ *and* $\mathrm{rank}(R) = r$ $\Rightarrow \exists U, V,\ U \in \mathbb{R}^{m\times m}, V \in \mathbb{R}^{n\times n}$*, orthogonal matrices such that:*

$$U^t R V = \Sigma = \mathrm{diag}(\sigma_1, \sigma_2, \ldots, \sigma_p), \tag{C.1}$$

with $p = \min\{m, n\}$, $\sigma_1 \geqslant \sigma_2 \geqslant \cdots \geqslant \sigma_p > 0$ and $\Sigma \in \mathbb{R}^{m\times n}$ is called the *SVD* of R. The σ_i are commonly referred as the *singular values*, u_i and v_i respectively columns of U and V are known as the *left* and *right* singular vectors of R.

Corollary 1.1. *If* $U^t R V = \Sigma$ *is the SVD of* $R \in \mathbb{R}^{m\times n}$*, with* $m \geqslant n$ *then for* $i = 1, \ldots, n : Rv_i = \sigma_i u_i$ *and* $R^t u_i = \sigma_i v_i$.

The singular values σ_i can be geometrically interpreted as the lengths of the semi-axis of an hyper-ellipsoid

$$E := \{Rx : \| x \| = 1\}.$$

The semi-axis directions are defined by u_i whereas their lengths are the singular values.

From the Corollary1.1 it follows that:

$$R^t R v_i = \sigma_i R^t u_i = \sigma_i^2 v_i,$$
$$R R^t u_i = \sigma_i^2 u_i.$$

Therefore, there is an intimate connection between the SVD of R and eigen-system of the symmetric matrices as RR^t and R^tR.

Finding the *Low-rank approximation* of R means to minimize the *Frobenius* norm[1] of $\| R - X \|_F$ such that $\mathrm{rank}(X) = k$, with $1 \leqslant k \leqslant r = \mathrm{rank}(R)$.

The SVD naturally provide a best k-rank approximation.

Theorem 2 (Low-rank approximation). *Be* $\hat{R}_k$ *a* k*-rank approximation of* R*, given by setting to zero all the* $r - k$ *trailing singular values of* R*, i.e.:*

$$\hat{R}_k = U\hat{\Sigma}_k V^t, \hat{\Sigma}_k = \mathrm{diag}(\sigma_1, \ldots, \sigma_k, 0, \ldots, 0)$$

Then the minimal error is given by the Euclidean norm of the singular values that have been zeroed out in the process:

$$\| R - \hat{R}_k \|_F = \sqrt{\sigma_{k+1}^2 + \cdots + \sigma_r^2}.$$

1 The Frobenius norm is a matrix norm of an $m \times n$ matrix A defined as (Golub & Van Loan, 1996):

$$\| A \|_F = \sqrt{\sum_{i=1}^{m}\sum_{j=1}^{n} |A_{ij}|^2}.$$

C.2 APPLYING SVD TO POLARBEAR DATASET

In order to build the deflation subspace containing common informations of several days of observations we apply the SVD following two different methods. The first one comes straightforwardly: it computes the best approximated RHS by means of the SVD on the matrix composed by several N_r RHSs, see subsect.C.2.1. The second one performs N_r Arnoldi runs and then builds the two-level preconditioner from the SVD applied to the matrix whose columns are the N_r deflation subspace basis, see details in subsect.C.2.2.

C.2.1 *SVD onto RHSs*

We performed a SVD onto the *RHS matrix*, R, a $N_p \times N_r$ matrix, whose columns are several RHSs, $R = (b_0|b_1|\dots|b_{N_r})$. We then compute the SVD onto the matrix R and selected the left singular vectors, (from the columns of U, see (C.1)) related to the most important singular values $\tilde{\sigma}$. Since σ_i^2 are eigenvalues of RR^t, we selected the $\tilde{\sigma}$ that satisfy

$$\tilde{\sigma}^2 \to \frac{\sigma_i^2}{E_{tot}} \geqslant 0.8. \tag{C.2}$$

i.e. the ones containing most of the energy (defined as $E_{tot} := \sum_k \sigma_k^2$), namely 80%.

The best estimate RHS of R, b_{best} was then assigned to the left singular vector $\tilde{U}$ related to the selected singular values $\tilde{\sigma}$ which satisfy the (C.2).

The SVD given the size of our problem ($N_p \sim 10^4$ and $N_r \lesssim 10$) does not require lot of time since its complexity is $\mathcal{O}(N_p^2)$ operations.[2]

We computed the SVD on R given two choices of $N_r = 4, 10$ and we have found only one singular value satisfying (C.2). Thus, for a chosen value of N_r, we can summarize the procedure as follows.

1. Get the best estimate RHS as $b_{best} = \tilde{U}$ via the SVD on the RHS matrix.
2. Run the Arnoldi algorithm in order to compute the deflation subspace basis. For the matrix B, we choose $M_{BD}A_0$ (see notation as in (5.20)) where A_0 is the system matrix associated to one of the RHSs, columns of R. The Arnoldi iterations start with b_{best}.
3. Build the deflation basis Z_D and the two-level preconditioner.
4. Run the PCG with M_{2l}, computed in the previous step, to all the data as we did in sect.sec:sigonlyseason.

The statistics of both the cases are summarized in tab.C.1, tab.C.2 and fig.C.1. As one can notice both the cases are very similar to the two-level preconditioner performances in sect.5.9.2.

2 The computational cost of `Numpy SVD` for a dense matrix is $2(n^2m + m^2n)$. In our case $\sim 2nm^2$since $m \gg n$.

This was quite expected since the inner core of the Arnoldi algorithm is to iterate via the power method on the Krylov subspace $\mathcal{K}_k(B, b)$. The basis on this space depends more on the matrix B than on the choice of the initial vector b.

Therefore, though it is useful to build a deflation subspace encoding informations of several daily RHSs it is more helpful to consider the degeneracies induced by the scanning strategy, different weather conditions (such as wind speed and pressure of water vapour) during several days of observation.

C.2.2 *SVD onto Deflation Subspaces*

To encompass the issue spotted at the end of subsect.C.2.1, we followed a procedure very similar to the one presented in the previous section: the difference is in the way we compute the final basis of the deflation subspace. In this section our aim is to build a two-level preconditioner with a deflation basis which takes into account as many approximated eigenvectors as we could with a small number of RHSs. The starting point of the procedure is the very same as the first step in subsect.C.2.1. Assuming we have chosen a set of N_r RHSs, as in C.2.1:

1. get the best estimate RHS as $b_{best} = \tilde{U}$;
2. run the Arnoldi algorithm N_r times, with the same Arnoldi starting vector b_{best} but with N_r Arnoldi matrices, $B_i = M_{BD}A_i$, with $i = 1, \dots, N_r$; [3]
3. each Arnoldi run yields r_i Ritz eigenvectors Z_{D_i} and we store all of them into a matrix,Z_{all};
4. perform SVD onto the matrix $Z_{all} = U_Z \Sigma_Z V_Z^t$;
5. set as the deflation basis $Z_D \equiv U_Z$ and build the two-level preconditioner from Z_D;
6. run the PCG with this two-level preconditioner to the whole set of data.

As in subsect.C.2.1, we run this procedure for two different choices of $N_r = 4, 10$. We summarize the results in tab.C.2 and in fig.C.1. Although this procedure requires to perform N_r runs Arnoldi algorithm ($\sim 20 \div 30$ minutes each), they can be distributed among an equal amount of processing elements and executed in parallel. However, this is an extra time which should be added to execution time of the PCG (in tab.C.2), which is basically the same as the one required for the cases described in subsect.C.2.1

3 From the definition of A in (5.11), it does depend daily on the scanning strategy via the pointing matrix P_i as well as the noise weights and filters defined in (5.7).

and 5.9.2 since the computation has been performed among N_r processes. It took $\sim$ **5** cpuh[4].

As one can notice in fig.C.1 and in tab.C.2, this procedure improves the convergence performances with a Speedup of 2 (with respect to the Jacobi preconditioner see sect.5.9.2). However, as we did in Chapt.5, it may be more helpful to look at the median values summarized in tab.C.1. They are consistent within the error bars to the values shown in tab.C.2.

Moreover, we have found that increasing N_r may help the convergence; on the other hand one has to take into account the computational resources required to perform N_r Arnoldi runs, as we have noticed above. A trade off among these two key-aspects can be found by considering N_r not larger than 20. In fig.C.1 one can notice how the peak moves toward smaller values of execution time and iteration steps as one considers 4 (top) and 10 (bottom) RHSs.

	N_r	PCG execution time [sec]	Iteration steps	$\| r^k \| / \| b \| (\times 10^{-8})$
SVD on RHS	4	256.1	21	6.5
SVD on RHS	10	248.3	21	6.4
SVD on Z_D	4	224.2	18	6.5
SVD on Z_D	10	175.4	14	5.2

Table C.1: Median values of PCG runs with the two-level preconditioner computed by means of SVD on several RHSs as described in subsect.C.2.1 and C.2.2.

	N_r	PCG execution time [sec]	Iteration steps	$\| r^k \| / \| b \| (\times 10^{-8})$
SVD on RHS	4	268.5 ± 81.7	21.7 ± 6.2	6.4 ± 1.8
SVD on RHS	10	263.4 ± 89.5	22.1 ± 7.0	6.5 ± 1.9
SVD on Z_D	4	247.1 ± 104.2	19.6 ± 7.9	6.4 ± 1.9
SVD on Z_D	10	186.8 ± 74.8	14.9 ± 6.0	5.6 ± 2.1

Table C.2: Mean and standard deviation of PCG runs with the two-level preconditioner computed by means of SVD on several RHSs as described in subsect.C.2.1 and C.2.2.

4 Of course, the number of cpuh increases by a factor N_r, with respect to the one referred in sect.5.9.2.

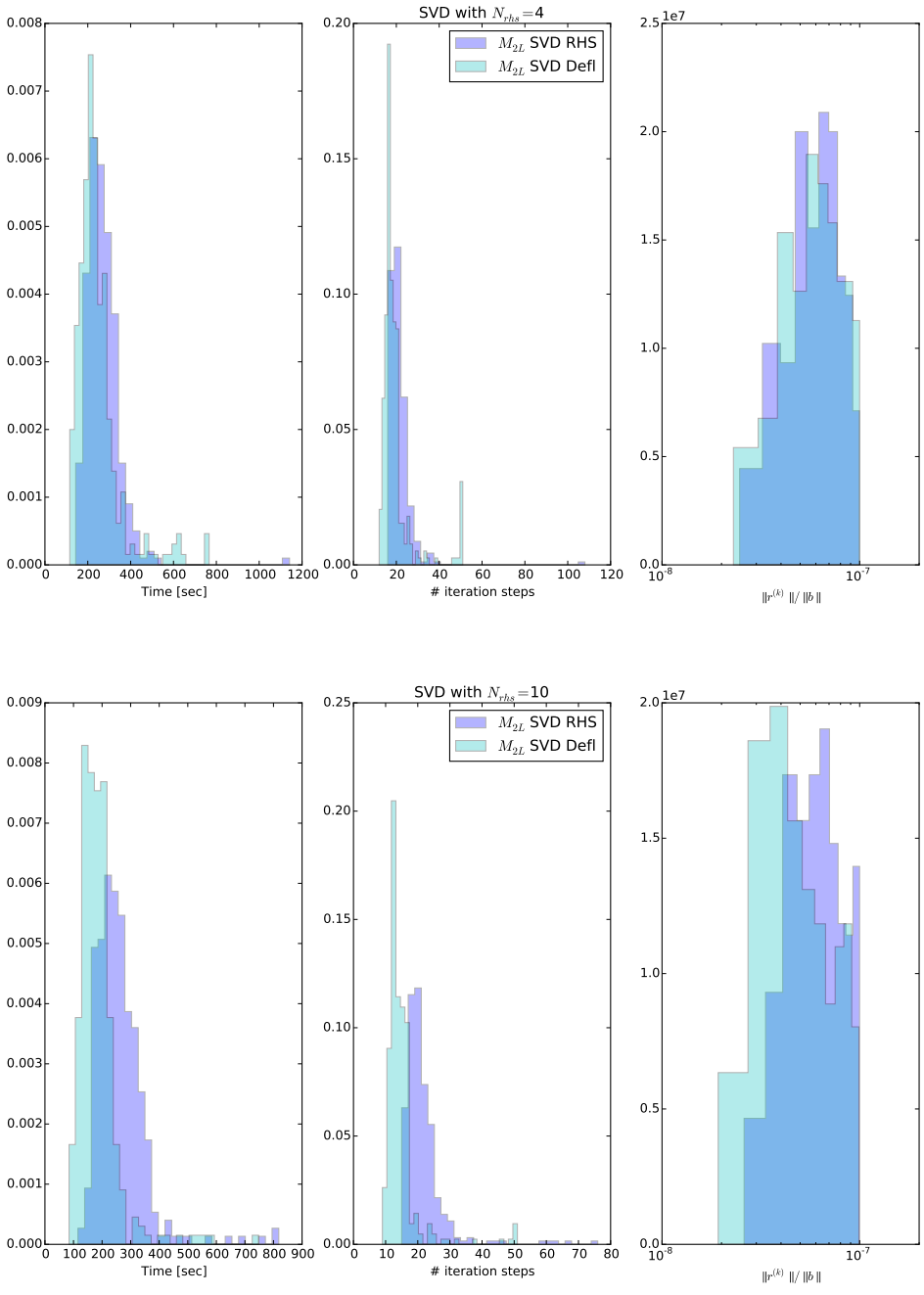

Figure C.1: Normed histograms of the PCG runs with the two-level preconditioner computed by means of SVD on several RHSs as described in sections C.2.1 and C.2.2. The top (bottom) panel compare the runs with $N_r = 4(10)$.

BIBLIOGRAPHY

Aad, G., et al. (2013). Measurements of Higgs boson production and couplings in diboson final states with the ATLAS detector at the LHC. *Phys. Lett., B726*, 88-119. ([Erratum: Phys. Lett.B734,406(2014)]) doi: 10.1016/j.physletb.2014.05.011,10.1016/j.physletb.2013.08.010

Abazajian, K. N., Adshead, P., Ahmed, Z., Allen, S. W., Alonso, D., Arnold, K. S., ... Kimmy Wu, W. L. (2016, October). CMB-S4 Science Book, First Edition. *ArXiv e-prints*.

Ade, P. A. R., Akiba, Y., Anthony, A. E., Arnold, K., Atlas, M., Barron, D., ... Polarbear Collaboration (2014a, April). Evidence for Gravitational Lensing of the Cosmic Microwave Background Polarization from Cross-Correlation with the Cosmic Infrared Background. *Physical Review Letters*, *112*(13), 131302. doi: 10.1103/PhysRevLett.112.131302

Ade, P. A. R., Akiba, Y., Anthony, A. E., Arnold, K., Atlas, M., Barron, D., ... Polarbear Collaboration (2014b, July). Measurement of the Cosmic Microwave Background Polarization Lensing Power Spectrum with the POLARBEAR Experiment. *Physical Review Letters*, *113*(2), 021301. doi: 10.1103/PhysRevLett.113.021301

Ade, P. A. R., Akiba, Y., Anthony, A. E., Arnold, K., Atlas, M., Barron, D., ... Zahn, O. (2014, Jul). Measurement of the cosmic microwave background polarization lensing power spectrum with the polarbear experiment. *Phys. Rev. Lett.*, *113*, 021301. Retrieved from https://link.aps.org/doi/10.1103/PhysRevLett.113.021301 doi: 10.1103/PhysRevLett.113.021301

Ade, P. A. R., Arnold, K., Atlas, M., Baccigalupi, C., Barron, D., Boettger, D., ... Polarbear Collaboration (2015, December). POLARBEAR constraints on cosmic birefringence and primordial magnetic fields. *Physical Review D*, *92*(12), 123509. doi: 10.1103/PhysRevD.92.123509

Ade, T. P. C. P. A. R., Akiba, Y., Anthony, A. E., Arnold, K., Atlas, M., Barron, D., ... Zahn, O. (2014). A measurement of the cosmic microwave background b-mode polarization power spectrum at sub-degree scales with polarbear. *The Astrophysical Journal*, *794*(2), 171. Retrieved from http://stacks.iop.org/0004-637X/794/i=2/a=171

Arnold, K., Ade, P. A. R., Anthony, A. E., Barron, D., Boettger, D., Borrill, J., ... Zahn, O. (2012, September). The bolometric focal plane array of the POLARBEAR CMB experiment. In *Millimeter, submillimeter, and far-infrared detectors and instrumentation for astronomy vi* (Vol. 8452, p. 84521D). doi: 10.1117/12.927057

Arnold, K., Stebor, N., Ade, P. A. R., Akiba, Y., Anthony, A. E., Atlas, M., ... Zahn, O. (2014). The simons array: expanding polarbear to three multichroic telescopes. In (Vol. 9153, p. 91531F-91531F-8). Retrieved from http://dx.doi.org/10.1117/12.2057332 doi: 10.1117/12.2057332

Aumont, J., Conversi, L., Thum, C., Wiesemeyer, H., Falgarone, E., Macías-Pérez, J. F., ... Tristram, M. (2010, May). Measurement of the Crab nebula polarization at 90 GHz as a calibrator for CMB experiments. *Astronomy and Astrophysics*, *514*, A70. doi: 10.1051/0004-6361/200913834

Baccigalupi, C. (2003, December). Cosmic microwave background polarisation: foreground contrast and component separation. *New Astronomy Review*, *47*, 1127-1134. doi: 10.1016/j.newar.2003.09.038

Bally, J., Langer, W. D., Stark, A. A., & Wilson, R. W. (1987, January). Filamentary structure in the Orion molecular cloud. *Astrophysical Journal, Letters*, *312*, L45-L49. doi: 10.1086/184817

Balser, D. S., Rood, R. T., Bania, T. M., & Anderson, L. D. (2011, September). H II Region Metallicity Distribution in the Milky Way Disk. *Astrophysical Journal*, *738*, 27. doi: 10.1088/0004-637X/738/1/27

Bardeen, J. M. (1980, October). Gauge-invariant cosmological perturbations. *Physical Review D*, *22*, 1882-1905. doi: 10.1103/PhysRevD.22.1882

Barkats, D., Aikin, R., Bischoff, C., Buder, I., Kaufman, J. P., Keating, B. G., ... Yoon, K. W. (2014, March). Degree-scale Cosmic Microwave Background Polarization Measurements from Three Years of BICEP1 Data. *Astrophysical Journal*, *783*, 67. doi: 10.1088/0004-637X/783/2/67

BICEP2 Collaboration, Ade, P. A. R., Aikin, R. W., Barkats, D., Benton, S. J., Bischoff, C. A., ... Yoon, K. W. (2014, June). Detection of B-Mode Polarization at Degree Angular Scales by BICEP2. *Physical Review Letters*, *112*(24), 241101. doi: 10.1103/PhysRevLett.112.241101

BICEP2 Collaboration, Keck Array Collaboration, Ade, P. A. R., Ahmed, Z., Aikin, R. W., Alexander, K. D., ... Yoon, K. W. (2016, January). Improved Constraints on Cosmology and Foregrounds from BICEP2 and Keck Array Cosmic Microwave Background Data with Inclusion of 95 GHz Band. *Physical Review Letters*, *116*(3), 031302. doi: 10.1103/PhysRevLett.116.031302

Biermann, P. (1976, December). On the radio continuum flux from the disks of spiral galaxies. *Astronomy and Astrophysics*, *53*, 295-303.

Bobylev, V. V., & Bajkova, A. T. (2013, November). Estimation of the pitch angle of the Galactic spiral pattern. *Astronomy Letters*, *39*, 759-764. doi: 10.1134/S1063773713110017

Borrill, J. (1999, November). MADCAP - The Microwave Anisotropy Dataset Computational Analysis Package. *ArXiv Astrophysics e-prints*.

Bronfman, L., Cohen, R. S., Alvarez, H., May, J., & Thaddeus, P. (1988, jan). A CO survey of the southern Milky Way - The mean radial distribution of molecular clouds within the solar circle. *The Astrophysical Journal*, *324*, 248. Retrieved from http://adsabs.harvard.edu/abs/1988ApJ...324..248B doi: 10.1086/165892

Bunn, E. F., Zaldarriaga, M., Tegmark, M., & de Oliveira-Costa, A. (2003, January). E/B decomposition of finite pixelized CMB maps. *Physical Review D*, *67*(2), 023501. doi: 10.1103/PhysRevD.67.023501

Challinor, A., & Peiris, H. (2009, May). Lecture notes on the physics of cosmic microwave background anisotropies. In M. Novello & S. Perez

(Eds.), *American institute of physics conference series* (Vol. 1132, p. 86-140). doi: 10.1063/1.3151849

Chandrasekhar, S. (1960). *Radiative transfer*.

Chatrchyan, S., et al. (2013). Observation of a new boson with mass near 125 GeV in pp collisions at $\sqrt{s}$ = 7 and 8 TeV. *JHEP*, *06*, 081. doi: 10.1007/JHEP06(2013)081

Chiang, H. C., Ade, P. A. R., Barkats, D., Battle, J. O., Bierman, E. M., Bock, J. J., ... Yoon, K. W. (2010, March). Measurement of Cosmic Microwave Background Polarization Power Spectra from Two Years of BICEP Data. *Astrophysical Journal*, *711*, 1123-1140. doi: 10.1088/0004-637X/711/2/1123

Choi, S. K., & Page, L. A. (2015, December). Polarized galactic synchrotron and dust emission and their correlation. *Journal of Cosmology and Astroparticle Physics*, *12*, 020. doi: 10.1088/1475-7516/2015/12/020

Crutcher, R. M. (2012, September). Magnetic Fields in Molecular Clouds. *Annual Review of Astronomy and Astrophysics*, *50*, 29-63. doi: 10.1146/annurev-astro-081811-125514

Dame, T. M., Hartmann, D., & Thaddeus, P. (2001, February). The Milky Way in Molecular Clouds: A New Complete CO Survey. *Astrophysical Journal*, *547*, 792-813. doi: 10.1086/318388

Das, S., Louis, T., Nolta, M. R., Addison, G. E., Battistelli, E. S., Bond, J. R., ... Wollack, E. (2014, April). The Atacama Cosmology Telescope: temperature and gravitational lensing power spectrum measurements from three seasons of data. *Journal of Cosmology and Astroparticle Physics*, *4*, 014. doi: 10.1088/1475-7516/2014/04/014

Davis, B. L., Berrier, J. C., Shields, D. W., Kennefick, J., Kennefick, D., Seigar, M. S., ... Puerari, I. (2012, April). Measurement of Galactic Logarithmic Spiral Arm Pitch Angle Using Two-dimensional Fast Fourier Transform Decomposition. *Astrophysical Journal, Supplement*, *199*, 33. doi: 10.1088/0067-0049/199/2/33

de Bernardis, P., Ade, P. A. R., Bock, J. J., Bond, J. R., Borrill, J., Boscaleri, A., ... Vittorio, N. (2000, November). Detection of anisotropy in the Cosmic Microwave Background at horizon and sub-horizon scales with the BOOMERanG experiment. *ArXiv Astrophysics e-prints*.

Delabrouille, J., Betoule, M., Melin, J.-B., Miville-Deschênes, M.-A., Gonzalez-Nuevo, J., Le Jeune, M., ... Toffolatti, L. (2013, May). The pre-launch Planck Sky Model: a model of sky emission at submillimetre to centimetre wavelengths. *Astronomy and Astrophysics*, *553*, A96. doi: 10.1051/0004-6361/201220019

Dodelson, S. (2003). *Modern cosmology*.

Dolgov, A. D., & Linde, A. D. (1982, October). Baryon asymmetry in the inflationary universe. *Physics Letters B*, *116*, 329-334. doi: 10.1016/0370-2693(82)90292-1

Doré, O., Teyssier, R., Bouchet, F. R., Vibert, D., & Prunet, S. (2001, July). MAPCUMBA: A fast iterative multi-grid map-making algorithm for CMB experiments. *Astronomy and Astrophysics*, *374*, 358-370. doi: 10

.1051/0004-6361:20010692

Dragone, C. (1978). Offset multireflector antennas with perfect pattern symmetry and polarization discrimination. *Bell System Technical Journal*, *57*(7), 2663–2684. Retrieved from http://dx.doi.org/10.1002/j.1538-7305.1978.tb02171.x doi: 10.1002/j.1538-7305.1978.tb02171.x

Eales, S., Dunne, L., Clements, D., Cooray, A., De Zotti, G., Dye, S., ... White, G. J. (2010, May). The Herschel ATLAS. *Publications of the ASP*, *122*, 499. doi: 10.1086/653086

Einstein, A. (1911). Über den Einfluß der Schwerkraft auf die Ausbreitung des Lichtes. *Annalen der Physik*, *340*, 898-908. doi: 10.1002/andp.19113401005

Einstein, A. (1917). Kosmologische Betrachtungen zur allgemeinen Relativitätstheorie. *Sitzungsberichte der Königlich Preußischen Akademie der Wissenschaften (Berlin), Seite 142-152.*.

Ellsworth-Bowers, T. P., Rosolowsky, E., Glenn, J., Ginsburg, A., Evans, N. J., II, Battersby, C., ... Svoboda, B. (2015, January). The Bolocam Galactic Plane Survey. XII. Distance Catalog Expansion Using Kinematic Isolation of Dense Molecular Cloud Structures with ^{13}CO(1-0). *Astrophysical Journal*, *799*, 29. doi: 10.1088/0004-637X/799/1/29

Errard, J., Feeney, S. M., Peiris, H. V., & Jaffe, A. H. (2016, March). Robust forecasts on fundamental physics from the foreground-obscured, gravitationally-lensed CMB polarization. *Journal of Cosmology and Astroparticle Physics*, *3*, 052. doi: 10.1088/1475-7516/2016/03/052

Filippini, J. P., Ade, P. A. R., Amiri, M., Benton, S. J., Bihary, R., Bock, J. J., ... Turner, A. D. (2010, July). SPIDER: a balloon-borne CMB polarimeter for large angular scales. In *Millimeter, submillimeter, and far-infrared detectors and instrumentation for astronomy v* (Vol. 7741, p. 77411N). doi: 10.1117/12.857720

Fixsen, D. J., Cheng, E. S., Gales, J. M., Mather, J. C., Shafer, R. A., & Wright, E. L. (1996, December). The Cosmic Microwave Background Spectrum from the Full COBE FIRAS Data Set. *Astrophysical Journal*, *473*, 576. doi: 10.1086/178173

Fuskeland, U., Wehus, I. K., Eriksen, H. K., & Næss, S. K. (2014, August). Spatial Variations in the Spectral Index of Polarized Synchrotron Emission in the 9 yr WMAP Sky Maps. *Astrophysical Journal*, *790*, 104. doi: 10.1088/0004-637X/790/2/104

Goldberg, J. N. (1967, November). Invariant Transformations and Newman-Penrose Constants. *Journal of Mathematical Physics*, *8*, 2161-2166. doi: 10.1063/1.1705136

Goldreich, P., & Kylafis, N. D. (1981). On mapping the magnetic field direction in molecular clouds by polarization measurements. *The Astrophysical Journal*, *243*, L75. Retrieved from http://adsabs.harvard.edu/abs/1981ApJ...243L..75G doi: 10.1086/183446

Golub, G. H., & Van Loan, C. F. (1996). *Matrix computations (3rd ed.)*. Baltimore, MD, USA: Johns Hopkins University Press.

Górski, K. M., Hivon, E., Banday, A. J., Wandelt, B. D., Hansen, F. K.,

Reinecke, M., & Bartelmann, M. (2005, April). HEALPix: A Framework for High-Resolution Discretization and Fast Analysis of Data Distributed on the Sphere. *Astrophysical Journal*, *622*, 759-771. doi: 10.1086/427976

Grain, J., Tristram, M., & Stompor, R. (2009, June). Polarized CMB power spectrum estimation using the pure pseudo-cross-spectrum approach. *Physical Review D*, *79*(12), 123515. doi: 10.1103/PhysRevD.79.123515

Greaves, J. S., Holland, W. S., Friberg, P., & Dent, W. R. F. (1999, February). Polarized CO Emission from Molecular Clouds. *Astrophysical Journal, Letters*, *512*, L139-L142. doi: 10.1086/311888

Guth, A. H. (1981, January). Inflationary universe: A possible solution to the horizon and flatness problems. *Physical Review D*, *23*, 347-356. doi: 10.1103/PhysRevD.23.347

Hanany, S., Ade, P., Balbi, A., Bock, J., Borrill, J., Boscaleri, A., ... Wu, J. H. P. (2000, December). MAXIMA-1: A Measurement of the Cosmic Microwave Background Anisotropy on Angular Scales of $10' - 5$deg. *Astrophysical Journal, Letters*, *545*, L5-L9. doi: 10.1086/317322

Hand, N., Addison, G. E., Aubourg, E., Battaglia, N., Battistelli, E. S., Bizyaev, D., ... Zunckel, C. (2012, July). Evidence of Galaxy Cluster Motions with the Kinematic Sunyaev-Zel'dovich Effect. *Physical Review Letters*, *109*(4), 041101. doi: 10.1103/PhysRevLett.109.041101

Hanson, D., Challinor, A., & Lewis, A. (2010, September). Weak lensing of the CMB. *General Relativity and Gravitation*, *42*, 2197-2218. doi: 10.1007/s10714-010-1036-y

Heyer, M., & Dame, T. (2015, aug). Molecular Clouds in the Milky Way. *Annual Review of Astronomy and Astrophysics*, *53*(1), 583–629. doi: 10.1146/annurev-astro-082214-122324

Hinshaw, G., Larson, D., Komatsu, E., Spergel, D. N., Bennett, C. L., Dunkley, J., ... Wright, E. L. (2013, October). Nine-year Wilkinson Microwave Anisotropy Probe (WMAP) Observations: Cosmological Parameter Results. *Astrophysical Journal, Supplement*, *208*, 19. doi: 10.1088/0067-0049/208/2/19

Hivon, E., Górski, K. M., Netterfield, C. B., Crill, B. P., Prunet, S., & Hansen, F. (2002, March). MASTER of the Cosmic Microwave Background Anisotropy Power Spectrum: A Fast Method for Statistical Analysis of Large and Complex Cosmic Microwave Background Data Sets. *Astrophysical Journal*, *567*, 2-17. doi: 10.1086/338126

Holder, G. P., Viero, M. P., Zahn, O., Aird, K. A., Benson, B. A., Bhattacharya, S., ... Zemcov, M. (2013, July). A Cosmic Microwave Background Lensing Mass Map and Its Correlation with the Cosmic Infrared Background. *Astrophysical Journal, Letters*, *771*, L16. doi: 10.1088/2041-8205/771/1/L16

Hu, W., & Dodelson, S. (2002). Cosmic microwave background anisotropies. *Annual Review of Astronomy and Astrophysics*, *40*(1), 171-216. Retrieved from https://doi.org/10.1146/annurev.astro.40.060401.093926 doi: 10.1146/annurev.astro.40.060401.093926

Hu, W., & Okamoto, T. (2002, August). Mass Reconstruction with Cosmic Microwave Background Polarization. *Astrophysical Journal*, *574*, 566-574. doi: 10.1086/341110

Hu, W., & White, M. J. (1997). A CMB polarization primer. *New Astron.*, *2*, 323. doi: 10.1016/S1384-1076(97)00022-5

Hubble, E. (1929, March). A Relation between Distance and Radial Velocity among Extra-Galactic Nebulae. *Proceedings of the National Academy of Science*, *15*, 168-173. doi: 10.1073/pnas.15.3.168

Inoue, Y., Ade, P., Akiba, Y., Aleman, C., Arnold, K., Baccigalupi, C., ... Zahn, O. (2016, July). POLARBEAR-2: an instrument for CMB polarization measurements. In *Millimeter, submillimeter, and far-infrared detectors and instrumentation for astronomy viii* (Vol. 9914, p. 99141I). doi: 10.1117/12.2231961

Jackson, J. M., Rathborne, J. M., Shah, R. Y., Simon, R., Bania, T. M., Clemens, D. P., ... Heyer, M. H. (2006, March). The Boston University-Five College Radio Astronomy Observatory Galactic Ring Survey. *Astrophysical Journal, Supplement*, *163*, 145-159. doi: 10.1086/500091

Keating, B. G., Shimon, M., & Yadav, A. P. S. (2013, January). Self-calibration of Cosmic Microwave Background Polarization Experiments. *Astrophysical Journal, Letters*, *762*, L23. doi: 10.1088/2041-8205/762/2/L23

Keisler, R., Hoover, S., Harrington, N., Henning, J. W., Ade, P. A. R., Aird, K. A., ... Zahn, O. (2015). Measurements of sub-degree b-mode polarization in the cosmic microwave background from 100 square degrees of sptpol data. *The Astrophysical Journal*, *807*(2), 151. Retrieved from http://stacks.iop.org/0004-637X/807/i=2/a=151

Kermish, Z. D., Ade, P., Anthony, A., Arnold, K., Barron, D., Boettger, D., ... Zahn, O. (2012, September). The POLARBEAR experiment. In *Millimeter, submillimeter, and far-infrared detectors and instrumentation for astronomy vi* (Vol. 8452, p. 84521C). doi: 10.1117/12.926354

Kitayama, T. (2014, June). Cosmological and astrophysical implications of the Sunyaev-Zel'dovich effect. *Progress of Theoretical and Experimental Physics*, *2014*(6), 06B111. doi: 10.1093/ptep/ptu055

Komatsu, E., Dunkley, J., Nolta, M. R., Bennett, C. L., Gold, B., Hinshaw, G., ... Wright, E. L. (2009, February). Five-Year Wilkinson Microwave Anisotropy Probe Observations: Cosmological Interpretation. *Astrophysical Journal, Supplement*, *180*, 330-376. doi: 10.1088/0067-0049/180/2/330

Kovac, J. M., Leitch, E. M., Pryke, C., Carlstrom, J. E., Halverson, N. W., & Holzapfel, W. L. (2002, December). Detection of polarization in the cosmic microwave background using DASI. *Nature*, *420*, 772-787. doi: 10.1038/nature01269

Krachmalnicoff, N., Baccigalupi, C., Aumont, J., Bersanelli, M., & Mennella, A. (2016, April). Characterization of foreground emission on degree angular scales for CMB B-mode observations . Thermal dust and synchrotron signal from Planck and WMAP data. *Astronomy and Astrophysics*, *588*, A65. doi: 10.1051/0004-6361/201527678

Lewis, A., & Challinor, A. (2006, June). Weak gravitational lensing of the CMB. *Physics Reports*, *429*, 1-65. doi: 10.1016/j.physrep.2006.03.002

Lewis, A., Challinor, A., & Lasenby, A. (2000). Efficient computation of CMB anisotropies in closed FRW models. *Astrophys. J.*, *538*, 473-476. doi: 10.1086/309179

Lewis, A., Challinor, A., & Turok, N. (2001, Dec). Analysis of cmb polarization on an incomplete sky. *Phys. Rev. D*, *65*, 023505. Retrieved from http://link.aps.org/doi/10.1103/PhysRevD.65.023505 doi: 10.1103/PhysRevD.65.023505

Lisenfeld, U., & Völk, H. J. (2000, February). On the radio spectral index of galaxies. *Astronomy and Astrophysics*, *354*, 423-430.

Louis, T., Grace, E., Hasselfield, M., Lungu, M., Maurin, L., Addison, G. E., ... Wollack, E. J. (2016, October). The Atacama Cosmology Telescope: Two-Season ACTPol Spectra and Parameters. *ArXiv e-prints*.

Martin, J., Ringeval, C., & Vennin, V. (2014, December). Encyclopædia Inflationaris. *Physics of the Dark Universe*, *5*, 75-235. doi: 10.1016/j.dark.2014.01.003

Miller, N. J., Shimon, M., & Keating, B. G. (2009, March). CMB beam systematics: Impact on lensing parameter estimation. *Physical Review D*, *79*(6), 063008. doi: 10.1103/PhysRevD.79.063008

Mizugutch, Y., Akagawa, M., & Yokoi, H. (1976). Offset Dual Reflector Antenna. *ISA Proceedings*, 2-5.

Mizuno, A., & Fukui, Y. (2004, December). Physical properties of molecular clouds as revealed by NANTEN CO survey: from the galactic center to the galactic warp. In D. Clemens, R. Shah, & T. Brainerd (Eds.), *Milky way surveys: The structure and evolution of our galaxy* (Vol. 317, p. 59).

Mukhanov, V. F., & Chibisov, G. V. (1981, May). Quantum fluctuations and a nonsingular universe. *ZhETF Pisma Redaktsiiu*, *33*, 549-553.

Oh, S. P., Spergel, D. N., & Hinshaw, G. (1999, January). An Efficient Technique to Determine the Power Spectrum from Cosmic Microwave Background Sky Maps. *Astrophysical Journal*, *510*, 551-563. doi: 10.1086/306629

Okamoto, T., & Hu, W. (2003, April). Cosmic microwave background lensing reconstruction on the full sky. *Physical Review D*, *67*(8), 083002. doi: 10.1103/PhysRevD.67.083002

Page, L., Hinshaw, G., Komatsu, E., Nolta, M. R., Spergel, D. N., Bennett, C. L., ... Wright, E. L. (2007, June). Three-Year Wilkinson Microwave Anisotropy Probe (WMAP) Observations: Polarization Analysis. *Astrophysical Journal, Supplement*, *170*, 335-376. doi: 10.1086/513699

Peacock, J. A. (1999). *Cosmological Physics*.

Penrose, R. (1967). Conserved Quantities and Conformal Structure in General Relativity. In J. Ehlers (Ed.), *Relativity theory and astrophysics. vol.1: Relativity and cosmology* (p. 147).

Penzias, A. A., & Wilson, R. W. (1965, July). A Measurement of Excess Antenna Temperature at 4080 Mc/s. *Astrophysical Journal*, *142*, 419-421. doi: 10.1086/148307

Perlmutter, S., Aldering, G., Goldhaber, G., Knop, R. A., Nugent, P., Castro, P. G., ... Project, T. S. C. (1999, June). Measurements of Ω and Λ from 42 High-Redshift Supernovae. *Astrophysical Journal*, *517*, 565-586. doi: 10.1086/307221

Planck Collaboration, Adam, R., Ade, P. A. R., Aghanim, N., Akrami, Y., Alves, M. I. R., ... et al. (2016, September). Planck 2015 results. I. Overview of products and scientific results. *Astronomy and Astrophysics*, *594*, A1. doi: 10.1051/0004-6361/201527101

Planck Collaboration, Adam, R., Ade, P. A. R., Aghanim, N., Alves, M. I. R., Arnaud, M., ... et al. (2016, September). Planck 2015 results. X. Diffuse component separation: Foreground maps. *Astronomy and Astrophysics*, *594*, A10. Retrieved from https://doi.org/10.1051/0004-6361/201525967 doi: 10.1051/0004-6361/201525967

Planck Collaboration, Adam, R., Ade, P. A. R., Aghanim, N., Arnaud, M., Aumont, J., ... et al. (2016, February). Planck intermediate results. XXX. The angular power spectrum of polarized dust emission at intermediate and high Galactic latitudes. *Astronomy and Astrophysics*, *586*, A133. doi: 10.1051/0004-6361/201425034

Planck Collaboration, Adam, R., Ade, P. A. R., Aghanim, N., Alves, M. I. R., Arnaud, M., ... Zonca, A. (2016). Planck 2015 results - x. diffuse component separation: Foreground maps. *A&A*, *594*, A10. Retrieved from https://doi.org/10.1051/0004-6361/201525967 doi: 10.1051/0004-6361/201525967

Planck Collaboration, Ade, P. A. R., Aghanim, N., Alves, M. I. R., Armitage-Caplan, C., Arnaud, M., ... et al. (2014a, November). Planck 2013 results. I. Overview of products and scientific results. *Astronomy and Astrophysics*, *571*, A1. doi: 10.1051/0004-6361/201321529

Planck Collaboration, Ade, P. A. R., Aghanim, N., Alves, M. I. R., Armitage-Caplan, C., Arnaud, M., ... et al. (2014b, November). Planck 2013 results. XIII. Galactic CO emission. *Astronomy and Astrophysics*, *571*, A13. Retrieved from https://doi.org/10.1051/0004-6361/201321553 doi: 10.1051/0004-6361/201321553

Planck Collaboration, Ade, P. A. R., Aghanim, N., Armitage-Caplan, C., Arnaud, M., Ashdown, M., ... et al. (2014, November). Planck 2013 results. IX. HFI spectral response. *Astronomy and Astrophysics*, *571*, A9. Retrieved from https://doi.org/10.1051/0004-6361/201321531 doi: 10.1051/0004-6361/201321531

Planck Collaboration, Ade, P. A. R., Aghanim, N., Arnaud, M., Arroja, F., Ashdown, M., ... et al. (2016a, September). Planck 2015 results. XIX. Constraints on primordial magnetic fields. *Astronomy and Astrophysics*, *594*, A19. doi: 10.1051/0004-6361/201525821

Planck Collaboration, Ade, P. A. R., Aghanim, N., Arnaud, M., Arroja, F., Ashdown, M., ... et al. (2016b, September). Planck 2015 results. XX. Constraints on inflation. *Astronomy and Astrophysics*, *594*, A20. doi: 10.1051/0004-6361/201525898

Planck Collaboration, Ade, P. A. R., Aghanim, N., Arnaud, M., Ashdown,

M., Aumont, J., ... et al. (2016, September). Planck 2015 results. XIII. Cosmological parameters. *Astronomy and Astrophysics*, *594*, A13. doi: 10.1051/0004-6361/201525830

Planck Collaboration, Ade, P. A. R., Aghanim, N., Alves, M. I. R., Armitage-Caplan, C., Arnaud, M., ... Zonca, A. (2014). Planck 2013 results. i. overview of products and scientific results. *A&A*, *571*, A1. Retrieved from https://doi.org/10.1051/0004-6361/201321529 doi: 10.1051/0004-6361/201321529

Planck Collaboration, Ade, P. A. R., Aghanim, N., Alves, M. I. R., Arnaud, M., Ashdown, M., ... Zonca, A. (2016). Planck 2015 results - xxv. diffuse low-frequency galactic foregrounds. *A&A*, *594*, A25. Retrieved from https://doi.org/10.1051/0004-6361/201526803 doi: 10.1051/0004-6361/201526803

Planck Collaboration, Ade, P. A. R., Aghanim, N., Arnaud, M., Ashdown, M., Aumont, J., ... Zonca, A. (2011). Planck early results. xx. new light on anomalous microwave emission from spinning dust grains. *A&A*, *536*, A20. Retrieved from https://doi.org/10.1051/0004-6361/201116470 doi: 10.1051/0004-6361/201116470

Planck Collaboration, Ade, P. A. R., Aghanim, N., Arnaud, M., Ashdown, M., Aumont, J., ... Zonca, A. (2016). Planck 2015 results - xiii. cosmological parameters. *A&A*, *594*, A13. Retrieved from https://doi.org/10.1051/0004-6361/201525830 doi: 10.1051/0004-6361/201525830

Planck Collaboration, Aghanim, N., Ashdown, M., Aumont, J., Baccigalupi, C., Ballardini, M., ... Zonca, A. (2017, February). Planck intermediate results. L. Evidence of spatial variation of the polarized thermal dust spectral energy distribution and implications for CMB B-mode analysis. *Astronomy and Astrophysics*, *599*, A51. doi: 10.1051/0004-6361/201629164

Planck HFI Core Team, Ade, P. A. R., Aghanim, N., Ansari, R., Arnaud, M., Ashdown, M., ... Zacchei, A. (2011). Planck early results. vi. the high frequency instrument data processing. *A&A*, *536*, A6. Retrieved from https://doi.org/10.1051/0004-6361/201116462 doi: 10.1051/0004-6361/201116462

Poletti, D., Fabbian, G., Jeune, M. L., Peloton, J., Arnold, K., Baccigalupi, C., ... Whitehorn, N. (2016, aug). Making maps of Cosmic Microwave Background polarization for B-mode studies: the POLARBEAR example. *eprint arXiv:1608.01624*, 1–26. Retrieved from http://arxiv.org/abs/1608.01624

Puglisi, G., Fabbian, G., & Baccigalupi, C. (2017, August). A 3D model for carbon monoxide molecular line emission as a potential cosmic microwave background polarization contaminant. *Monthly Notices of the Royal Astronomical Society*, *469*, 2982-2996. doi: 10.1093/mnras/stx1029

Puglisi, G., Poletti, D., Fabbian, G., & Baccigalupi, R., C. Stompor. (in prep.). Making polarization Cosmic Microwave Background maps with preconditioning. *A&A*.

Rees, M. J., & Sciama, D. W. (1968, February). Large-scale Density Inhomogeneities in the Universe. *Nature*, *217*, 511-516. doi: 10.1038/217511a0

Regan, M. W., Sheth, K., Teuben, P. J., & Vogel, S. N. (2002, July). Inner Molecular Rings in Barred Galaxies: BIMA Survey of Nearby Galaxies CO Observations. *Astrophysical Journal*, *574*, 126-133. doi: 10.1086/340793

Reichborn-Kjennerud, B., Aboobaker, A. M., Ade, P., Aubin, F., Baccigalupi, C., Bao, C., ... Zilic, K. (2010, July). EBEX: a balloon-borne CMB polarization experiment. In *Millimeter, submillimeter, and far-infrared detectors and instrumentation for astronomy v* (Vol. 7741, p. 77411C). doi: 10.1117/12.857138

Rest, A., Scolnic, D., Foley, R. J., Huber, M. E., Chornock, R., Narayan, G., ... Waters, C. (2014, November). Cosmological Constraints from Measurements of Type Ia Supernovae Discovered during the First 1.5 yr of the Pan-STARRS1 Survey. *Astrophysical Journal*, *795*, 44. doi: 10.1088/0004-637X/795/1/44

Riess, A. G., Filippenko, A. V., Challis, P., Clocchiatti, A., Diercks, A., Garnavich, P. M., ... Tonry, J. (1998, September). Observational Evidence from Supernovae for an Accelerating Universe and a Cosmological Constant. *Astronomical Journal*, *116*, 1009-1038. doi: 10.1086/300499

Riess, A. G., Macri, L. M., Hoffmann, S. L., Scolnic, D., Casertano, S., Filippenko, A. V., ... Foley, R. J. (2016, July). A 2.4% Determination of the Local Value of the Hubble Constant. *Astrophysical Journal*, *826*, 56. doi: 10.3847/0004-637X/826/1/56

Roman-Duval, J., Heyer, M., Brunt, C. M., Clark, P., Klessen, R., & Shetty, R. (2016, February). Distribution and Mass of Diffuse and Dense CO Gas in the Milky Way. *Astrophysical Journal*, *818*, 144. doi: 10.3847/0004-637X/818/2/144

Roman-Duval, J., Jackson, J. M., Heyer, M., Rathborne, J., & Simon, R. (2010, November). Physical Properties and Galactic Distribution of Molecular Clouds Identified in the Galactic Ring Survey. *Astrophysical Journal*, *723*, 492-507. doi: 10.1088/0004-637X/723/1/492

Rybicki, G. B., & Lightman, A. P. (1979). *Radiative processes in astrophysics*.

Seljak, U., & Zaldarriaga, M. (1996, October). A Line-of-Sight Integration Approach to Cosmic Microwave Background Anisotropies. *Astrophysical Journal*, *469*, 437. doi: 10.1086/177793

Seljak, U., & Zaldarriaga, M. (1997, March). Signature of Gravity Waves in the Polarization of the Microwave Background. *Physical Review Letters*, *78*, 2054-2057. doi: 10.1103/PhysRevLett.78.2054

Smith, K. M., & Zaldarriaga, M. (2007, Aug). General solution to the e-b mixing problem. *Phys. Rev. D*, *76*, 043001. Retrieved from http://link.aps.org/doi/10.1103/PhysRevD.76.043001 doi: 10.1103/PhysRevD.76.043001

Smoot, G. F., Bennett, C. L., Kogut, A., Wright, E. L., Aymon, J., Boggess, N. W., ... Wilkinson, D. T. (1992, September). Structure in the COBE differential microwave radiometer first-year maps. *Astrophysical Jour-*

nal, Letters, *396*, L1-L5. doi: 10.1086/186504

Starobinsky, A. A. (1982, November). Dynamics of phase transition in the new inflationary universe scenario and generation of perturbations. *Physics Letters B*, *117*, 175-178. doi: 10.1016/0370-2693(82)90541-X

Stebor, N., Ade, P., Akiba, Y., Aleman, C., Arnold, K., Baccigalupi, C., ... Zahn, O. (2016). The simons array cmb polarization experiment. In (Vol. 9914, p. 99141H-99141H-9). Retrieved from http://dx.doi.org/10.1117/12.2233103 doi: 10.1117/12.2233103

Stompor, R., Balbi, A., Borrill, J. D., Ferreira, P. G., Hanany, S., Jaffe, A. H., ... Wu, J.-H. P. (2002, January). Making maps of the cosmic microwave background: The MAXIMA example. *Physical Review D*, *65*(2), 022003. doi: 10.1103/PhysRevD.65.022003

Stompor, R., & Efstathiou, G. (1999, February). Gravitational lensing of cosmic microwave background anisotropies and cosmological parameter estimation. *Monthly Notices of the Royal Astronomical Society*, *302*, 735-747. doi: 10.1046/j.1365-8711.1999.02174.x

Story, K. T., Reichardt, C. L., Hou, Z., Keisler, R., Aird, K. A., Benson, B. A., ... Zahn, O. (2013, December). A Measurement of the Cosmic Microwave Background Damping Tail from the 2500-Square-Degree SPT-SZ Survey. *Astrophysical Journal*, *779*, 86. doi: 10.1088/0004-637X/779/1/86

Sunyaev, R. A., & Zeldovich, I. B. (1980, February). The velocity of clusters of galaxies relative to the microwave background - The possibility of its measurement. *Monthly Notices of the Royal Astronomical Society*, *190*, 413-420. doi: 10.1093/mnras/190.3.413

Suzuki, A., Ade, P., Akiba, Y., Aleman, C., Arnold, K., Baccigalupi, C., ... Zahn, O. (2016, August). The Polarbear-2 and the Simons Array Experiments. *Journal of Low Temperature Physics*, *184*, 805-810. doi: 10.1007/s10909-015-1425-4

Szydlarski, M., Grigori, L., & Stompor, R. (2014, December). Accelerating the cosmic microwave background map-making procedure through preconditioning. *Astronomy and Astrophysics*, *572*, A39. doi: 10.1051/0004-6361/201323210

Takakura, S., Aguilar, M., Akiba, Y., Arnold, K., Baccigalupi, C., Barron, D., ... Teply, G. (2017, May). Performance of a continuously rotating half-wave plate on the POLARBEAR telescope. *Journal of Cosmology and Astroparticle Physics*, *5*, 008. doi: 10.1088/1475-7516/2017/05/008

Tassis, K., & Pavlidou, V. (2015, July). Searching for inflationary B modes: can dust emission properties be extrapolated from 350 GHz to 150 GHz? *Monthly Notices of the Royal Astronomical Society*, *451*, L90-L94. doi: 10.1093/mnrasl/slv077

Tegmark, M. (1997a, October). CMB mapping experiments: A designer's guide. *Physical Review D*, *56*, 4514-4529. doi: 10.1103/PhysRevD.56.4514

Tegmark, M. (1997b, May). How to Make Maps from Cosmic Microwave Background Data without Losing Information. *Astrophysical Journal,*

Letters, *480*, L87-L90. doi: 10.1086/310631

The POLARBEAR Collaboration, Ade, P. A. R., Aguilar, M., Akiba, Y., Arnold, K., Baccigalupi, C., ... Zahn, A. (2017, may). A Measurement of the Cosmic Microwave Background B-Mode Polarization Power Spectrum at Sub-Degree Scales from 2 years of POLARBEAR Data. *Astrophysical Journal, Supplement*. Retrieved from http://arxiv.org/abs/1705.02907

Trumpler, R. J. (1934, August). Galactic Light Absorption. *Publications of the ASP*, *46*, 208-210. doi: 10.1086/124462

Tytler, D., O'Meara, J. M., Suzuki, N., & Lubin, D. (2000). Big bang nucleosynthesis. *Nuclear Physics B - Proceedings Supplements*, *87*(1), 464 - 473. Retrieved from http://www.sciencedirect.com/science/article/pii/S0920563200007210 doi: http://dx.doi.org/10.1016/S0920-5632(00)00721-0

Vallée, J. P. (2014, November). Catalog of Observed Tangents to the Spiral Arms in the Milky Way Galaxy. *Astrophysical Journal, Supplement*, *215*, 1. doi: 10.1088/0067-0049/215/1/1

Wald, R. (1984). *General relativity*. University of Chicago Press. Retrieved from https://books.google.it/books?id=ibSdQgAACAAJ

West, P. (1990). *Introduction to Supersymmetry and Supergravity* .

Wolfire, M. G., McKee, C. F., Hollenbach, D., & Tielens, A. G. G. M. (2003, April). Neutral Atomic Phases of the Interstellar Medium in the Galaxy. *Astrophysical Journal*, *587*, 278-311. doi: 10.1086/368016

Wright, E. L. (1996, November). Scanning and Mapping Strategies for CMB Experiments. *ArXiv Astrophysics e-prints*.

Yadav, A. P. S., Biswas, R., Su, M., & Zaldarriaga, M. (2009, June). Constraining a spatially dependent rotation of the cosmic microwave background polarization. *Physical Review D*, *79*(12), 123009. doi: 10.1103/PhysRevD.79.123009

Zaldarriaga, M., & Harari, D. D. (1995, September). Analytic approach to the polarization of the cosmic microwave background in flat and open universes. *Physical Review D*, *52*, 3276-3287. doi: 10.1103/PhysRevD.52.3276